LUND UNIVERSITY

Modeling of Elasticity and Damping for Filled Elastomers

Austrell, Per Erik

1997

Document Version:
Publisher's PDF, also known as Version of record

Link to publication

Citation for published version (APA):
Austrell, P. E. (1997). *Modeling of Elasticity and Damping for Filled Elastomers*. [Doctoral Thesis (monograph), Structural Mechanics]. Structural Mechanics, Lund University.

Total number of authors:
1

General rights
Unless other specific re-use rights are stated the following general rights apply:
Copyright and moral rights for the publications made accessible in the public portal are retained by the authors and/or other copyright owners and it is a condition of accessing publications that users recognise and abide by the legal requirements associated with these rights.
- Users may download and print one copy of any publication from the public portal for the purpose of private study or research.
- You may not further distribute the material or use it for any profit-making activity or commercial gain
- You may freely distribute the URL identifying the publication in the public portal

Read more about Creative commons licenses: https://creativecommons.org/licenses/

Take down policy
If you believe that this document breaches copyright please contact us providing details, and we will remove access to the work immediately and investigate your claim.

LUND UNIVERSITY

PO Box 117
221 00 Lund
+46 46-222 00 00

LUND UNIVERSITY | LUND INSTITUTE OF TECHNOLOGY
Division of Structural Mechanics | Sweden 1997 | Report TVSM-1009

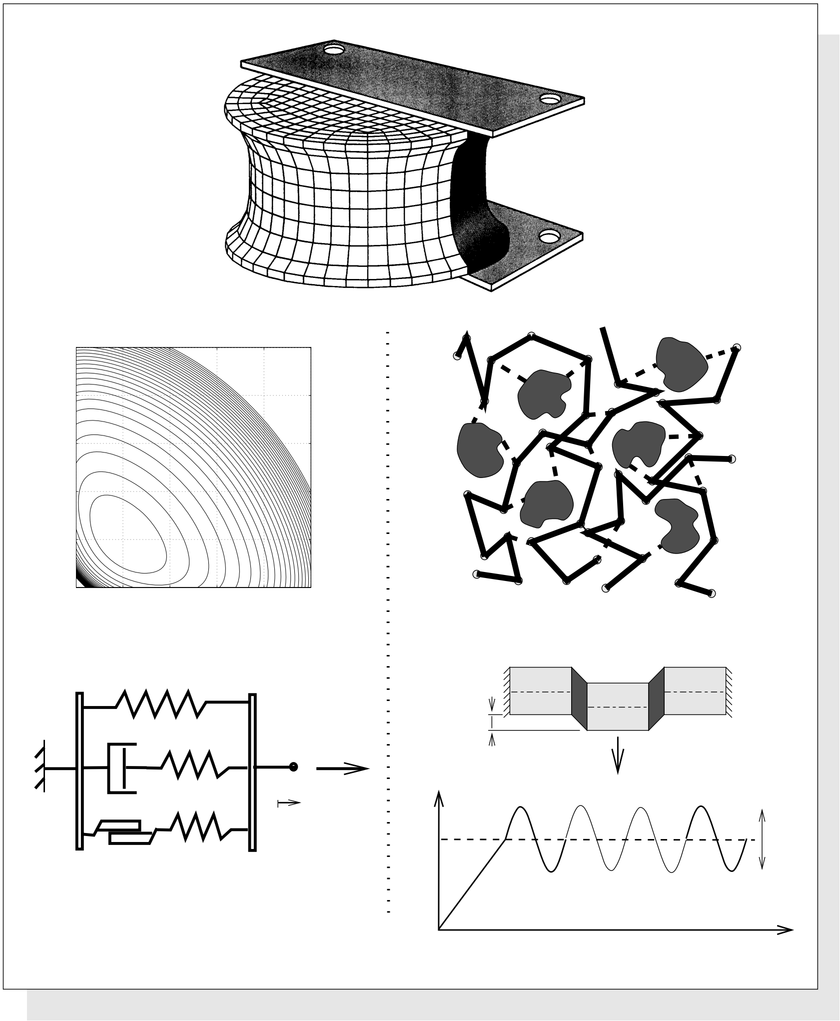

MODELING OF ELASTICITY AND DAMPING FOR FILLED ELASTOMERS

PER-ERIK AUSTRELL

LUND UNIVERSITY | LUND INSTITUTE OF TECHNOLOGY
Division of Structural Mechanics | Sweden 1997 | Report TVSM-1009
CODEN: LUTVDG / (TVSM-1009) / 1-222 / (1997) | I SSN 0281-6679

MODELING OF ELASTICITY AND DAMPING FOR FILLED ELASTOMERS

PER-ERIK AUSTRELL

PREFACE

This thesis is mainly a result of work in the project *Constitutive Parameters and Calculation Methods for Elastomeric Materials.* (In Swedish: "Materialparametrar och beräkningsmetoder för komponenter av gummimaterial"). The project started in July 1993 and ended in June 1996. It was financed by NUTEK-the Swedish National Board for Industrial and Technical development.

The project involved Structural Mechanics in Lund and the rubber manufacturers Forsheda, Skega and Trelleborg. The corporate research institutes IVF -the Swedish Institute of Production Engineering Research- and IFP -the Swedish Institute for Fibre and Polymer Research- were also connected to the project.

The focus was on mechanical behavior of elastomeric materials and computer methods applicable to design of elastomeric units. The activities were concentrated on elastic properties in the first part of the project, and the second part of the project was devoted to dynamic material properties. Constitutive models, experimental procedures, methods for evaluation of test data, and computational methods have been investigated.

The background of the project was a cooperation with Skega AB (today: Svedala-Skega AB) rubber company that started on a small scale in 1990. The cooperation developed during 1991 and 1992 and plans for an extended cooperation in a formal project were outlined in an application to NUTEK. It was the intention of the NUTEK committee that the project should also involve the other two large rubber manufacturers in Sweden; Forsheda AB and Trelleborg AB. (Trelleborg AB is Swedens largest rubber manufacturer.) The corporate research institutes IFP and IVF were also financed by NUTEK and coordinated to the project.

I wish to express my gratitude to the participants of the project for their interest and cooperation. A special appreciation is directed to Erik Östman and Sture Persson, Svedala-Skega rubber company, for their devotion, valuable discussions and help with the rubber specimens for the laboratory tests.

Part of the results in the project are three completed master thesis works that I very much enjoyed supervising. The works [35], [1] and [47] in the bibliography, have been the final efforts for M.Sc's Kristian Lönnqvist, Anders Thelin, Aylin Ali, and Martin Pilcher in their education at Lund Institute of Technology, and I wish to express my gratitude for their work. Martin Pilcher was also employed for some months at the department, and during that time he contributed to the project by report [48] and to the content of Chapter 6. It should also be mentioned that Section 7.2 is largely based on the work of Aylin Ali [1].

Much of the work, and an important part of it, is of experimental character. Bertil Enquist and Rizalina Brilliante are responsible for the function and handling of the laboratory equipment at the department. Their skillful aid in the laboratory tests is greatly appreciated and very important for the thesis.

The contact-free strain measurement was carried out together with Anders Heyden at the Department of Mathematics and I greatly appreciate that cooperation. I also want to thank Dr Tamas Pritz for interesting discussions on dynamic properties of elastomers, Dr Mats Berg for valuable discussions concerning modeling of damping in rubber springs, and Dr Matti Ristinmaa and Dr Christer Nilsson for valuable discussions on constitutive modeling.

Professor Hans Petersson established the contact with Erik Östman and Sture Persson at Svedala-Skega. The connection to "the real world" through the rubber companies gave me a focus in my work, and this was very important for my motivation.

Finally I wish to thank associate Professor Göran Sandberg for his encouragement and stimulating discussions during the course of this work and for his aid in the contacts with NUTEK.

Per-Erik Austrell, Lund, March 1997

ABSTRACT

Elasticity and damping are significant properties of rubber, taken advantage of in engineering applications. It is therefore important that the constitutive model accurately captures these aspects of the mechanical behavior.

In the first part of the thesis a description of theory and experiments for determination of hyperelastic parameters required for finite element analysis is provided. Test specimens and corresponding stress-strain relations for calibration of the hyperelastic models are discussed. Mechanical conditioning procedures are compared and fitting of the models are discussed, with special emphasis on a "cubic I1" model proposed by O.H. Yeoh. A strain energy plot to check the quality of the fitted model is presented, which reveals whether the model is valid for use in finite element analysis. The accuracy of existing test specimens, and a new axisymmetric combined compression and tension specimen proposed here, are investigated by finite element analysis. A modified hardness test for evaluation of hyperelastic constants is presented and evaluated by finite element analysis. Moreover, a method for contact-free strain measurement for evaluation of surface strain fields is presented. Experimental deformation gradients can also be obtained by this method.

The second part of the thesis concerns modeling of dynamic material properties of filled rubbers. Experiments show that constitutive models available in commercial finite element codes are not able to model the behavior of filled rubber vulcanizates in dynamic applications. One-dimensional models are used to examine the mechanisms of damping in these rubbers. The ability of the models to capture the frequency and amplitude dependence of the dynamic modulus and equivalent phase angle is investigated. The microstructure and the experimental results support a model with nonlinear elastic, viscous (rate-dependent) and frictional (rate independent) elements connected in parallel. A generalization of this one-dimensional viscoplastic model to multiaxial and large strains is proposed and evaluated in simple shear and uniaxial stress.

KEY WORDS:
hyperelasticity, carbon-black-filled rubbers, strain energy plot, mechanical conditioning, solid dumbbell test specimen, modified hardness test, contact-free strain measurement, rheological models, amplitude dependence, multiaxial viscoplastic model

CONTENTS

1. INTRODUCTION

This introduction presents the background and objective of the present work, a brief description of the molecular structure and manufacturing process for rubber vulcanizates, various mechanical properties, the general procedure in computer aided design of rubber units, and a discussion of constitutive models. Finally, this chapter also presents an overview of the contents of the thesis and some reading suggestions.

1.1. Background

The unique properties of elastomeric materials are taken advantage of in many engineering applications. Elastomeric units are used as couplings or mountings between stiff structures. Examples are shock absorbers, vibration insulators, flexible joints, sealings and suspensions.

The development of computers and analysis programs has given engineers a new tool in design and construction of elastomeric components. Computer simulation by finite element analysis have become increasingly important. The mechanical behavior for complicated geometries and loading cases can be evaluated. Both static and dynamic aspects can be analyzed by computer simulations. This has been recognized by the manufacturers of rubber products and their customers. The benefits are shorter time for product development and also quality improvements.

However, the possibilities available in the use of elastomers in construction, with less complicated technical solutions at a lower cost, are not fully utilized. Rubber components could be used more frequently in constructions if more engineers were familiar with the material.

Part of the problem lies in education and information. The material and its properties are not very well known among engineers working with design and construction. Courses on the mechanics of polymers are very limited at schools and universities. The skillful engineers in this field have usually acquired their knowledge through many years of experience and not from formal education.

Moreover, the complicated nature of the material behavior makes it difficult to devise general design rules and design tools. It was only recently that computers and programs became powerful enough for analysis of nonlinear elastic problems with large strains.

Nevertheless, it is essential for the manufacturers, in order to be competitive in high-tech applications, to acquire knowledge of the computer methods, material models and test methods available. This is necessary to meet the demands from customers who want to use the available tools, in for example the automotive industry or in the off-shore industry.

This development has focused on the lack of relevant material data for computer analysis. The design tools rely on the available material models and on relevant test data for calibration of these models. In many cases the only information available for the analysis is a value of the rubber hardness.

The wide variety of rubber compounds is a problem. Characterization of the different materials is costly and time consuming. Hence, there is a need for simple and reliable methods to characterize the different vulcanizates.

1.2. Objective

Elasticity and damping are characteristic properties of rubber, and it is therefore important that the constitutive model accurately capture these aspects of the mechanical behavior. The purpose of the thesis is to shed some light upon these aspects of constitutive modeling and to examine experimental procedures and test specimens for calibration of the models. The discussion is focused mainly on filled rubbers, since these are by far used most in technical applications.

A good description of the elastic behavior is essential, since design of rubber units usually starts with some form of static elastic analysis, with the purpose of deriving either a particular load-deflection curve or checking the stress levels in the unit. Well-established so-called hyperelastic constitutive models, derived from a strain energy function, are implemented in many commercial finite element codes. The first part of the thesis concerns these elastic models and the calibration to experiments.

With regard to dynamic applications, commercial finite element codes rely on viscoelastic constitutive models, which essentially are generalizations of linear viscoelasticity to large strains. These viscoelastic models are well suited for unfilled rubbers. However, rubbers in engineering applications are, as mentioned, usually loaded with fillers, giving mechanical properties that deviate from the properties of the pure rubber base. Viscoelasticity is not suitable for these rubbers, especially for highly filled materials. The deviations from viscoelasticity and aspects of the nonlinear dynamic behavior that are introduced by adding filler are discussed in the second part of the thesis.

1.3. Material properties

Here follows a brief description of molecular structure, manufacturing process and mechanical properties that can be found in general textbooks, for example in the comprehensive book by Freakly and Payne [16]. Other less extensive texts on engineering with rubber have been written by, for example, Göbel [24] and Lindley [33].

1.3.1. Molecular structure and manufacturing process

Rubber is a collective name for a broad group of materials with different chemical composition but similar molecular structure and mechanical properties. The word "rubber" originates from the pencil lead erasing property of natural gum rubber. The fact that all rubber materials are highly elastic polymers is the origin of the alternative and more descriptive name *elastomer.*

There are elastomers made from a wide variety of organic substances, but they are all polymers with very long molecular chains. The raw elastomeric material can be either natural or synthetic. Latex, the sap of a tropical "rubber" tree, coagulated in thin sheets and compressed into bales, is the raw material in natural rubber. The basic organic substance, the monomer, consists mainly of isoprene. There are no chemical bonds between the molecular chains, and as a consequence the raw material is of a soft and plastic consistency.

Natural rubber was used in the first elastomeric units manufactured, and it is still the most common material in general purpose applications. The most common synthetic rubber is made with butadiene as a base, and the main application is in car tires, because of the good abrasion resistance.

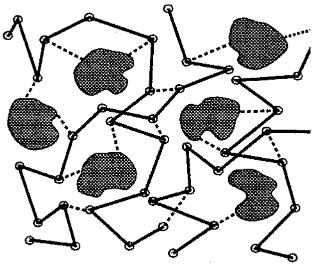

Figure 1.1: *Molecular structure for a carbon-black-filled rubber vulcanizate. Carbon particles, polymer chains and crosslinks are schematically illustrated.*

The important process of *vulcanization*, that was discovered by Charles Goodier in 1839, converts the plastic raw elastomeric material into a solid and elastic consistency. Vulcanization is a chemical process where the long molecular chains are linked together and thereby form a stable and more solid molecular structure. The cross linking is enabled by a small amount of sulfur that is mixed with the plastic raw material. When the mixture is heated to about 170^oC the vulcanization process starts and crosslinks are formed, connecting the molecular chains.

Fillers such as *carbon-black* are added in order to increase the stiffness of the material or, for some applications, to increase the resistance to wear. Carbon-black consists of very small particles of carbon ($20nm$ - 50μm) that are mixed into the raw rubber base before vulcanization. The filler and the elastomeric material are not chemically joined; they are separate phases in the vulcanized rubber connected only by the crosslinks. The rubber phase forms a continuous network, and the filler material forms agglomerates inside the rubber network. The material is thus a two-phase material made from constituents with completely different mechanical properties. Figure 1.1 shows schematically the structure on a molecular level of a carbon-black-filled vulcanizate. The polymer chains are shown as solid lines and crosslinks are shown as dashed lines.

Vulcanization and shaping are combined in the so-called *moulding* process. The rubber-filler mix is inserted into the mould cavity and heated to the appropriate temperature, and the vulcanization starts. The curing time is dependent on the temperature, the size of the unit and on how well heat is transferred to the unit.

Elastomeric units in technical applications are often composed of both rubber and steel. The attached steel parts are used to connect the rubber unit to other structures or to increase the stiffness of the unit. It is possible to attach steel parts to the rubber material in the moulding process. The steel parts are bonded, very efficiently, to the rubber. The bond is stronger than the rubber material itself in the sense that a rupture in a properly manufactured rubber-steel unit usually occurs in the rubber and not at the bonding surface between rubber and steel.

1.3.2. Mechanical properties

The main specific properties of elastomeric materials taken advantage of in engineering applications are the ability to sustain large straining without permanent deformation, the vibration damping property and the resistance to lubrication.

The *elastic property* is the most prominent characteristic feature of vulcanized rubber. The ability to store large amounts of strain energy and to release most of it in unloading is a primary function. The molecular structure enables it to undergo large deformations and recover almost completely in unloading. However, the material becomes less elastic and more leathery as more filler is mixed in to the compound.

The elasticity of rubber is due to the long tangled molecular chains and their ability to stretch and orient themselves in the direction of straining. This is possible because the repeated molecular units in the polymer can rotate freely about the bonds joining the units. Elongations of several hundred percent are possible.

Another characteristic feature of rubber is the large difference between the shear modulus and the bulk modulus. A typical carbon-black-filled rubber vulcanizate for technical applications has a shear modulus of about 1MPa and a bulk modulus

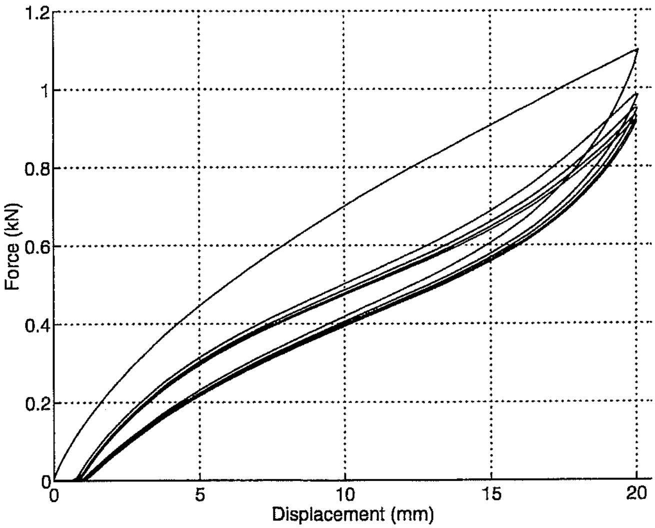

Figure 1.2: *Force-displacement relations for a rubber vulcanizate exposed to cyclic loading.*

of about 2000 MPa (Freakly and Payne [16] p. 32). The large volumetric stiffness compared to the shear stiffness indicates a *nearly incompressible* behavior. In many applications complete incompressibility is a good assumption.

Although rubber is a highly elastic material it is not perfectly elastic. A difference is always observed between the loading and the unloading curves in a stress-strain diagram. This phenomenon is referred to as *hysteresis*, and it is illustrated in Figure 1.2 for a carbon-black-filled rubber in planar tension. (Typical values of stress and strain will be given below for tension/compression and shear.) In cyclic loading there is thus always a part of the energy that is not recoverable. The area enclosed by the loading and unloading curves represents energy dissipated mainly as heat. In free vibrations this causes the amplitude of the vibrations to decrease, and this material property is therefore termed *damping.* Adding fillers to the rubber compound increases the damping. The origin and modeling of damping will be discussed further in the second part of the thesis.

Stress softening or Mullin's effect [42] is another phenomenon which has to be considered. This decrease in stiffness by straining is seen in Figure 1.2. If a previously unstrained rubber specimen is exposed to cyclic loading up to a specific strain level, the maximum stress and the distance between the loading and unloading curves will decrease in the first few load cycles. After about three to five load cycles a steady state will be reached at this specific maximum strain level. If the specimen is exposed to a new set of cyclic straining to a higher strain level, there will be a

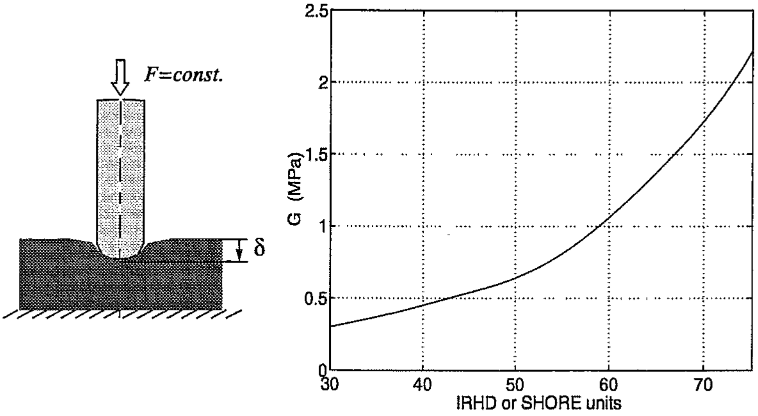

Figure 1.3: *Relationship between the shear modulus G and the hardness in IRHD or SHORE units.*

new decrease in stress and hysteresis until a new steady state is reached. The strain softening behavior originates from a gradual breakdown of molecular crosslinks and to configurational changes in the rubber network, with increasing strain.

In order to get stationary values in the testing of rubber specimens it is thus necessary to pre-strain the specimens before conducting the actual recording of corresponding force-displacement values. This is called *mechanical conditioning.*

The filler phase has a very small stress carrying capacity as compared to the rubber phase. The filler particles can be regarded as rigid inclusions embedded in the rubber matrix. Consequently the stress and strain in the rubber phase will reach higher levels in elastomeric units with filler added than will an equally loaded and identical unfilled unit. The filler will also affect the maximum elongation (at break), which is lowered by adding fillers. This effect of the filler on the rubber phase is called *strain amplification.*

Stiffness of a rubber vulcanizate is classified by a value of *hardness.* It is measured by an indentation test with a ball or needle with a spherical tip. A constant force is applied and the indentation depth is measured. There are two methods, the IRHD test (International Rubber Hardness Degrees) which is also the ISO standard test, and the Shore Hardness test. The scales of the tests are almost identical for rubbers in the range of 30-80 IRHD where most rubber mixes belong. The hardness test gives an indirect measure of the elastic modulus. This is sometimes the only value available for the modulus of the material. The relationship between the shear modulus G and hardness is indicated in Figure 1.3. The diagram is constructed from Lindley [33] (Table 3, p. 8). An extension of the hardness test is discussed in Chapter 7.

Simple shear is more linear than other homogeneous modes of deformation. The shear modulus is quite independent of the shear strain and it can therefore be re-

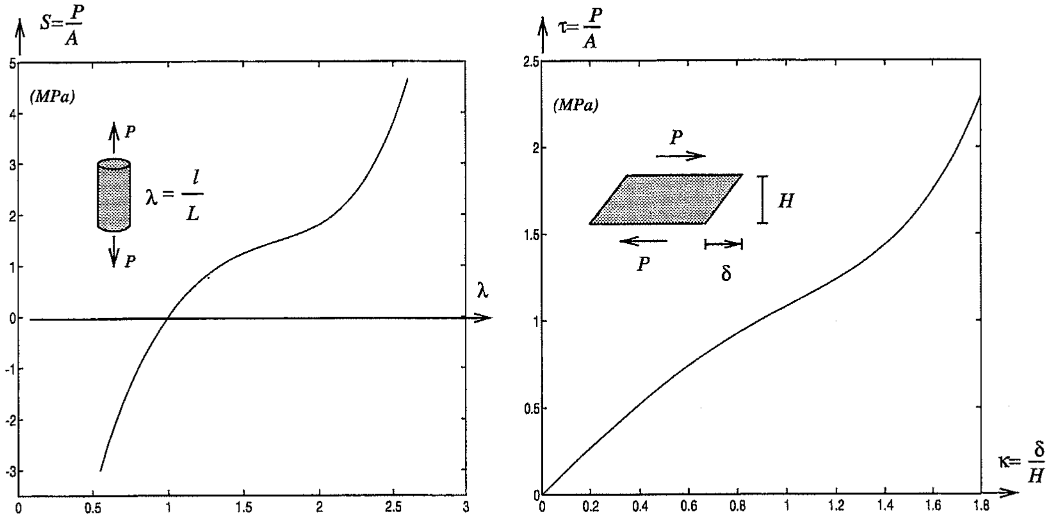

Figure 1.4: *Homogeneous deformations of a 60 IRHD rubber. Left: Uniaxial state of stress. Right: Simple shear.*

garded as a material constant at least for moderate strains. This is not the case for Young's modulus as can be seen in Figure 1.4, where loading curves in compression/tension and simple shear are shown for a 60 IRHD carbon-black-filled natural rubber vulcanizate. (The curve illustrating the uniaxial state of stress is composed of a tension test and a compression test.) The behavior of rubber in compression is progressive. For tension and simple shear the behavior is first digressive and then progressive for large strains.

Some dynamic properties will also be discussed briefly here, although this is mainly the concern of the second part of the thesis.

Dynamic tests, performed in simple shear with unfilled rubber vulcanizates for small amplitudes, yield *linear dynamic* response, a behavior characterized by sinusoidal response to sinusoidal excitation. The response is of the same frequency as the excitation. However the response is shifted by a phase angle δ.

Picturing the stress-strain loop yields an elliptic path, according to Figure 1.5. (The static load is assumed to be applied slowly.) The elliptic hysteresis is associated with dissipated energy. The energy loss for a strain cycle U_c is related to the phase angle δ according to $U_c = \pi\tau_0\kappa_0 sin\delta$, with τ_0 and κ_0 being the shear stress and strain amplitudes respectively. The expression will be derived in connection with linear viscoelastic models in Chapter 9.

The use of rubber components often involves both static and dynamic properties. Cyclic straining in combination with a static preload is a common load case. The

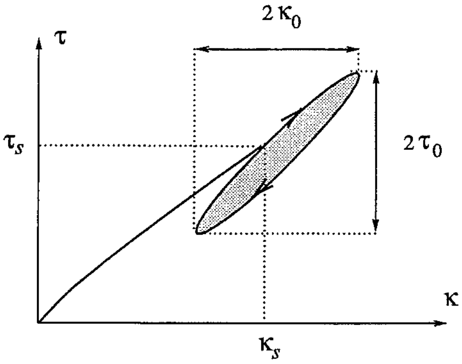

Figure 1.5: *Static and dynamic stress and strain.*

static and dynamic shear moduli are defined as

$$G_{stat} = \frac{\tau_s}{\kappa_s} \qquad G_{dyn} = \frac{\tau_0}{\kappa_0},$$

according to Figure 1.5. The *dynamic modulus* is always larger than the static modulus, as indicated in the figure.

The dynamic properties of rubber change with the influence of temperature and frequency. The dynamic modulus and the phase angle are frequency and temperature dependent. Increased temperature has a softening effect, and increased frequency has a stiffening effect. The dependence however, is quite weak [33] for frequencies below 1000 Hz and temperatures from 0 to $50°C$, for commonly used natural rubber vulcanizates.

Nonlinearities in the dynamic behavior appear as a distortion of the hysteresis loop. These nonlinearities are due to nonlinear elasticity of the rubber network, and, for filled rubbers, also due to the filler structure breakdown and reforming. The filler induced nonlinearity appears as a decrease of the dynamic shear modulus with increasing amplitude. Linear and nonlinear dynamic properties of rubber will be discussed further in the second part of the thesis.

1.4. Modeling

This section contains a brief discussion of design and modeling of elastomeric components. Finite element analysis and models describing the mechanical behavior of rubber materials are discussed.

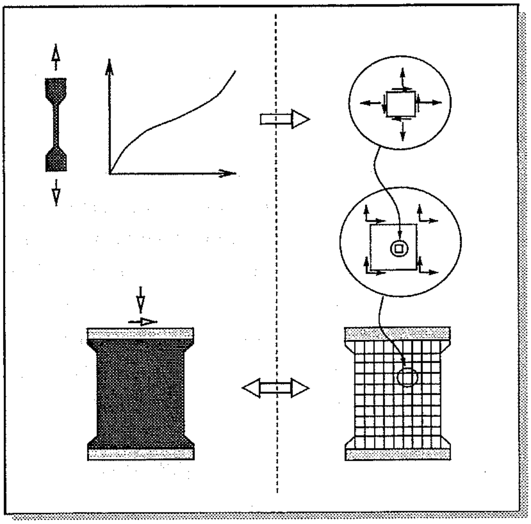

Figure 1.6: *Material characterization, finite element analysis, and comparative testing.*

The design of elastomeric components is mainly based on a static analysis with the purpose of deriving a particular load-deformation characteristic. This is achieved either by hand calculation methods or by computer calculation methods such as the finite element method. For rubber units with complex geometry, the hand calculation methods are of limited value and computer methods have to be used.

1.4.1. Design of elastomeric units

Design of rubber units relies on three essential constituents, illustrated in Figure 1.6, i.e.

- Laboratory tests of rubber specimens.
- Determination of parameters in the mathematical model of the particular elastomeric material.
- Geometric modeling and simulation of the unit's mechanical behavior.

The first item concerns the experimental stress-strain values for the particular elastomeric material. Test specimens, made of the same material as the rubber unit to be designed, are manufactured and tested in the laboratory. The obtained pairs of measured stress-strain values are then used to calibrate the *constitutive model*, i.e. the mathematical model connecting stress and strain.

The constitutive model is fitted to the experimentally obtained stress-strain relation, and the parameters in the model are determined by some fitting procedure, for example *the method of least squares.*

The first two items above, which are also the main subjects of the thesis, result in a set of parameters defining the constitutive model of the elastomeric material. These parameters, together with a geometric description and a specification of the loads, provide the input to the computer simulation in item three above.

The most versatile and successful computational method in solid mechanics is the *finite element method.* It provides a systematic procedure for analysis of structures of different types of material and arbitrary geometric form. The structure to be analyzed is divided into smaller parts, elements, connected in nodal points. The force-displacement relation for a particular element, i.e. the connection between nodal forces and displacements, can be obtained only if the relation between stress and strain in the element is known. This relation is provided by the constitutive model. The hierarchical construction of the finite element model is illustrated in Figure 1.6.

The well-known books of Zienkiewicz and Taylor (vol.1 and 2) [68] give a comprehensive treatment of several aspects of finite element analysis. An introduction to the finite element method can be found in e.g. [44].

An example of the capabilities provided by finite element analysis is shown in Figure 1.7. A simulation of mounting and compression of a sealing for concrete pipes has been carried out as a M.Sc. thesis work [47]. Rigid elements are used in the mounting and compression steps. The analysis involves several intricate features of finite element analysis, such as large strains, nonlinear material behavior, contact conditions, and nearly incompressible behavior. The analysis can, among other things, reveal whether the contact pressure between the pipe and the sealing is large enough.

The handling of incompressible material behavior is a specific problem in finite element analysis. A large difference between deviatoric (shear) and volumetric stiffness tends to make ordinary elements far too stiff, and even complete "locking" can be encountered. Special "hybrid" elements have been developed that can circumvent the locking phenomena.

Several general purpose finite element codes are available. Examples are ABAQUS, ANSYS, and NASTRAN, to mention some of the best known.

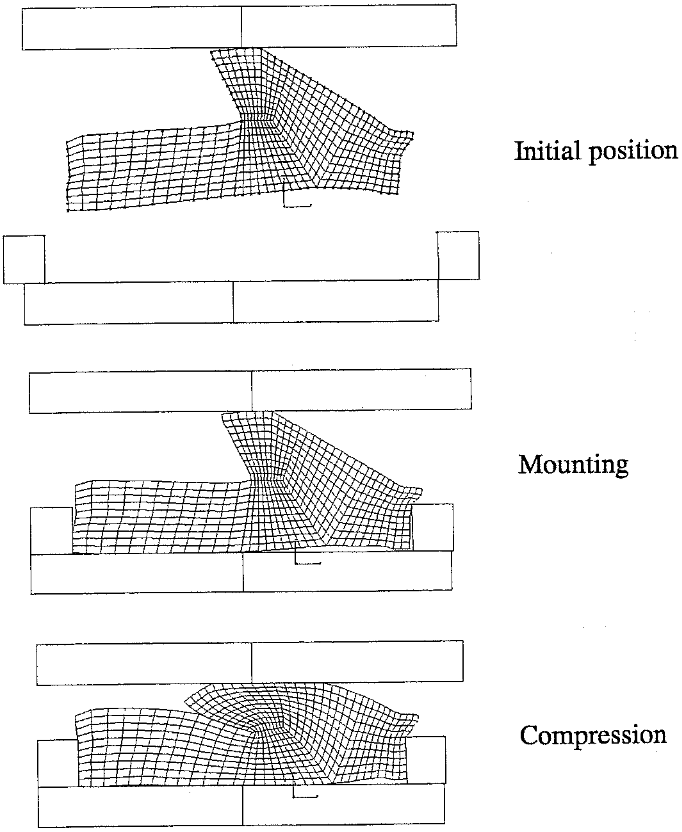

Figure 1.7: *Example: Analysis of a sealing by computer simulations by the finite element method.*

1.4.2. Constitutive models of rubber

A general overview of constitutive models and stress and strain measures is presented in books on continuum mechanics; see for example Malvern [37]. The discussion here will concern the rheological model in Figure 1.8. Modeling of elasticity and damping will be discussed briefly here in terms of the one-dimensional model.

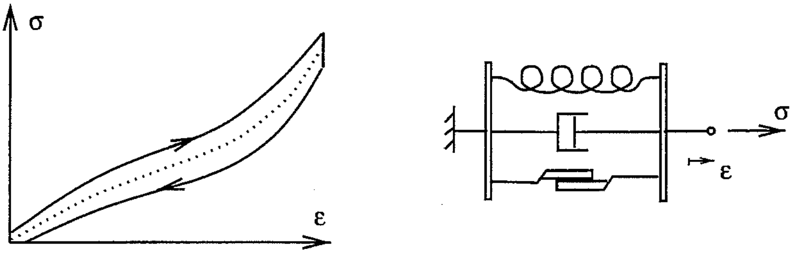

Figure 1.8: *One-dimensional mechanical analog of filled-rubber behavior.*

The elastic behavior is provided by the spring element, which is assumed to be nonlinear. Damping is provided by a rate-dependent viscous damper and a rate-independent element. The rate-independent part is symbolized by a frictional element, consisting of two blocks with sliding contact between the surfaces. The elastic, viscous, and frictional stresses act in parallel, and the sum of the stresses is added to the total stress, i.e.

$$\sigma = \sigma_e + \sigma_v + \sigma_f,$$

where σ_e is the nonlinear elastic stress, σ_v is the viscous stress, and σ_f is the frictional stress.

If the model is subjected to loading followed by unloading, the response in a stress-strain diagram will exhibit behavior as shown in Figure 1.8, giving a difference between the loading and unloading paths. The elastic response, i.e. the nonlinear spring characteristic, is indicated by the dotted line. The viscous part of the stress will gradually vanish if the strain rate is approaching zero. This is a reasonable assumption for rubbers without fillers. However, for filled rubbers there will always be a difference between the loading and unloading curves even if the strain rate is approaching zero. A rate-independent frictional stress component is therefore necessary to model the behavior of filled elastomers.

The model is consistent with the microstructure of a filled rubber as shown in Figure 1.1. The elastic stress and the rate-dependent resistance are due to the rubber network, and the rate-independent stress is due to the filler. The forces that develop in the rubber network and between the filler particles act in parallel. The damping due to the filler will add to the damping in the rubber network.

The model incorporates some important aspects of the mechanical behavior of filled rubbers. It provides a qualitative and conceptual understanding of properties such as frequency dependence, effects of static load on the dynamic modulus, distortion of the hysteresis loop, and amplitude dependence. However, it has some apparent nonphysical properties, and it should not be interpreted as an exact quantitative model of elastomeric materials. For example, the stress response can be discontinuous even if the strain is continuous and the model does not incorporate relaxation behavior. However, the sketched model is a starting point for modeling of elasticity and damping mechanisms in filled rubbers, and developments of it will be discussed further in the second part of the thesis.

A general constitutive model should be able to handle multiaxial stress and strain. Established models applicable to the behavior of rubber are nonlinear elastic models and viscoelastic models.

A theory of rubber elasticity based upon the molecular structure of the chain network, called the statistical theory, was developed by Treloar [63] and others. This theory led to a strain energy expression containing only one material parameter that can be identified as the shear modulus. Mooney [39] and Rivlin [51] developed the phenomenological theory of rubber elasticity. Mooney initiated the work and Rivlin developed a general theory. The basis of the phenomenological theory is a strain energy expression, postulated without molecular considerations. The elastic properties are determined by choosing a suitable strain energy expression. The first part of the thesis concerns applications of this theory.

Viscoelasticity provides a way to take into account time and frequency dependent properties of rubber behavior. A simple one-dimensional viscoelastic model is obtained by connecting a spring and a viscous damper in parallel. This specific model is known as the Kelvin-Voigt model.

The general theory of linear viscoelasticity was derived by applying Boltzmann's superposition principle to creep and relaxation behavior.

Connecting the rate-independent frictional element to the Kelvin-Voigt model yields a viscoplastic model. One-dimensional models, often expressed in terms of force-displacement relations, incorporating rate-independent damping, have been proposed as models of rubber components, for example in vehicle dynamics or earthquake protection applications. However, there seem to be no three-dimensional viscoplastic large strain models describing the behavior of filled rubbers. These models have so far mainly been applied to metals.

Most commercial finite element codes available for nonlinear analysis can handle nonlinear elastic problems by using hyperelastic constitutive models. However, in order to handle dynamic problems involving damping, only a few codes have this ability. The constitutive models in these codes combine hyperelasticity and viscoelasticity. These visco-hyperelastic models are modified linear viscoelastic models for large strains, with purely rate-dependent damping. Some commercial codes [26] include options for steady-state dynamic problems considering small viscoelastic vibrations overlaid on a large static elastic deformation.

1.5. Overview

This thesis can, of course, be read in many different ways. The abstract and this introduction is one level. The introduction to rubber elasticity (Chapter 2), the introduction to damping mechanisms (Chapter 8), and the summary in Chapter 14 is a second level. These parts give an overview without complicated mathematics and should be readable by non-specialists as well. There is also a description of basic concepts, such as strain and stress measures, provided in the Appendix.

The thesis is presented in two parts. The first concerns elastic properties, and the second concerns damping and dynamic properties.

The first part treats hyperelastic constitutive models and the correlation of these models to experiments. Chapter 2 gives an introduction to nonlinear elasticity and fit to test data. Hyperelastic models and the strain energy density are discussed in Chapter 3. Test specimens and corresponding stress-strain relations are discussed in Chapter 4. Mechanical conditioning and fit to test data are discussed in Chapter 5. Special emphasis will be on a three-parameter model proposed by O.H. Yeoh. The quality of the fitted model is checked by use of a strain energy plot. The ability of the models in fittings to test data for carbon-black-filled natural rubber vulcanizates is also investigated.

The accuracy of different test specimens, i.e. the deviation from the ideal homogeneous states of strain, are analyzed in Chapter 6.

Alternative test specimens and methods are discussed in Chapter 7. A new test specimen is proposed that can replace the standard dumbbell specimen, a method that uses a modified form of the hardness test to extract hyperelastic constants is presented, and a method for contact-free strain measurement is also presented in this chapter.

The second part concerns dynamic properties, with a discussion of damping mechanisms in filled elastomers. The ability to model the dependence of the dynamic modulus on frequency and amplitude is discussed. The introduction to this part (Chapter 8) gives an overview of experimental results and a brief discussion of dynamic material models. These models are discussed in more detail and compared with experiments in subsequent chapters.

Linear viscoelasticity is discussed in Chapter 9. Basic features such as the hereditary integral, relaxation modulus, and complex modulus are defined and specific models are illustrated by use of rheological models.

Rate-independent damping is discussed in Chapter 10 in terms of one-dimensional elasto-plastic models. A combination of rate-independent and rate-dependent damping is studied and compared with experiments in Chapter 11.

Models available in commercial finite element codes for dynamic behavior of rubber are modified linear viscoelastic models that take large strain into account. These models are the subject of Chapter 12.

Finally, in Chapter 13, a possible multiaxial large strain generalization of the one-dimensional viscoplastic model is discussed.

Part I

ELASTIC PROPERTIES

2. INTRODUCTION TO RUBBER ELASTICITY

This chapter serves as an introduction to nonlinear elastic material models. Hyperelastic models defined from a strain energy density function are used in finite element codes to define nonlinear elastic behavior. Basic concepts like the strain energy density, stress-strain relations, and least square fit to experimental data are introduced by use of a one-dimensional example. Incompressibility is also discussed. The subjects touched upon in the introduction are developed further, with the general hyperelastic constitutive model as a base, in subsequent chapters.

2.1. Nonlinear elastic bar

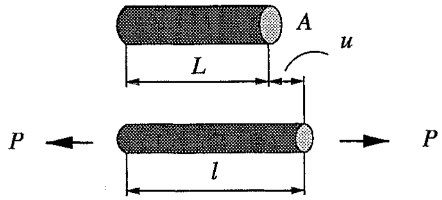

Figure 2.1: *Nonlinear elastic bar loaded by force P.*

The concept of hyperelasticity will be illustrated by a nonlinear elastic bar (cf. Figure 2.1. The simplest possible hyperelastic constitutive model, the one-parameter Neo-Hooke model, will be derived from the strain energy density $W(\lambda)$, with W the strain energy per undeformed volume of the bar and λ the stretch, defined as the length ratio of the deformed and the undeformed bar.

The uniaxial stress-stretch relation will be derived for the bar and an example of fit to experimental compression/tension data will be shown for the Neo-Hooke model.

Consider the nonlinear elastic bar, illustrated in Figure 2.1, with original length L and cross-section area A. The force P causes the displacement u at the end of the bar and increases its length to l giving the stretch $\lambda = l/L$.

The total strain energy U is computed by multiplying the strain energy density with W the volume, i.e.

$$U = ALW(\lambda)$$

The incremental work done by the external force P should be equal to the increment in total strain energy. Hence, the energy balance is stated as

$$Pdu = dU \ , \tag{2.1}$$

and the increment in total strain energy can be expressed by use of W as

$$dU = AL\,dW = AL\,\frac{dW}{d\lambda}\,d\lambda \ . \tag{2.2}$$

The displacement increment can also be written in terms of stretch by using

$$u = l - L = (\lambda - 1)L \ .$$

Differention yields

$$du = Ld\lambda. \tag{2.3}$$

Inserting (2.3) and (2.2) into the energy balance equation (2.1) yields

$$PLd\lambda = AL\,\frac{dW}{d\lambda}\,d\lambda \ .$$

Simplifying the expression gives

$$\frac{P}{A} = \frac{dW}{d\lambda} \ , \tag{2.4}$$

where P/A is the nominal stress, i.e. force per original cross section area, derived from the strain energy function.

It is seen from this one-dimensional example that the stress can be obtained directly from the strain energy density function. In the general multiaxial case, that will be dealt with in Chapter 3, the stresses are found in a similar manner from the strain energy density function.

2.2. The Neo-Hooke material

The strain energy function $W(\lambda)$ has to fulfill some general conditions:

- $W(1) = 0$ for $\lambda = 1$, i.e. the strain energy is zero in the unloaded case.
- $W(\lambda) \to \infty$ for $\lambda \to 0$ and for $\lambda \to \infty$, i.e. the strain energy should increase for increasing compression and tension.
- $dW/d\lambda = 0$ for $\lambda = 1$, the nominal stress has to be zero in the unloaded state.

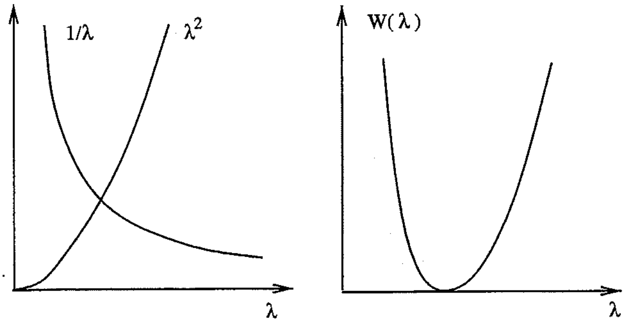

Figure 2.2: *Strain energy function* $W(\lambda)$ *constructed from a simple choice of functions.*

A strain energy function can be constructed from a simple choice of functions by using $1/\lambda$ and λ^2 according to Figure 2.2. A function that satisfies these conditions is given by

$$W(\lambda) = C(\lambda^2 + \frac{2}{\lambda} - 3) \; . \tag{2.5}$$

Inserting (2.5) into (2.4) results in

$$\frac{P}{A} = 2C(\lambda - \frac{1}{\lambda^2}) \; , \tag{2.6}$$

where C is an arbitrary material constant. Equation (2.6) is the nominal stress in the so-called Neo-Hooke material, which is the simplest possible hyperelastic model, with only one material parameter.

Before looking at the fit to experiments we note that the initial Young's modulus E_0 for the Neo-Hooke material can be derived according to

$$E_0 = \left. \frac{d}{d\lambda} \frac{P}{A} \right|_{\lambda=1} = 6C \; . \tag{2.7}$$

The Neo-Hooke material model has been shown to give quite good agreement with experiments of rubber in compression and moderate tension [16].

2.3. Fit to test data

In order to illustrate the fitting procedure and to prepare for the discussion in Chapter 5, the elastic parameter C in the Neo-Hooke model will be obtained here from experimental data by a least squares procedure. The experimental data in Figure 2.3 are nominal compression/tension stress values for a 65 IRHD carbon-black-filled rubber vulcanizate.

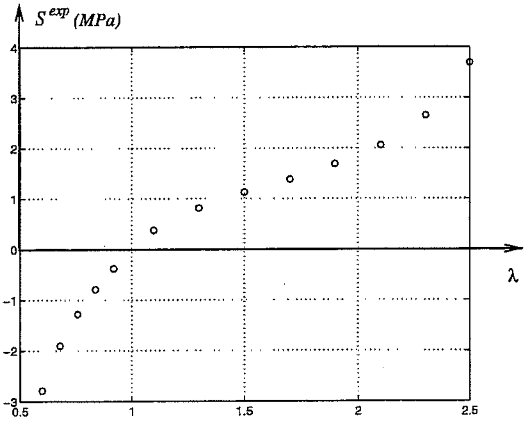

λ	$S^{exp}(MPa)$
0.60	-2.788
0.68	-1.904
0.76	-1.276
0.84	-0.792
0.92	-0.376
1.10	0.378
1.30	0.814
1.50	1.130
1.70	1.380
1.90	1.684
2.10	2.056
2.30	2.648
2.50	3.694

Figure 2.3: *Test data from compression and tension test.*

The nominal stress-stretch relation (2.6) should give a close fit to the experimental data points. Hence, the conditions to be fulfilled as closely as possible, for all data points, are

$$S_i^{teor}(\lambda_i) \approx S_i^{exp} \qquad i = 1...n \; , \tag{2.8}$$

where n is the number of data points. The tension and a compression stress-stretch relation S^{teor} is defined by (2.6) as

$$S_i^{teor}(\lambda_i) = \frac{P_i}{A} = 2C(\lambda_i - \frac{1}{\lambda_i^2}) \, .$$

Setting up the (approximative) equalities (2.8) at every experimental point yields

$$e_i = 2(\lambda_i - \frac{1}{\lambda_i^2})C - S_i^{exp} \; , \tag{2.9}$$

where e_i is the error between theory and experiment. Equation (2.9) can be expressed in matrix format as

$$\boldsymbol{e} = \boldsymbol{a}C - \boldsymbol{b}$$

where $\boldsymbol{e}$, $\boldsymbol{a}$, and $\boldsymbol{b}$ are n by 1 matrixes with

$$a_i = 2(\lambda_i - 1/\lambda_i^2) \quad \text{and} \quad b_i = S_i^{exp}.$$

In the method of least squares the "closest fit" is defined as the minimum of the sum, over all data points, of the square of the errors between theory and experiments i.e.

$$\Psi = \sum_{i=1}^{n} (S_i^{teor} - S_i^{exp})^2 = \sum_{i=1}^{n} e_i^2 = \boldsymbol{e}^T\boldsymbol{e} \, .$$

The nominal stress obtained from theory S_i^{teor} depends on the unknown elastic parameter contained in the strain energy function $W(\lambda)$. Minimizing Ψ with respect to the unknown parameter yields a value of the elastic parameter giving the best fit in the least squares sense. The explicit expression for Ψ is

$$\Psi = \boldsymbol{e}^T\boldsymbol{e} = (\boldsymbol{a}C - \boldsymbol{b})^T(\boldsymbol{a}C - \boldsymbol{b}) = \boldsymbol{a}^T\boldsymbol{a}C^2 - 2\boldsymbol{a}^T\boldsymbol{b}C + \boldsymbol{b}^T\boldsymbol{b}\,.$$

Finding the minimum of Ψ by

$$\frac{d\Psi}{dC} = 2\boldsymbol{a}^T\boldsymbol{a}C - 2\boldsymbol{a}^T\boldsymbol{b} = 0$$

yields the solution

$$C = \boldsymbol{a}^T\boldsymbol{b}/\boldsymbol{a}^T\boldsymbol{a}\,.$$

The values of $\boldsymbol{a}$ and $\boldsymbol{b}$ are obtained by the experimental data in Figure 2.3 giving $C = 0.632$ and thus an initial modulus $E_0 = 3.79\ MPa$.

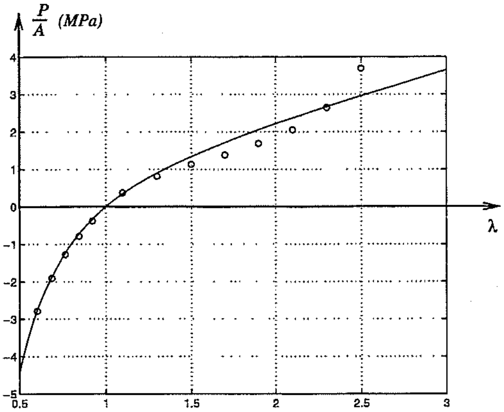

Figure 2.4: *Fit of the Neo-Hooke model to test data from compression and tension test.*

The fit is illustrated in Figure 2.4. It can be seen that the fit is good in compression but not so good in tension. The Neo-Hooke model is unable to capture the upturn of the experimental data in tension. Including more constants in the strain energy density function enables a closer fit in tension.

2.4. Incompressible behavior

It was mentioned in the introduction that the ratio between the bulk and shear modulus is approximately 2000 for a natural rubber vulcanizate, i.e. the material is almost incompressible. An example of the limiting case, complete incompressibility, will be shown here.

Suppose that a body of an incompressible material is only subjected to a hydrostatic pressure. In this case no strains develop in the body. Likewise, superposition of hydrostatic compression or tension on a state of stress in an incompressible material will not change the strains. Hence, the state of stress is not unique for a given state of strain. The hydrostatic pressure is not connected to the strains and is therefore an independent variable.

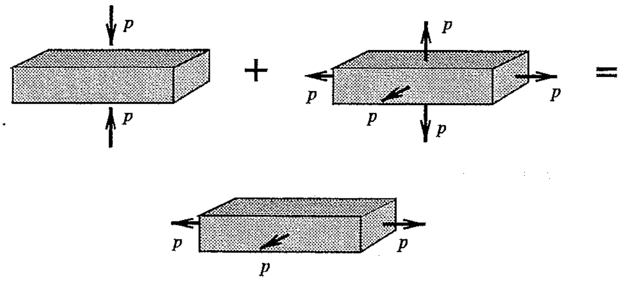

Figure 2.5: *Conversion of compression to equibiaxial tension by adding hydrostatic tension.*

An example is shown in Figure 2.5, where a compressive stress is converted into an equibiaxial stress by adding hydrostatic tension. This has implications for testing of rubber specimens because the example shows that different loading conditions in testing can give equivalent deformations.

2.5. Hyperelastic characterization

Hyperelastic characterization involves choice of strain energy function, type of test specimens, and test procedure. These subjects will be discussed in subsequent chapters. A review of methods to characterize the elastic behavior of rubber is given by Charlton and Young [11]. Discussions on characterization of rubber can also be found in documentation to finite element programs, see for example [26].

The characterization starts with a choice of strain energy density function. A large number of strain energy density functions for different types of rubbers have been proposed, with validity dependent on the strain range. Several choices with different numbers of constants are discussed by for example Charlton and Young, and Finney and Kumar [15], and Treloar [63]. Models suitable for carbon-black-filled natural rubbers are discussed by Yeoh [65] [66] and Davies et al. [13]. Some of these hyperelastic models are discussed in Chapter 3.

Test specimens and applicable analytical strain-stress expressions can be found in several sources; see for example [11] [63] [26]. A number of test specimens and corresponding analytical expressions are presented in Chapter 4. The accuracy of some specimens compared to the analytical expressions is the subject of Chapter 6.

The test procedure involves mechanical conditioning in order to avoid softening, and to achieve stationary test values. Procedures for conditioning are discussed in James and Green [28] and Yeoh [65]. This is also a subject discussed in Chapter 5.

3. CONSTITUTIVE LAW

The constitutive equation for a *hyperelastic material* is discussed in this chapter. It is defined as a relationship between total stress and total strain. We will start by recalling the concept of strain energy in connection with the simple one-dimensional example in the introduction. The strain energy plays a central role in defining a the constitutive relation. Stresses are determined by derivatives of the strain energy function. Stress and strain measures used in this chapter are discussed in Appendix.

3.1. The strain energy function

A material whose stresses can be defined by a strain energy function is termed a hyperelastic material. The strain energy function can be regarded as a potential function for the stresses. The *strain energy per unit volume in the reference configuration* W and its dependence on the strain measure is the subject of this section. The strain measure used here is the left Cauchy-Green deformation tensor $\mathbf{B}$. A general assumption is that W depends on all of the components of the strain measure, giving

$$W = W(\mathbf{B}).$$

The state of deformation however, is fully determined by the principal stretches and the principal directions. The strain energy function can therefore equivalently be expressed as

$$W = W(\lambda_1, \lambda_2, \lambda_3, \mathbf{n}_1, \mathbf{n}_2, \mathbf{n}_3)\ .$$

If the material is assumed to be isotropic, there will be no directional dependence and W is a function of the principal stretches only i.e.

$$W = W(\lambda_1, \lambda_2, \lambda_3)\ .$$

To obtain the principal stretches we have to find the roots of the characteristic polynomial of $\mathbf{B}$. It is, however, easier to obtain the coefficients of the characteristic polynomial, i.e. the strain invariants (cf. Appendix). Instead of using the principal stretches we could therefore express W as a function of the strain invariants

$$W = W(I_1, I_2, I_3)$$

with the strain invariants

$$\begin{cases} I_1 = tr(\mathbf{B}) = {\lambda_1}^2 + {\lambda_2}^2 + {\lambda_3}^2 \\ I_2 = \frac{1}{2}(tr(\mathbf{B})^2 - tr(\mathbf{B}^2)) = {\lambda_1}^2{\lambda_2}^2 + {\lambda_1}^2{\lambda_3}^2 + {\lambda_2}^2{\lambda_3}^2 \\ I_3 = det(\mathbf{B}) = {\lambda_1}^2{\lambda_2}^2{\lambda_3}^2 \end{cases} \tag{3.1}$$

In the case of an *incompressible* material there is no dependence on the third strain invariant, because this invariant expresses the volume change, giving

$$W = W(I_1, I_2)\ . \tag{3.2}$$

The form (3.2) of the strain energy density function will be used in the constitutive law described in the next section.

Expression (3.2) seems to indicate that all values of I_1 and I_2 are possible. However, the values of I_1 and I_2 are restricted due to the condition of incompressibility. If we consider principal directions we can use the condition $I_3 = 1$ to eliminate one of the principal stretches in the expressions of I_1 and I_2. The third principal stretch can be expressed as

$$\lambda_3 = \frac{1}{\lambda_1\lambda_2}\ . \tag{3.3}$$

Inserting (3.3) into (3.1), yields

$$\begin{cases} I_1 = {\lambda_1}^2 + {\lambda_2}^2 + \dfrac{1}{{\lambda_1}^2{\lambda_2}^2} \\ I_2 = {\lambda_1}^2{\lambda_2}^2 + \dfrac{1}{\lambda_2^2} + \dfrac{1}{\lambda_1^2} \end{cases} . \tag{3.4}$$

The values of λ_1 and λ_2 can now be chosen independently. The possible values of the invariants I_1 and I_2 for all choices of λ_1 and λ_2 are shown as the shaded area in Figure 3.1.

3.2. Constitutive model

The constitutive law for a class of incompressible nonlinear elastic material will be stated next.

According to the discussion in Chapter 2 there will be no strains developing in an incompressible body, only subjected to a hydrostatic pressure. Likewise, to a general state of stress we could add an arbitrary hydrostatic pressure without any corresponding strains developing. The only part of the stress that causes strain in an incompressible body is therefore the deviatoric part.

The constitutive law for a *hyperelastic, isotropic and incompressible* material is derived in a similar way as in the introductory example i.e. by use of an energy

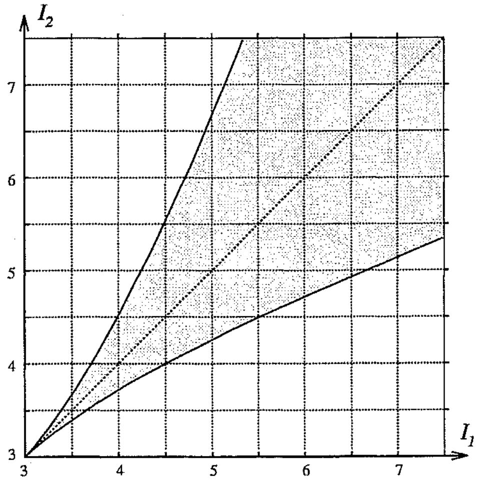

Figure 3.1: (I_1, I_2) *diagram restricted to incompressible deformation.*

principle. The derivation is, however not carried out here. See for example [37] or [6]. The constitutive law is given by

$$\sigma = 2(\frac{\partial W}{\partial I_1} + I_1 \frac{\partial W}{\partial I_2})\mathbf{B} - 2\frac{\partial W}{\partial I_2}\mathbf{B}^2 + p\,\mathbf{1} \tag{3.5}$$

where σ is the Cauchy stress tensor, $\mathbf{B} = \mathbf{F}\mathbf{F}^\mathrm{T}$ is the left Cauchy-Green deformation tensor and p is the pressure stress defined as

$$p = \frac{1}{3}(\sigma_{11} + \sigma_{22} + \sigma_{33})\ . \tag{3.6}$$

It is clearly seen, by subtracting the pressure stress from both sides of (3.5), that the constitutive relation is expressed in terms of the deviator stress

$$s = \sigma - p\,\mathbf{1}\ .$$

The constitutive model (3.5) depends entirely on the specific form of the strain energy density function.

The stress-strain relationships that will be derived in Chapter 4, are obtained from the general constitutive relation (3.5) in the cases of deformation without shear and simple shear. These special cases of (3.5) will be discussed next.

3.2.1. Principal directions; Rivlin's relations

Rivlin [51] showed that the differences in the principal stresses can be expressed without involving the unknown pressure stress. These relations are derived from the general expression (3.5) by eliminating the pressure stress.

Principal directions and the deformation gradient **F** for this case are discussed in Appendix. The left Cauchy-Green deformation tensor can be expressed as

$$\mathbf{B} = \mathbf{F}\mathbf{F}^{\mathbf{T}} = \begin{bmatrix} \lambda_1^2 & 0 & 0 \\ 0 & \lambda_2^2 & 0 \\ 0 & 0 & \lambda_3^2 \end{bmatrix} \qquad \mathbf{B}^2 = \begin{bmatrix} \lambda_1^4 & 0 & 0 \\ 0 & \lambda_2^4 & 0 \\ 0 & 0 & \lambda_3^4 \end{bmatrix} . \tag{3.7}$$

Inserting the value of the first invariant (3.1), and (3.7) into (3.5), yields

$$\begin{cases} \sigma_1 = 2\dfrac{\partial W}{\partial I_1}\lambda_1^2 + 2\dfrac{\partial W}{\partial I_2}((\lambda_1^2+\lambda_2^2+\lambda_3^2)\,\lambda_1^2 - \lambda_1^4) + p \\[2ex] \sigma_2 = 2\dfrac{\partial W}{\partial I_1}\lambda_2^2 + 2\dfrac{\partial W}{\partial I_2}((\lambda_1^2+\lambda_2^2+\lambda_3^2)\,\lambda_2^2 - \lambda_2^4) + p \\[2ex] \sigma_3 = 2\dfrac{\partial W}{\partial I_1}\lambda_3^2 + 2\dfrac{\partial W}{\partial I_2}((\lambda_1^2+\lambda_2^2+\lambda_3^2)\,\lambda_3^2 - \lambda_3^4) + p \end{cases}$$

where σ_i is the principal Cauchy stress and λ_i is the principal stretch in direction i. Subtracting equation two from one, three from one and three from two eliminates the pressure and *Rivlin's relations* are obtained

$$\begin{cases} \dfrac{\sigma_1-\sigma_2}{\lambda_1^2-\lambda_2^2} = 2\,(\dfrac{\partial W}{\partial I_1} + \lambda_3^2\,\dfrac{\partial W}{\partial I_2}) \\[2ex] \dfrac{\sigma_1-\sigma_3}{\lambda_1^2-\lambda_3^2} = 2\,(\dfrac{\partial W}{\partial I_1} + \lambda_2^2\,\dfrac{\partial W}{\partial I_2}) \\[2ex] \dfrac{\sigma_2-\sigma_3}{\lambda_2^2-\lambda_3^2} = 2\,(\dfrac{\partial W}{\partial I_1} + \lambda_1^2\,\dfrac{\partial W}{\partial I_2}) \end{cases} \tag{3.8}$$

with the unknown pressure eliminated.

3.2.2. Simple shear

The state of deformation in simple shear cf. Figure 3.2 is obtained from the deformation gradient **F** (derived in Appendix). The left Cauchy-Green deformation tensor **B** and $\mathbf{B}^2$ is in this case given by

$$\mathbf{B} = \mathbf{F}\mathbf{F}^{T} = \begin{bmatrix} 1+\kappa^2 & 0 & \kappa \\ 0 & 1 & 0 \\ \kappa & 0 & 1 \end{bmatrix} \qquad \mathbf{B}^2 = \begin{bmatrix} 1+3\kappa^2+\kappa^4 & 0 & 2\kappa+\kappa^3 \\ 0 & 1 & 0 \\ 2\kappa+\kappa^3 & 0 & 1+\kappa^2 \end{bmatrix} \tag{3.9}$$

where $\kappa = tan\theta$, with θ defined in Figure 3.2.

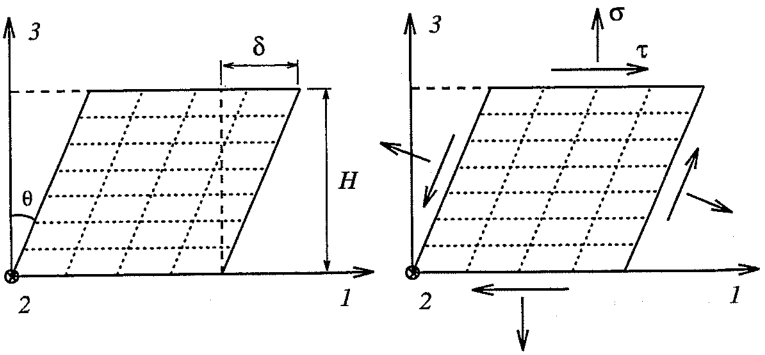

Figure 3.2: *Simple shear.*

The strain invariants are

$$\begin{cases} I_1 = tr(\mathbf{B}) = 3 + \kappa^2 \\ I_2 = \frac{1}{2}(tr^2(\mathbf{B}) - tr(\mathbf{B}^2)) = 3 + \kappa^2 \end{cases} . \tag{3.10}$$

Hence, the invariants are equal in the simple shear deformation.

Inserting (3.9) and (3.10) into (3.5) yields

$$\begin{bmatrix} \sigma_{11} & \sigma_{12} & \sigma_{13} \\ \sigma_{21} & \sigma_{22} & \sigma_{23} \\ \sigma_{31} & \sigma_{32} & \sigma_{33} \end{bmatrix} = 2(\frac{\partial W}{\partial I_1} + (3+\kappa^2)\frac{\partial W}{\partial I_2}) \begin{bmatrix} 1+\kappa^2 & 0 & \kappa \\ 0 & 1 & 0 \\ \kappa & 0 & 1 \end{bmatrix}$$

$$-2\frac{\partial W}{\partial I_2} \begin{bmatrix} 1+3\kappa^2+\kappa^4 & 0 & 2\kappa+\kappa^3 \\ 0 & 1 & 0 \\ 2\kappa+\kappa^3 & 0 & 1+\kappa^2 \end{bmatrix} + p \begin{bmatrix} 1 & 0 & 0 \\ 0 & 1 & 0 \\ 0 & 0 & 1 \end{bmatrix} .$$

Observe that, in contrast to small strain linear elasticity, normal stresses are present in all three directions. The only shear stress different from zero is $\tau = \sigma_{13} = \sigma_{31}$. The shear stress τ is found to be

$$\tau = 2(\frac{\partial W}{\partial I_1} + \frac{\partial W}{\partial I_2})\kappa \quad \text{with} \quad \kappa = tan\,\theta \, . \tag{3.11}$$

3.3. Strain energy functions

Two general strain energy function formats will be discussed here; the polynomial form and the Ogden form. These functions are expressed in terms of invariants and principal stretches respectively. Several other strain energy formats have been proposed. A discussion of strain energy density functions can be found in [11] and [15].

The polynomial form contains the elastic constants in a linear dependence while the Ogden form, with constants as exponents, gives a non-linear dependence of the constants. This makes it more complicated to fit the latter model to experiments. On the other hand, the advantage of the Ogden model is that in general a more stable and better fit to experimental data is obtained.

However, it will be shown in Chapter 5 that a special choice with three parameters in the polynomial form gives an accurate and stable fit to experimental data for natural rubber vulcanizates.

3.3.1. Polynomial form

A general form of the strain energy density function W, implemented in most of the general finite element programs capable of handling hyperelastic materials, is given by the series expansion

$$W = \sum_{i=0,j=0}^{\infty} C_{ij}(I_1 - 3)^i (I_2 - 3)^j \tag{3.12}$$

where C_{ij} are unknown constants. The sum is formally written as a sum to infinity but normally only a few terms are used.

The reason for writing the series in terms of $(I_1 - 3)$ and $(I_2 - 3)$ is that these terms are zero in the undeformed state, thereby giving $W = 0$ in the undeformed state, if we also require that $C_{00} = 0$.

The explicit version of (3.12), with the terms having an index sum less or equal to three, is written as

$$\begin{gathered} W = C_{10}(I_1 - 3) + C_{01}(I_2 - 3) \\ +C_{20}(I_1 - 3)^2 + C_{11}(I_1 - 3)(I_2 - 3) + C_{02}(I_2 - 3)^2 \\ +C_{30}(I_1 - 3)^3 + C_{21}(I_1 - 3)^2(I_2 - 3) + C_{12}(I_1 - 3)(I_2 - 3)^2 + C_{03}(I_2 - 3)^3 \\ +\ldots\ldots . \end{gathered}$$

Taking only the first term in the series yields the *neo-Hooke* material, i.e.

$$W = C_{10}(I_1 - 3) . \tag{3.13}$$

The neo-Hooke model was first derived from statistical mechanics [33], by considering the molecular structure of rubber. Although this model only contains one parameter it has been shown to give very good agreement with experiments in compression and moderate shear [16]. These are the two most important modes of deformation in engineering applications of rubber units. The first constant C_{10} in the series is therefore the most significant parameter.

The famous *Mooney-Rivlin* material is obtained by taking the first two terms in the series, giving

$$W = C_{10}(I_1 - 3) + C_{01}(I_2 - 3) \ . \tag{3.14}$$

The model shows good agreement with experiments on natural gum rubber, and it has been widely used in various applications. However, it is of more limited value for carbon-black-filled rubbers [65].

Another way of selecting terms in the series is by considering the so-called order of deformation. The logic in this characterization is derived from the order of the polynomial in λ^2 that is obtained by substituting the invariants with the corresponding expressions in principal stretches (3.1). The first invariant is expressed as a sum, $I_1 = \sum \lambda_i^2$, which is of the first order in λ^2. The second invariant is expressed as a sum, $I_2 = \sum \lambda_i^2 \lambda_j^2$ ($i \neq j$), which is of the second order in λ^2.

The *first order of deformation* material is the Neo-Hooke material. The *second order of deformation* material is found by taking terms that include I_1, I_1^2 and I_2, i.e.

$$W = C_{10}(I_1 - 3) + C_{01}(I_2 - 3) + C_{20}(I_1 - 3)^2 \tag{3.15}$$

a model with three parameters. The *third order of deformation* material is found by taking terms that include I_1, I_1^2, I_2, I_1^3 and $I_1 I_2$, i.e.

$$W = C_{10}(I_1-3)+C_{01}(I_2-3)+C_{20}(I_1-3)^2+C_{11}(I_1-3)(I_2-3)+C_{30}(I_1-3)^3 \tag{3.16}$$

a model with five parameters.

Yeoh [65] found that the dependence on the second invariant is very weak for carbon-black-filled natural rubbers. This has been verified by others, see for example Davies et al. [13].

By leaving out terms in (3.16) that include I_2 Yeoh obtained a model with three parameters that gave a good fit to experiment carried out on filled rubbers. Consequently, this strain energy function is written as

$$W = C_{10}(I_1 - 3) + C_{20}(I_1 - 3)^2 + C_{30}(I_1 - 3)^3 \ . \tag{3.17}$$

Apart from being a fairly simple model (i.e. only three parameters) and giving a good fit to experiments on carbon-black-filled rubbers, is it also possible to obtain the parameters from a shear test only. This is not possible for general choice of parameters.

3.3.2. Ogden model

The strain energy density is generally written

$$W = \sum_{i=1}^{N} \frac{2\mu_i}{\alpha_i^2}(\lambda_1^{\alpha_i} + \lambda_2^{\alpha_i} + \lambda_3^{\alpha_i} - 3) \,. \tag{3.18}$$

The Ogden model [43] can generally not be compared with the polynomial form, except for specific choices of the constants. For $N = 1$ and $\alpha_1 = 2$ the Neo-Hooke model is obtained. For $N = 2$ and $\alpha_1 = 2$ and $\alpha_2 = -2$ the Mooney-Rivlin model is obtained.

The stress-stretch relationships are obtained from the general constitutive equation (3.5). This equation requires derivatives with respect to the invariants. However, the Ogden model is expressed in terms of principal stretches. The derivatives with respect to the invariants can de derived by use of the chain rule. If incompressibility is assumed i.e. $W = W(I_1, I_2)$, the chain rule yields

$$\begin{bmatrix} \frac{\partial W}{\partial \lambda_1} \\ \frac{\partial W}{\partial \lambda_2} \end{bmatrix} = \begin{bmatrix} \frac{\partial I_1}{\partial \lambda_1} & \frac{\partial I_2}{\partial \lambda_1} \\ \frac{\partial I_1}{\partial \lambda_2} & \frac{\partial I_2}{\partial \lambda_2} \end{bmatrix} \begin{bmatrix} \frac{\partial W}{\partial I_1} \\ \frac{\partial W}{\partial I_2} \end{bmatrix} \,. \tag{3.19}$$

The desired derivatives are found by inversion of (3.19)

$$\begin{bmatrix} \frac{\partial W}{\partial I_1} \\ \frac{\partial W}{\partial I_2} \end{bmatrix} = \left(\frac{\partial I_1}{\partial \lambda_1}\frac{\partial I_2}{\partial \lambda_2} - \frac{\partial I_1}{\partial \lambda_2}\frac{\partial I_2}{\partial \lambda_1}\right)^{-1} \begin{bmatrix} \frac{\partial I_2}{\partial \lambda_2} & -\frac{\partial I_2}{\partial \lambda_1} \\ -\frac{\partial I_1}{\partial \lambda_2} & \frac{\partial I_1}{\partial \lambda_1} \end{bmatrix} \begin{bmatrix} \frac{\partial W}{\partial \lambda_1} \\ \frac{\partial W}{\partial \lambda_2} \end{bmatrix} \,. \tag{3.20}$$

The expressions should be evaluated considering incompressibility. This means that (3.4) should be used for the invariants and that $\lambda_3 = 1/\lambda_1\lambda_2$ is inserted into (3.18) before evaluating the derivatives.

3.4. Strain energy density plot

The strain energy function can be expressed in terms of principal stretches by inserting the invariants (3.4) i.e.

$$\begin{cases} I_1 = {\lambda_1}^2 + {\lambda_2}^2 + \dfrac{1}{{\lambda_1}^2{\lambda_2}^2} \\ I_2 = {\lambda_1}^2{\lambda_2}^2 + \dfrac{1}{\lambda_2^2} + \dfrac{1}{\lambda_1^2} \end{cases}$$

This yields a function depending on two principal stretches

$$W = W(\lambda_1, \lambda_2)$$

defined for all values of λ_1 and λ_2. (The third stretch invariant is determined by the incompressibility constraint.)

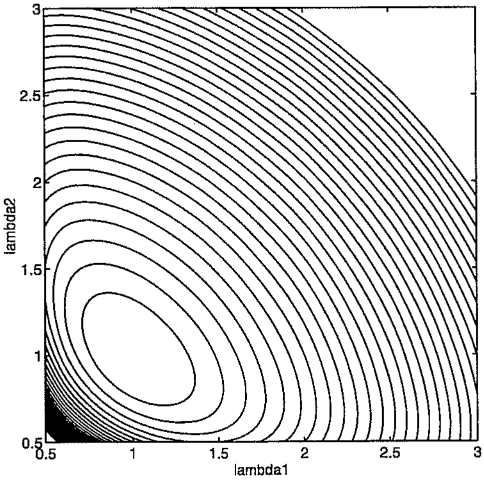

Figure 3.3: *Neo-Hooke model* $W(\lambda_1, \lambda_2)$.

The Neo-Hooke material expressed in terms of λ_1 and λ_2 is shown as an example in (3.21)

$$W = C_{10}({\lambda_1}^2 + {\lambda_2}^2 + \frac{1}{{\lambda_1}^2{\lambda_2}^2} - 3) \,. \tag{3.21}$$

A contour plot of this strain energy function, with $C_{10} = 0.5$, is shown in Figure 3.3. The Neo-Hooke strain energy function has only one minimum $W = 0$ occurring at $\lambda_1 = \lambda_2 = 1$, and the strain energy increases in all directions, starting from the undeformed state. This bowl-shaped strain energy function corresponds to a reasonable physical behavior for all choices of positive values of C_{10}.

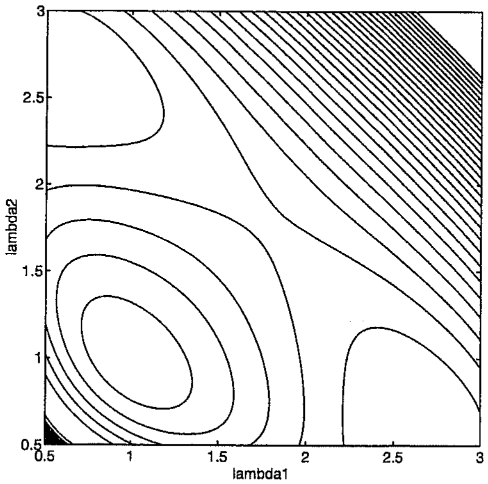

Figure 3.4: *Second order of deformation model* $W(\lambda_1, \lambda_2)$.

If more terms in the series (3.12) are included, a reasonable behavior is not guaranteed. Consider as an example the second order of deformation material shown in Figure 3.4. The values of the constants in the example are $C_{10} = 0.5$, $C_{01} = -0.05$ and $C_{20} = -0.05$. This choice of parameters yields negative values of the strain energy and local extremum points are present. This example calls for some caution in the choice of constants in the series (3.12).

The contour plot of $W(\lambda_1, \lambda_2)$ serves as a "fingerprint" of the hyperelastic model. It is useful for determining if a model obtained from a fit to experiments has good behavior for all values of λ_1 and λ_2 i.e. not only for those used in the testing. The strain energy plot will be discussed further in Chapter 5.

4. TEST OBJECTS AND STRESS-STRAIN RELATIONS

In the following sections specific tests will be described. These are the tension, compression and equibiaxial tests, the pure and simple shear tests and the independent biaxial test. The accuracy of the tests will be evaluated in Chapter 6.

Discussions concerning different tests for evaluation of elastic properties can also be found in [11] and [26].

4.1. General considerations

Tests for determination of hyperelastic parameters are usually designed to yield homogeneous states of deformation. All the tests described here, except tests using simple shear deformation, are also designed to have fixed principal directions during the deformation.

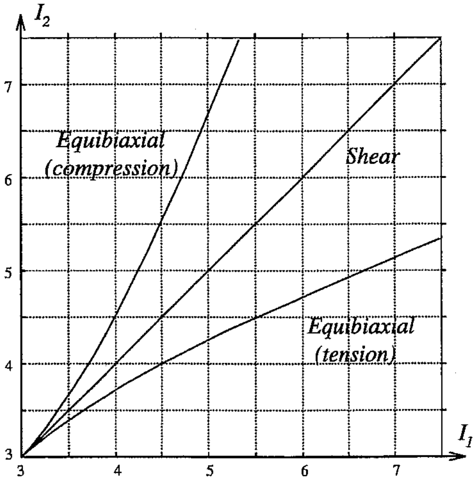

Figure 4.1: *Paths in the* (I_1, I_2) *plane.*

From a known state of homogeneous deformation it is possible to calculate the stress by use of the constitutive relation (3.5). The calculated stress is compared with the experimentally obtained values. Use of a fitting procedure makes it possible to assign values to the elastic parameters in the constitutive relation.

The tests are based on simple states of deformation and *complete incompressibility is assumed*, which makes it possible to obtain analytical expressions for the stress-stretch relations.

There are four states of deformation used in the tests described here. These are equibiaxial deformation, pure shear, simple shear and general biaxial deformation.

Three tests use the equibiaxial state of deformation, the tension test, the compression test and the equibiaxial test. The pure and simple shear tests are shown to give equal values of the strain invariants. The independent biaxial test is also discussed. The different tests leave different paths in the (I_1, I_2) plane, cf. Figure 4.1.

The tension, compression and equibiaxial test objects are all designed to give an equibiaxial deformation. The differences between the tests are in the states of stress applied to the specimens, (that can be different even if the state of strain is the same cf. Chapter 2).

Pure shear and simple shear are essentially the same state of deformation, but the test specimens are quite different in their design. The true biaxial test is the most general, but also the most complicated test to perform.

An ordinary uniaxial mechanical testing system usually has the capability of recording force and displacement between the loading heads. Some of the tests require measurement of the displacements in a defined zone. This is the case in the tension, the equibiaxial and the independent biaxial tests. These tests need extra equipment, like some form of extentiometers or optical methods, for measuring displacements, while for the rest of the tests loading head displacement is sufficient.

Some of the test objects are described in the International Standards (ISO) recommendations. The ISO norm contains a description of a tension, compression and simple shear specimens. The objects included in the ISO standard are adopted here.

4.2. Equibiaxial deformation

In the equibiaxial deformation two principal stretches are equal and the other stretch is determined from the condition of incompressibility.

4.2.1. Tension and compression test

The tension specimen according to ISO 37-1977 consists of an hourglass shaped membrane, a so called *dumbbell test piece*, as illustrated in Figure 4.2.

The dumbbell specimen according to ISO is a weak specimen, with forces normally less than $100N$, which requires a load cell for small forces. Moreover, the displacement should be measured within the zone where the predicted relations are valid. This requires clip gauges or other methods. Alternatively, a conversion curve

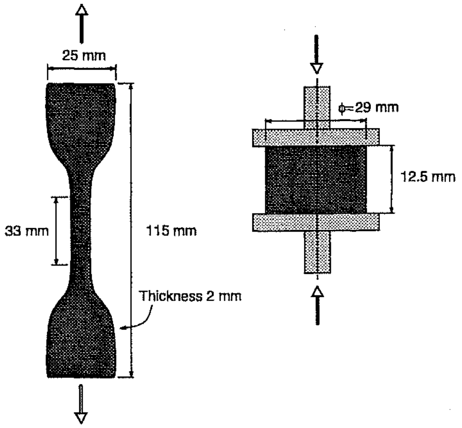

Figure 4.2: *Tension and compression specimens*

could be established giving a correction between loading head displacement and elongation of the homogeneous zone. A disadvantage is the difficulties in getting a slip-free connection to the specimen.

The compression specimen according to ISO 7743:1989 consists of a cylinder with a diameter of 29mm and a height of 12.5mm cf. Figure 4.2. The cylinder is compressed between two parallel highly polished flat metal plates. In order to accomplish the required homogeneous state of deformation the surfaces have to be lubricated with silicon grease. Deviation from the ideal homogeneous state of deformation appears in a barrel shape of the loaded specimen.

The displacement is measured directly from the loading head displacement.

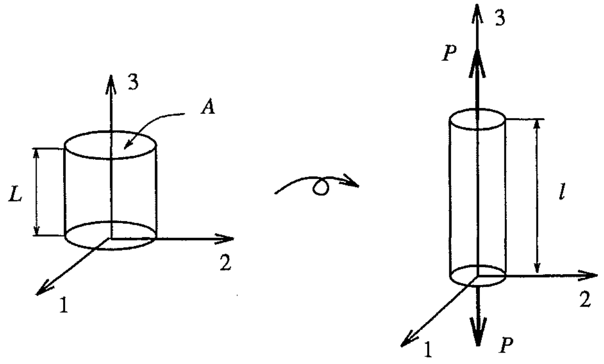

Figure 4.3: *Tension and Compression tests.*

In the *tension and compression tests* one stretch λ is determined by the prescribed displacement. It is calculated as

$$\lambda = \frac{L+\delta}{L}$$

where L is the original length in the tension or compression specimen and δ is the prescribed displacement. The two other stretches are equal and determined by the condition of incompressibility, giving

$$\begin{cases} \lambda_3 = \lambda \\ \lambda_1 = \lambda_2 = \dfrac{1}{\sqrt{\lambda}} \end{cases} . \tag{4.1}$$

The condition of incompressibility is fulfilled because $\lambda_1\lambda_2\lambda_3 = 1$. ($\lambda > 1$ corresponds to tension and $\lambda < 1$ to compression.)

The values of the invariants are found by inserting (4.1) into the general expression for the strain invariants, giving the invariants for the equibiaxial case

$$\begin{cases} I_1 = \dfrac{2}{\lambda} + \lambda^2 \\ I_2 = \dfrac{1}{\lambda^2} + 2\lambda \end{cases} . \tag{4.2}$$

They can be represented as a curve in the (I_1, I_2) plane as illustrated in Figure 4.1. Note that the curve representing the equibiaxial deformation is equivalent to the boundary curve in the (I_1, I_2) plane, for the possible values of the invariants, when incompressibility is considered. Compression is represented by the upper boundary curve and tension is represented by the lower boundary curve. (The undeformed state gives $I_1 = I_2 = 3$.)

The tension and compression tests have only one nonzero principal stress component. If we choose the third principal direction to be the loaded direction (cf. Figure 4.3), then the Cauchy stress tensor is written as

$$\boldsymbol{\sigma} = \begin{bmatrix} 0 & 0 & 0 \\ 0 & 0 & 0 \\ 0 & 0 & \sigma \end{bmatrix} \quad \text{with} \quad \sigma = P/a \, . \tag{4.3}$$

P is the force that develops in direction three and a is the deformed cross section area perpendicular to the loaded direction. This area can be calculated from the state of deformation according to (4.1), giving a relation between the deformed and undeformed cross section area,

$$a = \frac{1}{\lambda} A \, .$$

The stress component σ can be expressed by the force and the undeformed cross section area as

$$\sigma = \frac{P\lambda}{A} \, . \tag{4.4}$$

Rivlin's relations can now be used to obtain a predicted stress-stretch relation for tension and compression. Use of the second or third equation in (3.8) with the the stretch (4.1) and stress (4.3) yields

$$\frac{P}{A} = 2\,(\frac{\partial W}{\partial I_1} + \frac{1}{\lambda}\frac{\partial W}{\partial I_2})(\lambda - \frac{1}{\lambda^2}) \tag{4.5}$$

by use also of (4.4). This is the predicted *uniaxial stress-stretch relation* used in the tension and compression tests.

It is obvious from (4.5) that a constant Young's modulus can not be defined for an incompressible hyperelastic material. It has to be considered as a function of stretch. However, the *initial Young's modulus* E_0 can be calculated from the formula (4.5) by considering the slope at unit stretch,

$$E_0 = \lim_{\lambda \to 1} \frac{\partial}{\partial \lambda}(\frac{P}{A}) = 6\,(\frac{\partial W}{\partial I_1} + \frac{\partial W}{\partial I_2})_{I_1=I_2=3}\ . \tag{4.6}$$

Evaluating (4.6) for the strain energy function as the general series (3.12) yields the initial Young's modulus

$$E_0 = 6\,(C_{10} + C_{01})$$

i.e. only the first two constants have influence on the initial modulus.

4.2.2. Equibiaxial test

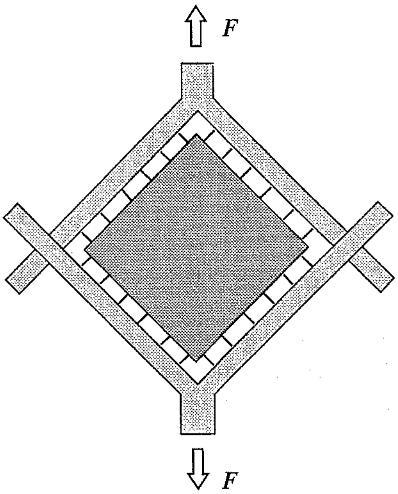

Figure 4.4: *Equibiaxial test object.*

The *equibiaxial test object* is a quadratic membrane with a series of small holes punched along the edges according to Figure 4.4. The membrane is connected to

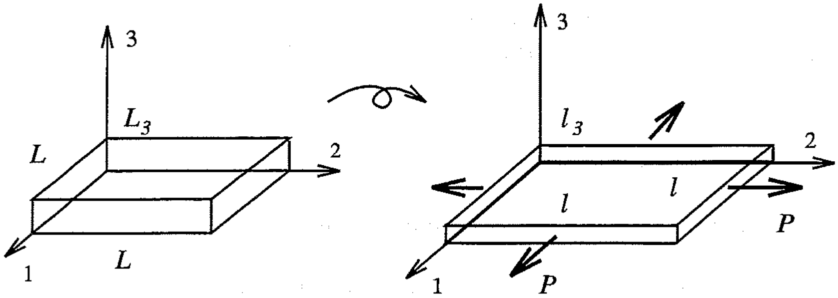

Figure 4.5: *Equibiaxial test*

two rigid frames by small hooks which slide freely along the frames. The membrane is loaded diagonally in an ordinary uniaxial testing machine. The force F recorded from the load cell has to be converted according to the equilibrium relation

$$P = F/\sqrt{2}\,,$$

where P is the force acting perpendicular to the sides of the membrane. The hooks and the holes yield nonhomogeneous deformation along the sides of the specimen, so displacements have to be measured in a marked square inside the edges. Displacement should be measured in the two perpendicular directions. It is reasonable to use the mean value of the two displacements. So the pair of force and displacement data which are compared with the predicted values are the above force P and the mean displacement in the homogeneous zone.

Clearly this test is complicated to set up and to perform. It requires a quite complicated construction and the displacement has to be measured separately. The test is not an ISO standard test.

Another way of creating an equibiaxial state approximately equal to the one described is by inflation of a circular membrane by pressurizing one side so that it forms a spherical shape.

The equibiaxial test is also based upon the equibiaxial state of deformation, but the prescribed displacements are not the same as in tension and compression. In the equibiaxial test the two equal stretches are controlled. By slightly changing the notation in (4.1) we can get a notation suitable for the equibiaxial test that indicates the prescribed stretches. If these stretches are denoted by λ_b, the principal stretches considering incompressibility become

$$\begin{cases} \lambda_1 = \lambda_2 = \lambda_b \\ \lambda_3 = \dfrac{1}{\lambda_b^2} \end{cases} . \tag{4.7}$$

In practice it is only possible to obtain values of $\lambda_b > 1$, due to the design of the test specimen. We can therefore only obtain the compression curve in the (I_1, I_2) plane cf. Figure 4.1, and the equibiaxial test is therefore equivalent to the compression test. The values of the invariants expressed with λ_b become

$$\begin{cases} I_1 = 2{\lambda_b}^2 + \dfrac{1}{\lambda_b^4} \\ I_2 = \lambda_b^4 + \dfrac{2}{\lambda_b^2} \end{cases} .$$

The relation between λ_b and λ in compression/tension is

$$\lambda_b = \frac{1}{\sqrt{\lambda}} . \tag{4.8}$$

Equation (4.8) makes it possible to compare the compression test with the equibiaxial test.

The biaxial state of stress has two equal nonzero principal stress components cf. Figure 4.5. Directions one and two are chosen as the loaded directions and the Cauchy stress tensor is written as

$$\boldsymbol{\sigma} = \begin{bmatrix} \sigma & 0 & 0 \\ 0 & \sigma & 0 \\ 0 & 0 & 0 \end{bmatrix} \quad \text{with} \quad \sigma = P/a , \tag{4.9}$$

where it is assumed that the cross section areas perpendicular to directions one and two are equal, thus giving the same force in the two directions. P is the force that develops in directions one and two and a is the deformed cross section area perpendicular to the loaded directions. This area can be calculated from the state of deformation according to (4.7), giving a relation between the deformed and undeformed cross section area.

$$a = \frac{A}{\lambda_b}$$

The stress component σ can now be expressed in terms of the force and the original cross section area as

$$\sigma = \frac{P}{A}\lambda_b . \tag{4.10}$$

Rivlin's relations are used to obtain the predicted stress-stretch relation for the equibiaxial test. The second or third equation in (3.8) with stretch and stress according to (4.7) and (4.10), yields

$$\frac{P}{A} = 2\,(\frac{\partial W}{\partial I_1} + \lambda_b^2\frac{\partial W}{\partial I_2})(\lambda_b - \frac{1}{\lambda_b^5}) . \tag{4.11}$$

This is the predicted stress-stretch relation for the *equibiaxial* test.

4.3. Shear deformation

The shear deformations termed pure shear and simple shear are treated in the same section because they have equal values of the strain invariants (I_1, I_2). In that sense the state of deformation is the same in pure shear and simple shear.

4.3.1. Pure shear test

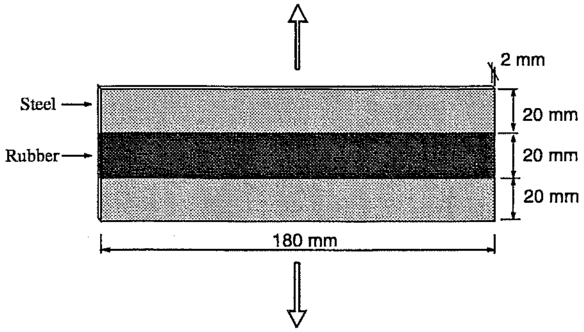

Figure 4.6: *The pure shear test specimen.*

The pure shear specimen is usually made of a thin rectangular strip of rubber connected to rectangular strips of metal according to Figure 4.6. The pure shear test is not included in the ISO standard. The requirements on the dimensions of the specimen are that it should be sufficiently wide compared to the height so that the end effects do not have too much influence. Ideally there should be a force perpendicular to the loading direction that maintains the constant width of the specimen during the deformation according to (4.16). This force is not present if a uniaxial testing machine is used and it is therefore required to keep the height small compared to the width.

The recorded values in the test are the force and the loading head displacements.

The pure shear deformation is arranged to have one principal value held fixed equal to one, during the deformation. The second principal direction is chosen to be the fixed and the third direction to be the direction with the prescribed stretch $\lambda > 1$.. The state of deformation is illustrated in Figure 4.7 and the principal values are

$$\begin{cases} \lambda_1 = \dfrac{1}{\lambda} \\ \lambda_2 = 1 \\ \lambda_3 = \lambda \end{cases} . \tag{4.12}$$

The strain invariants are equal, as mentioned above, and the value expressed in the

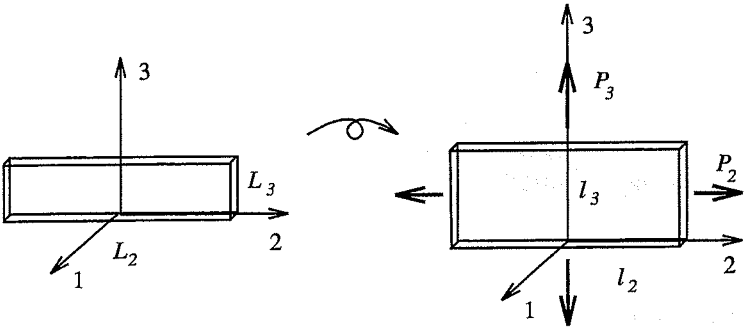

Figure 4.7: *Pure shear test.*

known stretch value λ is

$$I_1 = I_2 = \lambda^2 + 1 + \frac{1}{\lambda^2} \, . \tag{4.13}$$

There are two nonzero principal stress components in the pure shear test cf. Figure 4.7. The Cauchy stress tensor is

$$\sigma = \begin{bmatrix} 0 & 0 & 0 \\ 0 & \sigma_2 & 0 \\ 0 & 0 & \sigma_3 \end{bmatrix} \, . \tag{4.14}$$

P_2 and P_3 are the forces that develop in directions two and three, and a_2 and a_3 are the deformed cross section areas. The relation between deformed and undeformed cross section area is

$$a_2 = A_2 \quad \text{and} \quad a_3 = \frac{1}{\lambda} A_3 \, .$$

The stress components σ_2 and σ_3 can now be expressed by the force and the undeformed cross section areas as

$$\sigma_2 = \frac{P_2}{A_2} \quad \text{and} \quad \sigma_3 = \frac{P_3 \lambda}{A_3} \, . \tag{4.15}$$

The predicted stress-stretch relations for the pure shear test are also obtained by Rivlin's relations. Use of the first and the second equation in (3.8) with the stress and the stretch according to (4.15) and (4.12) respectively, yields

$$\begin{cases} \dfrac{P_2}{A_2} = 2\,(\dfrac{\partial W}{\partial I_1} + \dfrac{1}{\lambda^2}\dfrac{\partial W}{\partial I_2})(1 - \dfrac{1}{\lambda^2}) \\ \dfrac{P_3}{A_3} = 2\,(\dfrac{\partial W}{\partial I_1} + \dfrac{\partial W}{\partial I_2})(\lambda - \dfrac{1}{\lambda^3}) \end{cases} \, . \tag{4.16}$$

These are the predicted *pure shear stress-stretch relations.* Observe that in practice $\lambda > 1$ and that only the second relation is used for evaluation of laboratory tests.

4.3.2. Simple shear test

The simple shear test can be performed with at least two different test objects.

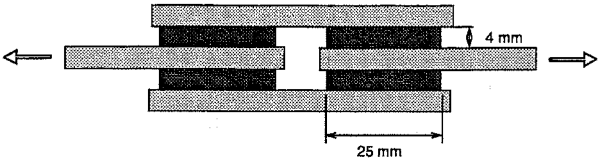

Figure 4.8: *Simple shear specimen; quadruple shear.*

One is the *quadruple shear test* according to ISO 1872-1976, illustrated in Figure 4.8. The quadruple shear specimen is made of four rectangular blocks of rubber, connected to metal. The force recorded is twice the shear force acting on each block and the loading head displacement is twice the deformation of each block.

The other is the so-called *double shear test* according to Figure 4.9 (not an ISO standard test). Two rubber cylinders are connected to metal cylinders. The force recorded is thus twice the shear force on each cylinder, and loading head displacement is the deformation of each cylinder.

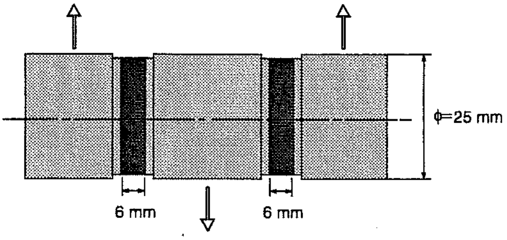

Figure 4.9: *Simple shear specimen; double shear.*

There is a difference in the loading of the two specimens. The height (i.e. perpendicular to the loading direction) is not fixed in the quadruple shear test and there will be no normal forces developing on the rubber surfaces connected to metal. In the double shear test, on the other hand, the height of the rubber cylinders is kept fixed and therefore normal forces develop perpendicular to the loaded direction.

Both tests show deviations from the ideal simple shear deformation because the theory predicts shear forces on the surfaces which are tilted by the deformation. The absence of correct forces on these surfaces result in an s-shape of the free surfaces and not a straight line as in ideal simple shear.

A relationship between the shear angle θ in simple shear and the stretch λ in pure shear can be obtained by comparing the strain invariant expressions (3.10) and (4.13) i.e.

$$3 + tan^2\theta = \lambda^2 + 1 + \frac{1}{\lambda^2}$$

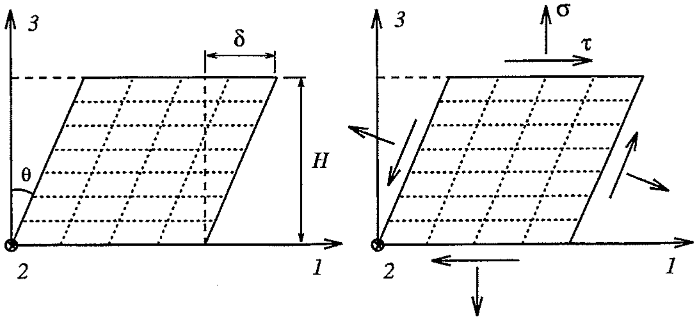

Figure 4.10: *Simple shear test.*

and solve for the shear angle giving

$$\theta = arctan(\sqrt{\lambda^2 + \frac{1}{\lambda^2} - 2}) \; . \tag{4.17}$$

From (4.17) we find the shear angle that produces the same strain invariants in simple shear as in pure shear, given a specific stretch λ in pure shear.

Pure shear and simple shear yield a straight line in the (I_1, I_2) plane as shown in Figure 4.1.

The shear stress according to (3.11) was found to be

$$\tau = 2\,(\frac{\partial W}{\partial I_1} + \frac{\partial W}{\partial I_2})\,\kappa \quad \text{with} \quad \kappa = tan\,\theta \; . \tag{4.18}$$

The shear force P is acting on the area A perpendicular to the third axis as illustrated in Figure 4.10. The area is not affected by the deformation, and the shear stress is

$$\tau = \frac{P}{A} \; . \tag{4.19}$$

The shear displacement δ and the height H yield

$$\kappa = tan\,\theta = \frac{\delta}{H} \tag{4.20}$$

where κ is called the *direct shear strain.* Inserting (4.19) and (4.20) into (4.18) gives

$$\frac{P}{A} = 2\,(\frac{\partial W}{\partial I_1} + \frac{\partial W}{\partial I_2})\frac{\delta}{H} \; , \tag{4.21}$$

which is the relation between shear force and shear displacement in the *simple shear test.*

An interpretation for the case of small strains, of equation (4.18) is provided if we let the shear angle approach zero i.e. $\kappa = tan\,\theta \approx \theta = \gamma_{13}$, where γ_{13} is the shear strain used in the linear theory of elasticity. Comparison with the linear relation, $\sigma_{13} = G\,\gamma_{13}$, where G is the shear modulus, shows that *initial shear modulus* G_0 can be obtained from (4.18) by considering the slope at zero shear angle

$$G_0 = \lim_{\kappa \to 0} \frac{\partial \tau}{\partial \kappa} = 2\,(\frac{\partial W}{\partial I_1} + \frac{\partial W}{\partial I_2})_{I_1=I_2=3}\,. \tag{4.22}$$

The expressions (4.22) and (4.6) are consistent with $E_0 = 3\,G_0$ for an incompressible linear elastic material.

Evaluating (4.22) for the strain energy function as the general series (3.12) yields the initial shear modulus

$$G_0 = 2\,(C_{10} + C_{01}) \tag{4.23}$$

where it is again observed that only the first two constants have influence on the initial modulus.

4.4. Independent biaxial deformation

Uniaxial tests and shear tests are simple to perform in an ordinary uniaxial test device. However, these tests can only produce specific paths in the region of possible invariant values. The independent biaxial test is the only test described here that fully covers the region of possible values of the invariants I_1 and I_2.

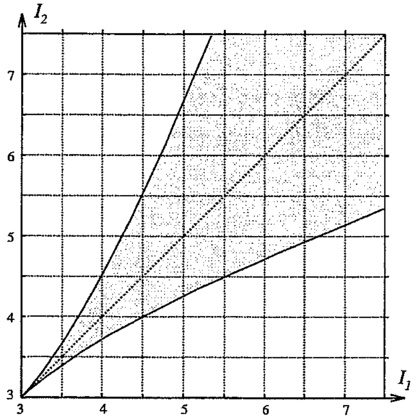

Figure 4.11: *Mapping from the* (λ_1, λ_2) *plane to the* (I_1, I_2) *plane.*

In order to cover the whole region, as illustrated in Figure 4.11, a true biaxial state of deformation has to be employed and the two principal values of stretch are then chosen independently.

The values of the strain invariants are given by

$$\begin{cases} I_1 = \lambda_1^2 + \lambda_2^2 + \dfrac{1}{{\lambda_1}^2{\lambda_2}^2} \\ \\ I_2 = \lambda_1^2\lambda_2^2 + \dfrac{1}{\lambda_1^2} + \dfrac{1}{\lambda_2^2} \end{cases}$$

according to (3.4), where the condition of incompressibility has been used to eliminate the third principal stretch component.

4.4.1. Independent biaxial test

Independent biaxial testing has been performed (see for example [27]), on quadratic membranes with a test equipment that resembles the equibiaxial rig shown in Figure 4.4, but with independent displacement control in two directions.

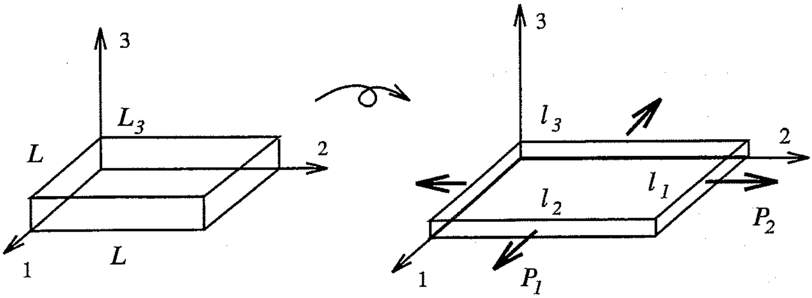

Figure 4.12: *Independent biaxial test.*

There are two nonzero principal stress components in the independent biaxial test as illustrated in Figure 4.12. Directions one and two are chosen as the loaded directions with $\lambda_1 > 1$ and $\lambda_2 > 1$. The Cauchy stress tensor is

$$\boldsymbol{\sigma} = \begin{bmatrix} \sigma_1 & 0 & 0 \\ 0 & \sigma_2 & 0 \\ 0 & 0 & 0 \end{bmatrix} \tag{4.24}$$

where the stress components are related to the forces and original areas.

P_1 and P_2 are forces in directions one and two, and a_1 and a_2 are the deformed cross section areas perpendicular to directions one and two. Assuming equal undeformed cross section areas, i.e. the test object is originally quadratic, yields $A_1 = A_2 = A$. The relations between deformed and undeformed cross section areas are

$$\begin{cases} a_1 = \lambda_3\lambda_2 A = \dfrac{A}{\lambda_1} \\ \\ a_2 = \lambda_3\lambda_1 A = \dfrac{A}{\lambda_2} \end{cases}$$

The stress components σ_1 and σ_2 can now be expressed by the force and the undeformed cross section areas as

$$\begin{cases} \sigma_1 = \dfrac{P_1}{a_1} = \dfrac{P_1\lambda_1}{A} \\ \sigma_2 = \dfrac{P_2}{a_2} = \dfrac{P_2\lambda_2}{A} \end{cases} . \tag{4.25}$$

Rivlin's relations are again used and the second and the third equation in (3.8) with the stress according to (4.25), yields

$$\begin{cases} \dfrac{P_1}{A} = 2\,(\dfrac{\partial W}{\partial I_1} + \lambda_2^2\dfrac{\partial W}{\partial I_2})(\lambda_1 - \dfrac{1}{\lambda_1^3\lambda_2^2}) \\ \dfrac{P_2}{A} = 2\,(\dfrac{\partial W}{\partial I_1} + \lambda_1^2\dfrac{\partial W}{\partial I_2})(\lambda_2 - \dfrac{1}{\lambda_1^2\lambda_2^3}) \end{cases} \tag{4.26}$$

the predicted stress-stretch relations for the *independent biaxial* test.

4.5. Volumetric deformation

In some cases, when a rubber part is fully or partially enclosed in a stiff structure, the volumetric behavior is important. For a finite element analysis of such a component, the ordinary hyperelastic constants do not sufficiently describe the material. In such cases the volumetric behavior, expressed by the bulk modulus of the material, is of central importance. The nearly incompressible hyperelastic material models implemented in finite element codes include the bulk modulus [26].

4.5.1. Bulk modulus test

The bulk modulus test specimen consists of a rubber cylinder that is placed in a hole in a metal fitting. The diameter of the hole is slightly larger than the diameter of the rubber cylinder. A plunger that fits snugly in the hole is lowered into the hole and thus compresses the rubber cylinder, see Figure 4.13. The surfaces of the rubber specimen should be sufficiently lubricated in order to ensure a homogeneous state of strain.

Initially the state of strain of the rubber cylinder will be similar to an ordinary compression test. After contact between the rubber specimen and the edges of the hole the curve will become much steeper and the slope will here represent the bulk modulus.

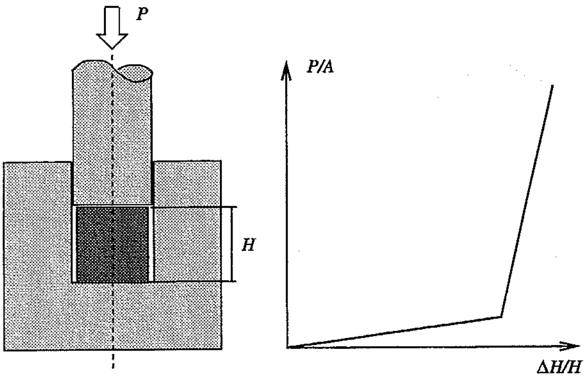

Figure 4.13: *The bulk modulus test specimen.*

The relation between the hydrostatic stress p and the volumetric strain $\Delta V/V_0$ is given by the bulk modulus K, according to

$$p = K\frac{\Delta V}{V_0}.$$

The hydrostatic stress is $p = P/A$ when the cylinder comes into contact with the hole. The volumetric strain can be expressed by $V_0 = A \cdot H$ and $\Delta V = A \cdot \Delta H$ in terms of the reduction in height, giving $\Delta V/V_0 = \Delta H/H$. Hence

$$\frac{P}{A} = K\frac{\Delta H}{H}\,, \tag{4.27}$$

where A denotes the cross section area and H denotes the height of the cylinder.

4.6. Summary

The theoretical relations derived for different states of deformation and stress are summarized here. Relations valid for tests with fixed principal directions are given in the table below.

Test method	Stretch	I_1, I_2 expressions	Nominal stress relation(s)
Tension and Compression	$\lambda_3 = \lambda$ $\lambda_1 = \lambda_2 = \frac{1}{\sqrt{\lambda}}$	$I_1 = \frac{2}{\lambda} + \lambda^2$ $I_2 = \frac{1}{\lambda^2} + 2\lambda$	$\frac{P}{A} = 2\,(\frac{\partial W}{\partial I_1} + \frac{1}{\lambda}\frac{\partial W}{\partial I_2})(\lambda - \frac{1}{\lambda^2})$
Equibiaxial tension	$\lambda_1 = \lambda_2 = \lambda_b$ $\lambda_3 = 1/\lambda_b^2$	$I_1 = 2{\lambda_b}^2 + \frac{1}{\lambda_b^4}$ $I_2 = \lambda_b^4 + \frac{2}{\lambda_b^4}$	$\frac{P}{A} = 2\,(\frac{\partial W}{\partial I_1} + \lambda_b^2\frac{\partial W}{\partial I_2})(\lambda_b^4 - \frac{1}{\lambda_b^2})$
Pure shear	$\lambda_1 = 1/\lambda$ $\lambda_2 = 1$ $\lambda_3 = \lambda$	$I_1 = I_2 = \lambda^2 + 1 + \frac{1}{\lambda^2}$	$\frac{P}{A} = 2\,(\frac{\partial W}{\partial I_1} + \frac{\partial W}{\partial I_2})(\lambda - \frac{1}{\lambda^3})$
Independent biaxial tension	λ_1 λ_2 $\lambda_3 = 1/\lambda_1\lambda_2$	$I_1 = \lambda_1^2 + \lambda_2^2 + \frac{1}{{\lambda_1}^2{\lambda_2}^2}$ $I_2 = \lambda_1^2\lambda_2^2 + \frac{1}{\lambda_1^2} + \frac{1}{\lambda_2^2}$	$\frac{P_1}{A} = 2\,(\frac{\partial W}{\partial I_1} + \lambda_2^2\frac{\partial W}{\partial I_2})(\lambda_1 - \frac{1}{\lambda_1^3\lambda_2^2})$ $\frac{P_2}{A} = 2\,(\frac{\partial W}{\partial I_1} + \lambda_1^2\frac{\partial W}{\partial I_2})(\lambda_2 - \frac{1}{\lambda_1^2\lambda_2^3})$

The nominal stress relation for simple shear is

$$\frac{P}{A} = 2\,(\frac{\partial W}{\partial I_1} + \frac{\partial W}{\partial I_2})\kappa \quad \text{with} \quad I_1 = I_2 = 3 + \kappa^2 \quad \text{and} \quad \kappa = \frac{\delta}{H}\,.$$

Compression, tension and shear was found to yield curves on the border and in the center of the region of possible values in the (I_1, I_2) plane.

All the states of deformation discussed here are homogeneous. It is, however, also possible to use nonhomogeneous states of deformation, if analytical relations for the force-deformation expressions are available. Nonhomogeneous independent biaxial testing, with analytical expression for the force-displacement relations, can be performed by using a combination of tension/compression and torsion of rubber cylinders [52].

5. TESTING AND EVALUATION OF TEST RESULTS

This chapter concerns the choice of the hyperelastic model and the fitting procedure, where the theoretical stress-stretch relations from Chapter 4 are fitted to test data. The abilities of the hyperelastic models to give a reasonable stable physical behavior are also discussed in this chapter.

Some of the inelastic effects in the mechanical behavior of rubber was discussed in the introduction (Chapter 1). These properties has to be accounted for in testing of rubber specimens. Carbon-black-filled rubber is, as mentioned in the introduction, not a completely elastic material. The main deviation from elasticity shows in strain softening (or Mullins' effect) and hysteresis. The use of an elastic material model to describe the mechanical behavior of rubber will therefore lead to inconsistencies, since it can not capture these effects. The elastic models have to be fitted to data from properly pre-strained test specimens.

5.1. General considerations

This section contains a discussion of general considerations in testing of rubber units such as pre-stretching, deformation level and rate dependence.

5.1.1. Mullins' effect

Cyclic straining of a rubber specimen will cause a successive decrease in stiffness and also in the distance between the loading and unloading curves, i.e. the hysteresis. The breakdown is, however, limited for each value of maximum stretch and stability is reached after about four to eight cycles. If the stretch is increased there will be further breakdown and a new stationary curve will be obtained. This curve passes below the previous stationary curve, i.e. the stiffness of the material has decreased cf. Figure 5.2 b.

Mullins [42] observed that if strain amplification (cf. Chapter 1) is taken into account, very small differences in softening between gum and filled vulcanizates are observed. He therefore concluded that the softening with deformation at strains larger than 0.1% is mainly due to effects in the rubber network and not due to interaction with the filler. The recovery from softening is however slower in filled vulcanizates. Mullins attributes this to the hindering effect of the filler.

He also concludes that only the unrecoverable part of the softening is due to breakdown of cross-links, while the recoverable part of the softening (after about 24 hours) is due to configurational changes in the rubber network.

Softening for strains below 0.1% is attributed to breaking of filler aggregates. This softening at very small strains due to the filler is to a large extent immediately recoverable according to Payne [45].

A proper treatment of the strain softening is of importance in testing of rubber specimens. The usefulness of obtained test data depends on how the pre-stretching or *mechanical conditioning* has been performed.

5.1.2. Mechanical conditioning

A rubber unit in working condition is subjected to stress softening and creep/relaxation phenomena. Models that take all the inelastic effects into account are not available in commercial codes. However, constitutive models that account for softening have been developed by Simo [54] and Godvinjee and Simo [18], although these models are not generally available in finite element codes.

Models for static analysis found in commercial codes are usually purely elastic. Laboratory tests designed to determine the elastic properties thus have to account for inelastic effects and stress softening in particular. It is relevant to perform some kind of pre-straining of the test specimens, because most rubber units in engineering applications are exposed to some form of periodic loading giving stress softening in operating conditions.

A rubber unit in operating conditions is also subjected to a nonhomogeneous state of deformation. That is, points at different geometric locations are subjected to different stretch levels as illustrated in Figure 5.1. This implies that different points are conditioned differently in the rubber unit under working conditions.

If the test specimen is pre-stretched to a maximum level of stretch selected to cover the stretch levels occurring in the applications, then test data will be too weak for all stretch values below the maximum stretch, because the essential volume of the unit considered is probably subjected to stretch levels far below the chosen maximum level.

This rises the question of how the mechanical conditioning influences test data for evaluation of hyperelastic constants.

Influence of the mechanical conditioning procedure

An investigation was carried out to determine the influence of the mechanical conditioning procedure. Pure shear specimens with dimensions according to Figure 4.6 were used in a test involving three different mechanical conditioning procedures. The procedures are illustrated in Figure 5.2. First cycle data were also recorded and compared with the conditioning procedures. Two of the three different conditioning

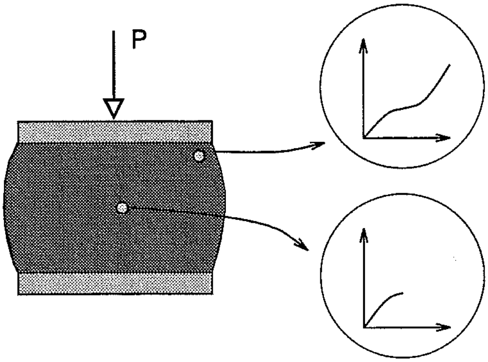

Figure 5.1: *Rubber unit subjected to nonhomogeneous deformation.*

procedures studied here take into account the differences in conditioning levels. The mechanical conditioning procedures studied here are discussed in [11], [65] and [28].

A total of nine pure shear specimens, divided into three groups, were used in the laboratory tests. Each of the conditioning procedures was performed on three pure shear specimens and the steady state values at eight levels were recorded. The nominal stress and the stretch were then computed for each specimen and experimental data from the three specimens in each group were averaged.

The maximum stretch level used was the same in all three procedures, and it was set to $\lambda = 2$, i.e the maximum direct nominal strain used in the tests was 100 % corresponding to a displacement of 20 mm, cf. Figure 4.6. The tests with multiple conditioning levels used eight levels at equal intervals with $\Delta\lambda = 0.125$. The stretch rate was set to $50\%/min = 8.3 \cdot 10^{-3}/s$ which corresponds to a deformation rate of $10mm/min$ for the pure shear specimens used in the tests. The stationary nominal stress (force / original area) at these levels was determined. First cycle data were also evaluated from the first cycle in the one-level conditioning procedure. The tests were carried out with an MTS tensile testing machine, and the temperature was kept at $23.5 \pm 0.5\,^oC$.

The pure shear specimens were made from a carbon-black-filled natural rubber vulcanizate with a nominal hardness of 60 IRHD, moulded from the same rubber mix by Svedala-Skega. The carbon-black content was 30 phr (parts per hundred of rubber by weight) of type N550 according to ASTM (American Society for Testing and Materials).

The variations in the manufactured test specimens were small and it was therefore decided that three specimens for each method of mechanical conditioning should be sufficient. The dimensions of the specimens were individually measured to account for the small deviations in dimensions.

The first method uses only one level of stretch in the conditioning procedure and it is also the maximum level of stretch used in the test. This method is illustrated in

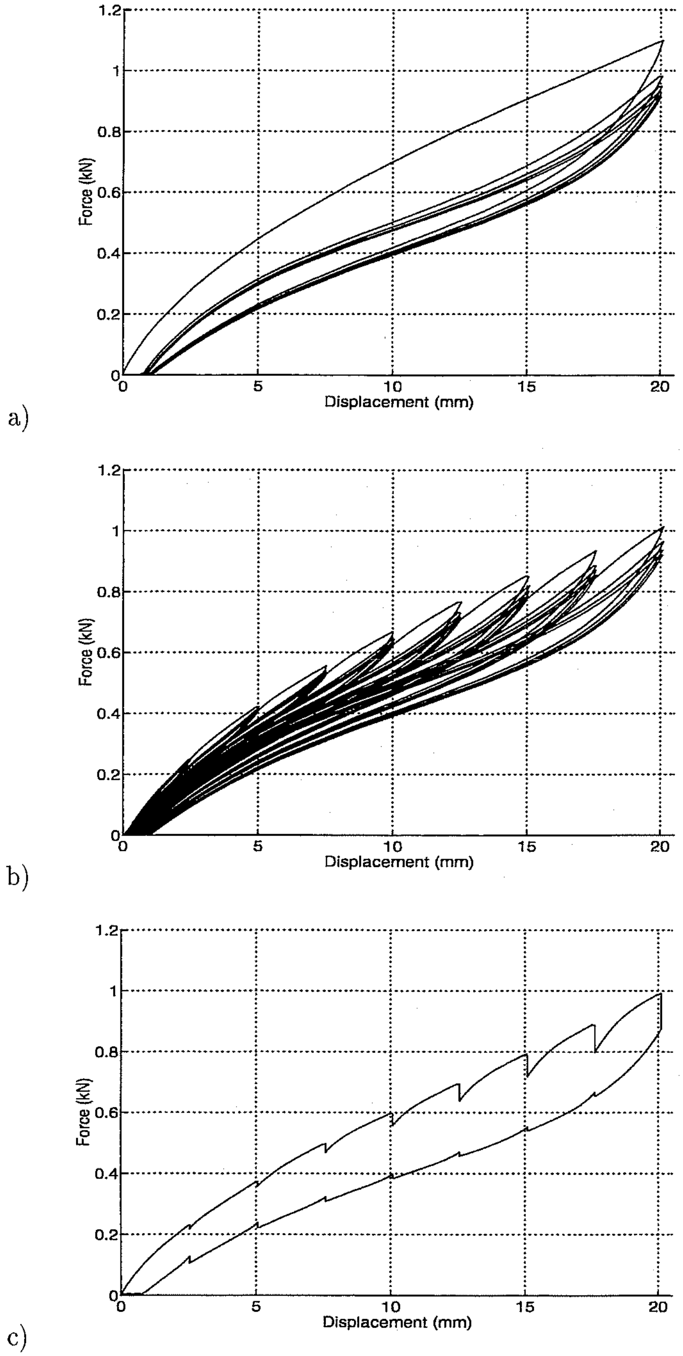

Figure 5.2: *Mechanical conditioning procedures; a) one- level b) progressive and c) intermittent conditioning.*

Figure 5.2 a) for the pure shear test and it is here termed *one-level conditioning.* The one-level procedure is the experimentally simplest procedure. Constant loading rate was used and the specimens were loaded to only one predetermined level according to Figure 5.2 a). Data from the first cycle were also recorded for the three specimens investigated in the one-level procedure. The resulting data points are displayed in Figure 5.3.

A disadvantage of this method, as discussed previously, is that it tends to lower the stiffness of the vulcanizate too much in regions of small stretch values. To overcome this drawback mechanical conditioning on different levels has to be performed. This is done in the other two procedures used in this study.

The second procedure is called *progressive conditioning.* The load is applied by constant rate load cycles between zero and a number of fixed stretch levels. The cycling on each level is continued until a steady state is reached at that level. Figure 5.2 b) illustrates this. The peak values in each of the steady state load cycles are recorded as the experimental data points displayed in Figure 5.3.

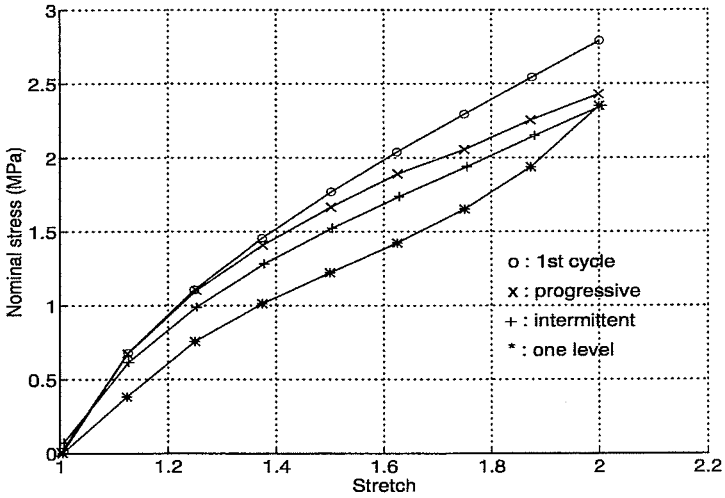

Figure 5.3: *Stationary average loading values for the three different conditioning procedures and first cycle data.*

The third procedure is called *intermittent conditioning.* The test specimen is loaded at constant speed to predetermined stretch levels where the stretch is kept constant until the stress has relaxed to a steady state value. This value is recorded for each of the predetermined stretch levels up to the maximum stretch level. (The same procedure was repeated in unloading for the same stretch levels.) A typical curve obtained in pure shear with this method is shown in Figure 5.2 c).

The intermittent conditioning procedure require a time delay on each level. The time delay to reach a stationary stress is dependent on the level of stretch in this relaxation process in the virgin material. The highest level $\lambda = 2$ required six minutes to obtain stationary value of stress, whereas the lowest level $\lambda = 1.125$ only required a delay of two minutes. The stationary data points in loading are shown in Figure 5.3.

Comparison of the methods

The results displayed in Figure 5.3 show the significant differences obtained between the different mechanical conditioning procedures.

The question of which of the procedures to prefer is difficult to answer. However, some conclusions can be made from the previous discussion and Figure 5.3. The one-level procedure can in general not be recommended because it tends to lower the stiffness of the material too much. The intermittent conditioning procedure, on the other hand, seems to be a strong candidate because conditioning by creep or relaxation due to a large static load (with or without a superimposed vibration) is common in applications. The nonhomogeneous state of stress caused by the static load yields creep or relaxation phenomena and conditioning to different levels in different parts of the unit. These aspects are covered in the intermittent conditioning procedure.

A disadvantage of both the progressive and the intermittent procedure is the quite complicated loading scheme required. However, it was found that a very slow constant rate loading (of a virgin material), with the same total time as in the intermittent method, produced approximately the same stress values as the intermittent method (cf. Section 5.5). This procedure is therefore an alternative to the intermittent method, and is simpler to perform.

As a final remark in this section it should be mentioned that in some applications there is no conditioning of the rubber unit in the operating condition, i.e unconditioned test data should be used to define the "elastic" parameters. This is the case for rubber units, such as fenders for example, that are exposed to single loadings with long periods of recovery.

5.1.3. Rate of deformation

The rate of loading of the test specimen should be chosen as stretch rate, because this measure is independent of the size of the specimen, in contrast to displacement rate. The stretch rate is calculated as

$$\dot{\lambda} = \frac{d}{dt}\frac{L+\delta}{L} = \frac{\dot{\delta}}{L}$$

where δ is the increase in distance in the homogeneous zone.

Loading rate is important for the one-level and the progressive conditioning procedures mentioned in the previous section. It was also mentioned above that the stress values obtained by the intermittent method can be obtained alternatively by a continuous stretching at a very low loading rate. Which loading rate should be used?

The rate of loading of the specimen should be chosen sufficiently low so that the stresses originating from viscous effects are minimized. Yeoh [65] recommends a stretch rate of $50\%/min$ "for reasons of expediency". However, according to the previous discussion the first cycle test with a stretch rate of $50\%/min = 8.3 \cdot 10^{-3}/s$ was not low enough to render equal test data compared to the intermittent method. It will be shown in Section 5.5 that to produce test data by continuous loading equal to the intermittent method, a stretch rate of approximately $3\%/min = 5 \cdot 10^{-4}/s$ is required. This is considerably lower than the stretch rate recommended by Yeoh.

5.1.4. State of strain and maximum stretch levels

Which maximum levels of stretch should be used in the different tests and which are the relevant states of strain?

The strain range should be limited to levels relevant for the actual application in order to achieve a hyperelastic model with as few constants as possible. This is obvious since the accuracy of the fit will be affected by the range of strain used in the fitting. Moreover, in order to minimize time and effort required for testing, reasonable strain ranges have to be chosen, especially if the lowest rate of strain mentioned above is used.

The dominant state of strain and strain range required are off course dependent on the application, and it is difficult to give general guidelines. However, excessive straining of tension test specimens to several hundred percent appears to be less relevant for most engineering applications, where moderate loading in compression and shear is dominant.

Göbel [24] states some allowable stress and strain values based on "existing practical experience". The values given suggest that the compressive strain should not exceed 25% and that the shear strain should be less than 50%. Davies et al. [13] investigated filled rubbers for strain ranges in tension and shear less than 100% and state that this covers the strains of major concern in most engineering applications.

Another reason to avoid excessive testing and limit the range of strain is that even if local large strains can appear in smaller regions of a moderately loaded component, is it more important that the hyperelastic model is accurate for the predominant strain level in the component.

The levels believed to cover most enginering applications that are used in this chapter, in Chapter 6, and in Chapter 7 are

$$0.5 < \lambda < 2.5 \quad \text{and} \quad \kappa < 2.0$$

for the tension/compression test and simple shear. This corresponds to a maximum value of $I_1 - 3 \approx 4$.

The value of first invariant I_1 can be used to compare different tests in order to obtain comparable strain ranges, because the strain energy density depends strongly on this invariant, especially for filled rubbers. The most reasonable way to compare, for example, a pure shear test with a tension test is to choose the maximum stretch level so that the maximum strain energy is equal in the different tests. This is approximately equal to perform tests (on filled rubbers), with equal values of the first invariant I_1.

5.1.5. Influence of temperature

The statistical or molecular theory of rubber elasticity predicts a proportionality of the modulus to the absolute temperature. This is usually referred to as the *Gough-Joule effect* and has been confirmed experimentally for unfilled rubbers.

The force at constant length in a rubber specimen at constant stretch increases linearly with temperature, in accordance with the theory, provided that the stretch is above the so-called thermoelastic inversion point ([63] pp. 25-26). At this stretch the thermal expansion exactly balances the Gough-Joule effect, giving a constant force with respect to temperature. Below this stretch the force decreases with temperature due to the thermal expansion. For a natural gum rubber in tension the thermoelastic inversion occurs at a stretch of approximately 10 %.

Treloar (p. 249) also shows the behavior of $\partial W/\partial I_1$ and $\partial W/\partial I_2$ for an unfilled natural rubber vulcanizate. The behavior of $\partial W/\partial I_1$ is proportional to temperature according to the Gough-Joule effect, while $\partial W/\partial I_2$ is shown to be constant. The reported change in $\partial W/\partial I_1$ is small, with a value of approximately $4\cdot 10^{-4}\ MPa/K$ for a value of $\partial W/\partial I_1 \approx 0.15 MPa$ at room temperature. This corresponds to a change of 0.3% per degree of temperature. (Note the connection to hyperelastic constants, for example; the Mooney-Rivlin model yields $\partial W/\partial I_1 = C_{10}$ and $\partial W/\partial I_2 = C_{01}$.)

The discussion above concerned unfilled rubbers. Fillers can change the behavior considerably, giving a falling modulus with increasing temperature according to Lindley [33] (p. 15).

The *standard laboratory temperatures* recommended in the ISO regulations are 23 ± 2^oC or 27 ± 2^oC.

5.2. Choice of hyperelastic model

The Mooney-Rivlin model with two parameters C_{10} and C_{01} is widely used in rubber elasticity, and it has been successfully fitted to experimental data of unfilled rubber vulcanizates.

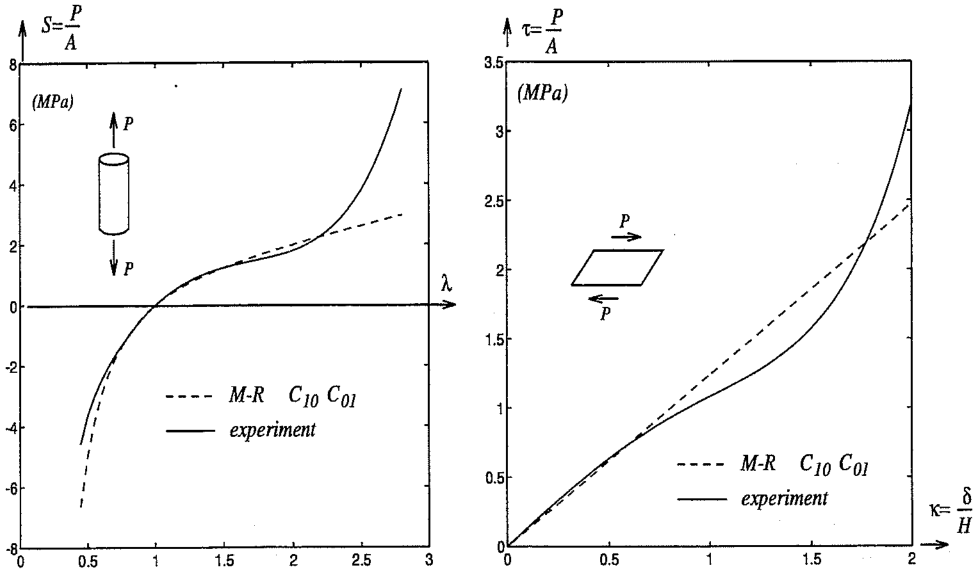

Figure 5.4: *The Mooney-Rivlin model compared to actual behavior of carbon-black-filled rubber in compression/tension and simple shear.*

However, rubbers in engineering problems are often carbon-black-filled vulcanizates of hardness 40-80 IRHD. For these rubbers the agreement with experiments is poor for this simple model. Figure 5.4 shows a comparison of the two-parameter Mooney-Rivlin model and actual behavior of a carbon-black-filled rubber of hardness about 65 IRHD. The Mooney-Rivlin model is linear in tension for large values of stretch, cf. Figure 5.4, where the actual behavior of a carbon-black-filled rubber specimen is progressive. There is also a deviation in simple shear according to Figure 5.4, where the Mooney-Rivlin model shows a linear behavior in simple shear.

The three-parameter model (3.17) proposed by O.H Yeoh [65] shows the qualitative behavior of a carbon-black-filled rubber vulcanizate. This model seems to be a good compromise between correct physical behavior and mathematical simplicity. However, it requires one more parameter than the Mooney-Rivlin model, but the gain is better agreement with the behavior of carbon-black-filled rubbers.

5.3. Fit to test data

The parameters in the hyperelastic model are obtained from experimental data by a fitting procedure, described in this section. The procedure is illustrated with the three-parameter Yeoh model and experimental data in compression/tension for a 65 IRHD carbon-black-filled rubber vulcanizate.

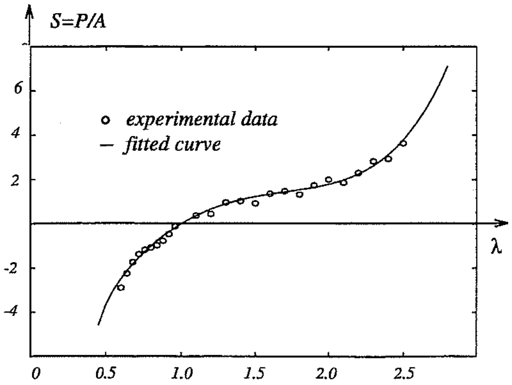

Figure 5.5: *Fit of the model to test data.*

Consider Figure 5.5 where the experimental data points and the stress-stretch relation from theory are shown schematically. The small circles correspond to the (λ_i, S_i) values $i = 1, ..., n$, where λ_i is the stretch and S_i is the nominal stress, obtained from experiments and n is the number of data points. The stress-stretch relation obtained from the constitutive model should closely fit the experimental data points, and the conditions to be fulfilled as close as possible, for every data point are

$$S_i^{teor} \approx S_i^{exp} . \tag{5.1}$$

This "closest fit" has to be defined in some way. In the method of least squares the "closest fit" is defined as the minimum of the sum, over all data points, of the square of the errors between theory and experiments i.e.

$$\Psi = \sum_{i=1}^{n} \left(S_i^{teor} - S_i^{exp}\right)^2 . \tag{5.2}$$

Relation (5.1) can be written alternatively as

$$S_i^{teor} / S_i^{exp} \approx 1 \tag{5.3}$$

and the corresponding sum of squares is written as

$$\Phi = \sum_{i=1}^{n} \left(S_i^{teor} / S_i^{exp} - 1\right)^2 \tag{5.4}$$

where the sum is expressed by the relative error. The form (5.4) is a normalized version of (5.2). The absolute error puts more emphasis on the higher stress values where the absolute error is higher, while the relative error gives equal weight to the data points.

The nominal stress obtained from theory S_i^{teor} depends on the unknown elastic parameters in the strain energy function $W(I_1, I_2)$. Minimizing Φ with respect to the unknown parameters yields a system of equations. The solution to the system is the elastic parameters giving the best fit in the least squares sense. The equation system is linear, if the polynomial form of strain energy function is used.

5.3.1. Example; Fit of the Yeoh model

The least square fitting procedure will be illustrated by use of the compression and tension experimental data given in Figure 5.6.

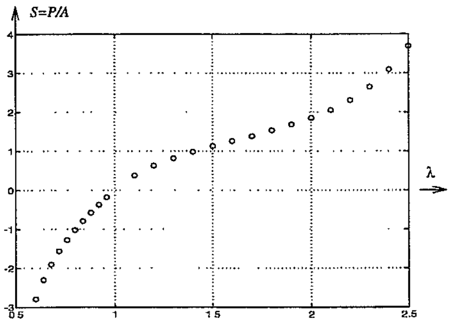

Figure 5.6: *Test data from compression and tension test (stress in MPa).*

In the general expression for the polynomial form, the strain energy function is given by the series (3.12). The first nine terms in this expression are

$$\begin{aligned} W &= C_{10}(I_1-3) + C_{01}(I_2-3) \\ &+C_{20}(I_1-3)^2 + C_{11}(I_1-3)(I_2-3) + C_{02}(I_2-3)^2 \\ &+C_{30}(I_1-3)^3 + C_{21}(I_1-3)^2(I_2-3) + C_{12}(I_1-3)(I_2-3)^2 + C_{03}(I_2-3)^3 \\ &+\ldots\ldots \end{aligned} \tag{5.5}$$

The cubic I1 model according to Yeoh [65], is used here to illustrate the least squares fitting procedure. The strain energy expression is

$$W = C_{10}(I_1-3) + C_{20}(I_1-3)^2 + C_{30}(I_1-3)^3$$

with three hyperelastic constants.

5.3.2. The over determined system of equations

The experimental data points, the S_i^{exp} values and corresponding stretches λ_i, are given in Figure 5.6.

The tension and a compression stress-stretch relation S^{teor} is defined by (4.5) giving

$$S^{teor} = 2(\frac{\partial W}{\partial I_1} + \frac{1}{\lambda}\frac{\partial W}{\partial I_2})(\lambda - \frac{1}{\lambda^2}) , \tag{5.6}$$

where λ is the stretch in the loaded direction. In order to evaluate (5.6) we have to determine partial derivatives $\partial W/\partial I_1$ and $\partial W/\partial I_2$. The general expression for the derivative with respect to the first invariant I_1 is

$$\begin{aligned} \frac{\partial W}{\partial I_1} &= C_{10} + 0 \\ &+2C_{20}(I_1-3) + C_{11}(I_2-3) + 0 \\ &+3C_{30}(I_1-3)^2 + 2C_{21}(I_1-3)(I_2-3) + C_{12}(I_2-3)^2 + 0 \\ &+ \ldots\ldots \end{aligned} \tag{5.7}$$

and the general expression for the derivative with respect to I_2 is

$$\begin{aligned} \frac{\partial W}{\partial I_2} &= 0 + C_{01} \\ &+0 + C_{11}(I_1-3) + 2C_{02}(I_2-3) \\ &+0 + C_{21}(I_1-3)^2 + 2C_{12}(I_1-3)(I_2-3) + 3C_{03}(I_2-3)^2 \\ &+ \ldots\ldots \end{aligned} \tag{5.8}$$

The expressions for the derivatives are inserted into (5.6).

We also have to express the invariants in terms of λ for compression and tension as

$$\begin{cases} I_1 = \frac{2}{\lambda} + \lambda^2 \\ I_2 = \frac{1}{\lambda^2} + 2\lambda \end{cases} \tag{5.9}$$

according to (4.2). These values are used in (5.7) and (5.8). Observe that the so obtained expression for S^{teor} is linear in the coefficients C_{ij}.

The uniaxial relation (5.6) with the three parameters according to Yeoh is

$$S^{teor} = 2(C_{10} + 2C_{20}(I_1-3) + 3C_{30}(I_1-3)^2)(\lambda - \frac{1}{\lambda^2}) . \tag{5.10}$$

From (5.9) we get the first invariant I_1 expressed in terms of λ. Inserting (5.9) into (5.10) yields

$$S^{teor} = 2(C_{10} + 2C_{20}(\frac{2}{\lambda} + \lambda^2 - 3) + 3C_{30}(\frac{2}{\lambda} + \lambda^2 - 3)^2)(\lambda - \frac{1}{\lambda^2}) \tag{5.11}$$

Setting up the (approximative) equalities at every experimental point consequently yields a linear system of equations. Normally the number of experimental points exceeds the number of coefficients, thus yielding an *overdetermined linear system of equations.* The experimental data points from a tension and a compression test given in Figure 5.6 are listed in the table below. These values are used in the relative error format of (5.3) and (5.11) is set up in each of the experimental points. The equations take the form

λ	S^{exp} (MPa)
0.6	-2.788
0.64	-2.30
0.68	-1.904
0.72	-1.564
0.76	-1.276
0.8	-1.02
0.84	-0.792
0.88	-0.576
0.92	-0.376
0.96	-0.18
1.1	0.378
1.2	0.630
1.3	0.814
1.4	0.98
1.5	1.130
1.6	1.258
1.7	1.380
1.8	1.536
1.9	1.684
2.0	1.852
2.1	2.056
2.2	2.306
2.3	2.648
2.4	3.092
2.5	3.694

$$\Longrightarrow \quad \begin{bmatrix} 1.5623 & 2.1663 & 2.2530 \\ 1.5664 & 1.6748 & 1.3431 \\ 1.5574 & 1.2570 & 0.7610 \\ 1.5461 & 0.9158 & 0.4069 \\ 1.5224 & 0.6369 & 0.1998 \\ 1.4951 & 0.4186 & 0.0879 \\ 1.4577 & 0.2523 & 0.0328 \\ 1.4282 & 0.1346 & 0.0095 \\ 1.3908 & 0.0565 & 0.0017 \\ 1.3897 & 0.0137 & 0.0001 \\ 1.4474 & 0.0816 & 0.0034 \\ 1.6049 & 0.3424 & 0.0548 \\ 1.7403 & 0.7952 & 0.2725 \\ 1.8159 & 1.4112 & 0.8225 \\ 1.8682 & 2.1796 & 1.9072 \\ 1.9227 & 3.1148 & 3.7844 \\ 1.9623 & 4.1854 & 6.6955 \\ 1.9419 & 5.2474 & 10.6347 \\ 1.9275 & 6.4096 & 15.9852 \\ 1.8898 & 7.5594 & 22.6782 \\ 1.8222 & 8.6096 & 30.5086 \\ 1.7289 & 9.5056 & 39.1978 \\ 1.5944 & 10.0751 & 47.7495 \\ 1.4401 & 10.3495 & 55.7838 \\ 1.2669 & 10.2620 & 62.3419 \end{bmatrix} \begin{bmatrix} C_{10} \\ C_{20} \\ C_{30} \end{bmatrix} = \begin{bmatrix} 1 \\ 1 \\ 1 \\ 1 \\ 1 \\ 1 \\ 1 \\ 1 \\ 1 \\ 1 \\ 1 \\ 1 \\ 1 \\ 1 \\ 1 \\ 1 \\ 1 \\ 1 \\ 1 \\ 1 \\ 1 \\ 1 \\ 1 \\ 1 \\ 1 \end{bmatrix}$$

This overdetermined system of equations can be written in matrix form as

$$\mathbf{Ac} = \mathbf{b} \ , \tag{5.12}$$

where $\mathbf{A}$ is a 25x3 matrix corresponding to the 25 experimental points, $\mathbf{c}$ is a 3x1 matrix with $c_1 = C_{10}$, $c_2 = C_{20}$, $c_3 = C_{30}$ and $\mathbf{b}$ is a 25x1 matrix.

The overdetermined system (5.12) can not be solved in the ordinary way because there is no unique solution to this system of equations. It has to be solved by a minimization procedure described in the next section.

5.3.3. Minimization of the residual

Inserting a trial solution $\mathbf{c}^*$ in (5.12) will always yield a difference between the left- and the right-hand side. This difference is expressed by the residual

$$\mathbf{e} = \mathbf{Ac}^* - \mathbf{b}$$

which is a vector containing the relative error in each data point. We want to find a solution $\mathbf{c}^*$ that minimizes the residual. The size of the residual $\mathbf{e}$ must be measured in some vector norm. Use of the L_2-norm of the residual

$$||\mathbf{e}||_2^2 = \mathbf{e}^T\mathbf{e}$$

yields an expression precisely equal to the sum of the squares of the relative error between theory and experiments, i.e

$$\Phi = ||\mathbf{e}||_2^2 = (\mathbf{Ac} - \mathbf{b})^T(\mathbf{Ac} - \mathbf{b}) = \sum_{i=1}^{n} (S_i^{teor}/S_i^{exp} - 1)^2 .$$

Minimizing Φ is equivalent to finding the solution to the equations

$$\frac{\partial \Phi}{\partial c_i} = 0 \quad i = 1, 2, ...9 . \tag{5.13}$$

Index notation yields

$$\frac{\partial \Phi}{\partial c_j} = \frac{\partial e_i^2}{\partial c_j} = 2e_i \frac{\partial e_i}{\partial c_j}$$

and

$$\frac{\partial e_i}{\partial c_j} = \frac{\partial}{\partial c_j}(A_{ik}c_k - b_i) = A_{ik}\delta_{kj} = A_{ij} .$$

With these expressions (5.13) becomes

$$A_{ij}A_{ik}c_k = A_{ij}b_i$$

which can be written in matrix form as

$$\mathbf{A}^T\mathbf{Ac} = \mathbf{A}^T\mathbf{b} . \tag{5.14}$$

Expression (5.14) is an ordinary linear system of equations with the same number of unknowns as the number of equations.

Applying (5.14) to the overdetermined system of equations yields an ordinary system of equations with three equations and three unknowns i.e.

$$\begin{bmatrix} 67.92 & 147.44 & 487.11 \\ 147.44 & 649.47 & 2717.13 \\ 487.11 & 2717.13 & 12699.74 \end{bmatrix} \begin{bmatrix} C_{10} \\ C_{20} \\ C_{30} \end{bmatrix} = \begin{bmatrix} 40.8894 \\ 87.6551 \\ 303.5157 \end{bmatrix} . \tag{5.15}$$

Solving (5.15) yields

$$C_{10} = 0.6803\, MPa \quad C_{20} = -0.0982\, MPa \quad C_{30} = 0.0188\, MPa .$$

We can conclude that in order to obtain the unknown elastic parameters we have to set up the matrices **A** and **b** and solve (5.14). The solution obtained in this way is the "closest fit" to experiments in the sense that the sum of the squares of the errors for all experimental points is minimized.

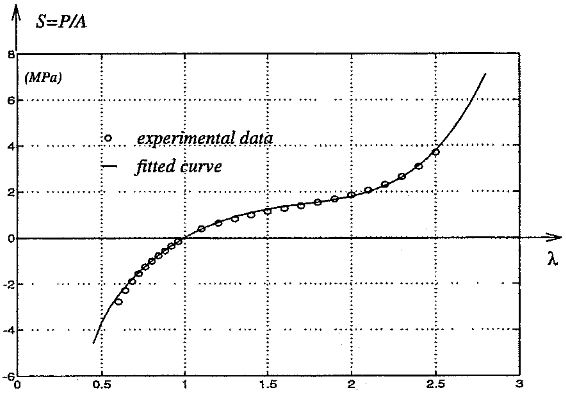

Figure 5.7: *Fitting of the three parameter model to experimental data.*

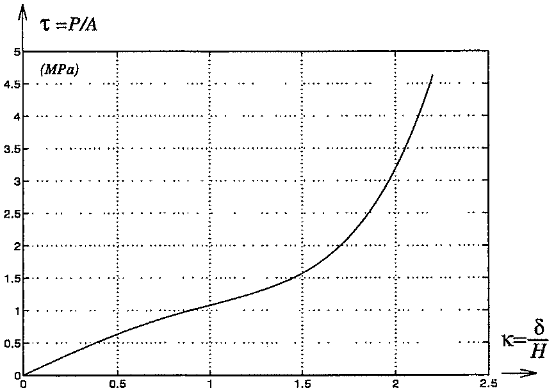

Figure 5.8: *Behavior in simple shear for the fitted three-parameter model.*

The experimental data points and the fitted curve are shown in Figure 5.7. The fitting to the experimental points is good, and the fitted curve is progressive outside the interval of experimental data. For this choice of parameters the least squares procedure generates a model with a good fit and reasonable behavior outside the interval of fitted points.

The behavior in simple shear shown in Figure 5.8 is also reasonable, with an increasing curve with the same characteristics as an experimentally obtained curve.

The strain energy plot in Figure 5.9 shows the strain energy function $W(\lambda_1, \lambda_2)$ as a physically reasonable bowl shaped function that is monotonically increasing.

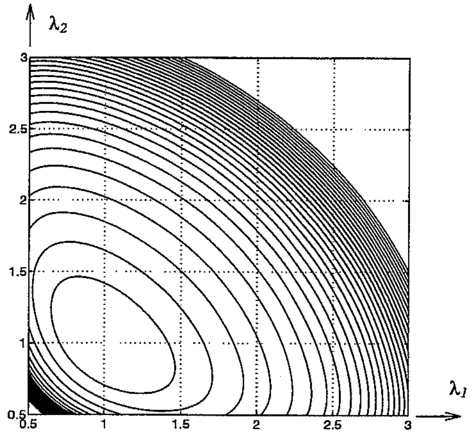

Figure 5.9: *Strain energy function for the three-parameter model.*

5.4. Stability of the fitted model

The good behavior of the fitted model in the previous section is not obtained automatically. Other sets of data and other choices of parameters can yield completely unsatisfactory behavior outside the fitted interval, as will be shown next.

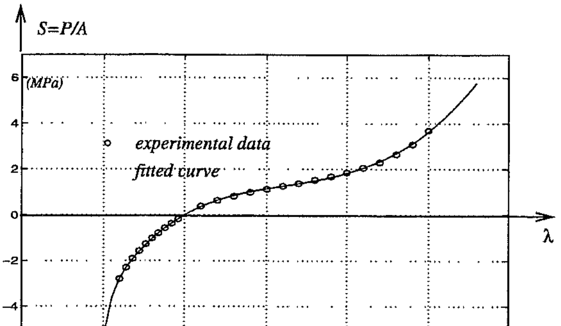

Figure 5.10: *Fitting of the five-parameter model to experimental data.*

The same experimental data were used to fit a model with the parameters C_{10}, C_{01}, C_{20}, C_{11} and C_{02} i.e. the first five in (5.5).

An equivalent overdetermined system according to (5.15) was established. Solv-

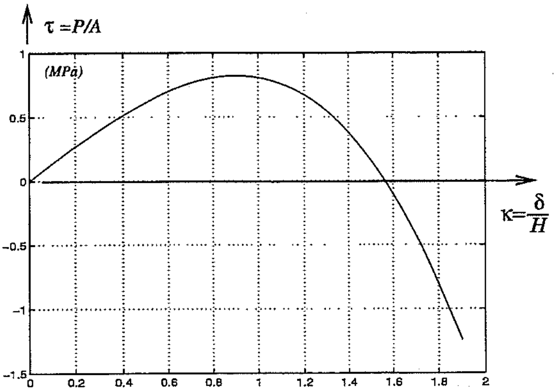

Figure 5.11: *Behavior in simple shear for the five-parameter model fitted to compression/tension data.*

ing for the five constants yields

$$C_{10} = 0.5259\,MPa \quad C_{01} = 0.1583\,MPa$$
$$C_{20} = 0.3300\,MPa \quad C_{11} = -0.8154\,MPa \quad C_{02} = 0.3453\,MPa\ .$$

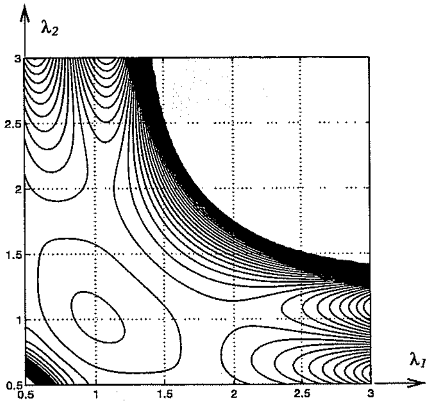

Figure 5.12: *Strain energy function for the five-parameter model.*

The experimental data points and the fitted curve are shown in Figure 5.10. It can be seen that the fitting to the experimental points is good in compression and tension, and the fitted curve is progressive outside the interval of experimental data. However, the behavior in simple shear according to Figure 5.11 is completely unsatisfactory, and this hyperelastic model can not be used in finite element analysis.

This unrealistic behavior can be revealed by looking at the strain energy plot in Figure 5.12. The strain energy plot shows the overall behavior of the model, and the deviation from the bowl shape shows that the model can not be used in finite element analysis.

5.5. Characterization of some vulcanizates

Hyperelastic constants for some filled natural rubber vulcanizates of nominal hardness between 40 and 78 IRHD have been evaluated by fit to test data obtained from shear and compression tests. The specimens were manufactured by the rubber companies Forsheda, Svedala-Skega and Trelleborg.

Intermittent conditioning was chosen for the test procedure, i.e. relaxed data for successively higher strain have been used. Hyperelastic constants were evaluated by a least squares fit according to the procedures described in Section 5.3.

5.5.1. Testing

Compression and the double shear specimens according to Figure 5.13, were used in the tests.

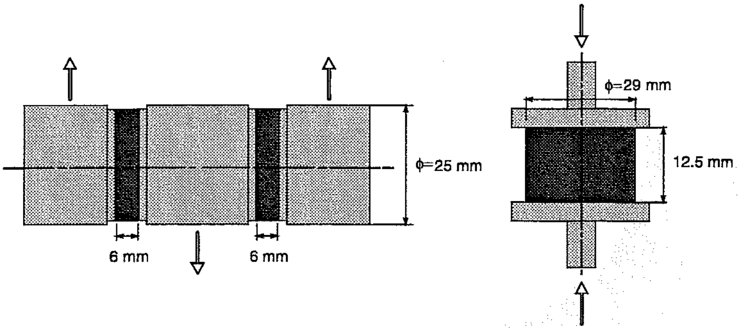

Figure 5.13: *Double shear and compression specimens.*

Nominal dimensions of the cylindrical compression specimens were height 12.5mm and diameter 29mm. Nominal dimensions of the two cylindrical rubber discs in the double shear specimen were thickness 6mm and diameter 25mm. Dimensions were checked individually and measured dimensions were used for calculation of stress and strain.

Testing was performed with relaxation at one millimeter intervals with successively longer relaxation times. The relaxation time for 1mm deformation was 30s and the relaxation time was increased by 30s for each mm of deformation. The compression specimens were tested to a maximum compression of 7mm and the

Company	IRHD	compression	shear
Forsheda AB	40	2	2
	50	2	2
Skega AB	50	3	3
Trelleborg AB	71	0	1
	78	0	1

Table 5.1: *Specimens and nominal hardness used in the testing.*

shear specimens were tested to $11mm$ displacement. The temperature was held at 23.5 ± 0.5^oC

An overview of the tested materials and the number of test specimens are given in Table 5.1. All materials are carbon-black-filled natural rubber vulcanizates.

A summary of experimental shear moduli evaluated as the secant moduli for 100% shear strain, and the estimated hardness values obtained from the diagram in Figure 1.3, are given in Table 5.2.

Company	nominal IRHD	G^{exp} (MPa)	estim. IRHD
Forsheda AB	40	0.46	40.6
	50	0.57	46.7
Skega AB	50	0.78	54.3
Trelleborg AB	71	1.13	61.2
	78	1.90	71.9

Table 5.2: *Nominal hardness and estimated hardness from experimentally evaluated shear moduli.*

Table 5.2 shows a substantial difference in shear modulus for materials with the same nominal hardness, and that highly filled materials can be difficult to evaluate by the hardness test.

Comparison of intermittent and slow continuous loading

Tests in compression and shear with very slow continuous loading were carried out and compared with the intermittent method. Previously unstrained 50 IRHD specimens from Skega according to Table 5.1 were used in the tests. The criterion for the continuous test was that the test should be conducted with a loading speed corresponding to the same total time as for the intermittent test. This corresponds to a shear strain rate of $1 \cdot 10^{-3}/s$ and a compression stretch rate of $5 \cdot 10^{-4}/s$. The outcome of the test is shown in Figure 5.14, where the dotted line is the continuous loading and the circles are intermittent test values for three test specimens (the same as in Figure 5.17).

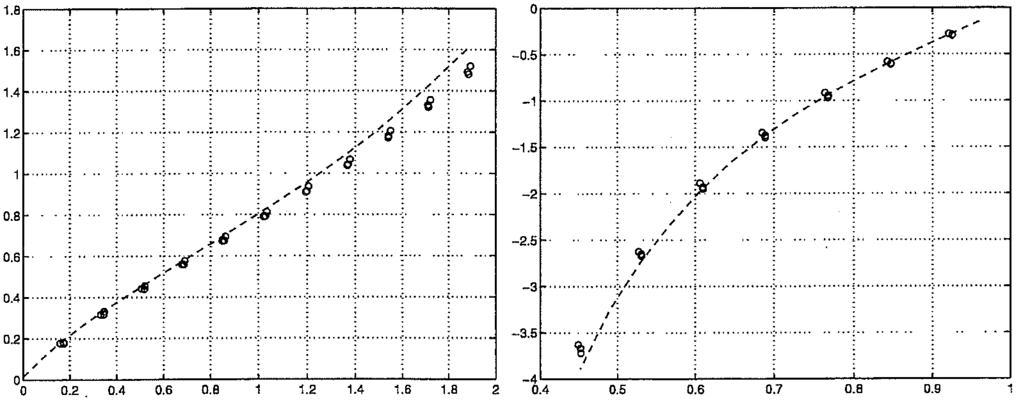

Figure 5.14: *Comparison of the intermittent method and a very slow continuous loading, with the same total time. Left: Shear stress (MPa) versus direct shear strain. Right: Compression; nominal stress (MPa) versus stretch.*

It can be seen that the continuous straining yields almost the same stress values as the intermittent method.

5.5.2. Evaluation of Yeoh constants

Yeoh's model was fitted to intermittent data according to the fitting procedure outlined in section 5.3. The intermittent data are shown as circles in the figures below. There is one circle for each specimen at each value of stretch. The solid line is the fitted hyperelastic model. It can be seen that the scatter in experimental data is small for these specimens. This is because the specimens were manufactured from the same batch and their dimensions were individually measured.

Forsheda

The fits to Forsheda's materials with nominal hardness 40 and 50 IRHD are shown in Figure 5.15 and Figure 5.16 respectively. Two shear specimens and two compression specimens were tested for each material. The diagrams to the left in the figures show the fit to double shear data and the diagrams to the right show the fit to compression data.

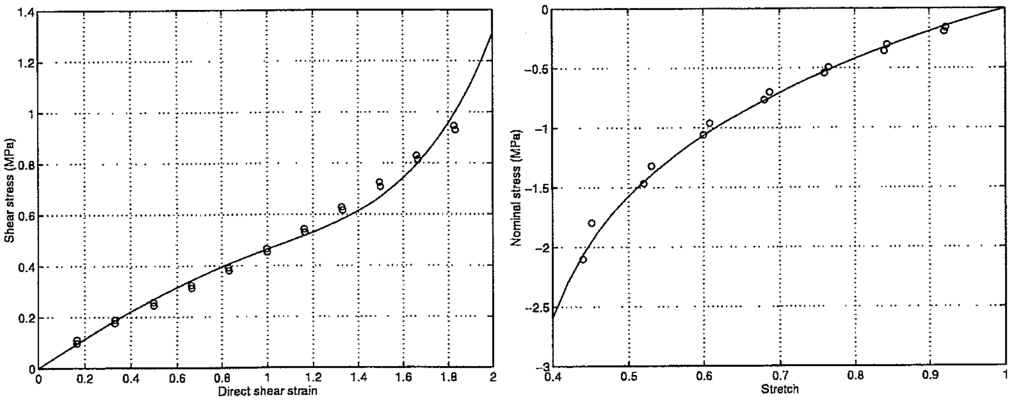

Figure 5.15: *Fit of Yeoh's model to Forsheda 40 IRHD material.*

The hyperelastic constants for the 40 IRHD material (cf. Figure 5.15) are

$$C_{10} = 0.2885 \qquad C_{20} = -0.0394 \qquad C_{30} = 0.0074 \qquad (MPa).$$

The fit of Yeoh's model to the second material from Forsheda, i.e. the 50 IRHD material, is shown in Figure 5.16 for shear and compression.

The constants for the 50 IRHD material are

$$C_{10} = 0.3493 \qquad C_{20} = -0.0363 \qquad C_{30} = 0.0069 \qquad (MPa).$$

Skega

The fit of Yeoh's model to the other material with a nominal hardness of 50 IRHD from Skega is shown in Figure 5.17. Three shear specimens and three compression

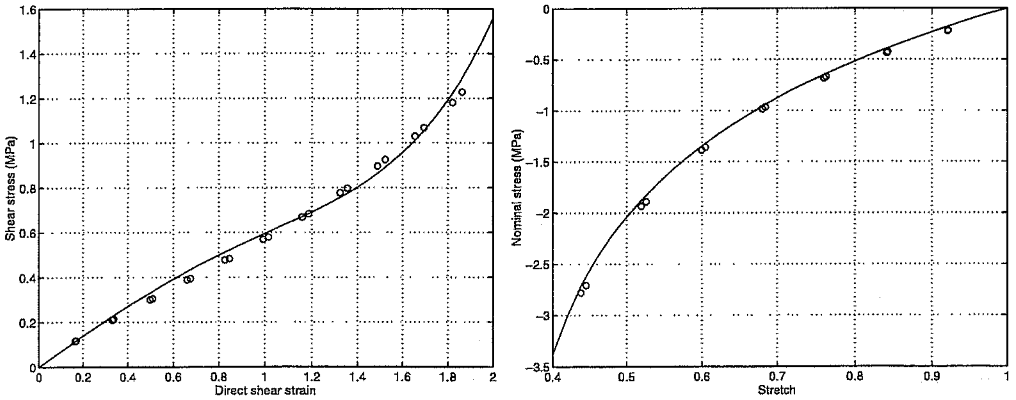

Figure 5.16: *Fit of Yeoh's model to Forsheda 50 IRHD material.*

specimens were tested. The diagram to the left shows the fit to double shear data and the diagram to the right shows the fit to compression data.

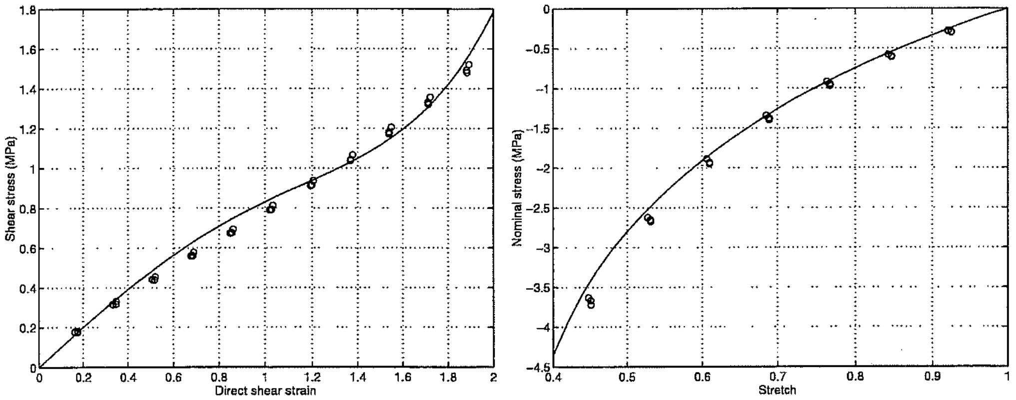

Figure 5.17: *Fit of Yeoh's model to Skega 50 IRHD material.*

The hyperelastic constants are

$$C_{10} = 0.5079 \qquad C_{20} = -0.0593 \qquad C_{30} = 0.0086 \qquad (MPa).$$

Trelleborg

Finally a fit to Trelleborg's shear specimens was conducted according to Figure 5.18, with the 71 IRHD material to the left and the 78 IRHD material to the right. These fits are very accurate due to the absence of compression data.

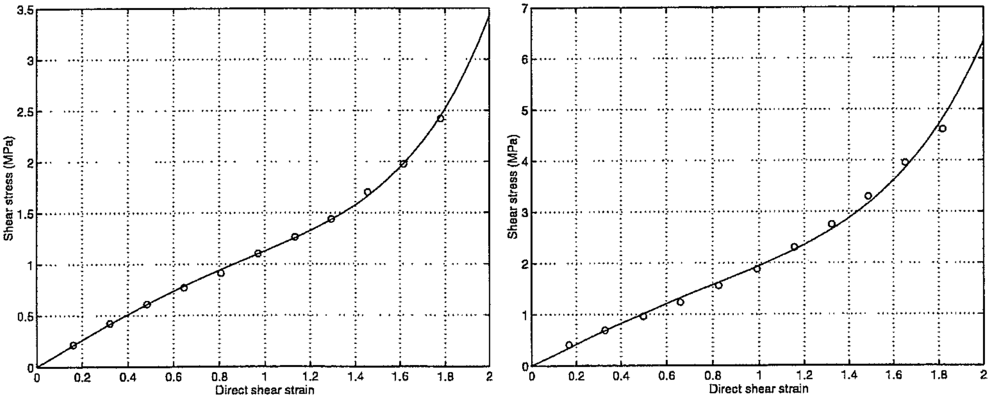

Figure 5.18: *Fit of Yeoh's model to shear data only for Trelleborg 71 and 78 IRHD material.*

The constants for the 71 IRHD material are

$$C_{10} = 0.6598 \qquad C_{20} = -0.0723 \qquad C_{30} = 0.0162 \qquad (MPa)$$

and for the 78 IRHD material

$$C_{10} = 1.0543 \qquad C_{20} = -0.0779 \qquad C_{30} = 0.0241 \qquad (MPa).$$

Summary

All the fitted models were stable according to the strain energy plot.

A summary of the hyperelastic constants for the tested materials is given in Table 5.3.

Company	IRHD	C_{10}	C_{20}	C_{30}
Forsheda AB	40	0.2885	-0.0394	0.0074
	50	0.3493	-0.0363	0.0069
Skega AB	50	0.5079	-0.0593	0.0086
Trelleborg AB	71	0.6598	-0.0723	0.0162
	78	1.0543	-0.0779	0.0241

Table 5.3: *Hyperelastic (Yeoh) constants and nominal hardness for five carbon-black-filled natural rubbers.*

6. EVALUATION OF TEST SPECIMENS

In order to evaluate the different commonly used rubber test specimens, a number of finite element analyses have been performed. The force-displacement relationships obtained from these analyses have been compared with the corresponding analytical expressions for the ideal states of deformation. In general, very good accuracy has been found for the test pieces. However, some improvements are proposed for some of the specimens in order to increase the accuracy of the tests.

The material model generally used here (the Yeoh model) is only dependent on the first strain invariant I_1. Therefore some analyses have been performed on the quadruple shear specimen with the Mooney-Rivlin material, with hyperelastic constants that also give a dependence on the second strain invariant I_2.

6.1. Introduction

Computer aided design of rubber units by means of the finite element method requires constitutive parameters obtained from experimental data. Rubber manufacturers usually have many different recipes for rubber vulcanizates of different stiffness to be used in different environments. Characterization of different materials requires a lot of laboratory testing, and the choice of test specimens to use is an important topic.

A general rule can be that the predominant state of deformation of the products to be analyzed should be represented in the material tests. I.e. if the products are mainly loaded in compression and shear, some compression and shear test pieces should be used in the material tests. It is also important that the test specimens have a roughly similar material distribution; if the products consist of solid sections of rubber then solid test pieces should also be used. Moreover, material testing is costly and time consuming. The material tests should therefore be chosen so that they are easily performed.

The state of strain in the test pieces should be as close as possible to the ideal homogeneous analytical state of strain. A number of different test pieces will be discussed, and primarily the accuracy of tests. The deformation of the test pieces has been simulated by finite element analysis using ABAQUS [26], and the force-displacement relationships obtained from these analyses have been compared with the corresponding analytical expressions.

Modifications are proposed for some of the test specimens. The purpose of these modifications is to improve the accuracy of the material tests, to receive stress-stretch relations that are closer to the analytical relations. The proposed improvements are all relatively simple to implement.

The finite element method only produces an approximation of the actual force deformation relationships. Therefore convergence analyses have been performed in order to ensure that the approximation does not affect the results.

6.2. Hyperelastic constants

The hyperelastic Yeoh constants used in the following analyses are shown in Table 6.1. The constants are determined from carbon-black-filled natural rubbers. The materials are listed in order of increasing nominal hardness. The 40, 50, 65 and 78 IRHD materials are the same as in Chapter 5.

IRHD	C_{10}	C_{20}	C_{30}
40	0.2885	−0.0394	0.0074
50	0.3493	−0.0363	0.0069
65	0.6803	−0.0982	0.0188
78	1.0543	−0.0779	0.0241

Table 6.1: *Hyperelastic constants used in the analysis.*

The Yeoh material model, generally used in this chapter, only takes the first strain invariant into account. Therefore some analyses have been performed on the quadruple shear specimen with the Mooney-Rivlin material model. By varying the material parameters for this material model, the effect of the second strain invariant can also be accounted for.

6.3. Shear test specimens

Pure shear and simple shear specimens are analyzed in this section, with dimensions according to Chapter 4.

6.3.1. Finite element models

The finite element model of the pure shear specimen according to Figure 4.6, with thickness $2mm$, height $20mm$, and width $180mm$, is shown in Figure 6.1. Three symmetry planes have been used, a displacement boundary constraint has been applied to the top surface. The total reaction force in the vertical direction on the lower symmetry plane is registered. Due to the symmetry the applied deformation should be half of the desired displacement and the reaction forces will be a quarter of the total reaction force for the complete model. The nominal stress is obtained

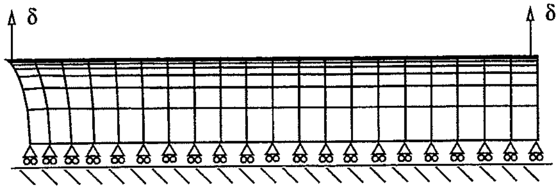

Figure 6.1: *Finite element model of pure shear specimen.*

by dividing the total reaction force with the cross-sectional area of the undeformed rubber membrane.

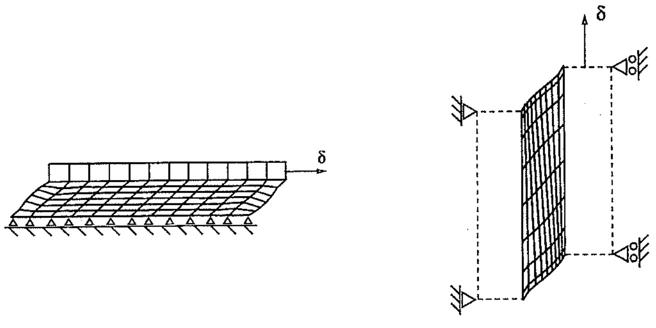

Figure 6.2: *Finite element model of quadruple shear specimen (left) and double shear specimen (right).*

The finite element model of the quadruple shear specimen according to Figure 4.8 is shown to the left in Figure 6.2. One of the four rectangular blocks of rubber, with dimensions height $4mm$, width $25mm$, and depth $20mm$, is modeled. A stiff section models the metal plate at the top of the shear specimen. This section is moved in the horizontal direction in order to obtain the desired deformation δ, and it is allowed to move freely in the vertical direction. The bottom plane of the rubber specimen is constrained in all directions and the total reaction force in the horizontal direction is registered.

The shear stress is expressed similarly to the pure shear specimen as the total reaction force in the loaded direction divided by the area of the cross section.

The double shear specimen is shown to the right in Figure 6.2. The deformation is imposed on the right surface in the vertical direction. This surface is also constrained in the horizontal direction. The left surface is constrained in all directions and the total reaction force in the vertical direction is registered.

6.3.2. Results for shear test specimens

The correspondence between the finite element solution and the theoretical expressions for pure shear and simple shear is studied here for the 65 IRHD material (cf. Table 6.1). From Figure 6.3 it can be seen that the test piece that has the best correspondence with the analytical expression for the shear deformation is the quadruple shear specimen, even if the difference between the quadruple shear and the double shear specimen is very small. The quadruple shear specimen is simpler to use in an ordinary tensile test machine as compared to the double shear specimen that requires arrangements to fix the specimen (perpendicular to the loading direction). A disadvantage of the quadruple shear specimen is that it is more complicated to manufacture.

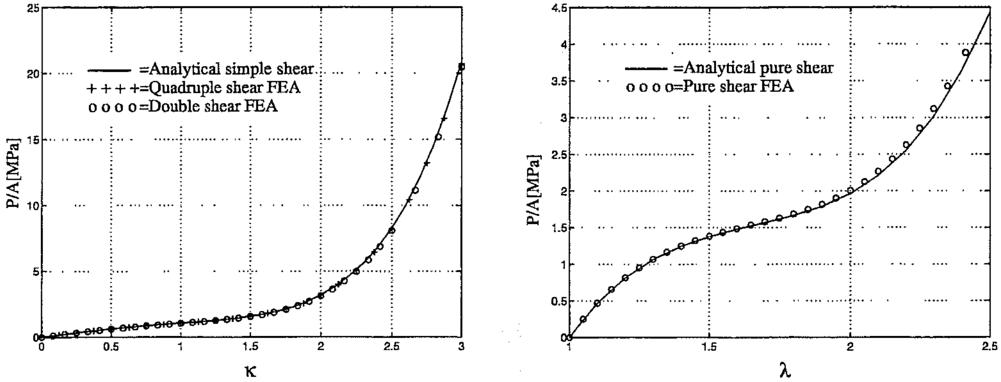

Figure 6.3: *FE simulation and analytical relations for shear deformations. Left: Simple shear and quadruple shear; shear stress versus direct shear strain. Right: Pure shear; nominal stress versus stretch.*

6.3.3. Dimensions of the pure shear specimen

There are two main deviations of the actual pure shear specimen from the ideal pure shear state of strain. Firstly, the horizontal force that should keep the vertical edges straight is missing, giving an hourglass shape in the width direction. Secondly, the thickness of the specimen will not be constant over the height. At the top and the bottom the rubber is fixed to the metal strips and the cross section will therefore become hourglass shaped also in the thickness direction.

Fortunately these two deviations affect the stiffness in opposite directions, and the accuracy of the specimen can be controlled by varying the height to width

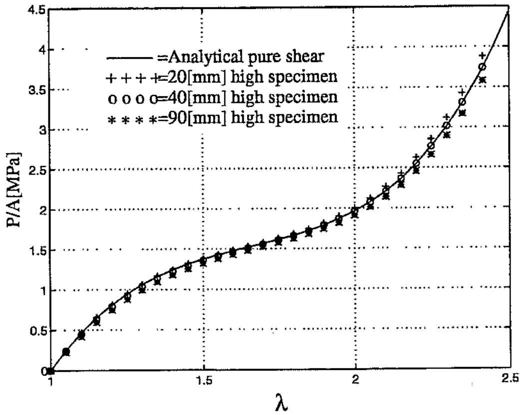

Figure 6.4: *Accuracy of the pure shear specimen with respect to the height. Nominal stress versus stretch.*

ratio. A stress-stretch relationship very close to the analytical can be obtained. This is shown in Figure 6.4, where results from finite element analyses are presented for three different heights of pure shear specimens with a width of $180mm$ and a thickness of $2mm$. It should be noted that the ideal height is determined for the 65 IRHD material and might be different for other rubber materials.

6.3.4. Effect of different materials

As mentioned earlier, the material model used in all the analyses of the test specimens is the Yeoh model, dependent only on the first strain invariant.

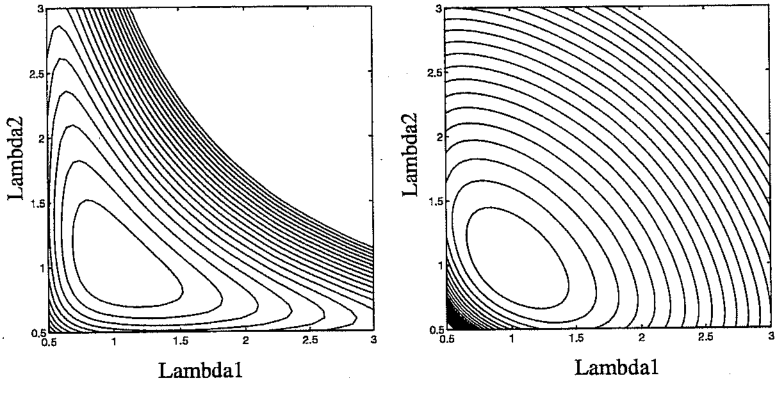

Figure 6.5: *Strain energy density plots for two different Mooney-Rivlin materials,* $C_{10} = 0; C_{01} = 0.5$ *(left) and* $C_{10} = 0.5; C_{01} = 0$ *(right).*

In order to evaluate the effect of the second strain invariant, three (constructed) sets of material constants, for the commonly used Mooney-Rivlin material model,

$$W = C_{10}(I_1 - 3) + C_{01}(I_2 - 3)$$

are used with varying dependence on the two strain invariants.

The shear modulus is $G = 2(C_{10} + C_{01})$ according to (4.23) and three sets of Mooney-Rivlin constants with the same shear modulus are used.

1. $C_{10} = 0.5$; $C_{01} = 0$, dependent on I_1 only.
2. $C_{10} = 0.25$; $C_{01} = 0.25$, dependent on both I_1 and I_2,
3. $C_{10} = 0$; $C_{01} = 0.5$, dependent on I_2 only.

The strain energy density function is visualized for the first and the third material in Figure 6.5.

Two simulations were performed with the quadruple shear model for each of these three sets of material constants. In one simulation the height of the rubber section is allowed to vary, i.e. similar to the standard quadruple shear analyses, and in the other the height of the specimen is held fixed, with the purpose of simulating a state of strain similar to the double shear test. The deformed specimens for these analyses are shown in Figure 6.6.

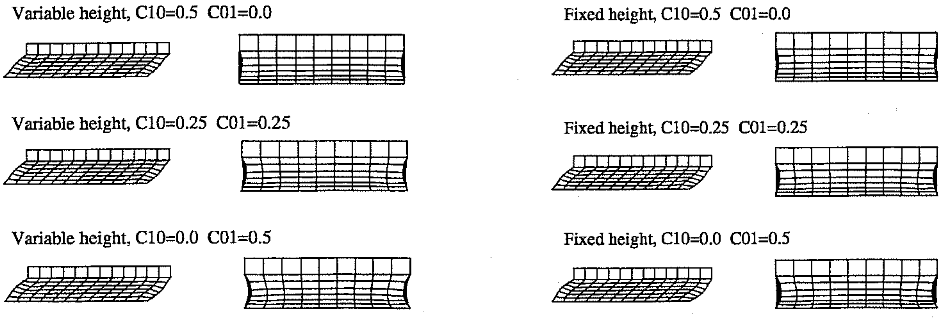

Figure 6.6: *Deformed finite element models for quadruple shear with different materials, with variable height (left) and fixed height (right).*

From Table 6.2 it can be seen that the height H of the quadruple shear specimen will be approximately constant, if a material model that is only dependent on the first strain invariant is used. However, if the material model is also dependent on the second strain invariant, the height of the rubber specimen will increase during shear deformation.

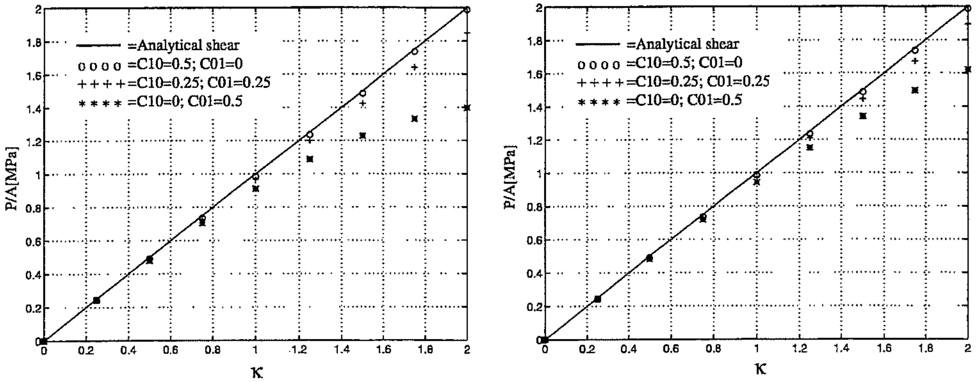

Figure 6.7: *Accuracy for quadruple shear specimen using the Mooney-Rivlin material model with varying dependence on the second strain invariant with free height (left) and fixed height (right). (Shear stress versus direct shear strain.)*

Height	C_{10}	C_{01}	δ	ΔH	F_S	F_N
Variable	0.5	0.0	4	$-1.8 \cdot 10^{-2}$	492.1	0
Variable	0.25	0.25	4	$5.1 \cdot 10^{-2}$	483.2	0
Variable	0.0	0.5	4	0.13	455.6	0
Fixed	0.5	0.0	4	0	492.4	−38.33
Fixed	0.25	0.25	4	0	486.0	104.7
Fixed	0.0	0.5	4	0	471.4	250.7

Table 6.2: *Table showing data from quadruple shear analyses with different sets of material constants.* F_S *is the shear force, and* F_N *is the resulting normal force on the upper surface.*

Plots showing the relations between stress and direct shear strain κ for the quadruple shear test are shown in Figure 6.7. From these plots it can be seen that a specimen highly dependent on the second strain invariant will be relatively weak in shear compared with the ideal analytic solution. It can also be seen that for this type of material a simple shear test specimen with the height held constant gives a better correspondence to the analytical relations. However, a material only dependent on the second strain invariant is a strange material hardly encountered in practice.

6.4. Tension and compression test specimens

The finite element models of the tension and compression specimens are shown in Figure 6.8. The dumbbell specimen is modeled with three dimensional solid elements (cf. Figure 6.8), with two symmetry planes.

The total reaction force and the deformation at a reference node corresponding to the measuring length are registered.

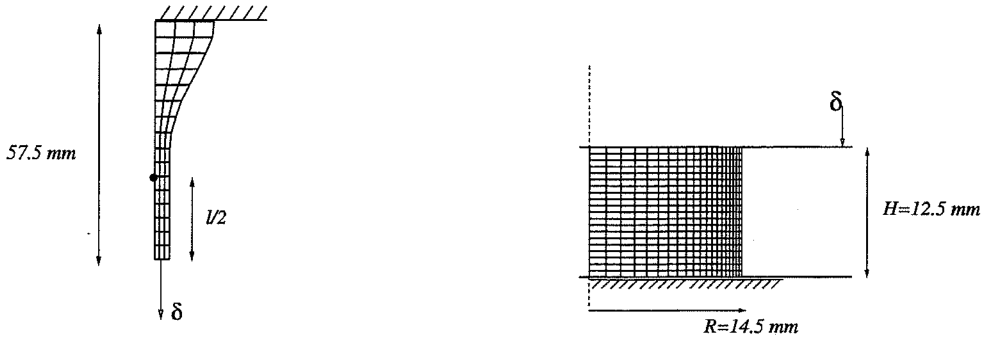

Figure 6.8: *Finite element models of the dumbbell test specimen (left) and an axisymmetric ISO standard compression test specimen (right).*

The ISO standard compression test is modeled with axisymmetric elements and the displacements are applied to the model using rigid surfaces and contact elements, see Figure 6.8. This was necessary, as one of the purposes of these analyses was to study the effect of friction between the compressing surfaces and the rubber specimen. From these analyses the total reaction force is registered for the bottom surface of the compression specimen.

6.4.1. Results for the tension specimen

The accuracy of the dumbbell tension test specimen is shown in Figure 6.9. It was analyzed with hyperelastic constants according to the 65 IRHD material in Table 6.1. Stresses for six different measuring lengths from the finite element analyses are plotted as circles together with a curve showing the analytical solution. The six measuring lengths are: $l = 13.1, 17.5, 21.9, 26.3, 30.6$, and 35 *mm*, with l according to Figure 6.8. The difference is small between the different lengths and the circles almost coincide in Figure 6.9. The relative error, calculated as the difference in stress divided by the analytical stress, for the shortest measuring length is also shown in Figure 6.9 (right).

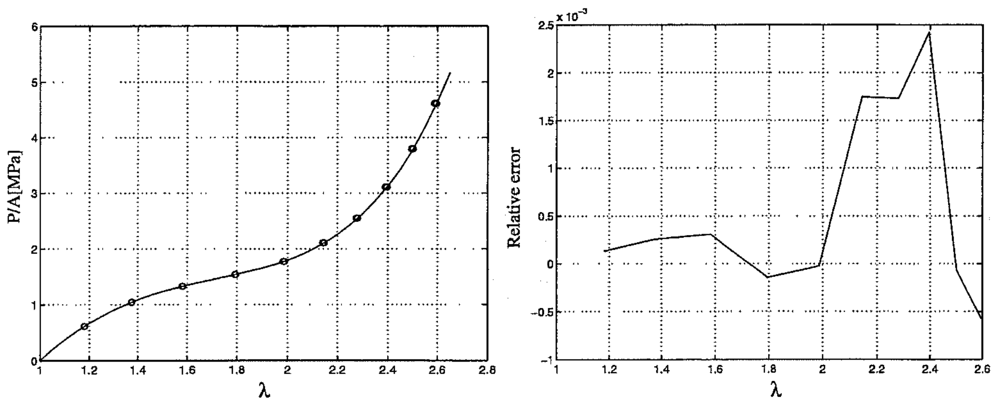

Figure 6.9: *FE simulations and analytical curve for dumbbell specimen (left) and relative error for the shortest measuring length (right).*

6.4.2. Results for compression specimens

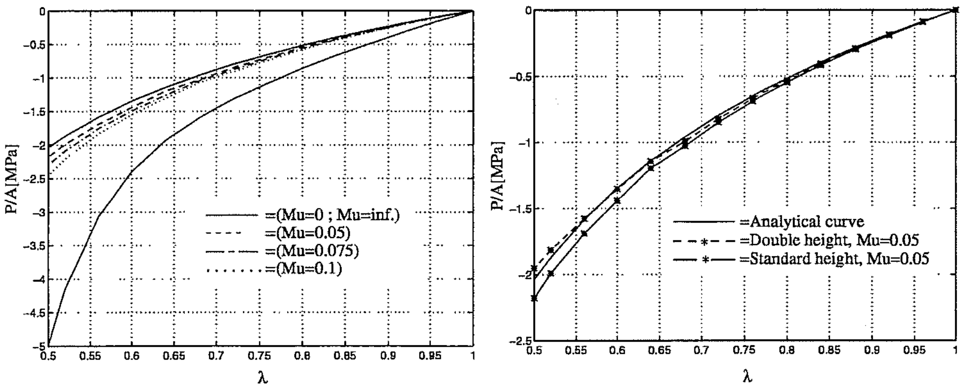

Figure 6.10: *Stress-stretch relations; compression specimens. Left: Effect of friction for the ISO standard specimen. Right: Effect of doubling the specimen height.*

The ISO standard compression specimen is, unless otherwise specified, analyzed here with hyperelastic constants obtained for the 50 IRHD material (cf. Table 6.1). Effects of specimen height, friction, and shape of the compressing rigid surface will be studied.

Preliminary tests [47] of rubber to metal friction, with the surfaces lubricated by silicon grease, for compressions up to 50% have shown coefficients of friction μ in the interval $0.05 < \mu < 0.15$. The coefficient will vary with the contact pressure. A large contact pressure will lead to a large coefficient of friction.

The effect of friction on the stress-stretch relationship is shown in Figure 6.10 (left). It can be seen that increasing friction leads to decreasing accuracy of the test, due to a nonhomogeneous state of strain, that can be seen as a barrel shape of the specimen.

In order to make the state of strain more homogeneous and thereby increase the accuracy, a test specimen with a height that is double the standard height (h=2×12.5=25 *mm*) is proposed. In Figure 6.10 (right) the stress-stretch curve for the high specimen is shown together with the standard specimen. It can be seen that the accuracy of the specimen has improved, although the analysis results for compression greater than 35% are not quite reliable since the finite element model is a bit weaker than the analytical solution.

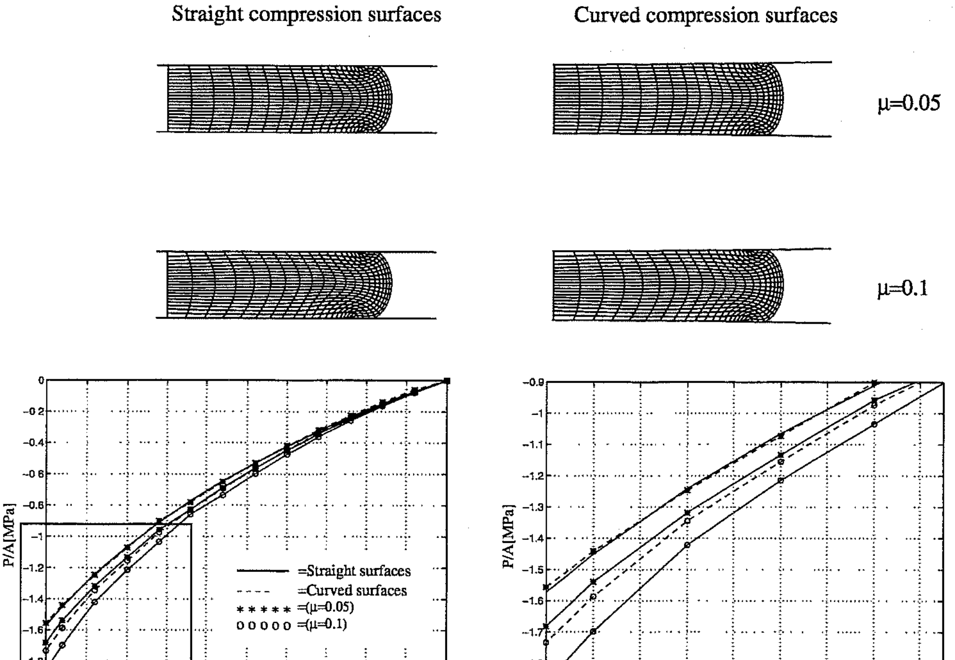

Figure 6.11: *Above: Deformed finite element models of compression test specimens with varying geometry of compression surfaces for different coefficients of friction,* $\lambda = 0.5$. *Below: Influence of compression surfaces and coefficients of friction compared to the analytical solution (solid line with no markers). The right graph is an enlargement of the marked section in the left graph.*

Another method to increase the accuracy of the compression test specimen could be to modify the compressing surfaces so that they are slightly curved. This should somewhat decrease the effects of the frictional forces acting on the end surfaces of the rubber specimen. A radius of curvature of approximately 1200 *mm* on the compressing surfaces has been found to give good results. Figure 6.11 shows the deformed mesh of compression specimens for straight and curved surfaces and for two different coefficients of friction. The hyperelastic constants in these analyses are according to the 40 IRHD material in Table 6.1. It can be seen that the introduction of a small curvature of the compression surfaces gives a more homogeneous state of deformation for the same value of the coefficient of friction.

From Figure 6.11 it can also be seen that a stress-stretch response very close to the analytical can be obtained for the 40 IRHD material and a coefficient of friction of 0.05, if the compression surfaces are curved with a very large radius (1200 *mm*).

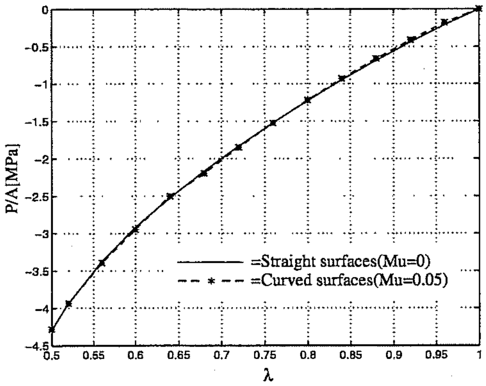

Figure 6.12: *Data from finite element analyses of compression test specimens with straight compression surfaces and no friction, and with curved compression surfaces with friction.*

An additional analysis has been performed for a rubber material with a significantly larger hardness, i.e. the 78 IRHD material according to Table 6.1. The stress-stretch curves for this material are shown in Figure 6.12. It can be seen that the curvature of the rigid surface improves the accuracy also for this material.

The introduction of a small curvature of the rigid surface would seem to be an improvement of this material test. However, the sensitivity to geometrical modifications of the compressing surfaces is disturbing. A small error in the alignment of the compressing surfaces can have a considerable influence.

6.5. Summary

In general, the quadruple shear specimen is both the simplest to use and most accurate shear specimen. It can be used with ordinary tensile test equipment without complicated fittings. Moreover, it does not require any special equipment to register the deformations, and it is shown to be close to the analytical solution. The quadruple shear specimen is included in the ISO standard.

If the pure shear specimen is to be used the height of the specimen should be taken into consideration. Figure 6.4 shows that the correspondence between test and theory is dependent on the height of the test specimen if the width and thickness are held constant.

The quadruple shear specimen has been analyzed with the Mooney-Rivlin material model and different sets of material constants in order to evaluate the effect of the second strain invariant I_2 on the deformation. This was done as the Yeoh material model otherwise used only takes the first strain invariant I_1 into account. It was found that a material that is strongly dependent on the second strain invariant will lead to an increasing height of the quadruple shear specimen during shear deformation. It was also found that this type of material will lead to a less accurate test and the response is in this case better if the height is held constant. This indicates that for materials with a significant dependence on the second strain invariant the double shear specimen should give more accurate results.

The dumbbell tension specimen is very accurate, but it has disadvantages. Some sort of device (clip gauges or other) has to be used in order to measure the displacement. The loads are also very small and will require a load cell for small forces. Another disadvantage is the difficulty to get slip-free connections at the ends.

The ISO standard compression specimen has also been analyzed, especially in order to evaluate the effect of friction between the compressing steel surfaces and the rubber specimen.

Two modifications of the specimen have been proposed, namely increasing the height of the rubber specimen and, alternatively, modifying the compressing surfaces by introduction of a large radius of curvature. It has been found that the higher model gives a stress-stretch response that is closer to the analytical. The introduced curvature of the compressing surfaces leads to a stress-stretch response that is very close to the analytical for carbon-black-filled rubber materials of varying hardness.

However, the analyses have indicated that the results are extremely sensitive to geometrical changes. An introduction of a radius of curvature of approximately 1200 mm on the compressing surfaces significantly changed the stress-stretch response. On the other hand practical tests according to Chapter 5 do not show very large scatter. The accuracy of the lubricated compression specimen requires further investigation.

An alternative combined compression and tension specimen will be discussed in Chapter 7.

7. ALTERNATIVE EXPERIMENTAL METHODS

In the first section, a new test specimen, named solid dumbbell, is presented as an alternative to the the standard tension and compression specimens. The solid dumbbell specimen is shown to be accurate, in both tension and compression, and easy to use.

In the second section, an extension of the standard hardness test is proposed. A number of indentation depths are chosen and the force for these depths is recorded. It is shown that by this modification, hyperelastic constants can be derived from the test. More information can thereby be provided from the test by a small extra effort.

In the third section, a new method to measure displacements and strains in, for example, rubber membranes without applying sensors to the specimens is described. This optical technique uses a CCD camera, a computer with frame grabber board and image analysis techniques.

7.1. Solid dumbbell test specimen

The *solid dumbbell* specimen proposed here is an alternative to the ISO membrane dumbbell test piece and the lubricated cylinder compression test. It is an axisymmetric specimen cf. Figure 7.1 which can be used for both tension and compression without changes of the setup in an ordinary tensile testing device.

The solid dumbbell also has the advantage of showing an almost linear relation between loading head displacement and gauge length displacement for rubber vulcanizates of widely varying stiffness. This makes it possible to use the test piece without clip gauges.

Another advantage is that, contrary to the membrane dumbbell specimen, the solid dumbbell, like many engineering products, consists of a solid piece of rubber. This means that the heat distribution during vulcanization and the cross-linking will be more similar to engineering products.

The solid dumbbell specimen is analyzed here by the finite element method in order to compare the behavior with the theoretical ideal.

Two different lengths of the specimen have been studied by finite element analysis. The longer model was also manufactured by Svedala-Skega in a 60 IRHD black filled natural rubber.

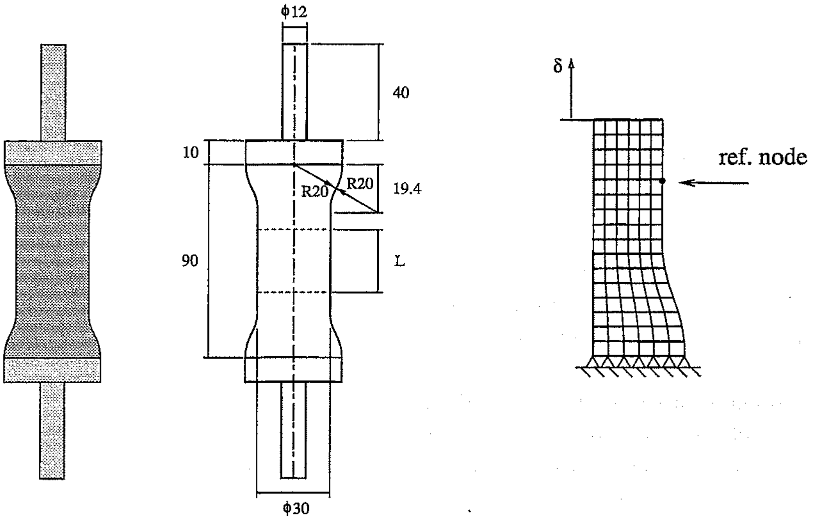

Figure 7.1: *The axisymmetric long solid dumbbell specimen (dimensions in mm) and the finite element model.*

Preliminary tests showed that it was stable to approximately 30% compression. In order to improve the stability of the specimen, a shorter specimen was also considered. The shorter model, with a $10mm$ shorter rubber part (cf. Figure 7.1), was suspected to give slightly less accurate results, but the benefit would be an ability to undergo greater compression.

7.1.1. Finite element modeling

The solid dumbbell specimen is modeled with axisymmetric elements and one symmetry plane. The 65 IRHD material according to Table 6.1 was used in the analysis unless otherwise specified. In the finite element analysis the displacements of the nodes on the horizontal symmetry plane are prescribed. The bottom surface is constrained in all directions. Moreover, a node is chosen to represent the "homogeneous zone", see Figure 7.1, and the displacement of this node is also registered. The total vertical reaction force on the bottom surface is also registered. From this the stress and stretch in the "homogeneous zone", with length L according to Figure 7.1, can be calculated.

7.1.2. Long solid dumbbell

Stress-stretch data derived from finite element analysis are shown for a number of measuring lengths L. When the graphs are studied it is important to remember that the stability problems that will occur during mechanical testing will not be

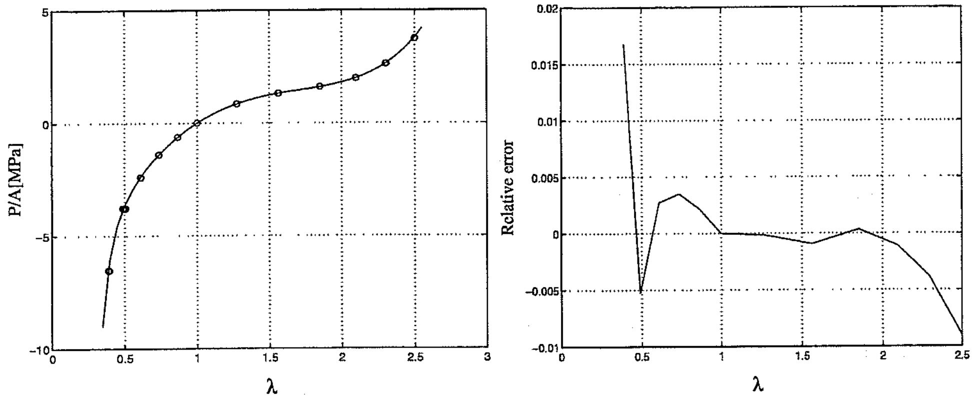

Figure 7.2: *FE simulations and analytical curve for long solid dumbbell specimen (left) and relative error for the shortest measuring length (right).*

represented in these axi-symmetric finite element analyses. As mentioned, the long solid dumbbell has in practical testing been found to be stable for compression values up to approximately 30%.

Figure 7.2 shows the stress-stretch relationships for the longer model as compared to the ideal compression/tension curve shown as a solid line (left) and the relative error (right).

Data for eight different measuring lengths $L = 6.25$, 12.5, 18.75, 25, 31.25, 37.5, 43.75, and 50 mm are displayed as almost coinciding circles. It can be seen that the ideal analytical compression/tension curve is followed well for all lengths L.

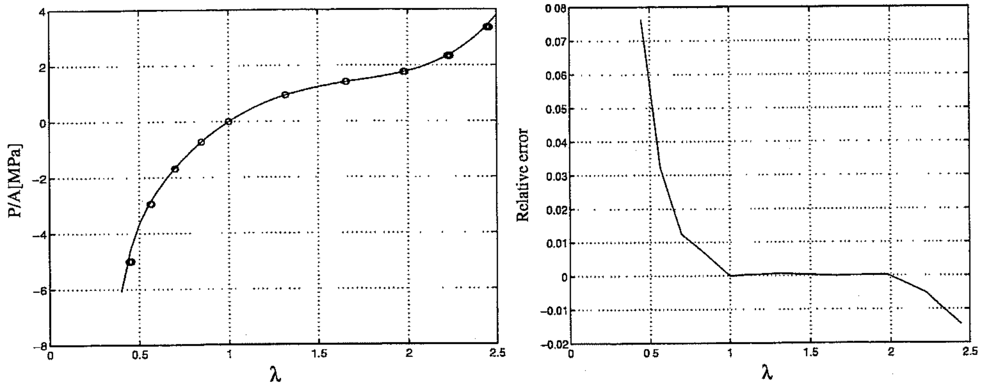

Figure 7.3: *FE simulations and analytical curve for short solid dumbbell specimen (left) and relative error for the shortest measuring length (right).*

Figure 7.2 also shows the relative error, for the shortest measuring length, between the finite element analysis and the analytical expression for compression/tension. The error in the interval $0.5 < \lambda < 2.5$ is less than 1%.

7.1.3. Short solid dumbbell

The rubber part of the finite element model was shortened $10mm$ to $80mm$ and the analysis was repeated. Figure 7.3 shows the stress-stretch relationships from the finite element analyses of the shorter solid dumbbell specimen, compared with the analytical expression for compression/tension. The stress-stretch relationships are displayed for eight different measuring lengths (L according to Figure 7.1), namely 5, 10, 15, 20, 25, 30, 35, and 40 *mm*. Here too, the ideal compression/tension curve is followed quite well for all lengths L.

The relative error between the finite element results and the analytical expression is shown in Figure 7.3 (right). If this figure is compared with the figure representing the longer model, Figure 7.2, it can be seen that the shorter model is almost as accurate as the longer model in tension but less accurate in compression when λ approaches 0.5.

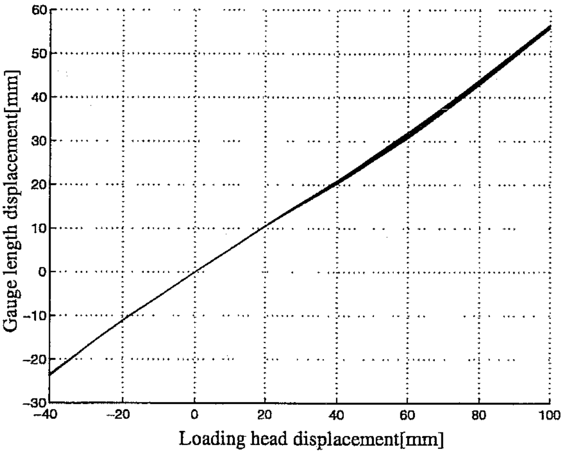

Figure 7.4: *Loading head displacement versus gauge length displacement for the short solid dumbbell test specimen for various material parameters from 40-78 IRHD.*

The short solid dumbbell test specimen shows an approximately linear relation, almost independent of rubber stiffness, between loading head displacement and gauge length displacement for $L = 30mm$. Figure 7.4 shows this relation for the four rubbers specified in Chapter 6 (Table 6.1), with nominal hardness varying between 40 and 78 IRHD. It can be seen that the four graphs almost coincide. This is one of the advantages of the specimen, i.e. testing can be performed without clip gauges (or similar devices) to register the stretch. The curve in Figure 7.4 could be used instead, or alternatively a conversion factor could be used to translate the values for loading head displacements to gauge length displacements.

7.1.4. Summary

A combined tension and compression *solid dumbbell* test specimen has been evaluated by finite element analysis for two different lengths. The longer specimen is slightly more accurate, while the shorter specimen can undergo greater compression without loss of stability. These test pieces can be used with ordinary tensile test equipment. Moreover, in the finite element analysis they show an almost linear relation between loading head displacement and the homogeneous zone displacement for hyperelastic constants obtained for different carbon-black-filled rubbers of hardness from 40-78 IRHD. The curve in Figure 7.4 can therefore be used as a general conversion curve, almost independent of the rubber hardness, to translate loading head displacement into homogeneous zone displacement. Alternatively, but less accurately a conversion factor could be calculated by fitting a straight line to the average curve in Figure 7.4.

7.2. Hyperelastic constants from a modified hardness test

A modification of the standard hardness test is proposed in this section. It is shown that more information can be obtained from the test by a small extra effort. Hyperelastic constants can be derived from the indentation forces for a number of fixed indentation depths. This is in contrast to the standard test, where a constant force is applied and the depth is measured.

The method relies on an energy balance. The total work done by the external force must be equal to the total stored strain energy in the rubber material. This, together with the restrictions on the strains invoked by the incompressibility constraint, is the basis for the proposed method. The hyperelastic constants can thereby be evaluated by use of a tabulated state of strains derived from a finite element analysis of the hardness test, performed once but valid for rubbers of different hardness. The hyperelastic constants are determined by solving a system of equations with the number of equations equal to the number of hyperelastic constants. The system matrix is almost independent of the rubber hardness.

7.2.1. ISO hardness test

The hardness test specified in the International Standard (ISO) is based on measurement of the indentation of a needle with spherical tip or a rigid ball with diameter 2.5 *mm* into a test piece. The standard test piece is a cylinder with smooth and parallel upper and lower surfaces, with diameters of 50 *mm* and thickness 10 *mm*.

The difference δ between the depths of indentation into the rubber under a small contact force (0.3 N) and a larger total force (5.4 N) is measured, cf. Figure 7.5. From this difference, the hardness in international rubber hardness degrees IRHD is derived by using a table given in ISO 48-1979(E) that connects indentation depth to hardness in IRHD. The table is devised so that, for a rigid material, when depth of indentation $\delta = 0$, IRHD=100, while when δ is infinitely large, IRHD=0.

7.2.2. Previous work on relationship hardness - modulus

Many analytical expressions connecting results from the hardness test to modulus have been presented, see [14], [41], [64], and [53]. The ISO standard specifies an empirical relation derived by Scott [53] connecting the indentation depth δ in *mm* to Young's modulus E in MPa according to

$$F = 1.9 \cdot \delta^{1.35} r^{0.65} E \ ,$$

with the indenting force F in N and the indenter radius r in *mm*.

Lindley [33] gives an empirical relation between hardness and the initial Young's modulus. He also relates hardness to shear modulus according to Figure 7.5.

Muhr and Thomas [41] use classical theory of elasticity and an energy balance to obtain an equivalent average shear strain level by comparing the work input in the

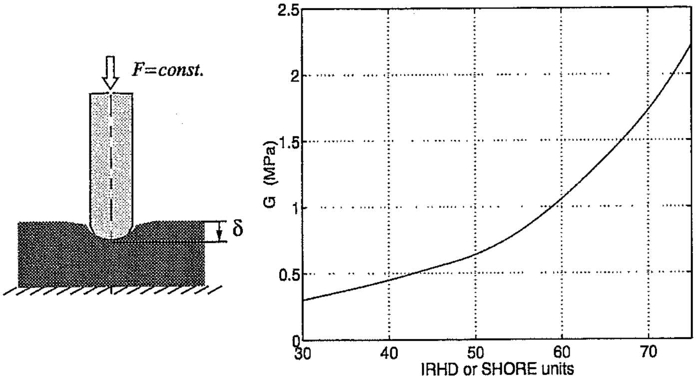

Figure 7.5: *Relation between the shear modulus G and the hardness in IRHD units according to Lindley.*

hardness test with the strain energy associated with simple shear. However, they do not use this energy equivalence to derive the shear modulus. Instead they use the formula

$$G = 24.4 \cdot \delta^{-3/2} \tag{7.1}$$

assuming an indenter force according to ISO 48. G is in Nm^{-2} and δ in meters.

Chang and Sun [10] use nonlinear finite element analysis to show that the linear elastic Hertz contact solution also is reasonably accurate in describing the hardness test of rubber vulcanizates.

The method proposed here that combines energy balance and finite element analysis to obtain hyperelastic constants seems to be a novel approach.

7.2.3. The basic assumption of the modified hardness test

The method investigated is based on a balance of energy. Stored strain energy in the rubber material is equaled to work done by the external indenter force. The hardness test is modified so that, instead of applying a constant force and measuring the indentation, the forces required for certain fixed indentation depths are measured cf. Figure 7.6.

A basic assumption is that the state of deformation for a certain indentation depth is almost independent of the stiffness of the rubber material due to the near incompressibility of rubber.

Figure 7.6 shows schematically the deformed mesh and the external force P as a function of the indentation depths. The work done by the external force is represented by the area under the curve and it can be calculated by integrating from zero to the depth u_k; this external work must be equal to the total stored strain energy i.e.

$$\int_0^{u_k} P(u)du = \sum_{i=1}^{n_e} W_i \cdot V_i \,, \tag{7.2}$$

where n_e is the number of elements in the finite element model, V_i is the volume of element i and W_i is the strain energy density for element i.

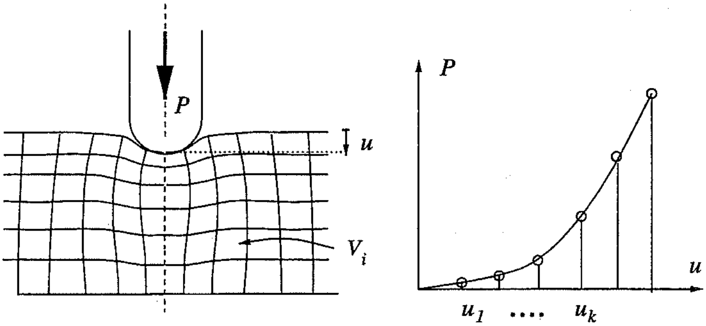

Figure 7.6: *Indentation by needle with spherical tip and the external force P as a function of depth.*

Different expressions for the strain energy density can be used. Here the Yeoh strain energy function (cf. Chapter 5) is used again

$$W = C_{10}(I_1 - 3) + C_{20}(I_1 - 3)^2 + C_{30}(I_1 - 3)^3 \,. \tag{7.3}$$

Inserting (7.3) into (7.2) yields

$$\int_0^{u} P(u)du = \sum_{i=1}^{n_e} C_{10}(I_1^i - 3)V_i + C_{20}(I_1^i - 3)^2 V_i + C_{30}(I_1^i - 3)^3 V_i \,. \tag{7.4}$$

The almost incompressibel behavior of rubber gives reason to assume that the deformation state for a certain indentation depth is fairly independent of the stiffness of the rubber material. If it turns out that this assumption is correct, then the states of strain for each element, in terms of the strain invariants I_1 and I_2, at each indentation depth can be tabulated. The hyperelastic constants are evaluated from (7.4) by use of the tabulated invariant values found from the finite element analysis. Since there are three unknown hyperelastic parameters in (7.4), at least three equations corresponding to three indentation depths are needed. Here six indentation depths will be used giving six equations to solve, by a least squares method, for the three hyperelastic constants.

The advantage of the method is that we need to do only a small number of (here six) finite element calculations once and for all. The tabulated values of the strain invariants can then be used to calculate hyperelastic parameters for rubbers of different hardness.

7.2.4. Test of the assumption by FE analysis

In order to check the basic assumption, i.e. independence of material stiffness for a certain indentation depth, finite element analysis for different rubber stiffnesses was carried out using ABAQUS [26]. Three different materials of nominal hardness 40, 50 and 78 IRHD, with hyperelastic constants given in Table 7.1 were used in the analysis. The constants were evaluated in Chapter 5 (Table 5.3).

	40 IRHD	50 IRHD	78 IRHD
C_{10}	0.2885	0.5079	1.0543
C_{20}	-0.0394	-0.0593	-0.0779
C_{30}	0.0074	0.0086	0.0241

Table 7.1: *Nominal hardness and hyperelastic (Yeoh) constants used in the analysis.*

The symmetry of the rubber piece and the loading conditions test allow modeling with axisymmetric elements. Incompressibility requires use of hybrid elements. A model according to Figure 7.7, with $19 \times 14 = 266$ 4-noded (CAX4H) elements of hybrid formulation were used. The dimensions are in accordance with the standard ISO test, i.e. the rigid ball has a diameter of 2.5 mm and the test piece has a radius of 25 mm and a height of 10 mm. Smaller elements were chosen in the area under the circular indenter, which is modeled by a rigid surface.

Different vertical displacements are applied through the rigid surface and contact elements (IRS21A). The contact was modeled without friction corresponding to a lubricated indentation test. Figure 7.7 shows the resulting deformed geometry predicted by the finite element analysis.

To compare the states of strain for the three different materials, the invariants I_1 and I_2 are plotted as functions of element numbers. I_1 and I_2 for the 40 IRHD material are plotted in Figure 7.8, in order of increasing magnitude. The same order in element numbers is then used in the corresponding plots for the 50 IRHD and the 78 IRHD materials. For a closer examination of the assumption, I_1 and I_2 for the most influenced elements are plotted in Figure 7.9.

The curves in Figure 7.8 and Figure 7.9 are very similar for the three rubber materials, which confirms the assumption that the state of strain for a fixed indentation depth is almost independent of the stiffness.

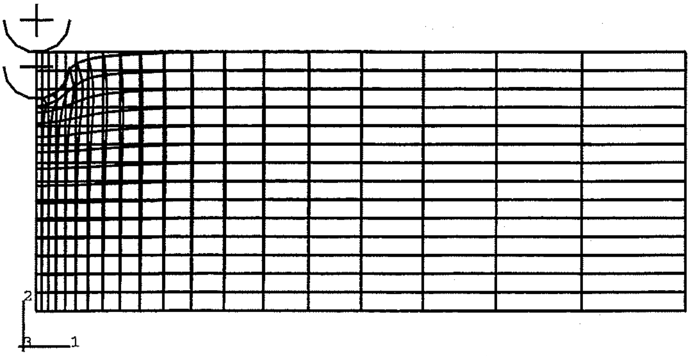

Figure 7.7: *Axisymmetric finite element analysis of the ISO hardness test. Rigid ball; diameter* 2.5 *mm. Test piece; radius* 25 *mm and height* 10 *mm.*

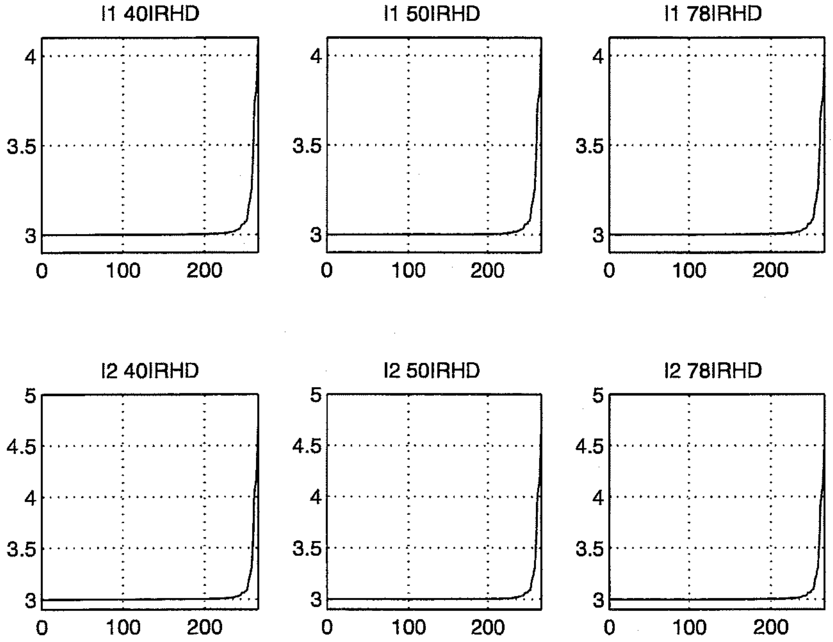

Figure 7.8: I_1 *and* I_2 *for different rubber hardnesses.*

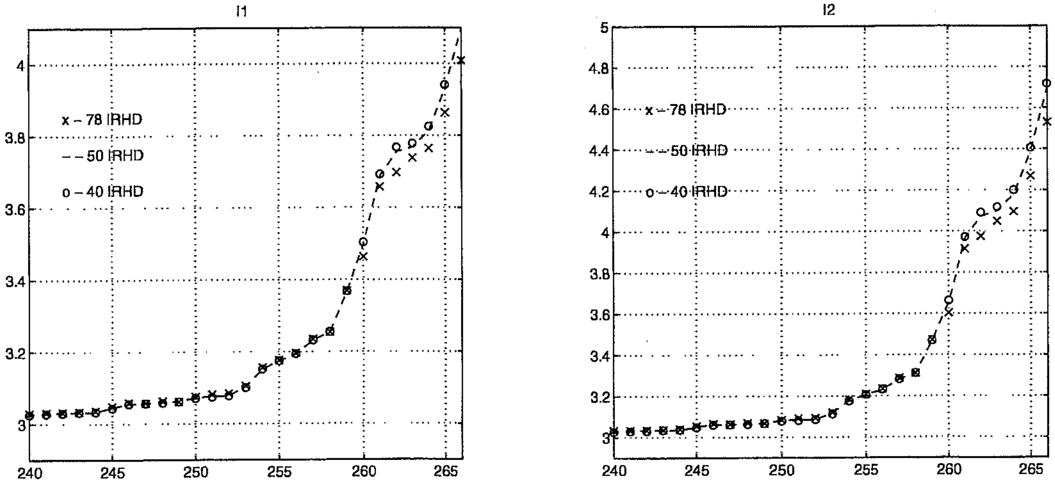

Figure 7.9: *I_1 and I_2 for the most influenced elements.*

7.2.5. Evaluation of hyperelastic parameters

The problem of obtaining the hyperelastic constants will now be formulated as a matrix problem by using a slightly changed version of the balance equation (7.4). It was found that an incremental form of (7.4) was more advantageous from a numerical point of view. Instead of total work and strain energy the additional work applied when the force increases from P_k to P_{k+1} is equaled to the corresponding increase in strain energy. Rewriting the expression for differences in applied work and stored strain energy yields

$$\int_{u_k}^{u_{k+1}} P(u)du = C_{10}\Delta_k^{k+1}\sum_{i=1}^{n_e}(I_1^i-3)V_i+C_{20}\Delta_k^{k+1}\sum_{i=1}^{n_e}(I_1^i-3)^2V_i+C_{30}\Delta_k^{k+1}\sum_{i=1}^{n_e}(I_1^i-3)^3V_i \tag{7.5}$$

where Δ_k^{k+1} indicates differences in the sum of invariants (it is assumed that $u_0 = 0$). Six different indentation depths were simulated using the FE model in Figure 7.7. The indentation forces P from the finite element analysis for the 40, 50, and 78 IRHD materials are plotted as functions of the indentation depths in Figure 7.10.

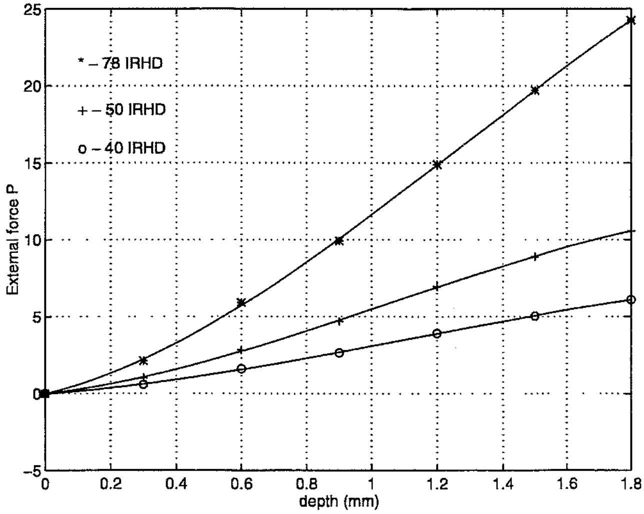

Figure 7.10: *External force P as a function of the indentation depth.*

A third order polynomial was fitted to the computed values. The fitted polynomials are shown with solid lines in Figure 7.10. The total external work done by the indenter force at a particular depth was integrated from the polynomial. This work at the six depths is given in Table 7.2.

The number of equations obtained from (7.5), by applying it for the six indentation depths, exceeds the number of hyperelastic constants. Since there are only three unknown constants, an overdetermined linear system of equations is obtained, which is solved by the method of least squares (cf. Chapter 5).

Depth (mm)	40 IRHD	50 IRHD	78 IRHD
0.3	0.0820	0.1424	0.2957
0.6	0.4021	0.7020	1.4642
0.9	1.0345	1.8239	3.8174
1.2	2.0204	3.5763	7.5496
1.5	3.3657	5.9570	12.738
1.8	5.0430	8.8918	19.340

Table 7.2: *Total work done by the external force P_k at different depths u_k.*

The strain invariants in (7.5) were determined from the principal stretches obtained by finite element analysis using the 50 IRHD material parameters in Table 7.1. The first strain invariant for each element according to (7.5) is obtained from the stretches ($I_1 = \lambda_1^2 + \lambda_2^2 + \lambda_3^2$) for six indentation depths.

Equation (7.5) is set up for each of the depths. The overdetermined system can be written in matrix form as

$$\mathbf{A}\mathbf{c} = \mathbf{b} \tag{7.6}$$

where $\mathbf{A}$ is a 6×3 matrix obtained from the principal stretches given by finite element analysis of the 50 IRHD material. $\mathbf{c}$ is a 3×1 column vector with the hyperelastic constants. The matrix $\mathbf{b}$ is a 6×1 column vector containing differences in the work done by the external force P between the depths (taken from Table 7.2). A least squares solution is found from the ordinary (3×3) system

$$\mathbf{A}^T\mathbf{A}\,\mathbf{c} = \mathbf{A}^T\mathbf{b}. \tag{7.7}$$

The matrix $\mathbf{A}$ is set up once (using the 50 IRHD hyperelastic parameters) and the only change for different materials is in the right side, matrix $\mathbf{b}$, that contains the work required for an increase in indentation.

$$\mathbf{A} = \begin{bmatrix} 0.2497 & 0.0081 & 0.0005 \\ 1.1158 & 0.1102 & 0.0206 \\ 2.3050 & 0.5596 & 0.2233 \\ 3.6491 & 1.6873 & 1.3063 \\ 5.1895 & 4.9489 & 7.1565 \\ 6.6290 & 11.3516 & 27.6477 \end{bmatrix} \qquad \mathbf{c} = \begin{bmatrix} C_{10} \\ C_{20} \\ C_{30} \end{bmatrix} \tag{7.8}$$

The external work matrix $\mathbf{b}$ varies with the hardness, and here $\mathbf{b}40$, $\mathbf{b}50$ and

b78 correspond to 40, 50, and 78 IRHD materials.

$$\mathbf{b}40 = \begin{bmatrix} 0.0820 \\ 0.3201 \\ 0.6326 \\ 0.9857 \\ 1.3453 \\ 1.6773 \end{bmatrix} \quad \mathbf{b}50 = \begin{bmatrix} 0.1412 \\ 0.5608 \\ 1.1219 \\ 1.7524 \\ 2.3807 \\ 2.9348 \end{bmatrix} \quad \mathbf{b}78 = \begin{bmatrix} 0.2957 \\ 1.1685 \\ 2.3532 \\ 3.7622 \\ 5.1579 \\ 6.6026 \end{bmatrix} \tag{7.9}$$

These matrices contain the increase in external work between the fixed depths, obtained by subtracting consecutive rows in Table 7.2.

Hyperelastic parameters for the three rubber materials were calculated, by (7.7), with the external work matrices according to (7.9), giving the values in Table 7.3.

	40 IRHD	50 IRHD	78 IRHD
C_{10}	0.2859	0.5056	1.0616
C_{20}	-0.0413	-0.0670	-0.1121
C_{30}	0.0091	0.0124	0.0302

Table 7.3: *Calculated hyperelastic parameters from the matrix form of the balance of energy.*

A comparison in compression/tension and simple shear is shown in Figure 7.11. The hyperelastic models calculated by the matrix expression (7.7) in Table 7.3 are compared with the correct behavior of the hyperelastic models given by Table 7.1. The dashed lines correspond to the hyperelastic models calculated from the modified hardness test and the solid lines correspond to the hyperelastic models in Table 7.1. It can be seen that the agreement is good in both shear, compression and tension up to 100%.

7.2.6. Discussion

The state of strain in the finite element model of the hardness test is mainly a state of compression combined with some shear of the elements. It is therefore not surprising that the correspondence is best in compression and also good in shear, while the fits, according to Figure 7.11, deviate more for tensile strains (larger than 100%). However, combinations of compression and shear are the most common states of strain in applications and the deviation in tension is therefore not alarming.

The method was evaluated here with hyperelastic models obtained from carbon-black-filled natural rubber vulcanizates and it was shown that the method is valid for these rubbers. The question of whether the constraints on the state of strain imposed by the near incompressibility are strong enough to make the method more generally valid deserves further investigation. To assess this, evaluation must also be carried out for hyperelastic models obtained from other vulcanizates. The principal stretch values from the finite element analysis are stored, and these tabulated stretch values can be used for evaluation of other hyperelastic models.

The sensitivity of the method to the number of indentation depths could also be investigated.

The method should also be verified experimentally. This can be done by manufacturing hardness test, compression and shear specimens from the same material batch and comparing the hyperelastic constants obtained from the compression and shear tests with the hyperelastic constants obtained from the matrix solution (7.7).

7.2.7. Summary

Rubber components have broad application in industry and finite element analysis is being used more and more in design and development of these components. The rubber manufacturers offer a wide variety of rubber compounds for use in different applications and environments. Manufacturing test specimens, testing them in the laboratory and evaluating material parameters for finite element analysis is costly and time consuming. It is therefore necessary to establish simple methods to derive material parameters for the computer simulations.

The hardness test is a standard test frequently used to classify rubber stiffness. The proposed method is therefore a rational way to obtain constants for finite element analysis from the test by employing a slight modification.

The basic assumption is that the state of strain for a certain indentation depth is almost independent of the stiffness of the rubber material. This was verified by finite element analysis for three sets of hyperelastic constants obtained from carbon-black-filled natural rubber vulcanizates, with nominal hardness from 40 to 78 IRHD. The method investigated is based on an equivalence of the external work done by the external force and the strain energy stored in the rubber material. The problem of determining the hyperelastic constants is transferred into a matrix problem. The hyperelastic constants are solved from a small system of equations with a system matrix almost independent of the rubber hardness. This matrix was evaluated from a tabulated state of principal stretches found from a finite element analysis of the hardness test (for the 50 IRHD material), performed once and for all.

In practical application of the method the external experimental force is obtained for a number of (here six) indentation depths and integrated. The differences obtained in external work between the fixed depths enter the matrix problem as the vector $\mathbf{b}$ in (7.7), while the matrix $\mathbf{A}$ is constant due to the restrictions on the state of strain imposed by the near incompressibility.

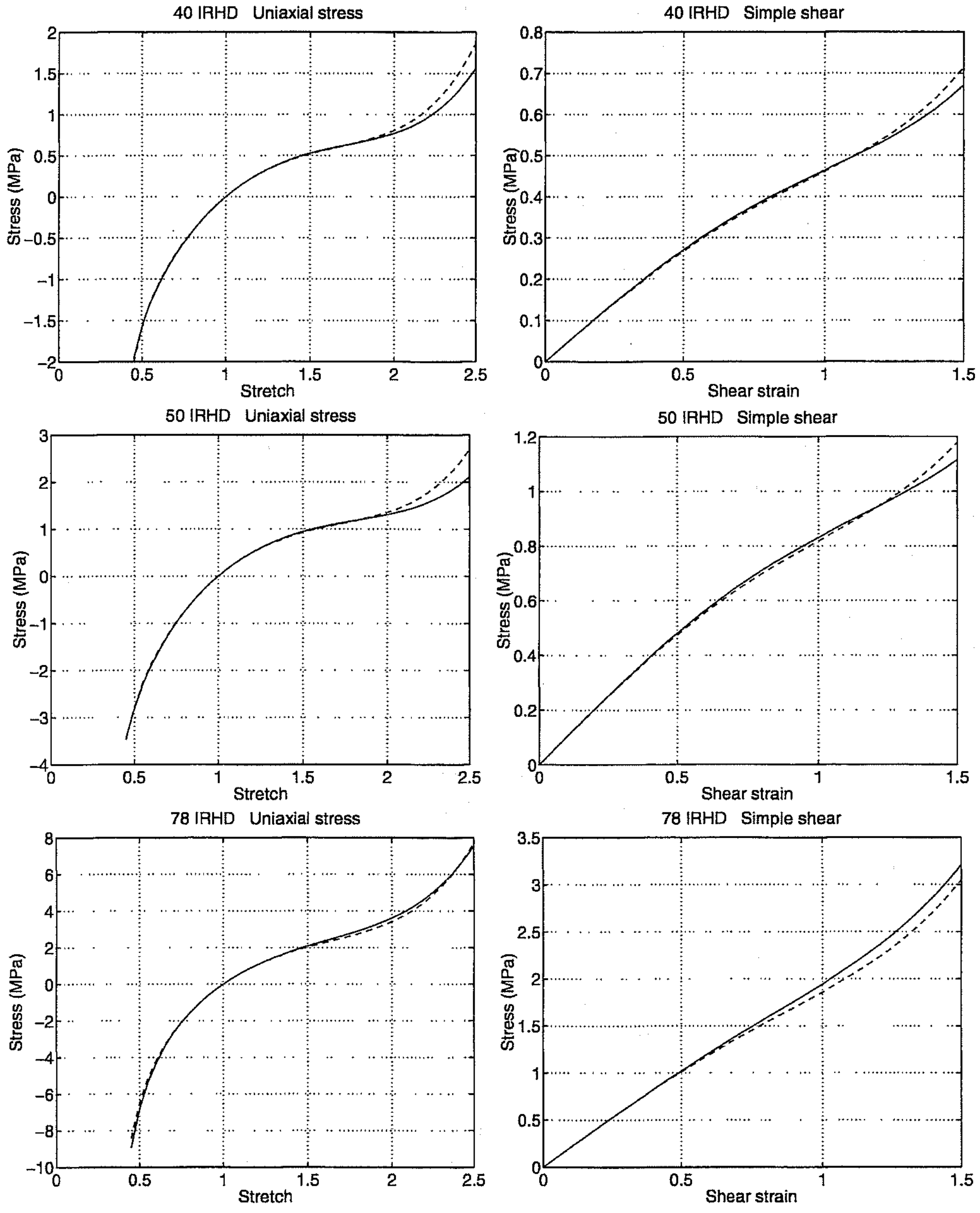

Figure 7.11: *Comparison of hyperelastic models from the modified hardness test (dotted lines) and the hyperelastic models used in the finite element analysis (solid lines) for 40 (above), 50 (middle), and 78 IRHD material (below). The models are evaluated here for compression/tension and simple shear.*

7.3. Contact-free strain measurement

Conventional strain and deformation gauges produce recordings only for one or a few points, and they are very difficult to use when it comes to small specimens or a small area of one specimen. A new method for measuring displacements and strains in mechanical test pieces without applying sensors to the specimens is described. This optical technique uses a CCD camera, a computer with frame grabber board and image analysis techniques. The displacements and strains at the surface of the test piece are obtained by analysis of the movements of dots painted on the specimen. The complete displacement field on the surface can be determined by attaching a finite element grid to the image and using shape function interpolation. An application example is presented. A large strain test performed on a rubber membrane is analyzed.

The proposed method comprises a CCD camera and image analysis techniques within MATLAB [36]. This numeric computation and visualization software, is used to investigate relative displacements and surface strains by use of distinct markers on the specimen. The proposed optical technique is both full-field measuring and non-contacting. Other optical techniques that serve these demands have been described by Gonzales [20], Gåsvik [23] and Sjödahl [55].

7.3.1. Experimental setup

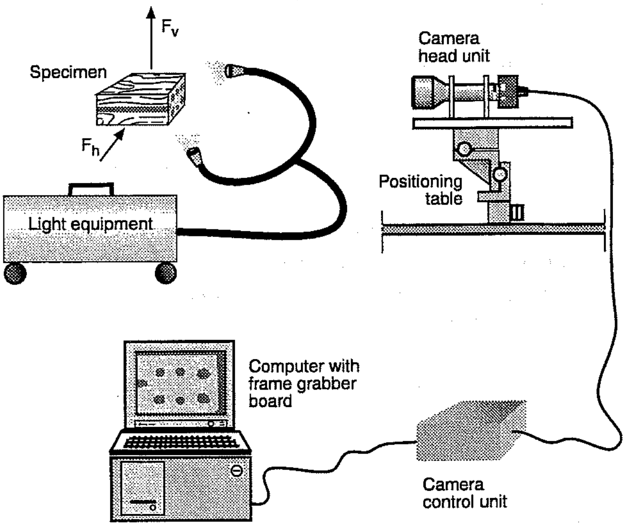

Figure 7.12: *The experimental setup.*

The equipment, illustrated in Figure 7.12, comprises a CCD camera, lenses, enlargement tubes, light equipment, positioning table, a video monitor and a computer with frame grabber board. Images are captured and stored in the computer with the help of the frame grabber board to which the analogue monochrome camera (739 x 575 pixels) is connected. The camera head unit, the lens and tube together with fibre light guides are mounted on top of a positioning table which is manually adjustable in three directions. Five available lenses with fixed focal lengths combined with different tube lengths can produce images of objects with heights of 0.8, 2.5, 5, 10, 20, 40 and 60 mm. The image width is about 1.29 times larger than its height.

The test specimen is marked with dots of ink or paint and mounted in the testing machine. A sequence of images is then captured at intervals depending on time, force, or displacement. Recordings of force and displacement can be made together with each image. This is accomplished by program routines linked to the frame grabber routines that make it possible to receive and capture digital or analogue signals from the testing machine at the same instant as images are captured.

7.3.2. Program function

User interaction with the graphic interface and the image analysis algorithms are described in this section. As a general reference to digital image processing, see [20].

One time-saving feature of the algorithm is that the dots that are marked with a box in the first image in a sequence are tracked through the image sequence, and their centers of mass are calculated automatically for each image in the sequence.

The implementation is done as a menu-driven process, using MATLAB's graphical interface. When the user starts the program, a menu appears at the top left of the screen. First the user writes the name of the files containing the images in pgm-format in an editable text box. Then the first image in the sequence is shown on the screen.

The next step is to locate the different marked dots on the specimen using the cursor. Marking the top left and the bottom right corner of a box situated around the dot makes the program write out the box in the image. The steps described above are repeated until all dots have been surrounded by boxes.

Finally, the user starts the analysis, and the images in the sequence are treated one after another. The marked dots are tracked through the sequence and new boxes need not be entered in the other images. A number of diagrams are shown, giving the x- and y-displacements of dot number 2, 3 and so on, relative to the first dot. The x- and y-centroid displacements for all dots and pictures in the sequence are stored in two matrices.

When a box around a marked dot is entered by the user, the center of mass of the dot is calculated. First the marked area is picked out, giving a smaller image, (see the left part of Figure 7.13). Then this new image is inverted if the marked dot is black against a lighter background, in order to give a white dot against a black background. To eliminate boundary defects, the new image is thresholded to give an image with intensity values zero on the boundaries of the box and larger intensity values on the actual dot. In this way the image can be regarded as a surface area with mass distribution given by the image intensities. The fact that the image intensities are zero at the boundaries makes the program less sensitive to the placements of the boxes. The output will be the same if the frames of the boxes are outside the dots and do not contain any other dark areas.

The first order area moments, $\mathbf{s}_I$, are calculated using

$$\mathbf{s}_I = \int_\Omega \mathbf{X}w(\mathbf{X})dA = \int_\Omega \begin{bmatrix} X \\ Y \end{bmatrix} w(X,Y)dA = \begin{bmatrix} S_1 \\ S_2 \end{bmatrix}, \tag{7.10}$$

where Ω denotes the box around the dot, $w(\mathbf{X})$ denotes the image intensity at point $\mathbf{X}$ and dA denotes the area measure. Naturally the integrals are calculated using finite sums, because the image intensity is a discrete function. This means that

$$\mathbf{s}_I = \sum_{i=x_{min}}^{x_{max}} \sum_{j=y_{min}}^{y_{max}} \begin{bmatrix} i \\ j \end{bmatrix} w(i,j) = \begin{bmatrix} S_1 \\ S_2 \end{bmatrix}, \tag{7.11}$$

where the lower left corner of the box has coordinates (x_{min}, y_{min}) and the upper right corners has coordinates (x_{max}, y_{max}). Then the coordinates of the center of mass are calculated as

$$\mathbf{X}_{TP} = \frac{\mathbf{s}_I}{M}, \tag{7.12}$$

where M is defined as

$$M = \int_\Omega w(\mathbf{X})dA = \sum_{i=x_{min}}^{x_{max}} \sum_{j=y_{min}}^{y_{max}} w(i,j). \tag{7.13}$$

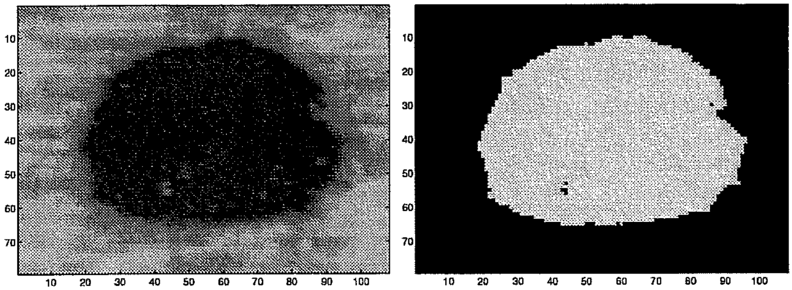

Figure 7.13: *Graphical illustration of the image intensities around a marked point. The original image is shown to the left, the inverted and thresholded image to the right.*

The location of the center of mass relative to the lower left corner of the box is stored for each box. When a new image is considered in the sequence, the new center of mass is calculated using the same box, even if the marked dot has moved. If the dot has moved more than one pixel in any direction, the box is translated so that the relative position of the center of mass is preserved. If the pixel values at the boundaries of the box are different from zero when the center of mass is calculated, a new calculation of the center of mass is done. This process is repeated until the box surrounds the dot. In most cases this calculation need only be done once for each image. However, in the last images of a sequence, where the deformations are large, the calculation may be done several times though usually only twice. In this way the marked dots are tracked through the sequence.

7.3.3. Surface strain analysis

By combining finite element technique with the centroid displacement information from the dots, it is possible to extrapolate displacements of the dots and get information about the complete experimental displacement field of the surface.

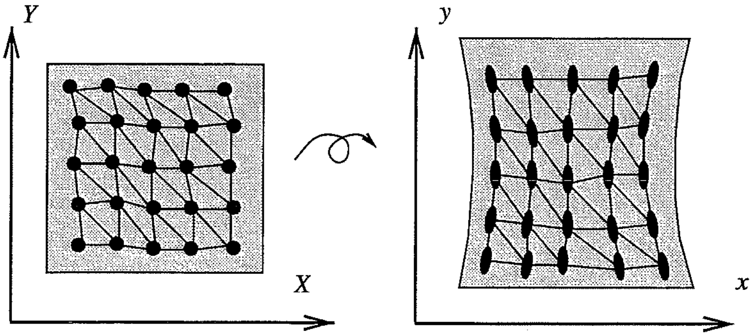

Figure 7.14: *Finite element mesh attached to the centroids of the dots.*

The deformation of the surface is expressed by a mapping, from the undeformed to the deformed configuration, defined for every point at the surface. The location of a point in the undeformed configuration is uniquely determined by coordinates $\mathbf{X} = (X,Y)$ and by $\mathbf{x} = (x,y)$ for the same point in the deformed configuration. The mapping is expressed as

$$\begin{bmatrix} x \\ y \end{bmatrix} = \begin{bmatrix} x(X,Y) \\ y(X,Y) \end{bmatrix} \quad \Longleftrightarrow \quad \mathbf{x} = \mathbf{x}(\mathbf{X}). \tag{7.14}$$

The convention of using capital letters for quantities referring to the undeformed configuration and lower case letters for the deformed configuration, is used.

The surface is divided into triangular elements with nodes at centroids of the dots as illustrated in Figure 7.14. The deformation is described by

$$\mathbf{x} = \mathbf{X} + \mathbf{u}(\mathbf{X}), \tag{7.15}$$

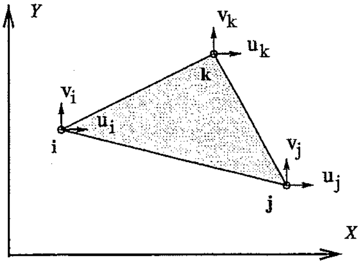

Figure 7.15: *Triangular element and nodal displacements.*

where $\mathbf{u}$ is the displacement of a point located at $\mathbf{X}$ at the undeformed surface.

The displacements at the nodes are interpolated by linear functions defined for each element, i.e. linear shape functions are used. This is a standard technique used in finite element analysis; see [44] for further information. The element displacements, $\mathbf{u}^e$, are interpolated as

$$\mathbf{u}^e = \mathbf{N}^e(\mathbf{X})\,\mathbf{d}^e,$$

where $\mathbf{N}^e$ is the shape function matrix and $\mathbf{d}^e$ is the element displacement vector given by

$$\mathbf{N}^e = \begin{bmatrix} N_i & 0 & N_j & 0 & N_k & 0 \\ 0 & N_i & 0 & N_j & 0 & N_k \end{bmatrix} \qquad \mathbf{d}^e = \begin{bmatrix} u_i & v_i & u_j & v_j & u_k & v_k \end{bmatrix}^T,$$

with the element displacements defined in Figure 7.15. The shape function associated with node i is expressed as

$$N_i = \frac{1}{2A}\Big(X_jX_k - X_kY_j + (Y_j - Y_k)\,X + (X_k - X_j)\,Y\Big)\,,$$

where A is the element area and the shape functions N_j and N_k are found by cyclic permutation of indices.

Experimental surface strains can be obtained from the attached finite element mesh. The deformation gradient defined by $\mathbf{F} = \partial\mathbf{x}/\partial\mathbf{X}$ is the basis for several definitions of strain used in constitutive theories. For the triangular elements used here the deformation gradient is constant and expressed by the displacements as

$$\mathbf{F}^e = \mathbf{1} + \frac{\partial\mathbf{u}^e}{\partial\mathbf{X}} \tag{7.16}$$

by differentiation of relation (7.15).

There are several definitions of strain [37] that can be constructed from the deformation gradient. The Lagrange strain tensor, defined as $\boldsymbol{E} = (\boldsymbol{F}^T\boldsymbol{F} - \mathbf{1})/2$, is a commonly used measure of strain. This strain at the surface of a stretched rubber membrane is obtained in the application example below.

7.3.4. Application example

Evaluation of surface strains were performed on a series of images from a stretched rubber membrane according to Figure 7.16. The specimen consists of a membrane of original dimensions 10 × 10 × 2 *mm* bonded to steel plates. The loading head on the right hand side was displaced by 10 *mm*. Twenty images were captured with two images at each millimeter of displacement.

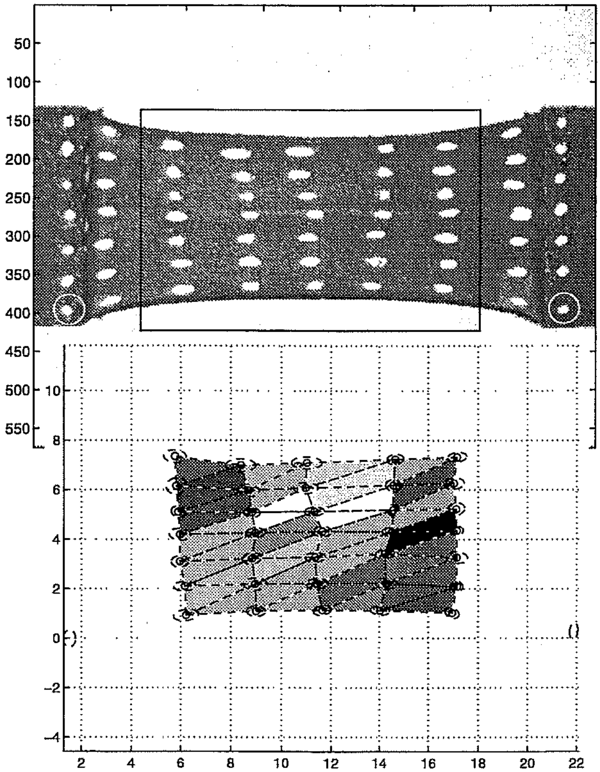

Figure 7.16: *The deformed membrane and mesh at maximum displacement. The strain in the x-direction is also displayed for the deformed membrane.*

A finite element mesh was constructed from centroid data, for the dots marked with a frame in Figure 7.16. Equivalent ellipses were drawn to indicate the deformed dots together with two reference nodes on the steel plates, marked with circles, in Figure 7.16.

The Lagrange surface strains were evaluated for each element, and the variation of the strain component E_{xx} (x in horizontal direction) is indicated in Figure 7.16 by a grey scale, with white for the largest strain value and black for the smallest strain value within the mesh.

7.3.5. Discussion

One drawback of this implementation is that the user has to mark the dots with boxes before they can be processed. It would be fairly easy to write a program that automatically detects the dots and then track them through the sequence, if there is some a priori information available of what the dots look like.

In the present implementation it is only possible to treat white dots against black background or black dots against white background at the same session. A simple extension would be to have a new menu where the user can select white or black dot after the box has been marked. This could also be done automatically if the dots were detected automatically.

Another drawback is that it is necessary to paint small dots on the specimens. If the specimens had some texture, it would be possible to estimate local deformations using correlation techniques. This texture could be made, for example, by spraying ink on the specimen, giving a large number of small dots and other textures. Using this texture, it is possible to correlate different areas in subsequent images.

7.3.6. Summary

A robust and straightforward non-contacting method for experimental deformation analysis has been described. Distinct dots are applied to the test specimen. The image analysis algorithm makes it possible to automatically track the motions of the dots and compute their centroid coordinates in a sequence of images. A method to interpolate displacements and compute surface strains has also been devised, by the use of finite element shape functions. The analysis procedure can be developed further. An automatic procedure for detection of the dots on the first image would be time saving.

Part II

MODELING OF DAMPING

8. INTRODUCTION TO DAMPING MECHANISMS

This part concerns dynamic properties of rubber with special interest in filled rubbers and modeling of the amplitude dependence. Experiments and models of the dynamic behavior are discussed. One section in this chapter describes experiments carried out at the departmental laboratory. The experimental findings are compared with viscoelastic and viscoplastic models in subsequent chapters. Rate-dependent and rate-independent damping are discussed in terms of one dimensional and multiaxial models. The limitations of existing viscoelastic models are discussed.

In Chapter 9 linear viscoelasticity is discussed, and some important subjects are considered such as the relaxation function and the complex modulus. The linear viscoelastic models are purely rate-dependent models with linear dynamic behavior. These models are well suited for unfilled rubbers, but they can not explain some important properties of filled rubbers. Examples are the rate-independent character of damping required to explain the hysteresis in quasi-static loading and the amplitude dependence of the dynamic modulus in harmonic loading. Rate-independent damping is discussed in Chapter 10 in terms of one-dimensional elasto-plastic models. It is shown that these models are able to capture the amplitude dependence of filled rubbers in harmonic loading. A combination of rate-independent and rate-dependent damping is studied and compared with experiments in Chapter 11. The one-dimensional model used is a model with viscoelastic and elasto-plastic stress contributions added. Models available in commercial finite element codes for dynamic behavior of rubber are modified linear viscoelastic models to take large strain into account, and the subject of Chapter 12. Finally in Chapter 13 a possible generalization of the one-dimensional viscoplastic model to the multiaxial case is discussed.

8.1. Definition of dynamic modulus and damping

Steady state harmonic excitation is an important loading case, and the dynamic modulus and damping have to be defined for the nonlinear case as well. A general definition is required because the response to a sinusoidal excitation is not perfectly sinusoidal when nonlinearities are present even for small vibrations. Figure 8.1 shows two hysteresis loops for a sample subjected to a pure sinusoidal strain. The left path is elliptic, corresponding to linear dynamic (viscoelastic) behavior. The right path is a more general hysteresis where nonlinearities are present. The stress response contains higher harmonic components, i.e. multiples of frequency of the strain input.

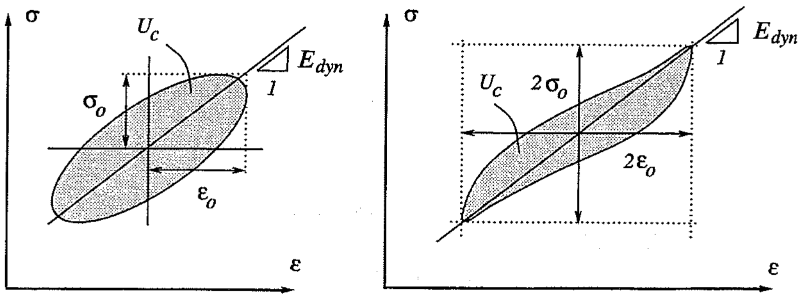

Figure 8.1: *Linear viscoelastic and general hysteresis loop for harmonic excitation.*

In Chapter 1 the dynamic modulus and phase angle were defined for linear dynamic behavior. The dynamic modulus was defined as $E_{dyn} = \sigma_0/\epsilon_0$. The damping, expressed by hysteresis work, was connected to the phase angle δ according to $U_c = \pi\sigma_0\epsilon_0 \sin\delta$. (This will be shown in Chapter 9.)

Definitions consistent with linear viscoelasticity for the dynamic modulus E_{dyn} and normalized damping d are

$$E_{dyn} = \frac{\sigma_0}{\epsilon_0} \qquad d = \frac{U_c}{\pi\sigma_0\epsilon_0}\,. \tag{8.1}$$

The definition of dynamic modulus is the same used in linear viscoelasticity and the definition of normalized damping coincides with the phase angle at moderate damping, i.e. $d \approx \delta$.

If the nonlinearities are not too severe, i.e. the deviation from the sinusoidal shape is small, then a least squares fit, of an harmonic function with the same fundamental frequency as the input, to the response will give approximately the same dynamic modulus and phase angle as the definition above. This can be viewed as an equivalent viscoelastic damping.

8.2. Microstructure and dynamic properties

The origin of the damping property of rubber can be understood from the molecular structure of the material. Vulcanized rubber is made up of very long cross-linked polymer molecules. The damping is increased when filler, usually carbon-black, is added to the rubber compound. Carbon-black consists of very small particles of carbon (20nm - 50μm), which are mixed into the raw rubber base before vulcanization. The material is thus a two-phase material made up of constituents with completely different mechanical properties. Figure 8.2 shows schematically the structure at a molecular level of a carbon-black-filled vulcanizate. The cross-links are shown as

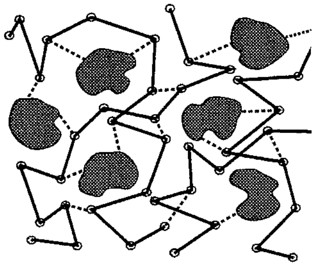

Figure 8.2: *Molecular structure for a carbon-black-filled rubber vulcanizate. Carbon particles, polymer chains (solid lines) and crosslinks (dashed lines) are schematically illustrated.*

dashed lines and the carbon particles forms agglomerates inside the rubber network (solid lines).

The damping property of filled rubbers, i.e. the ability to dissipate mechanical energy into heat, is mainly due to two kinds of mechanisms. One is of viscous character - the origin of the viscous damping being the resistance in reorganization of the molecular chains within the rubber phase. This reorganization of the long molecular chains can not occur instantaneously, giving a rate dependent resistance of a viscous character. The other mechanism is due to the filler; damping is increased by adding fillers to the rubber compound. The filler particles can be regarded as rigid compared to the stiffness of the rubber matrix. The filler particles, as mentioned above, form agglomerates and these build a filler structure [60] inside the rubber network. When the composed rubber material is being deformed there will be forces developing in the filler interfaces and the filler structure will break. The increased damping must therefore be attributed to a resistance in the rubber-carbon interfaces and in the carbon-carbon interfaces. It will be argued that this part of the damping is rate-independent and responsible for the nonlinear dynamic behavior of filled rubbers that appears as amplitude dependence of the dynamic stiffness and phase angle.

The dynamic properties of rubber are dependent on frequency, temperature, static load and amplitude.

Figure 8.3 shows the frequency dependence of the dynamic modulus and phase angle for a filled rubber. The dynamic shear modulus and phase angle are shown as functions of frequency. The effect of changing the temperature is also shown in the figure. The values given are approximate and strongly dependent also on the amplitude, which will be discussed below.

Figure 8.4 shows the temperature dependence of the dynamic shear modulus and phase angle for a filled rubber. Values given are approximate and dependent also on the amplitude. The dynamic modulus decreases, with increasing temperature. The effect of changing the frequency is also shown in the figure. The general behavior shown in Figure 8.4 is the same for all rubbers, although the temperature scale can

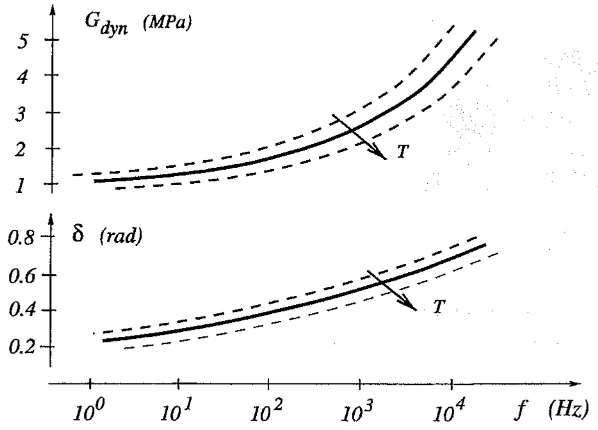

Figure 8.3: *Frequency dependence of dynamic shear modulus and phase angle for a filled natural rubber. Influence of temperature is also shown.*

be shifted by additives in the rubber compound.

Three temperature regions are indicated. The first is the glassy region where the thermal motion of the polymer molecules is reduced. In this range almost no intermolecular motion is possible and the material is glass-like and brittle. Mechanical behavior of rubber in this temperature range is dependent on the interatomic bonds. The modulus is therefore considerably high ($\approx 1\ GPa$) in this region, while damping represented by the phase angle is low. The second region is the transition region, with a drastic drop in dynamic modulus and maximum damping shown as a peak in the phase angle. The third temperature region is the rubbery region with a considerably low dynamic modulus ($\approx 1\ MPa$). Rubbers in working conditions must be in the end of the transition region or in the rubbery region in order to have rubber-like properties.

The indicated shift of the modulus and phase curves in Figure 8.4 is a general property valid for a variety of polymers over a wide frequency and temperature range. The frequency-temperature correspondence has been summarized by Williams, Landel, and Ferry [62] in an empirical universal function valid for amorphous polymers at temperatures above the glassy region. An important consequence of this correspondence is that modulus and phase curves over many decades of frequency can be obtained by performing experiments in a limited frequency range at different temperatures. The wide frequency range is covered by shifting the limited frequency data along the frequency axis. Low temperature measurements correspond to high frequencies and high temperature measurements correspond to low frequencies. The composed curves is effectively mirror images of the temperature curves in Figure 8.4.

Special emphasis will here be on strain amplitude dependence of the dynamic modulus. The modulus is seen to decrease with increasing strain amplitude. This effect is sometimes denoted the Payne effect due to investigations of reinforced elas-

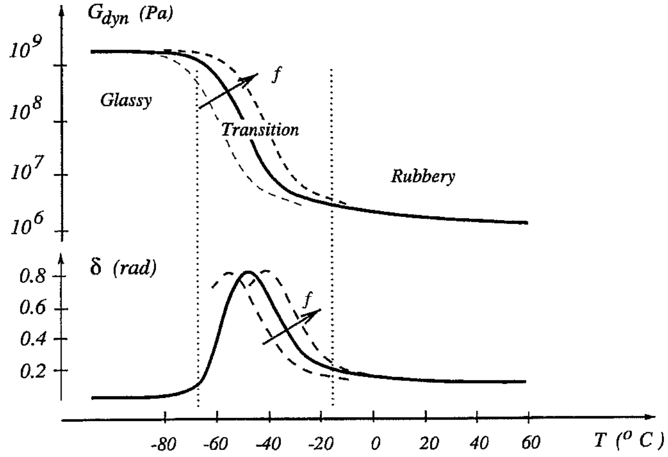

Figure 8.4: *Temperature dependence of dynamic shear modulus and phase angle for a filled natural rubber. Influence of frequency is also shown.*

tomers made by Payne [45]. He interpreted the decline in modulus by increasing strain amplitude as a result of breaking of the filler structure. The structure is composed of aggregates held together by van der Waals bonds. Payne found that the modulus is almost recoverable upon return to small amplitudes, i.e. the filler structure largely reforms for an amplitude cycle. It is clear that the mechanisms involved should not be confused with the Mullin's effect, which is attributed to breaking of cross-links within the rubber network [42], with recovery times of about 24 hours.

Payne also observed that the shape of the decline in modulus by increasing strain amplitude was almost independent of frequency for low frequencies, and he also refers to Warnaka [61] who observed the same frequency independence for higher frequencies, up to 1500 Hz.

A comprehensive review of dynamic properties of carbon-black-filled rubbers and the amplitude dependence can be found in the often-cited article by Medalia [38].

Harris and Stevenson [25] have made experimental investigations of several nonlinear aspects of the dynamic behavior of, especially, filled rubbers. They investigated effects of frequency, amplitude, and elastic nonlinearity for filled and unfilled rubbers. For unfilled rubbers it is clearly seen that the hysteresis loop has an elliptic shape for small amplitudes and preload and the behavior is viscoelastic. For filled rubbers a significant effect of the strain amplitude on the dynamic modulus is reported. Figure 8.5 shows the equivalent complex modulus, reproduced from [25], for natural rubbers (NR) with different carbon-black loading. The amount of black varied from 45 phr (parts per hundred of NR by weight) to 75 phr. The rubbers are all of approximately the same hardness (about 55 IRHD). This was accomplished by using three different types of carbon-black and by balancing the reinforcing effect by addition of a high-viscosity aromatic oil. Figure 8.5 shows the strain amplitude

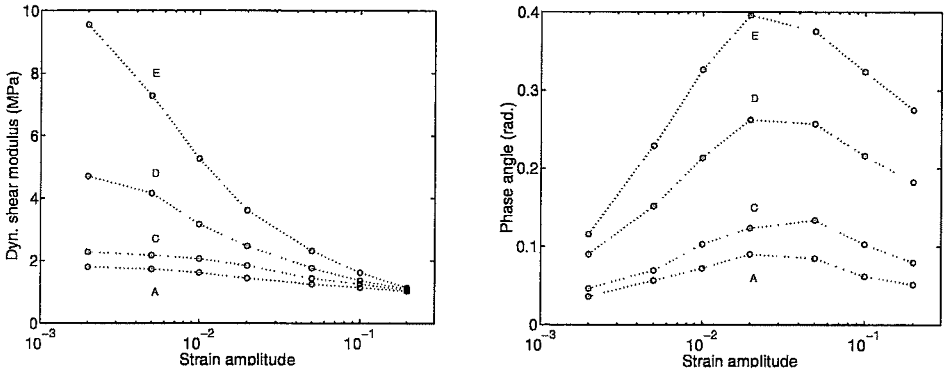

Figure 8.5: *Amplitude dependence of dynamic shear modulus and phase angle for some filled natural rubbers of various filler contents. A-E represent increasing filler contents. (Reproduced from Harris and Stevenson.)*

influence in simple shear. The vulcanizates are denoted A,B,C,D,E in [25] in order of increasing reinforcement of carbon-black. The carbon-black content varied from 30 to 75 phr, i.e. parts per hundred of rubber by weight (75 phr for vulcanizate E). Vulcanizate B and C behaved similarly. B is therefore left out in the reproduction (cf. Figure 8.5). The vulcanizate with the highest damping and variation in dynamic modulus is the one with the highest filler content.

Harris and Stevenson also report that the stress response for harmonic loading in simple shear is influenced by higher harmonic components, resulting in a distorted elliptic shape which tends towards a parallelogram. The most significant contribution is from the third harmonic component. The ratios of the third and the first harmonic component are reported for vulcanizate E for a 1 Hz test at different amplitudes. The maximum ratio is 0.035 for a strain amplitude of 5%.

8.3. Experimental results

Several tests have been carried out in order to show the influence of the rate independent damping present in carbon-black-filled rubbers and to illustrate the deviations from viscoelastic behavior. The experimental results will also be compared with model behavior in subsequent chapters.

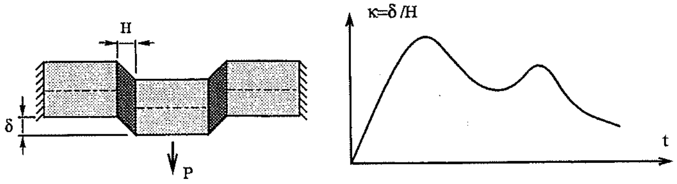

Figure 8.6: *Displacement controlled double shear. Specimen and an arbitrary strain history.*

The tests were performed in displacement-controlled simple shear for different strain histories, with a setup schematically shown in Figure 8.6. This mode of deformation was chosen in order to reduce the influence of elastic nonlinearities. The "direct shear strain" determined as $\kappa = \delta/H$ is used as strain measure in all shear tests. (This measure is connected to the Lagrange shear strain $E_{12} = \kappa/2$.) The shear stress is the force on each of the rubber discs divided by the circular cross-sectional area A, i.e. $\tau = P/2A$. (Diameter $D = 25mm$ and height $H = 6mm$.)

The same double shear specimen according to Figure 8.6 was used throughout all the experiments since the purpose was to investigate the behavior of a typical filled elastomer and not to perform a study of the variation in material properties. The material was a 55 IRHD carbon-black-filled SBR (styrene-butadiene) rubber vulcanizate with 78 phr filler (N330), manufactured by Svedala-Skega rubber company. The relatively high content of filler was balanced by a mineral oil. This vulcanizate is similar to vulcanizate E discussed earlier, since the dynamic properties of SBR and NR polymer are similar and the filler content and the hardness are approximately equal.

All tests were performed with a servo-hydraulic test machine from MTS systems with a load cell of 10kN maximum capacity. The system is fully computerized with a strain history function generator and data logging capabilities. The test machine is located in a climate-controlled environment. The temperature was held at $23.5 \pm 0.5^{o}C$ for all tests.

The experiments are divided into quasi-static and steady state dynamic experiments. The quasi-static experiments were relaxation tests, tests with low frequency sinusoidal strain at different amplitudes, and also a test with a triangular periodic strain to check the sensitivity of the stress response to the shape of the strain history time function. The steady state dynamic tests were performed for different frequencies and amplitudes, with frequencies from 1 to 20 Hz and shear strain amplitudes from 0.02 to 0.15. The tests are compared with the behavior of the models discussed in Chapter 10 and Chapter 11.

A concern in all tests has been to eliminate effects of damage (Mullin's effect). The test specimen was therefore conditioned before testing in order to establish stationary material behavior.

8.3.1. Quasi-static experiments

A set of relaxation tests was performed according to Figure 8.7, in order to determine the influence of the step size on the relaxation modulus. This modulus is given by relaxation stress divided by the strain step κ_s according to

$$G_R(t) = \tau_R(t)/\kappa_s \qquad \tau_R = P(t)/2A\,. \tag{8.2}$$

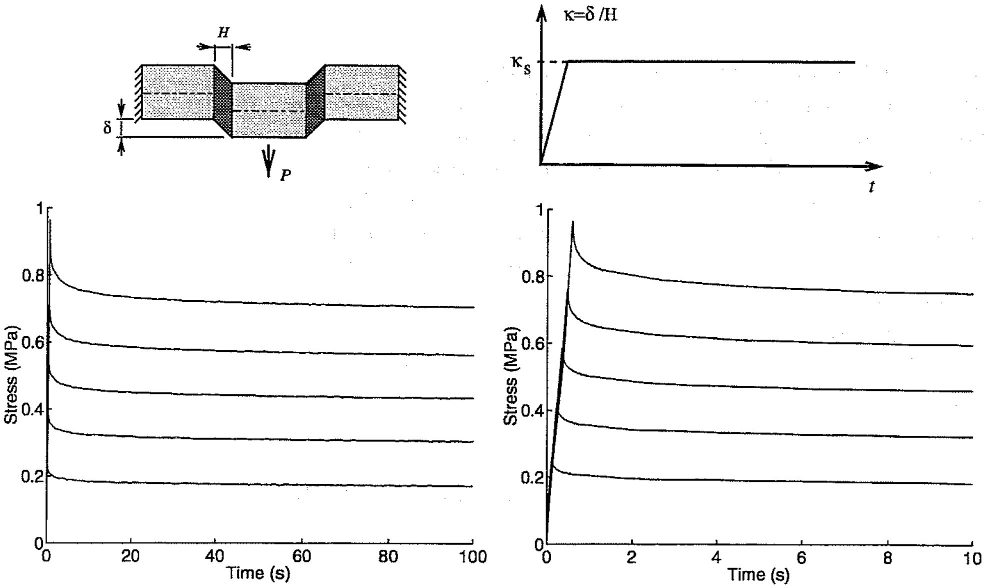

Figure 8.7: *Relaxation test in shear. Strain steps: [0.2 0.4 0.6 0.8 1.0]. Relaxation stress for 100s and a closer view of the first 10s.*

The relaxation tests were carried out at five levels of shear strain

$$\kappa_s = \begin{bmatrix} 0.2 & 0.4 & 0.6 & 0.8 & 1.0 \end{bmatrix}$$

according to Figure 8.7. The ramp strain rate was constant for the five levels, $\dot{\kappa} = 1.66s^{-1}$ and the stress was allowed to relax for 100 s. The stress relaxation is shown for the different strain levels for a time interval of 100 s and for the first 10 s.

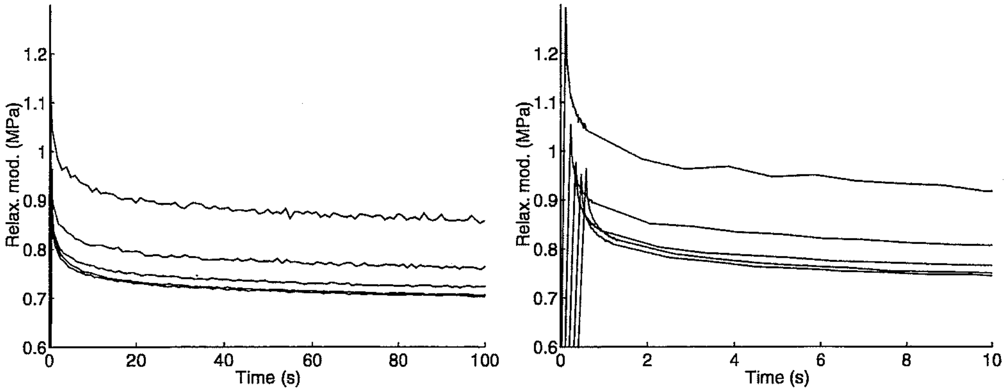

Figure 8.8: *Relaxation modulus in shear i.e. relaxation stress divided by the magnitude of the strain steps;* κ_s*=[0.2 0.4 0.6 0.8 1.0] for 100 s and a closer view of the first 10 s. The largest relaxation modulus corresponds to the smallest strain step.*

The dependence of the step size is clearly seen in Figure 8.8 in contrast to what could be expected from viscoelasticity (cf. Chapter 9). The largest relaxation modulus corresponds to the smallest strain step, i.e. κ_s=0.2, the second largest for κ_s=0.4, and the third for κ_s=0.6. Hence, the relaxation modulus decreases with the step size.

The second quasi-static test set was a test with a sinusoidal strain history and different amplitudes in order to investigate the influence of amplitude and to check the shape of the hysteresis loop. The tests were performed at f =0.05 Hz with shear strain amplitudes

$$\kappa_0 = \begin{bmatrix} 0.1 & 0.3 & 0.5 \end{bmatrix}$$

and a static strain κ_s =0.5 according to Figure 8.9.

Although the test was carried out in simple shear, which is an almost linear state of deformation, there is substantial deviation from the elliptical shape that characterizes linear viscoelastic behavior. The shape tends towards a parallelogram.

It is also seen in Figure 8.9 that the dynamic modulus falls with increasing amplitude. The frequency dependence was negligible for similar quasi-static tests performed at f =0.01 Hz and f =0.1 Hz.

The third quasi-static test was a test with a triangular shaped periodic shear strain that was compared with a harmonic test with the same amplitude and frequency according to Figure 8.10. This test was performed for the purpose of investigating the sensitivity of the stress response to the shape of the shear strain time function. The shear strain amplitude κ_0=0.5 and the prestrain κ_s=0.5.

The shape of the strain has a very small influence in this quasi-static test. In Figure 8.10 the triangular and the sinusoidal strain histories yield almost the same hysteresis loops. This is also a property that is in contrast to viscoelastic behavior.

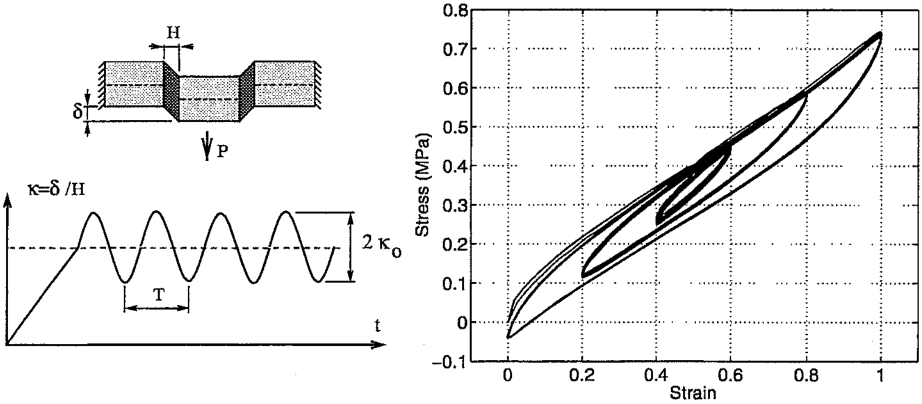

Figure 8.9: *Double shear specimen and strain history in quasi-static harmonic tests (left). Hysteresis loops for different amplitudes (right). Strain amplitudes* κ_0*=[0.1 0.3 0.5] at f=0.05 Hz.*

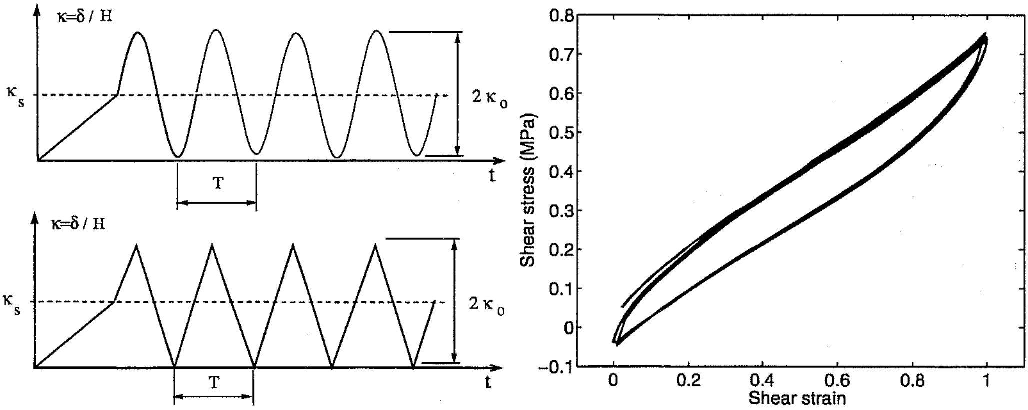

Figure 8.10: *Check of sensitivity of the hysteresis loop to the shape of the strain history. A sinusoidal and a triangular shear strain history were tested at 0.05 Hz.*

8.3.2. Steady state dynamic experiments

Tests with different combinations of amplitude and frequency were performed in order to investigate the influence of amplitude and frequency of the dynamic modulus and phase angle. A total of 20 tests were performed with the same setup and strain history as for the quasi-static tests according to Figure 8.9, although for smaller amplitudes and higher frequencies. The prestrain was held constant, $\kappa_s = 0.2$, and all combinations of frequency f and amplitude κ_0 in (8.3) were tested.

$$f = [1 \quad 5 \quad 10 \quad 15 \quad 20]Hz \qquad \kappa_0 = [0.02 \quad 0.05 \quad 0.1 \quad 0.15]. \tag{8.3}$$

The dynamic modulus was computed in each test as the quotient

$$G_{dyn} = \frac{\tau_0}{\kappa_0}, \tag{8.4}$$

where $\tau_0 = \Delta P/(2A)$ is the shear stress amplitude and $\Delta P = P_{max} - P_{min}$. A harmonic function was fitted by a least squares procedure to the stress response time functions. The stress amplitude and the phase angle were evaluated from the fitted function. The shape of the hysteresis loops for these tests does not deviate too much from the elliptic, and the dynamic modulus and phase angle should not deviate from what would be obtained by the definitions in Section 8.1. Typical shapes are shown in Figure 8.13.

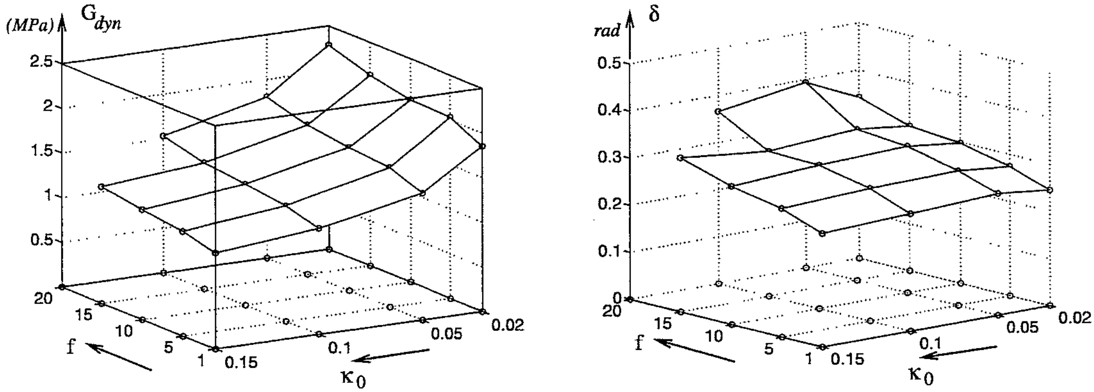

Figure 8.11: *Dynamic modulus and damping determined from double shear tests with different frequencies (f) and amplitudes (κ_0).*

The dependences of the dynamic shear modulus and phase angle on frequency and amplitude are shown in Figures 8.11 and 8.12. The test with maximum frequency and amplitude (20Hz with 15% strain amplitude) could not be evaluated due to limitations in the testing equipment. The diagrams in 8.12 are views of the three dimensional plots showing frequency and amplitude dependence.

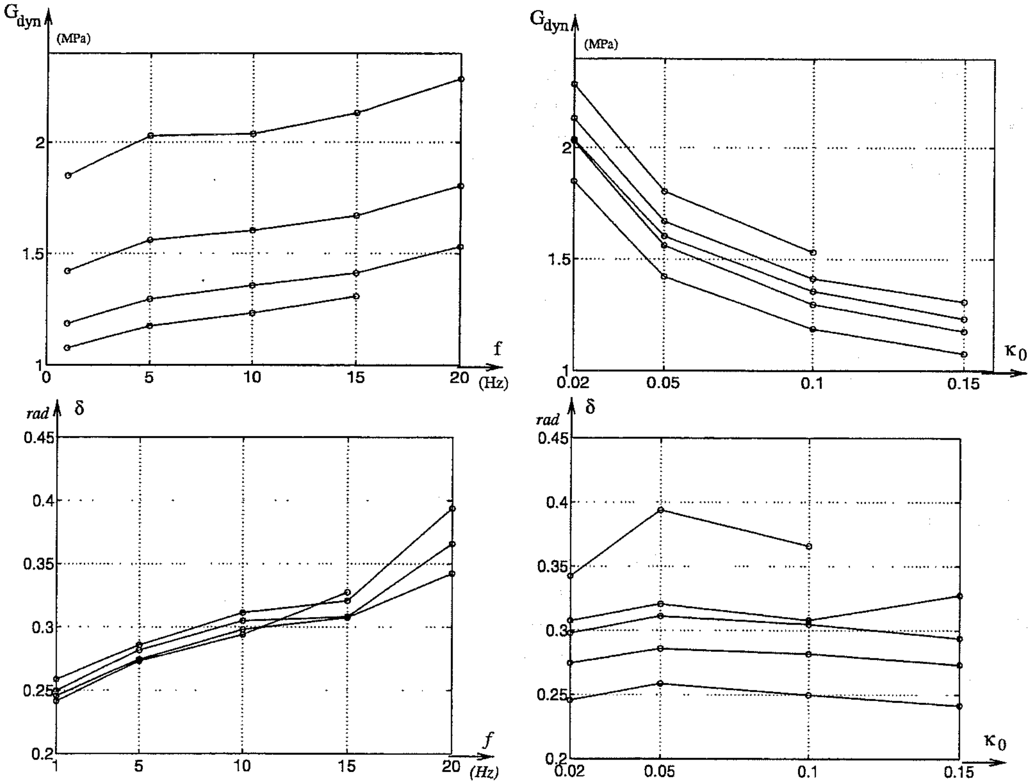

Figure 8.12: *Above: Two views of the dynamic modulus in Figure 8.11 showing the frequency (f) and amplitude (κ_0) dependence. Below: Two views of the equivalent phase angle in Figure 8.11 showing the frequency (f) and amplitude (κ_0) dependence.*

A moderate increase in dynamic modulus with frequency and a quite substantial decrease in modulus with increasing amplitude can be seen in Figure 8.12. Moreover, an important observation is that the experiments indicate a separable amplitude and frequency dependence. The curves are of the same shape and can approximately be generated by translation of a single curve in each diagram. This is in accordance with Payne's [45] and Warnaka's [61] observations discussed previously.

In order to check the reversibility of the dynamic modulus amplitude dependence, a test with increasing and decreasing amplitude was performed. The influence of damage on the dynamic modulus amplitude dependence has been tested for the simple shear specimen. The test was performed in a continuous sequence with increasing and decreasing amplitude harmonic strain history according to Figure 8.13. The frequency was 5 Hz with 15 cycles for each of the amplitudes (κ_0) in the sequence, given by

$$\kappa_0 = \left[\begin{array}{ccccc} 0.02 & 0.05 & 0.1 & 0.05 & 0.02 \end{array} \right],$$

with the same prestrain as in the previous test, i.e. $\kappa_s = 0.2$.

The resulting stress-strain loop is also shown in the figure. It can be seen that the two smallest loops do not coincide. The lower one is the the last and the softening is probably due to warming of the specimen by hysteresis work.

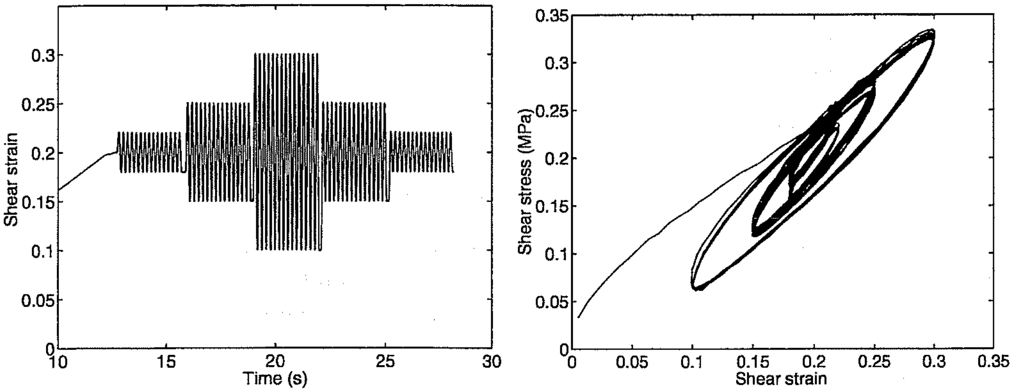

Figure 8.13: *Reversibility of the amplitude dependence of the dynamic modulus. Hysteretic loops (right) for the strain history (left). Testing in simple shear with frequency* $f = 5$ *Hz and amplitudes* $\kappa_0 = 0.02$, 0.05, 0.1, 0.05, *and* 0.02.

Evaluating the stress history in the same way as the previously discussed harmonic tests yields

κ_0	0.02	0.05	0.1	0.05	0.02
G_{dyn}	1.95	1.56	1.32	1.51	1.88

The important conclusion is that most of the decline in the modulus is recoverable and that damage therefore plays a minor role in the explanation of the amplitude dependence. This is in accordance with Payne's observations [45].

8.3.3. Summary of experimental findings

Deviations from linear dynamic behavior lie in the underlying nonlinear elastic properties and in the damping mechanisms introduced by the filler.

For unfilled rubbers a linear viscoelastic behavior can be observed in simple shear, which is a linear mode of deformation if the strains are not too large. In the case of filled rubbers, nonlinear dynamic behavior is present even for simple shear due to breakdown and reforming of the carbon-black structure.

The dynamic properties of carbon-black-filled rubbers according to the references and the experimental findings in Section 8.3 are summarized here.

- In quasi-static loading it can be observed that a difference between loading and unloading curves is present irrespective of how low the loading rate is. It was also observed that the hysteresis loop in quasi-static loading takes the approximate shape of a parallelogram (cf. Figure 8.9).
- The shape of the strain history does not appreciately influence the shape of the hysteresis loop (cf. Figure 8.10).
- In relaxation tests a step size dependence is observed, where the smallest strain step yields the largest relaxation modulus. The relaxation modulus falls with increasing step size towards an asymptotic value (cf. Figure 8.8).
- In harmonic loading it can be observed that the dynamic modulus shows a considerable amplitude dependence. The modulus declines with amplitude towards an asymptotic value for large amplitudes. The damping represented by the equivalent phase angle reaches a maximum where the decline in modulus is the greatest (cf. Figure 8.5).
- The dynamic modulus has been shown to be almost recoverable for a strain cycle in harmonic testing (cf. Figure 8.13). The mechanisms on microstructural level involved must therefore be different from the mechanisms involved in the Mullins effect. The explanation is breakdown and reforming of the carbon-black structure.
- The shape of the decline of the dynamic modulus with amplitude is insensitive to frequency. Experiments indicate that the amplitude and frequency dependence are separable (cf. Figure 8.12).

In the next section an introduction to modeling of the observed phenomena will be given, including references to previous work.

8.4. One dimensional models of damping

This section is intended as an introduction to modeling of damping in elastomeric materials. Basic properties of different models will be discussed. The viscous rate-dependent and the frictional rate-independent damping present in carbon-black-filled rubbers will be discussed briefly. A more thorough presentation of these subjects follows in subsequent chapters.

The simple one-dimensional model of elastic and damping properties, cf. Figure 8.14, was discussed in the introduction (Chapter 1). The elastic behavior is provided by the spring element, which is assumed to be nonlinear. Damping is modeled by the rate-dependent viscous damper and the rate-independent frictional element. The frictional element makes it possible to model hysteresis in quasi-static load cases, i.e. when the strain rate approaches zero.

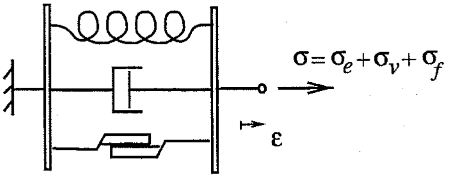

Figure 8.14: *Simple one-dimensional rheological model including nonlinear elastic, viscous, and frictional properties.*

The elastic, viscous, and frictional forces act in parallel, and the total stress is the sum of the stresses in the elements, i.e. $\sigma = \sigma_e + \sigma_v + \sigma_f$. The viscous stress σ_v corresponds to dissipative stresses in the rubber network. Stresses in the filler phase and in the rubber-filler interfaces are responsible for the rate-independent contribution σ_f.

This model incorporates some important aspects of the mechanical behavior of filled rubbers, and it is a starting point for modeling of damping in filled rubbers. Frequency dependence, effects of static load on the dynamic modulus, distortion of the elliptic shape of the hysteresis loop, and amplitude dependence are properties of the simple model. However, it has some unphysical properties, e.g. discontinuous stress response for continuous strain and inability to exhibit relaxation behavior.

Models without these drawbacks will be outlined here. Four simple one-dimensional models, which exhibit reasonable qualitative physical behavior, are presented in this introduction. The first is the viscoelastic "standard linear solid" model that exhibits a linear dynamic behavior due to purely rate-dependent damping and linear elastic behavior. (Linear viscoelasticity is discussed further in Chapter 9.) The second is an analogous nonlinear viscoelastic model, with linear rate-dependent damping and nonlinear elastic behavior. Multiaxial nonlinear viscoelastic models of this kind are the subject of Chapter 12. The third model is a rate-independent damping model that exhibits an amplitude-dependent (equivalent) dynamic modulus. The rate-independent damping model is discussed further and generalized in Chapter 10. The fourth model combines the rate-dependent and rate-independent models. This makes it possible to describe transient and steady state dynamic behavior of filled rubbers. The model is generalized in a systematic way in Chapter 11.

8.4.1. The standard viscoelastic solid

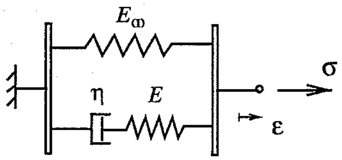

Figure 8.15: *Standard viscoelastic solid (also called Zener model).*

The linear standard viscoelastic solid, also called the Zener model, shown in Figure 8.15 represents a special case in the class of linear viscoelastic models, although it has all the qualitative features of more sophisticated viscoelastic solid models. This incorporates relaxation behavior and elastic response to very fast and very slow loading.

The springs are assumed to have linear characteristics and the dashpot stress σ_v is proportional to strain rate with the proportionality factor η, i.e. $\sigma_v = \eta\dot{\varepsilon}$.

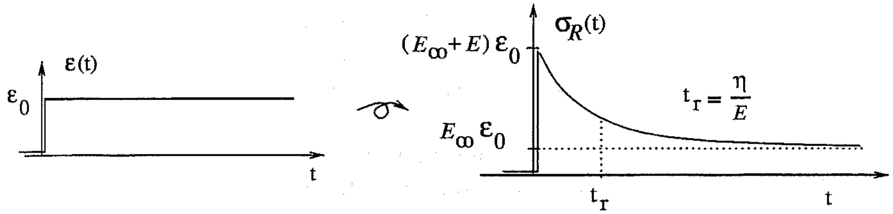

Figure 8.16: *Relaxation behavior of the standard viscoelastic solid; stress is relaxed to a long-term value.*

It will be shown in Chapter 9 that this model responds with an exponentially declining stress to a suddenly applied constant strain. The relaxation stress is shown in Figure 8.16. Initially the model responds elastically, because the dashpot acts as a rigid member to fast loading. The initial modulus is thus determined by the two parallel springs. The stress is then relaxed to a long-term value determined by the spring with modulus E_∞ The relaxation time $t_r = \eta/E$ is a model parameter that determines the rate of relaxation.

Figure 8.17 shows the response to a sinusoidal strain. Low frequency excitation yields an almost elastic dynamic modulus close to E_∞, and high frequency excitation also yields an almost elastic response with the dynamic modulus close to $E_0 = E + E_\infty$. The dynamic modulus thus increases with frequency from E_∞ to $E + E_\infty$. Maximum hysteresis (damping) occurs for an intermediate frequency.

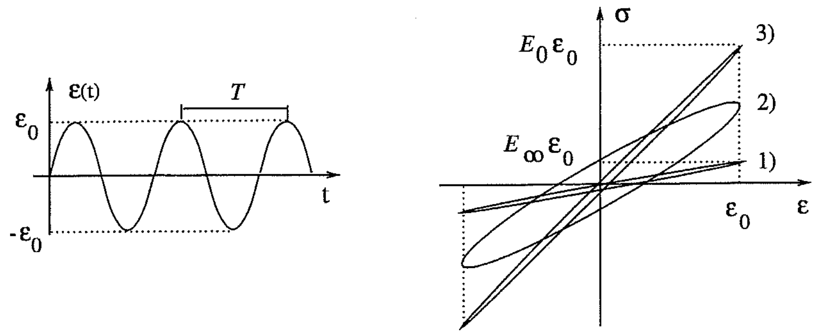

Figure 8.17: *Elliptical hysteresis loops for sinusoidal excitation at different frequencies for the standard viscoelastic solid. Excitation with increasing frequency from 1) to 3).*

Some properties of the linear dynamic behavior of the viscoelastic solids are summarized here:

- The dynamic modulus is independent of amplitude.
- Harmonic excitation yields a phase-shifted harmonic response with the same frequency.
- The hysteresis loop has an elliptic shape.
- The dynamic modulus increases with frequency.

8.4.2. A nonlinear viscoelastic solid

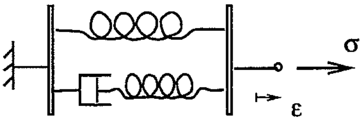

Figure 8.18: *Nonlinear viscoelastic rheological model.*

The nonlinear property of rubber can be incorporated into the concept of viscoelasticity. The model in Figure 8.18 is assumed to be composed of nonlinear springs and a linear dashpot. The behavior of the model is similar to the linear version described previously. However, the nonlinearity distorts the hysteresis loop and the dynamic modulus is influenced by static load. A model obtained from neo-Hooke hyperelasticity (will be derived in Chapter 12) with parameters $C_{10} = 0.5$ $t_r = 0.15s$ and the amount of normalized relaxation $g = 0.2$ was evaluated in cyclic compression/tension. Normalized relaxation $g = 0.2$ means that 20% of the initial stress is relaxed at infinite time. The model behavior for a strain amplitude $\epsilon_0 = 0.3$ is illustrated in Figure 8.19.

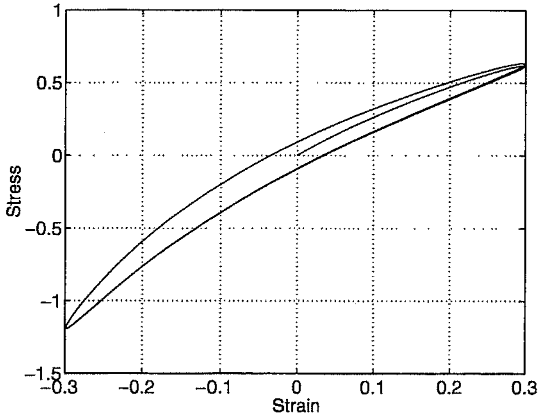

Figure 8.19: *Stress-strain response to a sinusoidal strain input.*

It is seen that in this case we clearly have a nonlinear dynamic behavior with a distorted elliptical hysteresis loop.

8.4.3. A simple frictional solid model

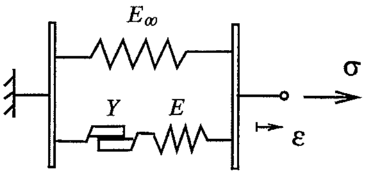

Figure 8.20: *A one-dimensional rheologic model including elastic and frictional properties.*

A solid model with rate-independent damping properties is represented by the rheologic model in Figure 8.20. This model is analogous to the Zener model except for the dissipative element; the dashpot has been replaced by frictional blocks.

The rate-independent stress in the frictional element is limited to $\sigma_f = \pm Y$ for fully developed friction.

It will be shown in Chapter 10 that the hysteresis loop is parallelogram-shaped, according to Figure 8.21. The shape of the hysteresis loop is the same for different kinds of periodic strain excitation, provided that the amplitude ϵ_0 is the same.

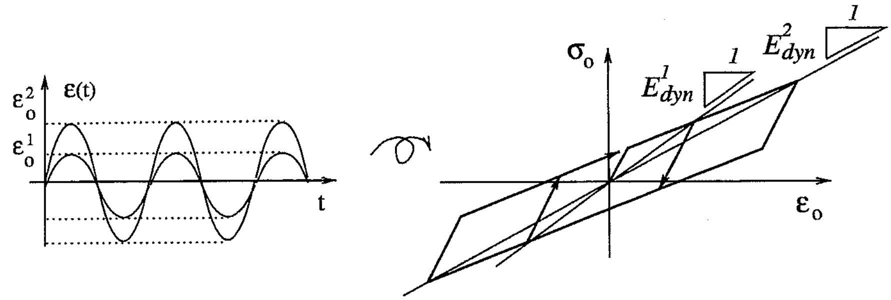

Figure 8.21: *Amplitude dependence of the dynamic modulus for the frictional model.*

Hence, a sine, sawtooth or square shaped periodic function yields the same response, regardless of the frequency, if the amplitude is the same. The amplitude dependence of the dynamic modulus of the model is also illustrated in Figure 8.21. Maximum stress and maximum strain occur simultaneously and the dynamic modulus is calculated at this point as $E_{dyn} = \sigma_0/\epsilon_0$. It is clear that the modulus decreases with increasing strain amplitude.

The rate-independent frictional element thus introduces a nonlinearity that is seen in the amplitude dependence and the parallelogram-shaped hysteresis loop, contrary to linear dynamics, where a sinusoidal strain results in a sinusoidal stress and thereby an elliptic hysteresis loop.

The stress response for the frictional solid model can be resolved into Fourier components, which are multiples of the input frequency. This has been done for the stress response of a sinusoidal strain input with frequency 1 Hz and amplitude $\epsilon_0 = 0.1$. The model parameters used are $E_\infty = 1$, $E = 1$ and $Y = 0.015$.

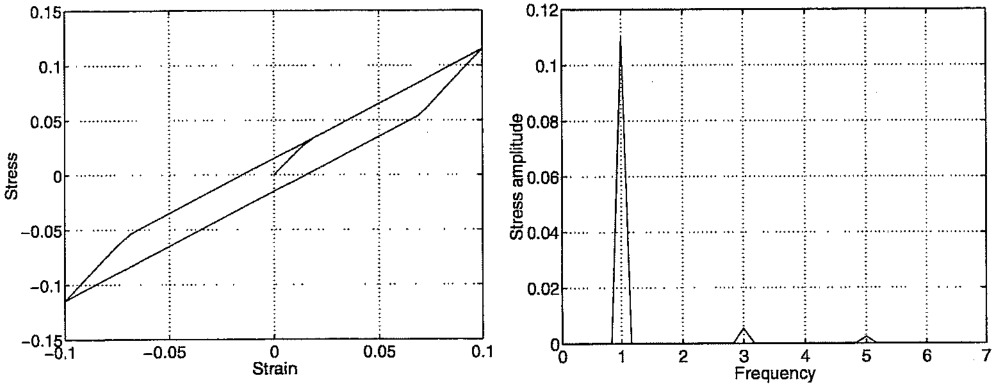

Figure 8.22: *Hysteresis loop (left) and Fourier components in the stress response (right) for the frictional model.*

The resulting stress is, according to Figure 8.22, composed of odd multiples of the fundamental frequency. This is in accordance with the experimental findings of Harris and Stevenson [25].

Some properties (discussed further in Chapter 10) of the frictional damping are summarized here:

- The hysteresis loop has the shape of a parallelogram.
- The hysteresis is independent of the rate (frequency) of loading.
- The dynamic stiffness decreases with amplitude.
- Harmonic excitation yields a non-harmonic response that can be resolved into harmonic components that are odd multiples of the excitation frequency.

8.4.4. A combined viscous and frictional model

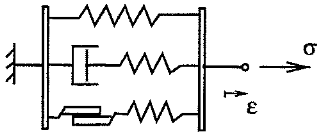

Figure 8.23: *Five-parameter model including elastic, viscous, and frictional properties.*

A combination of viscous and frictional damping is needed to account for the inelastic effects in carbon-black-filled rubbers. The model in Figure 8.23 is obtained by connecting the Zener model and the corresponding frictional model in parallel. It gives a reasonable representation of damping in filled rubbers, supported by micro mechanical behavior and experimental observations. The total damping stress is the sum of the viscous and the frictional stresses. Step size dependent relaxation and amplitude dependent dynamic modulus are properties of the model, discussed further in Chapter 11.

In Chapter 13 a possible generalization to the multiaxial case is discussed.

8.5. Modeling of dynamic behavior: Previous work

Models for viscoelastic analysis, with the elastic behavior based on hyperelasticity, for arbitrary and large strains, have been developed by Simo [54], Lubliner [34], and Johnson et al. [30]. Simo's model also includes modeling of damage. Large strain viscoelastic models for nearly incompressible and compressible analysis are implemented in the finite element codes ABAQUS and MARC.

A modification of the theory for the important case of small steady state vibrations superposed on a large static hyperelastic state of strain was proposed by Morman [40]. This model has been implemented in the finite element code ABAQUS. Similar models have been developed and implemented into finite element code by for example Zdunek [67].

Experimental investigations suggest that unfilled rubbers can be modeled by viscoelastic models [25], whereas the behavior of filled rubbers can not, according to the previous discussion. The amplitude dependence of the dynamic stiffness is significant in filled rubbers and it is in general more important than the influence of frequency and temperature. The amplitude dependence is not included in the viscoelastic models.

Godvinjee and Simo [19] explain the amplitude dependence by damage in a viscoelastic damage model for large strains. However, they also report that in cyclic loading the shape of the hysteresis loop is very sensitive to the shape of the periodic loading history. Moreover, the decline in amplitude for successive larger amplitudes is irreversible. These essential drawbacks of the theory imply that viscoelasticity is not suited for filled rubbers.

A one-dimensional model of the amplitude dependence for periodic sinusoidal loading was suggested by Kraus [31]. This model explains the amplitude dependence by continuous breaking and reforming of van der Waals forces between carbon-black aggregates.

The Kraus model has been investigated and evaluated by many researchers, see for example Ulmer [59] and Vieweg [60]. The latter finds that the sigmoidal decline (in logarithmic coordinates) of the dynamic modulus does not depend on frequency for the investigated range $0.06 - 20\ Hz$.

Rate-independent damping mechanisms have been employed to model the amplitude dependence of the dynamic stiffness for discrete damper models, usually expressed in terms of force and displacement relations, see for example [7] and [12].

However, in terms of three-dimensional large strain models there appears to be no counterpart to the one-dimensional models that incorporate modeling of rate independence (cf. Figure 8.23) for filled rubbers. It will be argued that viscoplasticity is necessary to explain the nonlinear dynamic behavior of these rubbers.

9. LINEAR VISCOELASTIC MODELS

This chapter provides a background to several concepts concerning the dynamic properties of rubber. The purpose is to define some important issues such as complex modulus, creep and relaxation functions, and to provide some understanding of viscoelastic material behavior. Linear viscoelastic behavior will be illustrated for transient and periodic loading. The subjects covered in this chapter can be found in several textbooks; see for example [37], [49] or [56].

Viscoelastic material models combine elastic and viscous characteristics. The constitutive relations are defined in terms of time functions of stress $\sigma(t)$ and strain $\epsilon(t)$. Hence, the response becomes time dependent, in contrast to ideally linear elastic materials where a one-to-one relation exists between the current stresses and current strains. The constitutive equations can be defined by an integral or by a differential equation.

Rheological models consisting of spring and dashpot assemblages are often used to illustrate viscoelastic material behavior. The mechanical behavior of a specific viscoelastic material in a uniaxial case is analogous to the behavior of a proper combination of springs and dashpots.

With harmonic excitation the response will be a phase shifted harmonic function with the same frequency. This property of linear viscoelasticity makes it possible to define a complex modulus independent of amplitude and a function only of frequency.

9.1. Creep and relaxation

Material behavior explainable by linear viscoelastic models includes, for example, creep and relaxation phenomena. Creep is an increasing strain as response to a step-stress loading, and relaxation is a decreasing stress as response to a step-strain loading.

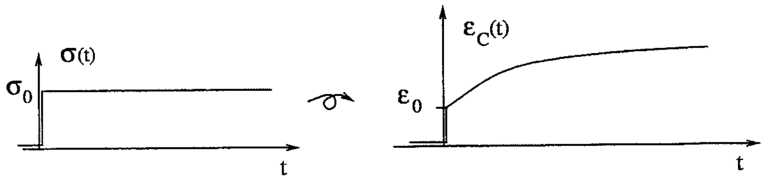

Figure 9.1: *Creep behavior; increasing strain as response to a stress step.*

For a linear viscoelastic material the creep compliance $J_C(t) = \epsilon(t)/\sigma_0$ (cf. Figure 9.1) is a characteristic function independent of the stress step σ_0. This function is unique for a specific linear viscoelastic material.

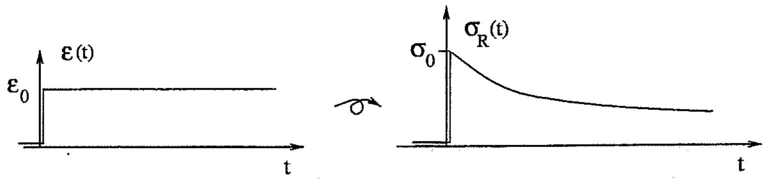

Figure 9.2: *Relaxation behavior; decreasing stress as response to a strain step.*

For a linear viscoelastic material, the relaxation modulus $E_R(t) = \sigma(t)/\epsilon_0$ (cf. Figure 9.2) is a characteristic function independent of the strain step ϵ_0. This function is unique for the specific linear viscoelastic material.

It can be shown that the instantaneous elasticity, i.e. the relationship between the creep compliance and the relaxation modulus at $t = 0$, is $E_R(0) = 1/J_C(0)$.

9.2. The hereditary integral

The behavior of a linear viscoelastic material can be defined from this single step response function. Linearity and superposition (Boltzmann's superposition principle) leads to the constitutive equation defined as a convolution integral (also called hereditary integral). The stress history corresponding to any strain history can be obtained from this integral. The constitutive model is defined by the relaxation modulus, or for the inverse relation, the creep compliance.

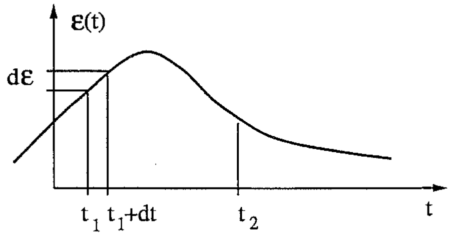

Figure 9.3: *An arbitrary strain history.*

An arbitrary strain history $\epsilon(t)$, cf. Figure 9.3, can be considered as a sum of a large number of differential, positive and negative strain steps. A strain step $d\epsilon$ at time t_1 causes a stress change $d\sigma$. At time t_2 the stress change has been relaxed to

$$d\sigma(t_2) = E_R(t_2 - t_1)\, d\epsilon(t_1) \; .$$

Summation of all stress changes at time t_2 due to all previous strain steps yields

$$\sigma(t_2) = \int_{-\infty}^{t_2} E_R(t_2 - t)\, \frac{d\epsilon}{dt} dt\,. \tag{9.1}$$

This is the hereditary integral that defines the linear viscoelastic stress response for an arbitrary strain history. Hence, from knowledge of the relaxation modulus the stress $\sigma(t_2)$ can be derived by (9.1) for an arbitrary strain history $\epsilon(t)$.

The inverse relation can be obtained by applying stress steps and assembling the creep histories, giving the relation

$$\epsilon(t_2) = \int_{-\infty}^{t_2} J_C(t_2 - t)\, \frac{d\sigma}{dt} dt \tag{9.2}$$

In connection with the finite element method, where strain and displacement are the basic unknown quantities, the form (9.1) defined by the relaxation modulus is preferred.

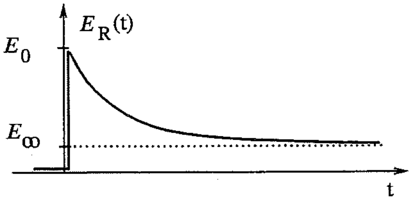

Figure 9.4: *The relaxation modulus of a viscoelastic solid.* E_0 *is the instantaneous modulus and* E_∞ *is the long-term modulus.*

Linear viscoelastic theory can model both fluid and solid material behavior. The main interest here is models with solid properties. It is therefore required that the creep response is limited, and that the relaxation has a limit different from zero according to Figure 9.4.

An example of a relaxation process can be obtained by assuming a simple exponential law given by

$$E_R(t) = E_\infty + (E_0 - E_\infty)\, e^{-t/t_r}$$

this is the relaxation modulus associated with the Zener model, which will be discussed further in relation to rheologic models in section 9.4. The parameter t_r is the relaxation time.

9.3. Harmonic excitation and complex modulus

The response to a stationary sinusoidal strain history is of interest in many engineering applications. The stress corresponding to a stationary sinusoidal strain can be expressed by a complex modulus. The constitutive relation (9.1) will be used to determine an expression for the complex modulus. Consider the sinusoidal strain in complex notation

$$\epsilon^* = \epsilon_0 e^{i\omega t} = \epsilon_0(cos(\omega t) + isin(\omega t)) \tag{9.3}$$

where the real or imaginary part is interpreted as the physical strain. Inserting (9.3) into the convolution integral (9.1) yields an expression that resembles the Fourier transform. The Fourier transform is a complex valued function depending on the parameter $\omega = 2\pi/T$ i.e. the angular frequency for the vibration, with T being the periodic time.

The form of the relaxation modulus $E_R(t)$ is inadequate for Fourier transform methods since the transform is defined only for absolute convergent functions. This requires that the function to be transformed fulfills the condition

$$\int_{-\infty}^{\infty} \mid f(t) \mid dt < \infty \, . \tag{9.4}$$

The relaxation modulus, cf. Figure 9.4, does not fulfill the requirement in (9.4). The long-term modulus E_∞ has to be separated from $E_R(t)$. A dimensionless relaxation function $e(t)$ is therefore introduced, according to

$$E_R(t) = E_\infty(1 + e(t)) \, . \tag{9.5}$$

The function $e(t)$ has the property $e(t) \to 0$ when $t \to \infty$. The dimensionless relaxation function now fulfills the requirement in (9.4) and the constitutive relation (9.1) may now be written as

$$\sigma(t_2) = E_\infty \int_{-\infty}^{t_2} (1 + e(t_2 - t)) \frac{d\epsilon(t)}{dt} dt \, . \tag{9.6}$$

Introducing a change of variables $\tau = t_2 - t$ and substituting the complex strain (9.3) into (9.6) yields

$$\sigma(t_2) = E_\infty(1 + i\omega \int_0^{\infty} e(\tau) e^{-i\omega\tau} d\tau) \epsilon_0 e^{i\omega t_2} \, . \tag{9.7}$$

In (9.7) the Fourier transform of the dimensionless relaxation function can now be identified as

$$e^*(\omega) = \mathcal{F}(e(\tau)) = \int_0^{\infty} e^{-i\omega\tau} e(\tau) d\tau$$

and (9.7) can now be expressed as

$$\sigma^* = E^*(\omega)\epsilon^* \tag{9.8}$$

with the complex modulus

$$E^*(\omega) = E_\infty(1 + i\omega e^*(\omega)) \, . \tag{9.9}$$

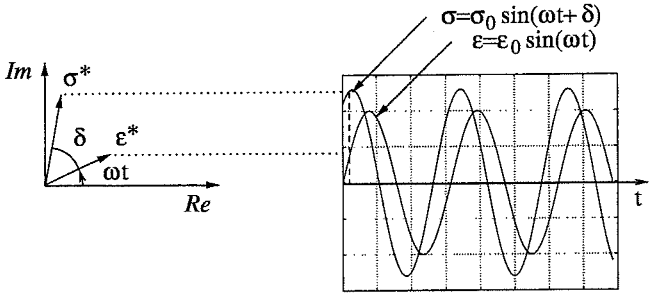

Figure 9.5: *The real or imaginary part of the complex strain and stress represents the harmonic motion.*

Hence, the hereditary integral (9.1) is converted into a relation between the complex strain and stress given by a simple multiplication by a complex function, the complex modulus.

The stress response σ^* can therefore be written as a complex number in polar form as

$$\sigma^* = \sigma_0 e^{i(\omega t+\delta)} \ . \tag{9.10}$$

The response to a steady-state sinusoidal strain is thus a steady-state sinusoidal stress with the same frequency, but out of phase. The phase relationships are conveniently shown in the rotating-vector representation according to Figure 9.5.

9.3.1. Interpretation of the complex modulus

In view of (9.8), the complex modulus can be expressed as

$$\sigma^* = \mid E^* \mid e^{iarg(E^*)} \epsilon_0 e^{i\omega t} = \mid E^* \mid \epsilon_0 e^{i(\omega t + arg(E^*))} \ . \tag{9.11}$$

Comparing (9.11) with (9.10) yields an interpretation of the complex modulus in terms of measurable quantities according to

$$\mid E^* \mid = \frac{\sigma_0}{\epsilon_0} \quad \text{and} \quad arg(E^*) = \delta$$

i.e. the absolute value $\mid E^*(\omega) \mid$ is the amplitude ratio of stress and strain and the phase angle $arg(E^*(\omega))$ is the phase shift between stress and strain. The absolute value $\mid E^*(\omega) \mid$ is here called the *dynamic modulus* (also called the absolute modulus).

Note that the dynamic modulus and the phase angle are functions of the angular frequency ω only. Hence, for a linear viscoelastic material, the dynamic modulus is independent of the strain amplitude ϵ_0.

The complex modulus

$$E^* = \frac{\sigma^*}{\epsilon^*} = \frac{\sigma_0 e^{i(\omega t+\delta)}}{\epsilon_0 e^{i\omega t}} = \frac{\sigma_0}{\epsilon_0} e^{i\delta}$$

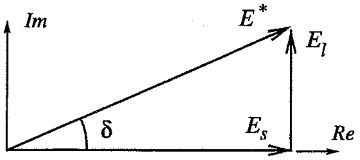

Figure 9.6: *Relation between polar and rectangular form of the complex modulus.*

can alternatively be expressed in rectangular form

$$E^* = \frac{\sigma_0}{\epsilon_0} cos\delta + i\frac{\sigma_0}{\epsilon_0} sin\delta \tag{9.12}$$

where the real part E_s is termed *storage modulus* and the imaginary part E_l is termed *loss modulus.* Hence,

$$E_s = \frac{\sigma_0}{\epsilon_0} cos\delta \quad \text{and} \quad E_l = \frac{\sigma_0}{\epsilon_0} sin\delta \; .$$

The storage modulus is said to represent in-phase response and the loss modulus is said to represent out-of-phase response, according to Figure 9.6.

An alternative representation of the rectangular form is

$$E^* = E_s(1 + tan\,\delta) \; ,$$

where $tan\,\delta$ is called the *loss factor.*

The relation between the polar and the rectangular form of the complex modulus can be simplified for small values of δ. The approximate equalities $sin\,\delta \approx tan\,\delta \approx \delta$ and $cos\,\delta \approx 1$ yield

$$E_s \approx\mid E^* \mid \qquad \text{and} \qquad E_l \approx\mid E^* \mid \delta \; .$$

For example, $\delta = 0.2\,rad$ yields $sin\,\delta = 0.199$, $cos\,\delta = 0.980$, and $tan\,\delta = 0.203$.

9.3.2. Hysteresis and energy dissipation

For cyclic loading, viscoelastic materials dissipate energy, which for instance results in damping of free vibrations. The area enclosed by the loading and unloading curves (cf. Figure 9.7) represents the energy dissipated as heat.

Harmonic excitation yields harmonic response with the same frequency but out of phase for a linear viscoelastic material, according to the previous discussion. Consequently, if the strain $\epsilon = \epsilon_0 \sin(\omega t)$ and the stress $\sigma = \sigma_0 \sin(\omega t + \delta)$ are plotted in the (σ, ϵ) plane, an elliptic path is obtained, as shown in Figure 9.7. The hysteresis is dependent on the angular frequency ω through the complex modulus.

The energy dissipated during one cycle is

$$U_c = \oint \sigma d\epsilon = \sigma_0 \epsilon_0 \omega \int_0^T cos(\omega t) sin(\omega t + \delta) dt \; . \tag{9.13}$$

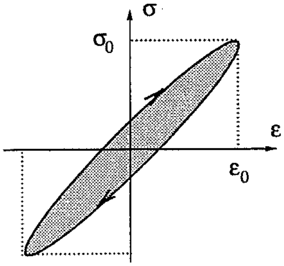

Figure 9.7: *The stress $\sigma = \sigma_0 sin(\omega t + \delta)$ and the strain $\epsilon = \epsilon_0 sin(\omega t)$ plotted in the (σ, ϵ) plane, giving an elliptical hysteresis loop.*

Expression (9.13) is evaluated by using the trigonometric formula $sin(\omega t + \delta) = sin\omega t\, cos\delta + cos\omega t\, sin\delta$, giving

$$U_c = \pi\sigma_0\epsilon_0 sin\,\delta\ .$$

We observe that dissipated heat increases with the phase difference δ and the largest dissipation is obtained for $\delta = \pi/2$.

9.4. Rheological models

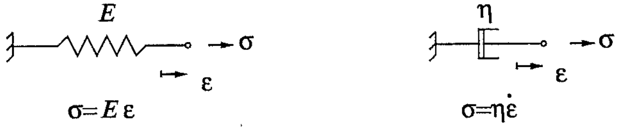

Figure 9.8: *Basic elements in rheological models; the linear spring and the dashpot.*

An illustrative way to interpret and describe the nature of viscoelastic behavior is to use rheological models. These are mechanical analogue assemblages of linear springs and dashpots. The elastic behavior is due to the linear springs and the viscous behavior is due to the dashpots, according to Figure 9.8. The stress in the linear spring is proportional to strain $\sigma = E\epsilon$ and the dashpot stress is proportional to strain rate $\sigma = \eta\dot{\epsilon}$, where the dot denotes time derivative, and η is the viscosity coefficient (Ns/m^2).

Simple viscoelastic models can be obtained with linear springs and dashpots coupled in series and in parallel. The spring and dashpot combination in series yields the Maxwell model, which is a viscoelastic fluid model. The spring and dashpot components coupled in parallel yield the Kelvin model, which is a crude viscoelastic solid model. The Kelvin model is not particularly physical. For example, a sudden application of strain yields a discontinuous stress response.

The simplest viscoelastic solid model with reasonable physical behavior is obtained by a spring and a Maxwell element coupled in parallel. This is the standard linear solid model, also called the Zener model. By invoking several Maxwell elements in parallel with the spring, the generalized Maxwell model is obtained.

In the following subsections, the relaxation modulus $E_R(t)$ and the complex modulus $E^*(\omega)$ will be derived for the models mentioned.

9.4.1. The Maxwell model

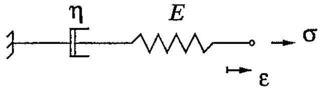

Figure 9.9: *The Maxwell model.*

The Maxwell element is illustrated in Figure 9.9. The relaxation behavior with a totally relaxed stress suggests that the element is a simple model of a linear viscoelastic fluid. The normalized relaxation behavior given by $E_R(t)$ is the fundamental function that defines the behavior of a linear viscoelastic material as mentioned earlier. Hence, the stress-strain relation for the Maxwell model is found by applying a step strain and evaluating the stress response.

The two elements in Figure 9.9 are coupled in series, and the requirement on the strain is $\epsilon = \epsilon_{spring} + \epsilon_{dashpot}$. The time derivative is

$$\dot{\epsilon} = \dot{\epsilon}_{spring} + \dot{\epsilon}_{dashpot} \,. \tag{9.14}$$

Inserting $\dot{\epsilon}_{spring} = \dot{\sigma}/E$ and $\dot{\epsilon}_{dashpot} = \sigma/\eta$ into (9.14) and rearranging yields

$$\dot{\sigma} + \frac{E}{\eta}\sigma = E\,\dot{\epsilon}\,, \tag{9.15}$$

which is the differential equation that defines the stress-strain relation for the Maxwell model.

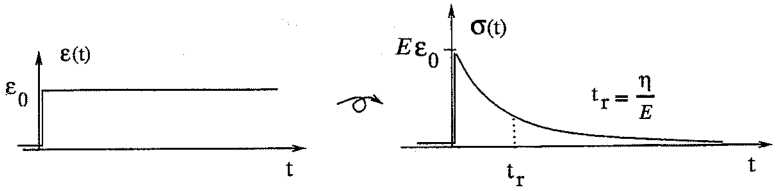

Figure 9.10: *Relaxation behavior of the Maxwell model; stress is relaxed to zero.*

The normalized relaxation behavior $E_R(t)$ can be derived by solving (9.15) for a step strain. For $t > 0$ we have $\dot{\epsilon} = 0$, giving

$$\dot{\sigma} + \frac{E}{\eta}\sigma = 0 \quad t > 0 \tag{9.16}$$

On application of the step strain the dashpot acts as a rigid member due to the infinitely large strain rate at $t = 0$. Hence, the initial stress is defined entirely by the elastic spring, and the initial condition for the differential equation is $\sigma(0) = E\,\epsilon_0$, i.e. the instantaneous elastic response. Solving (9.16) yields

$$\sigma(t) = E\,\epsilon_0\,e^{-\frac{E}{\eta}t}$$

The step strain stress response is illustrated in Figure 9.10, and we conclude that the relaxation modulus for the Maxwell model is

$$E_R(t) = E\,e^{-t/t_r}$$

where the relaxation time is defined as $t_r = \eta/E$.

The complex modulus $E^*(\omega)$ for the Maxwell model can be determined by solving (9.15) for a steady-state sinusoidal strain history

$$\epsilon^* = \epsilon_0 e^{i\omega t}\ .$$

Inserting a trial solution $\sigma = Ce^{i\omega t}$ into (9.15) yields the stationary solution

$$C = E\frac{i\omega}{i\omega + E/\eta}\epsilon_0 = E\frac{i\omega t_r}{i\omega t_r + 1}\epsilon_0\ .$$

Consequently we find the complex modulus

$$E^*(\omega) = E\frac{i\omega t_r}{1 + i\omega t_r} \tag{9.17}$$

for the Maxwell model.

9.4.2. The Zener model

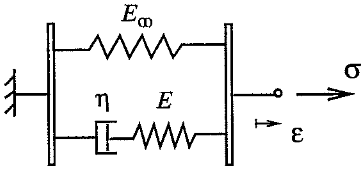

Figure 9.11: *The Zener model. A spring coupled in parallel with a Maxwell element.*

A simple rheological model that behaves like a solid can be achieved with a spring and Maxwell element coupled in parallel. This is the so-called Zener or standard linear solid model, according to Figure 9.11. The Zener model is the simplest viscoelastic model with solid properties that reflects the behavior of real solid materials in the sense that the relaxation behavior is reasonable and the creep response is limited.

Let us denote the stress in the spring with σ_∞ and the stress in the Maxwell element with σ_M. The total stress in the standard linear solid model, cf. Figure 9.11, is then given by

$$\sigma = \sigma_\infty + \sigma_M \,. \tag{9.18}$$

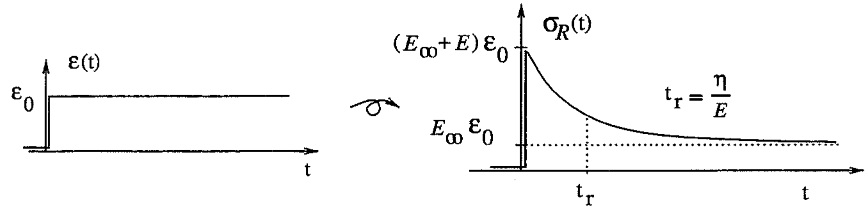

Figure 9.12: *Relaxation behavior of the Zener model; stress is relaxed to a long-term value.*

The stress in the spring is determined according to Hooke's law, i.e. $\sigma_\infty = E_\infty\epsilon$ and the response to a step strain history is therefore

$$\sigma_R(t) = E_\infty\epsilon_0 + Ee^{-\frac{E}{\eta}t}\epsilon_0 \qquad t > 0\,. \tag{9.19}$$

Hence, the relaxation modulus for the Zener model is

$$E_R(t) = E_\infty(1 + \frac{E}{E_\infty}e^{-t/t_r})\,. \tag{9.20}$$

The step strain response (9.20) is illustrated in Figure 9.12.

The complex modulus $E^*(\omega)$ for the Zener model can be determined by solving for a stationary sinusoidal strain. The strain is given by

$$\epsilon^* = \epsilon_0 e^{i\omega t}\,. \tag{9.21}$$

The stress is given by inserting the Maxwell stress (9.17) into (9.18) according to

$$\sigma^* = E_\infty\epsilon^* + E\frac{i\omega t_r}{1 + i\omega t_r}\epsilon^*\,. \tag{9.22}$$

Hence, the complex modulus for the Zener model is

$$E^*(\omega) = E_\infty(1 + \frac{E}{E_\infty}\frac{i\omega t_r}{1 + i\omega t_r})\,. \tag{9.23}$$

Another way to determine the complex modulus (9.23) is by Fourier transforming the dimensionless relaxation function according to (9.5), given by

$$e(t) = \frac{E}{E_\infty}e^{-t/t_r}\,,$$

giving

$$e^*(\omega) = \mathcal{F}(e(t)) = \int_0^\infty e^{-i\omega t}\frac{E}{E_\infty}e^{-t/t_r}dt = \frac{E}{E_\infty}\frac{t_r}{1 + i\omega t_r}.$$

and using (9.9) then yields the same expression as (9.23).

9.4.3. The generalized Maxwell model

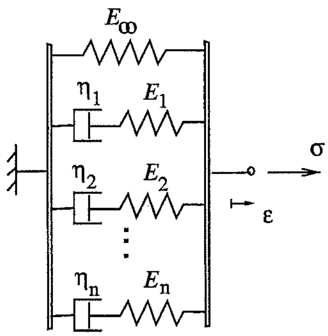

Figure 9.13: *The generalized Maxwell model.*

The Zener model from the previous section can be generalized by adding more Maxwell elements in parallel with the linear spring cf. Figure 9.13. This yields a model with properties qualitatively the same as the Zener model but with better ability to accurately fit experimental data.

We denote the stress in the spring component with σ_∞ and the stress in the first Maxwell element with σ_{M1}, etc. The total stress in the generalized model is

$$\sigma = \sigma_\infty + \sigma_{M1} + \sigma_{M2} + \dots \sigma_{Mn} \ . \tag{9.24}$$

The relaxation modulus for the generalized model is consequently established by summing the individual Maxwell modulis giving a so called Prony series

$$E_R(t) = E_\infty + \sum_{j=1}^{n} E_j e^{-t/t_{rj}} \ . \tag{9.25}$$

The complex modulus for the generalized Maxwell model can be derived in a similar manner, i.e. by summing the complex moduli,

$$E^*(\omega) = E_\infty + \sum_{j=1}^{n} E_j \frac{i\omega t_{rj}}{1 + i\omega t_{rj}} \ ,$$

giving the complex modulus for the generalized model.

Another way to determine the complex modulus, is as mentioned previously, by Fourier transforming the dimensionless relaxation moduli.

9.5. Properties of linear viscoelastic solids

To understand the behavior and restrictions of the rheological models for different strain histories, we will examine the behavior for different loading rates (frequencies). The generalized Maxwell model responds approximately elastically for both very slow and very fast loading. This is because the dashpots behave like rigid members for fast loading rates and because the dashpot stresses are relaxed for slow loading rates. This behavior can also be identified from the relaxation function. The instantaneous elastic and the long-term response is

$$E_R(0) = E_\infty + \sum_{j=1}^{n} E_j \qquad E_R(\infty) = E_\infty$$

according to (9.25), and the model gives elastic behavior for both cases.

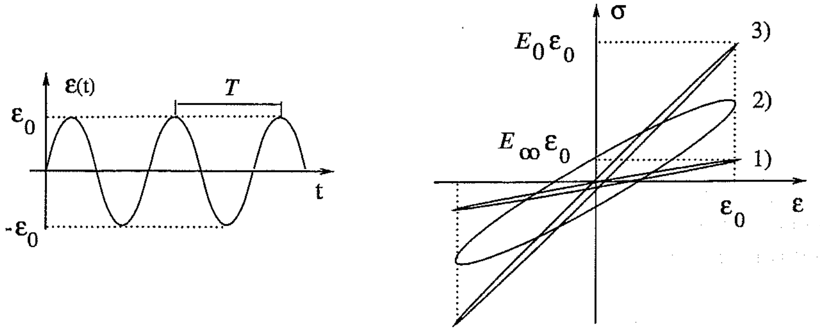

Figure 9.14: *Linear viscoelastic solid response to sinusoidal excitation.*

Looking at harmonic excitation, the behavior is similar. Consider three cases; low, medium, and high frequency i.e.

$$1)\quad \omega t_r \ll 1 \qquad 2)\quad \omega t_r \approx 1 \qquad 3)\quad \omega t_r \gg 1$$

The elliptic paths in the (σ, ϵ) plane for the three cases are illustrated in Figure 9.14. Low and high frequencies yield approximately elastic behavior.

9.5.1. Harmonic response of the Zener model

The Zener model is a fundamental viscoelastic model. It is therefore instructive to examine it quantitatively for harmonic excitation. First we will define an alternative set of constants related to the relaxation behavior according to Figure 9.15.

The rheological model is defined from three parameters, namely $[E_\infty, E, \eta]$. The alternative set of constants is defined from the instantaneous elasticity $E_0 = E_\infty + E$ and the relative amount of relaxation g (cf. Figure 9.15), and the relaxation time t_r.

The relation between the two sets is

$$E_0 = E_\infty + E \qquad g = \frac{E}{E_0} \qquad t_r = \eta / E \tag{9.26}$$

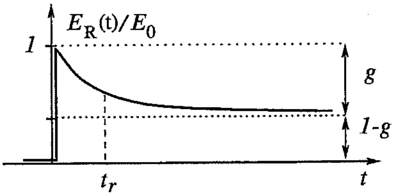

Figure 9.15: *The relative amount of relaxation g defined in terms of the normalized relaxation modulus.* E_0 *is the instantaneous modulus.*

The complex modulus for the Zener model is given in (9.23); inserting (9.26) yields

$$E^*(\omega)/E_0 = 1 - g + g\frac{i\omega t_r}{1 + i\omega t_r} \,. \tag{9.27}$$

Elastic behavior is obtained if E^* is real, i.e. for $\omega t_r = 0$ and $\omega t_r = \infty$. For intermediate frequencies E^* is complex, giving hysteresis. The absolute value and the phase of E^* are shown in Figure 9.16 as functions of normalized frequency ωt_r.

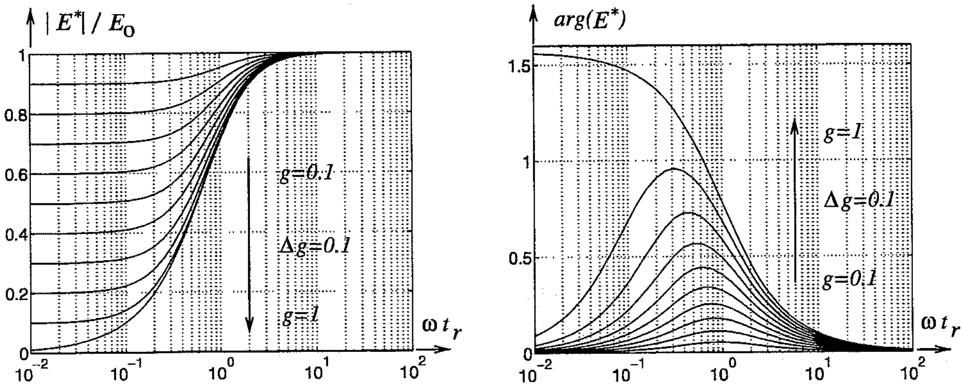

Figure 9.16: *The absolute value and the phase of* E^* *as functions of normalized frequency* ωt_r *for different values of normalized amount of relaxation* g.

Maximum phase angle (and hysteresis) occurs at $\omega t_r \approx 1$ for values of say $g \leq 0.5$. The assumption $tan\delta \approx \delta$ then yields an approximation of the maximum phase angle $\delta_{max} = max\{arg(E^*)\}$ from (9.27) as

$$\delta_{max} = \frac{g}{2-g} \qquad (\text{ for } \omega t_r \approx 1 \text{ and } g \leq 0.5) \,.$$

The expression is reasonably accurate for $g \leq 0.5$. Evaluating for $g = 0.5$ yields the exact $\delta_{max} = 0.34$ and the approximate $\delta_{max} = 0.33$.

9.6. Summary of linear viscoelastic properties

We have found that linear viscoelastic behavior is defined by an integral that depends on a single relaxation modulus for the material

$$\sigma(t) = \int_{-\infty}^{t} E_R(t-s)\,\frac{d\epsilon}{ds}ds$$

and that damping and hysteresis, dependent on the loading rate, can be modeled. The response to slow and fast loading is elastic in the limit.

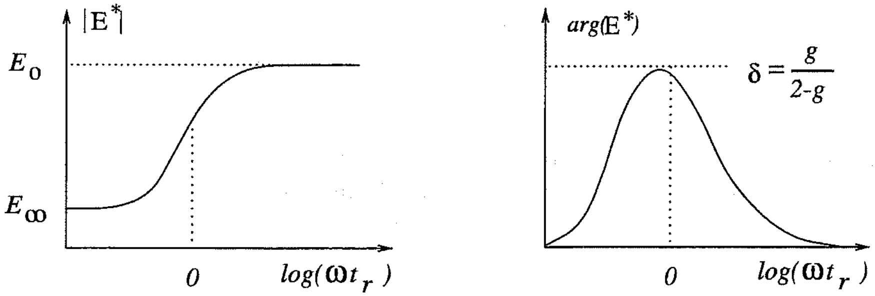

Figure 9.17: *Zener model; frequency dependence of the complex modulus for* $g \leq 0.5$.

The behavior in stationary harmonic loading can be characterized by a complex modulus that depends on frequency but is independent of the amplitude.

$$\sigma^* = E^*(\omega)\epsilon^*$$

Harmonic excitation consequently yields a phase-shifted harmonic response with the same frequency, and the shape of the hysteresis loop is thus elliptical.

The Zener model is a simple example of a linear viscoelastic solid model with physically reasonable properties. Figure 9.17 shows schematically the frequency dependence.

10. FRICTIONAL SOLID MODELS

The concern of this chapter is modeling of rate-independent damping by the model shown in Figure 10.1, with a number of frictional elements in parallel. An important issue is to model the amplitude dependence, i.e. the decreasing dynamic modulus E_{dyn} with increasing strain amplitude. This will be shown in detail for the simple frictional model with one frictional element (discussed in Chapter 8). It will also be shown that quasi-static harmonic behavior of filled rubbers can be modeled by this rate-independent model. The simple frictional model was discussed qualitatively by Gregory [22]. He concludes that the hysteresis loop for heavily filled rubbers approaches a trapezoidal form in accordance with the behavior of the simple model. Models with frictional elements coupled in series are discussed by Turner [57] and Coveney et al. [12]. These models are shown to fit the dynamic modulus and phase angle for experiments on highly filled rubbers in shear.

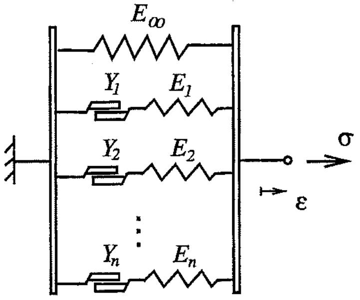

Figure 10.1: *The generalized frictional solid model.*

The model used here with frictional elements in parallel (cf. Figure 10.1) is an elasto-plastic model. The behavior has to be evaluated by an algorithm, where it is essential to distinguish if the current stress in the element has reached the yield limit Y_i or if the stress is in the elastic region. The relation between stress and strain rates can in principle be expressed by an effective elasto-plastic modulus E^{ep}, though it will not be derived explicitly. Hence, stress and strain rates are related as

$$\dot{\sigma} = E^{ep}\dot{\epsilon}$$

and we find that maximum stress and strain occurs simultaneously. This is in contrast to viscoelastic behavior, and it implies that relaxation and creep can not be represented. Moreover, due to the stress limits Y_i, the response to harmonic strain can not be a single harmonic stress component of the same frequency as is the case in viscoelasticity. We can conclude that the response to a sinusoidal strain can not be sinusoidal.

10.1. A simple frictional solid model

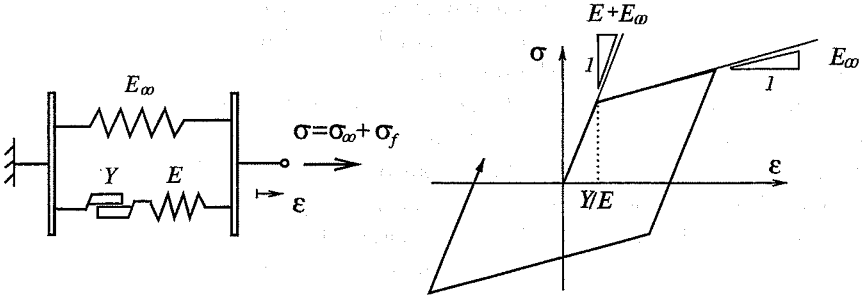

Figure 10.2: *Frictional model including elastic and frictional properties.*

The friction damped solid is represented by the model in Figure 10.2. It is similar to the Zener model with the rate dependent dashpot changed to a rate-independent frictional element. In terms of plasticity theory this is a one-dimensional elastic perfectly plastic model [37].

The hysteresis loop for the total stress, also shown in Figure 10.2, is the sum of the frictional stress shown in Figure 10.3 and the elastic stress (in the spring with the modulus E_∞) i.e.

$$\sigma = \sigma_\infty + \sigma_f.$$

The rectangular hysteresis according to Figure 10.3 is tilted due to the elastic stress $\sigma_\infty = E_\infty \epsilon$ giving the hysteresis shown in Figure 10.2.

The parallelogram-shaped hysteresis loop is the same for different kinds of periodic strain excitation with the same amplitude. That is, a sine, sawtooth or square shaped periodic function yields the same response, regardless of the frequency, if the amplitude is the same. This is in accordance with the experimental results shown previously cf. Figure 8.10.

10.1.1. Stress response for the basic element

The rate-independent damping is symbolized by two blocks with sliding friction that is fully developed when the stress in the element reaches $\sigma_f = Y$. The stress-strain relationship for the basic element, according to Figure 10.3, must be evaluated for increments of strain and stress. Strain is a sum of elastic and (frictional) plastic strain $\epsilon = \epsilon^e + \epsilon^p$.

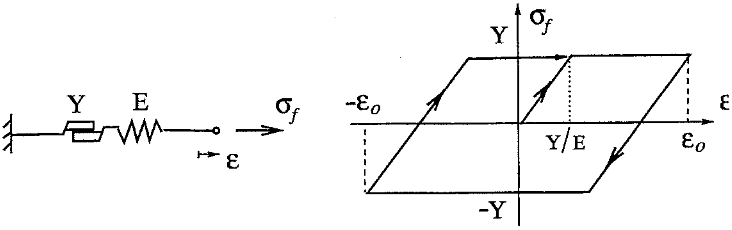

Figure 10.3: *Frictional stress in the simple model.*

To obtain an algorithm an incremental relation given by

$$\Delta\epsilon = \Delta\epsilon^e + \Delta\epsilon^p$$

is employed. The task is to find the stress increment $\Delta\sigma_f$. It can be derived from the elastic part, because the stress is the same in the elastic and the frictional element giving $\sigma_f = E\,\epsilon^e$. Hence, the stress increment can always be expressed as

$$\Delta\sigma_f = E\Delta\epsilon^e$$

A trial stress is determined from the assumption that the strain increment is purely elastic. Suppose that the current stress σ_f is known. The trial stress is then

$$\sigma^{trial} = \sigma_f + E\Delta\epsilon\ .$$

The total stress is limited to $-Y < \sigma_f < Y$; this condition is tested for each increment. If the trial stress σ^{trial} is larger than the yield stress, then at least a part of the strain increment is plastic. Eventually we have $\Delta\epsilon^e = 0$, if the strain increment is purely plastic. We get the condition

$$if \quad | \sigma^{trial} | > Y \quad then \quad \sigma_f = \pm Y\ . \tag{10.1}$$

Hence, the stress has to be scaled back to $\sigma_f = \pm Y$ if the condition (10.1) is fulfilled. A scale factor $\alpha = Y/\sigma^{trial}$ is introduced and the stress is consequently obtained as $\sigma_f = \alpha\sigma^{trial}$. If the condition (10.1) is not fulfilled then we have a purely elastic stress and $\sigma = \sigma^{trial}$ i.e. the strain increment is elastic.

The algorithm for determining the stress can now be written

```
$i = 1, 2, 3...$
    $\Delta\epsilon = \epsilon^{i+1} - \epsilon^i$
    $\sigma^{trial} = \sigma_f^i + E\Delta\epsilon$
    $\alpha = Y/\sigma^{trial}$
    $if\ \ \alpha > 1\ \ then\ \ \alpha = 1$
    $\sigma_f^{i+1} = \alpha\sigma^{trial}$
```

10.1.2. Dynamic modulus and damping

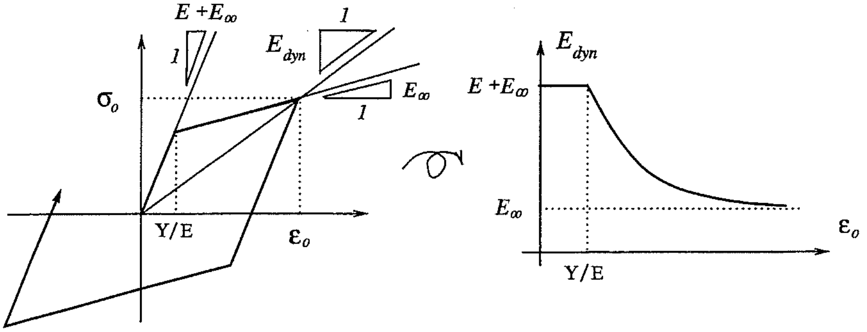

Figure 10.4: *Amplitude dependence in the simple frictional model.*

The amplitude dependence of the simple frictional model is illustrated in Figure 10.4. Maximum stress and maximum strain occur simultaneously, and the dynamic modulus is calculated at this point as $E_{dyn} = \sigma_0/\epsilon_0$. If the strain amplitude is below the yield limit $\epsilon_s = Y/E$, the model is fully elastic with a constant modulus $E + E_\infty$. When strain amplitude exceeds the yield limit, we have $\sigma_0 = Y + E_\infty\epsilon_0$ and the dynamic modulus decreases with the inverse of amplitude according to

$$E_{dyn} = \frac{\sigma_0}{\epsilon_0} = E_\infty + \frac{Y}{\epsilon_0} \qquad \epsilon_0 > \epsilon_s\ . \tag{10.2}$$

In order to determine the damping, the definition (8.1) discussed in Chapter 8 will be used. The damping can be determined from the area enclosed in one cycle. This area is the same for the basic element and it is simpler to determine that area (cf. Figure 10.3).

We have to look at two cases. If the strain amplitude is below the yield strain then the area enclosed is zero and the damping $d = 0$. Otherwise, the area is $U_c = 4Y(\epsilon_0 - \epsilon_s)$ and the stress amplitude is $\sigma_0 = Y + E_\infty\epsilon_0$. The damping given by the normalized dissipated energy (8.1) in each cycle is thus given by

$$d = \frac{4}{\pi}\frac{\epsilon_0 - \epsilon_s}{(1 + E_\infty\epsilon_0/Y)\epsilon_0} \qquad \epsilon_0 > \epsilon_s\ .$$

Introducing the normalized strain $\alpha = \epsilon_0/\epsilon_s$ yields the expressions

$$\frac{E_{dyn}}{E_\infty} = 1 + \frac{E}{E_\infty}\frac{1}{\alpha} \qquad \text{and} \qquad d = \frac{4(\alpha - 1)}{\pi(1 + \frac{E_\infty}{E}\alpha)\alpha}$$

for $\epsilon_0 > \epsilon_s = Y/E$. If the quotient $h = E/E_\infty$ is also introduced as a parameter, the expressions can be illustrated according to Figure 10.5 for different values of h. A value $h = 1$ corresponds to a 50% reduction of the modulus.

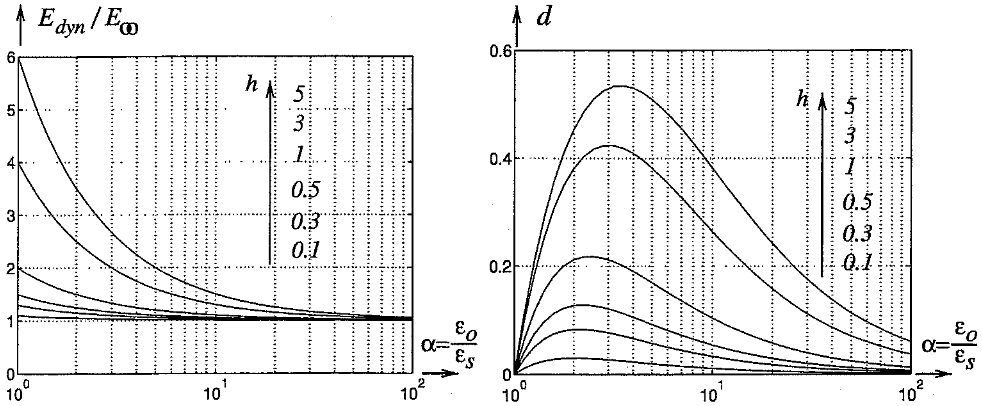

Figure 10.5: *Amplitude dependence of dynamic modulus and damping in the simple frictional solid model.*

10.2. Generalized frictional solid model

Including more frictional elements yields a model according to Figure 10.1.

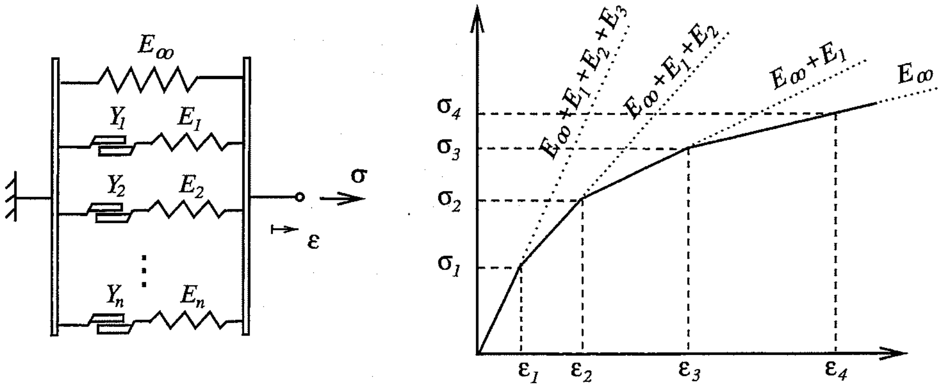

Figure 10.6: *The generalized frictional solid model and corresponding initial loading curve.*

The model parameters can be obtained from the initial loading curve. It is a piecewise linear curve according to Figure 10.6. The elements are assumed to yield in the order $1, 2, ..n$ i.e. from above in Figure 10.6, and a particular break point means that limit load has been reached in one element. The parameters are determined directly from

$$E_i = \frac{\sigma_i - \sigma_{i-1}}{\epsilon_i - \epsilon_{i-1}} - \frac{\sigma_{i+1} - \sigma_i}{\epsilon_{i+1} - \epsilon_i} \qquad \text{and} \qquad Y_i = E_i \epsilon_i \; . \tag{10.3}$$

The inverse relation, i.e. the break points obtained from the model parameters, is given by

$$\epsilon_i = \frac{Y_i}{E_i} \qquad \text{and} \qquad \sigma_i = \sum_{k=1}^{i-1} E_k \epsilon_k + (E_\infty + \sum_{k=i}^{n} E_k)\,\epsilon_i$$

where it is assumed that the first sum vanishes if $i = 1$.

The dynamic modulus for the generalized model is also found directly from the loading curve. Values of the dynamic modulus for amplitudes corresponding to the break point strains are

$$E^i_{dyn} = \frac{\sigma_i}{\epsilon_i}. \tag{10.4}$$

Damping for strain amplitudes corresponding to the break point strains can be calculated by summing the enclosed areas for the frictional elements that have yielded at the particular strain amplitude and using definition (8.1).

The generalized model has been implemented in MATLAB [36] for evaluation of general strain histories for an arbitrary number of frictional elements. The algorithm in subsection 10.1.1 was used for each of the frictional elements.

10.3. Fit to quasi-static experiments

The generalized model was fitted to the quasi-static experiments in simple shear described in Chapter 8 in order to show the frictional character of damping in filled rubbers at low frequencies. The experimental hysteresis loops were almost independent of the frequency variation for the three frequencies $f = 0.01, 0.05$ and $0.1\ Hz$. This indicates that a major part of the damping has a frictional origin at low strain rates. The amplitudes tested were $\kappa_0 = 0.1$, 0.3 and 0.5 for a pre-strain of $\kappa_s = 0.5$.

A generalized frictional model according to Figure 10.6 with three frictional elements was fitted to the experiment in order to show the model's ability to capture hysteresis and stiffness.

The model is simply fitted to the loading curve up to $\kappa = 0.5$ and the model is obtained directly according to the previous discussion. The parameters are

$$G = 0.7 \qquad G_i = [\,0.778 \;\; 0.185 \;\; 0.174\,] \qquad Y_i = [\,0.0211 \;\; 0.0124 \;\; 0.0235\,] \tag{10.5}$$

with values in MPa. Figure 10.7 shows the model compared to experiments. It can be seen that the shapes of the hysteresis loops with the sharp edges, the stiffnesses and the enclosed areas is modeled with good accuracy.

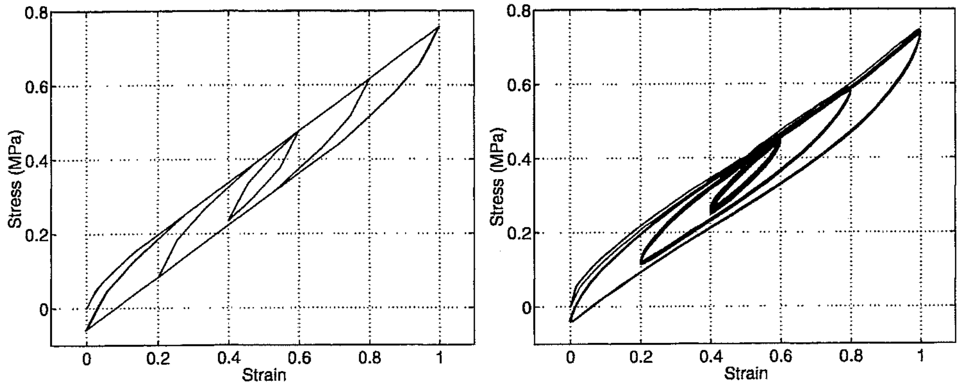

Figure 10.7: *The generalized frictional model fitted to loading curve compared to quasi-static experiments at* $f = 0.05$ *Hz. Left: Model. Right: Experiments.*

10.4. Fit to stationary dynamic experiments

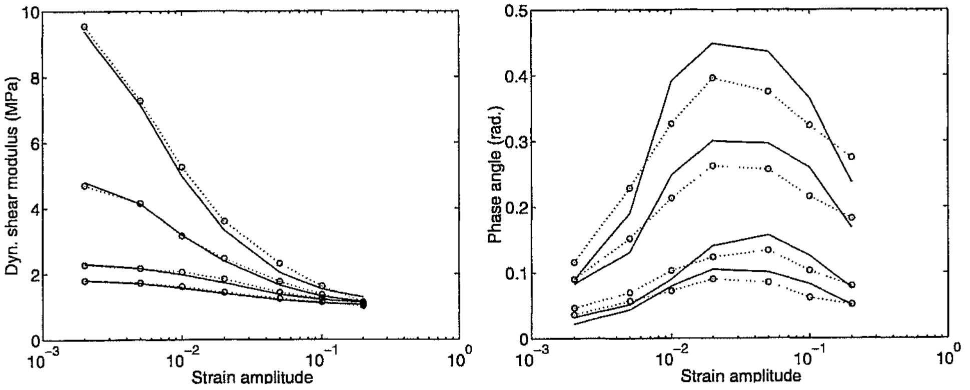

Figure 10.8: *The generalized frictional model fitted to dynamic experiments from Harris and Stevenson.*

The generalized frictional model was also fitted to the steady state dynamic data reported by Harris and Stevenson [25] discussed in Chapter 8 cf. Figure 8.5. We recall that the experimental data reproduced in Figure 8.5 were obtained from simple shear tests carried out on four natural rubbers with different contents of filler.

Four models, each with six frictional elements were fitted. The behavior of the models are shown by solid lines, and the reported measurements are indicated by circles in Figure 10.8). The models were obtained mainly by a direct fit to the dynamic modulus data using (10.4). Some adjustments were made to capture the phase angle correctly. The dynamic moduli and phase angles were derived from harmonic functions fitted to the model responses.

It can be seen that the model captures quantitatively the amplitude dependence of the reported rubbers, with various degree of filler. The overall behavior is in good agreement with the experiments, although it can be seen that the phase angle predicted by the model is in general a bit too large.

Six elements were chosen for simplicity, and no attempts were made to optimize the number of elements. Models with fewer elements can be used (will be shown in Chapter 11), although more work is required to fit of the models. The purpose here was to show the general capability to capture the amplitude dependence.

10.5. Summary

Frictional (elasto-plastic) one-dimensional models were shown to give a good representation of filled rubbers under cyclic loading. The amplitude dependence of the dynamic modulus and the phase angle for the simple frictional model are schematically shown in Figure 10.9. The qualitative behavior is in accordance with experiments on filled rubbers. However, a generalized model was needed in order to make quantitative fits.

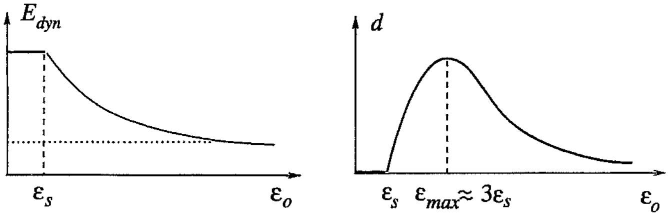

Figure 10.9: *Amplitude dependence of the dynamic modulus and phase angle for the simple frictional model.*

The generalized model was fitted with good accuracy to quasi-static experiments in simple shear described in Chapter 8. It was also shown that this model could fit the amplitude dependence of the dynamic modulus and phase angle for steady state dynamic data reported by Harris and Stevenson [25].

11. COMBINED VISCOUS AND FRICTIONAL MODELS

The discussion in the previous chapters focused on two sources of damping in filled rubbers, namely viscous damping in the rubber base and frictional damping in the rubber-carbon and carbon-carbon interfaces. The total damping stress is here assumed to be the sum of the viscous and the frictional stresses. Hence, in terms of rheological models, the viscous and frictional elements should be connected in parallel. The purpose here is to check this assumption for quasi-static and steady state dynamic load cases.

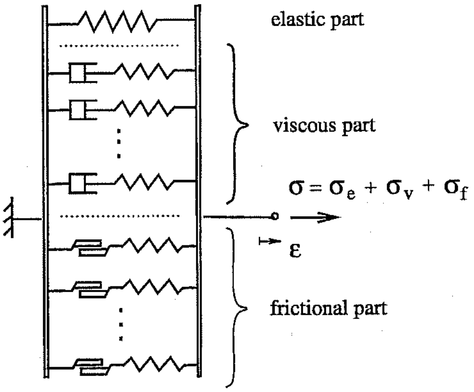

Figure 11.1: *One-dimensional rheologic model including elastic, viscous, and friction properties.*

The experimental observations presented in Chapter 8 indicated that the amplitude and frequency dependence of the dynamic shear modulus were almost independent of each other, support the assumption.

Connecting the Zener model and the simple frictional model in parallel yields a physically reasonable representation of damping in filled rubbers, supported by micro mechanical behavior and experimental observations. This yields a five parameter model that will be fitted to the stationary dynamic experiments described earlier.

However, in order to obtain better fit to experiments, a generalization according to Figure 11.1 is required. Several viscous elements make it possible to conduct a fit of the dynamic modulus to a wider frequency range, or in the time range, fit the relaxation behavior over a wider time range. Likewise, several frictional elements make it possible to closely fit the amplitude dependence for large variations in amplitude. Moreover, according to the previous discussion, frequency and amplitude dependence can be fitted separately.

The generalized model has been implemented in MATLAB [36] for evaluation of general strain histories for an arbitrary number of frictional and viscous elements.

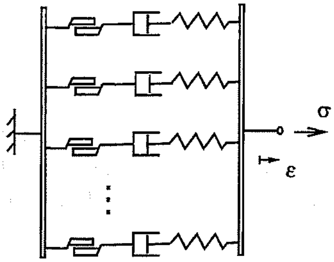

Figure 11.2: *Rheologic model with interrelated elastic, viscous, and frictional properties.*

11.1. Previous work

One-dimensional models of the type described here have been used as discrete models of dampers often described in terms of a force and displacement relationship, i.e. with structural and material properties mixed. A general model according to Figure 11.2 was proposed by Kümmlee [32]. He used it to model a cylindrical torsional shaft coupling for wide temperature, frequency, and torsional amplitude ranges. For these wide ranges of frequency and amplitude he found it necessary to use the general model in Figure 11.2. Kümmlee also mentions the model used here, shown in Figure 11.1, and attributes it to Japs [29].

Similar models have been used for example in vehicle dynamics or earthquake protection applications. Berg [7] has proposed a five-parameter rubber spring model with elastic, frictional and viscous forces in parallel, for dynamic analysis of rail vehicles.

11.2. Fit of the combined model to experiments.

The model in Chapter 10, obtained from quasi-static data, will be extended to rate-dependent effects, and it will be shown that the model in Figure 11.1 can be made to fit both quasi-static and steady-state dynamic experimental data to a reasonable engineering accuracy.

The fitting procedure is performed independently for the elastic, viscous and frictional part. The stress expression with additive stresses

$$\sigma = \sigma_e + \sigma_f + \sigma_v$$

is the basis for the fitting procedure.

11.2.1. Fit to quasi-static experimental data

The quasi-static model will be fitted to the relaxation test described in Chapter 8 and compared to the other quasi-static tests described in the same chapter. The experiments were, apart from the relaxation test for different strain steps, a test with harmonic straining for different amplitudes at $0.05Hz$, and a test with a triangular shaped periodic strain that was compared with a harmonic test with the same amplitude.

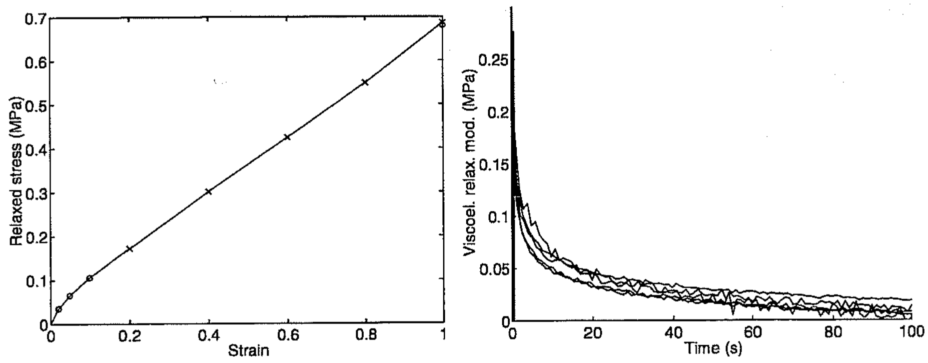

Figure 11.3: *Left: The relaxed loading curve, without viscoelastic contribution. Right: The viscoelastic relaxation modulus, i.e. viscoelastic stress only.*

Quasi-static parameters can be fitted according to the following procedure.

- Obtain an experimental loading curve for sufficiently low strain rate. This eliminates the viscous stresses. The rate-independent part of the model is then obtained by a fit to the loading curve, see Figure 11.3 (left). Model parameters for $\sigma_e + \sigma_f$ are determined.
- Conduct a relaxation test and subtract the elasto-plastic model response obtained by parameters determined from the loading curve. Fit the viscous part of the model to $\sigma_{exp} - (\sigma_e + \sigma_f)$, see Figure 11.3 (right). Model parameters for σ_v are thereby determined and the complete model is thus determined.

The relaxation tests described in Chapter 8 were used to derive model parameters for the combined viscous and frictional model. The parameters in the frictional part were derived from the relaxed stress values in the strain interval 0.2 to 1.0 and in the interval 0 to 0.2 from the loading curve in slow quasi-static loading. The resulting relaxed loading curve is shown in Figure 11.3 (left diagram). The 100s relaxed stress values are shown with crosses.

The frictional model parameters were determined from the loading curve according to (10.3). The points used are marked as circles on the loading curve in Figure 11.3. The viscoelastic parameters were determined from a fit to the normalized relaxation curve in Figure 11.3, where the elasto-plastic part is separated according to the previously outlined procedure. The model parameters are

$$\begin{aligned} &G_\infty = 0.645\ MPa \\ &G_{fi} = [\,0.778\ \ 0.185\ \ 0.174\,]\ MPa \qquad Y_i = [\,0.0156\ \ 0.0092\ \ 0.0174\,]\ MPa \qquad (11.1) \\ &G_{vi} = [\,0.503\ \ 0.0671\ \ 0.0839\,]\ MPa \quad t_{ri} = [\,0.1\ \ 2\ \ 30\,]\ s \end{aligned}$$

Figure 11.4 shows the model behavior compared to the relaxation test, which is the basis for the fit of the model. The diagram to the left shows relaxation shear data for the total time (i.e. 100s) compared to the model according to (11.1), and the diagram to the right shows the same data for the first 10s compared to the model. Figure 11.4 readily shows the ability to model the step size dependent relaxation behavior of carbon-black filled rubbers.

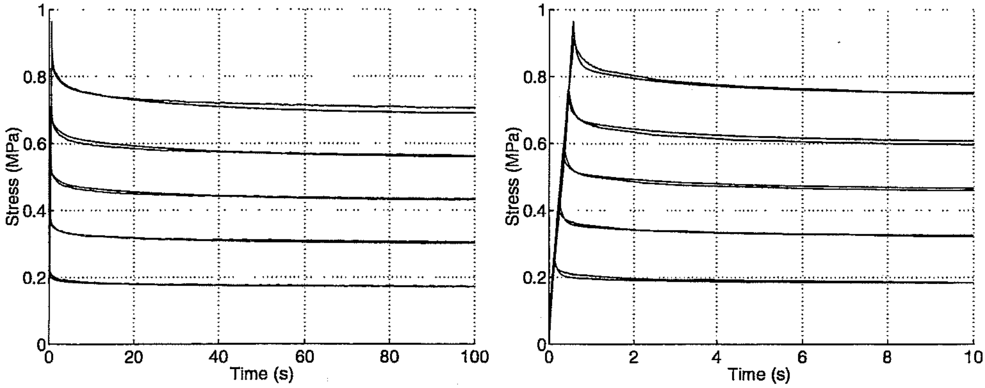

Figure 11.4: *Comparison of model behavior and test for relaxation in shear. Strain steps: [0.2 0.4 0.6 0.8 1.0]. Left: Relaxation stress, 100s. Right: A closer view of the first 10s.*

The model obtained from relaxation data, according to (11.1) was compared to the quasi-static harmonic loading shown in Figure 11.5. Although this is a completely different loading case, the model quite accurately captures the essential features of the material behavior.

The model (11.1) was also compared to the shape sensitivity test. Figure 11.6 shows the model behavior compared to experiments. It can be seen that both the model and the experimental data are insensitive to the shape of shear strain history, i.e. a triangular and a sinusoidal strain history yields similar hysteresis loops. This is a feature of the rate independent models discussed in Chapter 10, which yielded complete insensivity. The small differenses in the model behavior shown here is attributed to the viscoelastic part.

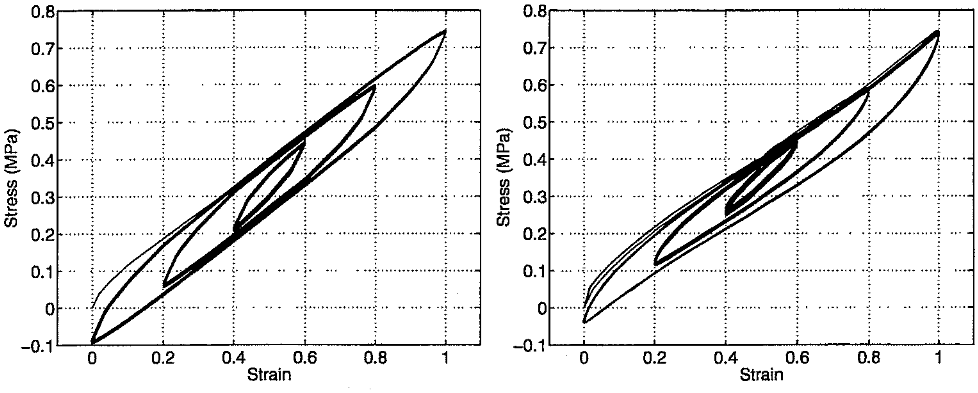

Figure 11.5: *Comparison of model behavior and test for quasi-static harmonic shear at 0.05 Hz. Strain amplitudes: [0.1 0.3 0.5]. Left: Model. Right: Experiments.*

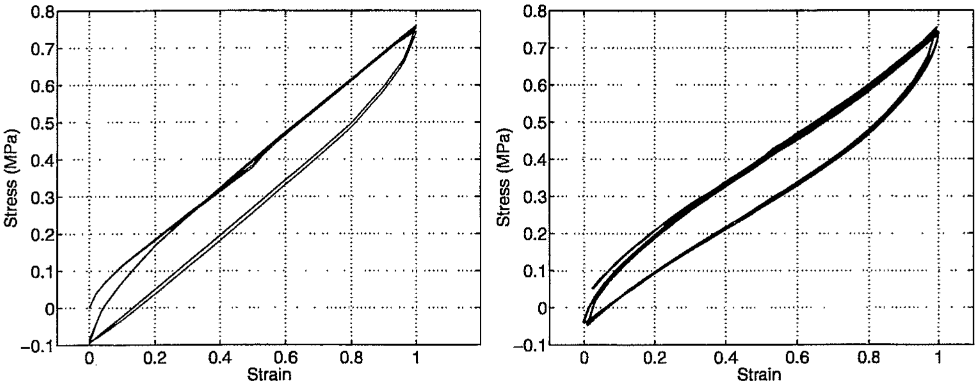

Figure 11.6: *Test of shape sensitivity. Comparison of model behavior and test for quasi-static harmonic and triangular shear strain at 0.05 Hz. Left: Model. Right: Experiments.*

11.2.2. Fit to steady-state harmonic experimental data

The contributions to the dynamic modulus in the complex plane including the frictional contribution can be approximately represented by the basic Fourier component of the response as an equivalent complex modulus. This yields an interpretation of the total dynamic modulus illustrated in Figure 11.7.

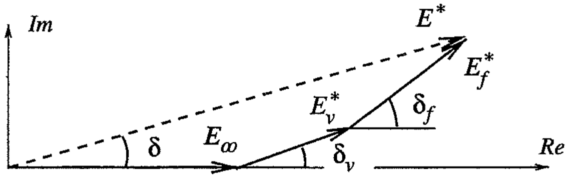

Figure 11.7: *The equivalent complex modulus including elastic, viscous, and frictional contributions.*

The dynamic modulus $E_{dyn} = \mid E^* \mid$ is the length of the vector in the complex plane, and the normalized damping d is approximately the angle. For reasonable values of damping corresponding to, say, $\delta < 0.4$, we can use the approximation $sin\,\delta \approx tan\,\delta \approx \delta$ and $cos\,\delta = 1$. The dynamic modulus is approximately the sum of the elastic, viscous and frictional modulus,

$$E_{dyn} \approx E_\infty + E^f_{dyn}(\epsilon_0) + E^v_{dyn}(\omega) \ ,$$

i.e. the total dynamic modulus is the sum of the constant elastic modulus, the frequency dependent viscous modulus and the amplitude dependent frictional modulus. The damping is also found approximately from Figure 11.7 as

$$d \approx (E^v_{dyn} d_v + E^f_{dyn} d_f)/E_{dyn} \ ,$$

i.e. the total normalized damping can be expressed as a weighted sum of the viscous and frictional damping.

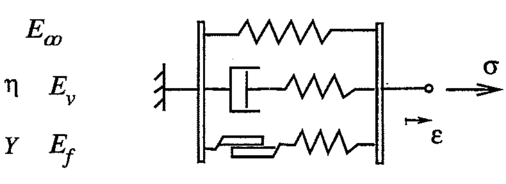

Figure 11.8: *Five-parameter model including elastic, viscous, and frictional properties.*

Fitting procedure for the five-parameter model

A fitting procedure will be outlined for the five-parameter model in Figure 11.8. For this model we can express frictional and viscous contributions as

$$E^f_{dyn}(\epsilon_0) = E_f \frac{\epsilon_s}{\epsilon_0} \quad \text{and} \quad E^v_{dyn}(\omega) = E_v \frac{\omega t_r}{\sqrt{1+(\omega t_r)^2}}, \tag{11.2}$$

obtained from (10.2) and (9.17) respectively, with $\epsilon_s = Y/E_f$ and $t_r = \eta/E_v$. The parameters are obtained in the following order: the static parameter first, then the amplitude dependence and last the frequency dependence.

1)

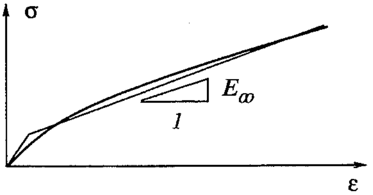

Figure 11.9: *The elastic part of the five-parameter model.*

1. The first concern is to get the static level correct. This is done by determining E_∞ from the loading curve according to Figure 11.9.

2)

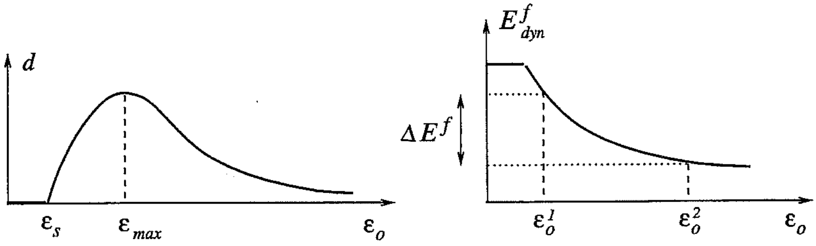

Figure 11.10: *The frictional part of the five-parameter model.*

2. The two parameters that control the amplitude dependence is the second concern (cf. Figure 11.10). The yield limit ϵ_s is chosen so that the shape of the normalized damping curve corresponds to the experimentally obtained curve. The maximum damping for the five-parameter model occurs for $\epsilon_{max} \approx 3\epsilon_s$ according to Figure 10.9. The change in dynamic modulus due to the amplitude dependence, cf. (11.2), is

$$\Delta E^f_{exp} = E_f \epsilon_s (1/\epsilon^1_0 - 1/\epsilon^2_0)$$

where the strain range used in the fit is given by ϵ^1_0 and ϵ^2_0, and ΔE^f_{exp} is the experimentally obtained change in modulus. This determines E_f.

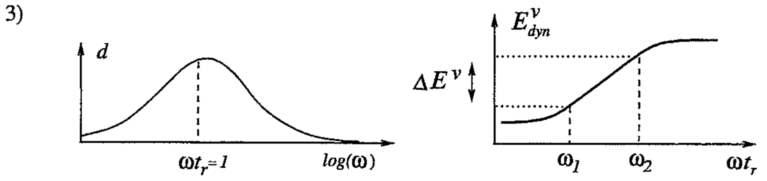

Figure 11.11: *The viscous part of the five-parameter model.*

3. Finally the two parameters that control the frequency dependence are determined (cf. Figure 11.11). The relaxation time t_r is obtained from the shape of the experimental normalized damping curve. The maximum damping for the model occurs for $\omega t_r \approx 1$. The change in dynamic modulus due to frequency, cf. (11.2), is

$$\Delta E^v_{exp} = E_v\left(\frac{\omega_2}{\sqrt{1+(\omega_2 t_r)^2}} - \frac{\omega_1}{\sqrt{1+(\omega_1 t_r)^2}}\right)t_r$$

   where ω_1 and ω_2 is the frequency range, and ΔE^v_{exp} is the experimentally obtained change in modulus. This determines E_v.

The procedure was applied to the experimental data for the steady state harmonic experiments described in Chapter 8, giving the parameters

$$\begin{aligned} &G_\infty = 0.90\ MPa \\ &G_f = 1.15\ MPa \quad Y = 0.0184\ MPa \\ &G_v = 0.52\ MPa \quad t_r = 0.013s. \end{aligned} \tag{11.3}$$

Figures 11.12 and 11.13 show the frequency and amplitude dependence of dynamic modulus and phase angle compared to experiments. The model is shown by solid lines and the measured data are shown with circles connected by dotted lines. The dynamic modulus and phase angle of the model and the experiments were derived by fitting a harmonic function to the response. The dynamic modulus and phase angle were then derived from the fitted harmonic function. From the figures it can be seen that the dynamic modulus is accurately described by the model, while the phase is less accurately captured.

The model behavior with regard to the phase angle could be improved if one more frictional element was used. This was shown for completely rate independent models in Chapter 10. However, the purpose here was to show that steady state dynamic behavior can be modeled quite accurately with a limited number of constants.

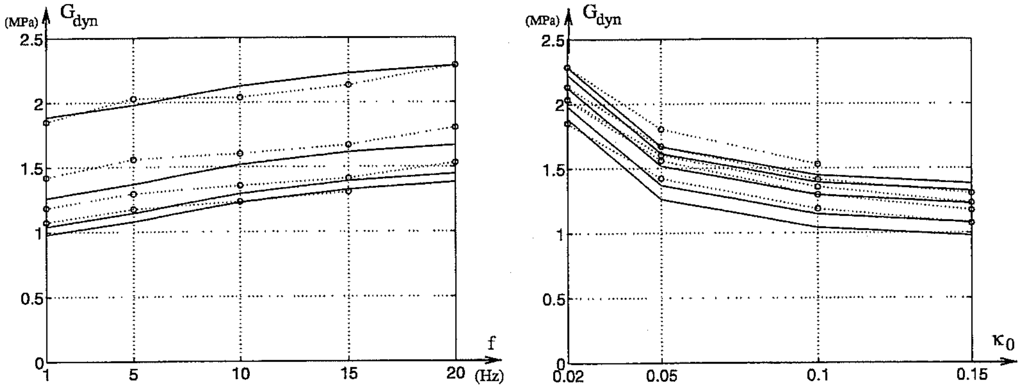

Figure 11.12: *Five-parameter model: Fit of the frequency (f) and amplitude (κ_0) dependence of the dynamic shear modulus. Solid lines: Model. Circles: Experimental data.*

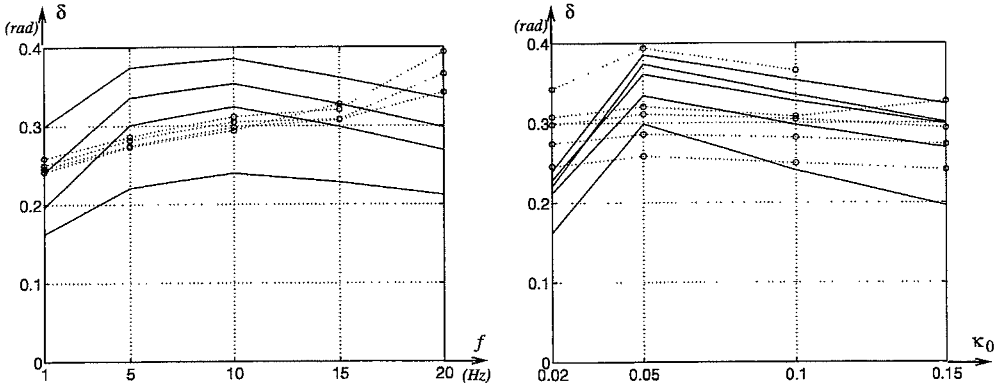

Figure 11.13: *Five-parameter model: Fit of the frequency (f) and amplitude (κ_0) dependence of the phase angle in shear. Solid lines: Model. Circles: Experimental data.*

11.3. Summary

It was shown that a combination of rate-independent and rate-dependent damping is needed to account for the inelastic effects present in carbon-black filled rubbers. The one-dimensional model used here is a model with viscoelastic and elasto-plastic stress contributions added. Step-size dependent relaxation modulus and amplitude dependent dynamic modulus are properties of the model.

The model was compared to quasi-static and dynamic experiments, and fitting procedures for quasi-static and dynamic experiments were discussed.

The quasi-static model was obtained from relaxation test data, and this model was compared to experiments with periodic loading of different amplitudes and shape of the strain history. The model was shown to agree well with the experiments obtained in simple shear.

A model with only five parameters was fitted to stationary dynamic data, and it was shown to model the frequency and amplitude dependence of the dynamic modulus well, while the phase angle was not so well fitted although it is of the right size.

12. MULTIAXIAL LARGE STRAIN VISCOELASTIC MODELS

The constitutive theory for a visco-hyperelastic incompressible solid is briefly outlined here, and evaluated for simple shear and compression/tension. The theory is based on linear viscoelasticity, given by the convolution integral expression (9.1), to allow for large deformations.

The strain energy density is also essential in large strain viscoelastic analysis. In three-dimensional constitutive models, that allow for large viscoelastic strains, the elastic part is modeled as hyperelastic.

Two versions of these constitutive theories are implemented in finite element codes. One is intended for large strain transient analysis and one for small vibrations superimposed on a large hyperelastic deformation. Visco-hyper-elastic formulations are implemented in the finite element codes ABAQUS and MARC. In ABAQUS, the small vibration model is based on the work of Morman [40], and for the arbitrary large strain formulation Simo [54] is referenced.

12.1. A large strain visco-hyperelastic model

The visco-hyperelastic large strain constitutive model implemented in ABAQUS [26] will be stated and evaluated here for the incompressible case. The model is given in terms of Kirchoff stress, which is equivalent to Cauchy stress for complete incompressibility. Hence, the Cauchy stress tensor $\boldsymbol{\sigma}$ ("true stress") for this constitutive model is given by

$$\boldsymbol{\sigma} = \boldsymbol{s}^e - \sum_{i=1}^{N} \boldsymbol{s}_i^{ve} + p\boldsymbol{I} \tag{12.1}$$

where $\boldsymbol{s}^e$ is the instantaneous hyperelastic deviatoric stress tensor, $\boldsymbol{s}_i^{ve}$ the i'th viscoelastic deviatoric stress tensor, $\boldsymbol{I}$ the unit tensor, and

$$p = (\sigma_{11} + \sigma_{22} + \sigma_{33})/3$$

is the hydrostatic pressure. (Note that p is an independent variable due to incompressibility.) The instantaneous hyperelastic deviatoric stress tensor is given by

$$\boldsymbol{s}^e = 2(\frac{\partial W_0}{\partial I_1} + I_1\frac{\partial W_0}{\partial I_2})\mathbf{B} - 2\frac{\partial W_0}{\partial I_2}\mathbf{B}^2$$

where W_0 is the instantaneous strain energy density, I_1 and I_2 are the invariants of $\boldsymbol{B} = \boldsymbol{F}\boldsymbol{F}^T$, with $\boldsymbol{F}$ being the deformation gradient (cf. Appendix). The i'th viscoelastic deviatoric stress tensor s_i^{ve} is given by

$$s_i^{ve} = \frac{g_i}{t_{ri}} \int_0^t e^{-s/t_{ri}} sym\{\boldsymbol{K}(t-s)\} ds$$

where $sym\{\cdot\}$ is the symmetric part of the tensor inside the brackets and the function $\mathbf{K}$ is given by

$$\boldsymbol{K}(t-s) = \boldsymbol{F}_t(t-s)^{-1} s^e(t-s) \boldsymbol{F}_t(t-s). \tag{12.2}$$

The normalized moduli g_i and the relaxation times t_{ri} define the viscous behavior. Further, $\boldsymbol{F}_t(t-s)$ is the relative deformation tensor defined by

$$\boldsymbol{F}_t(t-s) = \boldsymbol{F}(t-s)\boldsymbol{F}^{-1}(t) \ .$$

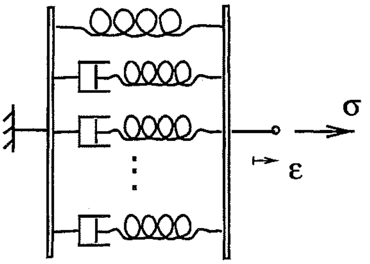

Figure 12.1: *Nonlinear elastic one-dimensional rheologic analog to the large strain viscoelastic constitutive theory.*

An intuitive understanding of this visco-hyperelastic constitutive theory can be gained from the equivalent one-dimensional rheological model, according to Figure 12.1, composed of nonlinear elastic springs and viscous dashpots. The stresses in the viscous elements correspond to the stress components s_i^{ve} in (12.1), and the stress in the spring not connected to a dashpot corresponds to the long-term hyperelastic stress. The model shows an instantaneous and long-term nonlinear elastic response similar to the standard linear solid model discussed in Chapter 9. The main difference, compared to the standard linear solid model, is that it allows for nonlinearity of the elastic response.

The similarity to the standard linear solid model unfortunately also holds for the drawbacks found earlier in viscoelastic modeling of the behavior of filled rubbers. The step size and amplitude dependence observed experimentally, according to Chapter 8, can not be represented by this constitutive theory. Hence, the theory is better suited to fit the behavior of unfilled elastomers.

12.2. Principal directions

States of deformation with fixed principal directions are used in testing of elastomers. The constitutive model will be specialized accordingly in this section.

The state of strain in principal directions is obtained from the deformation gradient (derived in the Appendix) i.e.

$$\mathbf{F}(t) = \begin{bmatrix} \lambda_1(t) & 0 & 0 \\ 0 & \lambda_2(t) & 0 \\ 0 & 0 & \lambda_3(t) \end{bmatrix}$$

giving an expression for $\mathbf{K}$ in (12.2) that is diagonal, and explicitly of the form

$$\boldsymbol{K}(t-s) = sym\{\boldsymbol{F}_t(t-s)^{-1}\boldsymbol{s}^e(t-s)\boldsymbol{F}_t(t-s)\} = \boldsymbol{s}^e(t-s)\ .$$

Hence, the Cauchy stress is given by

$$\boldsymbol{\sigma}(t) = \boldsymbol{s}^e(t) - \sum_{i=1}^{N} \frac{g_i}{t_{ri}} \int_0^t e^{-s/t_{ri}} \boldsymbol{s}^e(t-s)ds + p\boldsymbol{I}\ .$$

Eliminating the pressure in accordance with Rivlins relations (3.8), yields

$$\sigma_i(t) - \sigma_j(t) = s_i^e(t) - s_j^e(t) - \sum_{i=1}^{N} \frac{g_i}{t_{ri}} \int_0^t e^{-s/t_{ri}}(s_i^e(t-s) - s_j^e(t-s))ds \qquad (12.3)$$

with

$$s_i^e(t) - s_j^e(t) = 2(\frac{\partial W_0}{\partial I_1} + \lambda_k^2 \frac{\partial W_0}{\partial I_2})(\lambda_i^2 - \lambda_j^2)$$

The integers i, j, k are combinations of $1, 2, 3$. Relations for pure shear, equibiaxial strain, etc. found in Chapter 4 can be derived from (12.3) in a similar manner for this visco-hyperelastic theory.

12.3. Evaluation of uniaxial stress

The expression for principal directions (12.3) is specialized here to compression/tension.

The state of stress and strain is according to

$$\sigma_1 = \sigma = P\lambda/A, \quad \sigma_2 = \sigma_3 = 0 \quad \text{and} \quad \lambda_1 = \lambda, \quad \lambda_2 = \lambda_3 = 1/\sqrt{\lambda}$$

where P and λ are the force and the stretch in direction one respectively, and A is the undeformed cross section area perpendicular to direction one (cf. Chapter 4).

Using (12.3) yields

$$\sigma(t) = \sigma^e(t) - \sum_{i=1}^{N} \frac{g_i}{t_{ri}} \int_0^t e^{-s/t_{ri}} \sigma^e(t-s)ds$$

where the elastic stress $\sigma^e(t)$ is the Cauchy stress derived in Chapter 4

$$\sigma^e(t) = 2(\frac{\partial W_0}{\partial I_1} + \frac{1}{\lambda}\frac{\partial W_0}{\partial I_2})(\lambda^2 - \frac{1}{\lambda}) . \tag{12.4}$$

The nominal stress becomes

$$P(t)/A = [\sigma^e(t) - \sum_{i=1}^{N} \frac{g_i}{t_{ri}} \int_0^t e^{-s/t_{ri}} \sigma^e(t-s)ds]/\lambda(t) \tag{12.5}$$

i.e. a convolution integral for evaluation of stress history in compression/tension.

12.3.1. Relaxation of the visco-hyperelastic model

The relaxation behavior of the visco-hyperelastic model with one viscoelastic stress component will be derived for uniaxial stress. The model is a nonlinear elastic equivalent to the standard linear solid model. The model is defined by the instantaneous strain energy density $W_0(I_1, I_2)$ and the parameters g and t_r.

Relaxation yields $\lambda(t) = \lambda_0 = const.$ for $t > 0$, and according to (12.4) the relaxation Cauchy stress becomes

$$\sigma_R(t) = \sigma_0^e - \frac{g}{t_r} \int_0^t e^{-s/t_r} \sigma_0^e \, ds \qquad t > 0$$

where

$$\sigma_0^e = 2(\frac{\partial W_0}{\partial I_1} + \frac{1}{\lambda_0}\frac{\partial W_0}{\partial I_2})(\lambda_0^2 - \frac{1}{\lambda_0})$$

is the constant elastic stress. This yields

$$\sigma_R(t) = \sigma_0^e(1 - g(1 - e^{-t/t_r})) \qquad t > 0 . \tag{12.6}$$

The relaxation response according to (12.6) is shown in Figure 12.2, and we find a single relaxation curve if the stress response is normalized with respect to the initial elastic response.

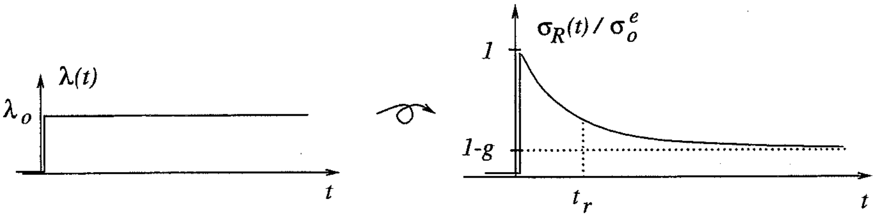

Figure 12.2: *Relaxation response for the visco-hyperelastic model in uniaxial stress.*

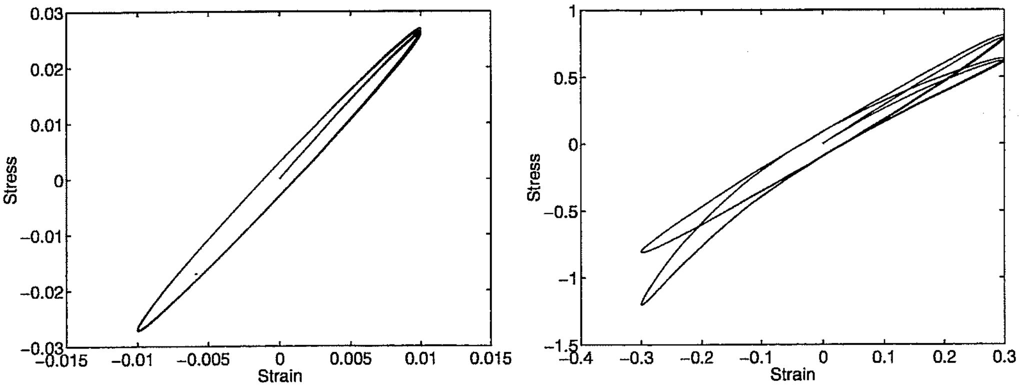

Figure 12.3: *Comparison of the linear Zener model and the visco-hyperelastic Neo-Hooke model in uniaxial stress for sinusoidal shear strain at 1Hz. Left: Small strain amplitude (1%). Right: Large strain amplitude (30%).*

12.3.2. Numeric evaluation for general strain histories

The convolution integral expression (12.5) was evaluated numerically by a convolution integral routine in MATLAB [36]. This routine enables evaluation for general strain histories. A sinusoidal strain history is studied here.

A Neo-Hooke based visco-hyperelastic model with parameters

$$C_{10}^{0} = 0.5MPa \qquad g = 0.2 \qquad t_r = 0.15s$$

was compared with a linear Zener model for sinusoidal strain at 1Hz, with a set of corresponding parameters, i.e. $E_\infty = 2.4MPa$, $E = 0.6MPa$, and $\eta = 0.09MPas$.

The behavior for small strains is almost identical to the behavior of the linear viscoelastic Zener model. For large strains the nonlinearity in the elastic behavior of the Neo-Hooke based model is seen in Figure 12.3.

12.4. Evaluation of simple shear

In order to further evaluate the constitutive model simple shear will also be considered.

The state of strain in simple shear is obtained from the deformation gradient (derived in the Appendix) given by

$$\mathbf{F}(t) = \begin{bmatrix} 1 & 0 & \kappa(t) \\ 0 & 1 & 0 \\ 0 & 0 & 1 \end{bmatrix} \qquad \mathbf{F}^{-1}(t) = \begin{bmatrix} 1 & 0 & -\kappa(t) \\ 0 & 1 & 0 \\ 0 & 0 & 1 \end{bmatrix}.$$

If the elastic response is derived from a strain energy density, dependent only on the first invariant (e.g. as for the Yeoh model), then the elastic deviatoric response is given by

$$s^e = 2(\frac{\partial W_0}{\partial I_1})\mathbf{B}$$

where the left Cauchy-Green deformation tensor $\mathbf{B}$ now is given by

$$\mathbf{B} = \mathbf{F}\mathbf{F}^T = \begin{bmatrix} 1+\kappa^2 & 0 & \kappa \\ 0 & 1 & 0 \\ \kappa & 0 & 1 \end{bmatrix} . \qquad (12.7)$$

The shear stress s_{13} is found from the deviatoric stress tensor

$$s_{13}(t) = s_{13}^e - \sum_{i=1}^{N} \frac{g_i}{t_{ri}} \int_0^t e^{-s/t_{ri}} sym\{\boldsymbol{F}_t(t-s)^{-1} s^e(t-s) \boldsymbol{F}_t(t-s)\}_{13} ds$$

with

$$\begin{aligned} & sym\{\boldsymbol{F}_t(t-s)^{-1} s^e(t-s)\boldsymbol{F}_t(t-s)\}_{13} = \\ & \tfrac{1}{2}[K_{31}(t-s) + K_{13}(t-s)] = \\ & 2\frac{\partial W_0}{\partial I_1}[\kappa(t-s) + \tfrac{1}{2}\kappa(t-s)(\kappa(t-s) - \kappa(t))\kappa(t)] = \\ & s_{13}^e(t-s)[1 + \tfrac{1}{2}(\kappa(t-s) - \kappa(t))\kappa(t)] \end{aligned}$$

Then if we write $\tau(t) = s_{13}(t)$ the expression for the shear stress as a function of time becomes

$$\tau(t) = \tau^e(t) - \sum_{i=1}^{N} \frac{g_i}{t_{ri}} \int_0^t e^{-s/t_{ri}} \tau^e(t-s)[1 + \frac{1}{2}(\kappa(t-s) - \kappa(t))\kappa(t)] ds \; , \qquad (12.8)$$

i.e. a convolution integral for evaluation of shear stress history in simple shear.

12.4.1. Relaxation of a Neo-Hooke visco-hyperelastic model

The relaxation behavior in simple shear of a Neo-Hooke based model with one viscoelastic stress component will be derived. The model is a nonlinear elastic equivalent to the standard linear solid model and has a one-dimensional representation according to Figure 12.4.

Hence, the model parameters are C_{10}^0, g and t_r and the elastic stress is

$$s^e = 2C_{10}^0 \boldsymbol{B} = G\boldsymbol{B}$$

where G is the shear modulus and $\boldsymbol{B}$ is given by (12.7).

Relaxation yields $\kappa(t) = \kappa_0 = const$ for $t > 0$. The stress in relaxation can, according to (12.8), be expressed as

$$\tau_R(t) = \tau^e(t) - \frac{g}{t_r} \int_0^t e^{-s/t_r} \tau^e(t-s) ds \quad \text{with} \quad \tau^e(t-s) = G\kappa(t-s) = G\kappa_0$$

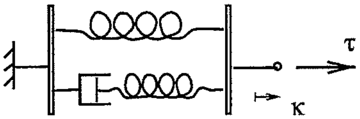

Figure 12.4: *Nonlinear elastic one-dimensional rheologic analog to the Neo-Hooke based viscoelastic model.*

being the constant elastic shear stress at time $t-s$. This yields

$$\tau_R(t) = G\kappa_0 - \frac{g}{t_r}\int_0^t e^{-s/t_r} G\kappa_0 ds = G\kappa_0(1-g(1-e^{-t/t_r})) \qquad t>0\ .$$

Hence we can conclude that it is possible to obtain a relaxation modulus

$$G_R(t) = G(1-g(1-e^{-t/t_r})) \tag{12.9}$$

similar to linear viscoelasticity, for a Neo-Hooke based model in simple shear. The relaxation response according to (12.9) is shown in Figure 12.5.

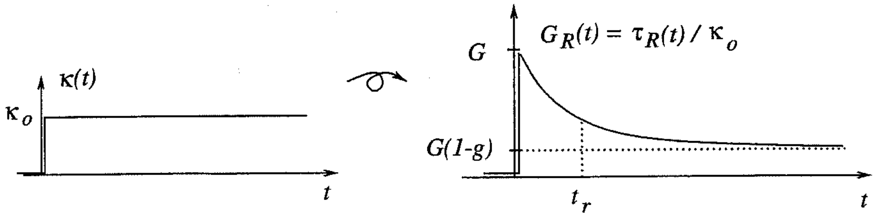

Figure 12.5: *Relaxation response for the Neo-Hooke based viscoelastic model in simple shear.*

12.4.2. Numeric evaluation of a Yeoh visco-hyperelastic model

The convolution integral expression (12.8) has also been implemented in a MATLAB routine for general strain histories, and is here evaluated for a sinusoidal strain history.

A Yeoh based (cf. (3.17)) visco-hyperelastic model is here compared with the linear Zener model for sinusoidal shear strain at $1Hz$. This model contains three hyperelastic parameters, and they were chosen according to

$$C_{10}^0 = 0.5 \quad C_{20}^0 = -0.05 \quad C_{30}^0 = 0.005 \quad (MPa)\ .$$

The initial shear modulus ($G = 2C_{10}^0 = 1MPa$) is the same as for the model illustrated in the uniaxial stress case (cf. Figure 12.3). The viscous parameters are the same as for the Neo-Hooke based model, i.e. $g = 0.2$ and $t_r = 0.15s$.

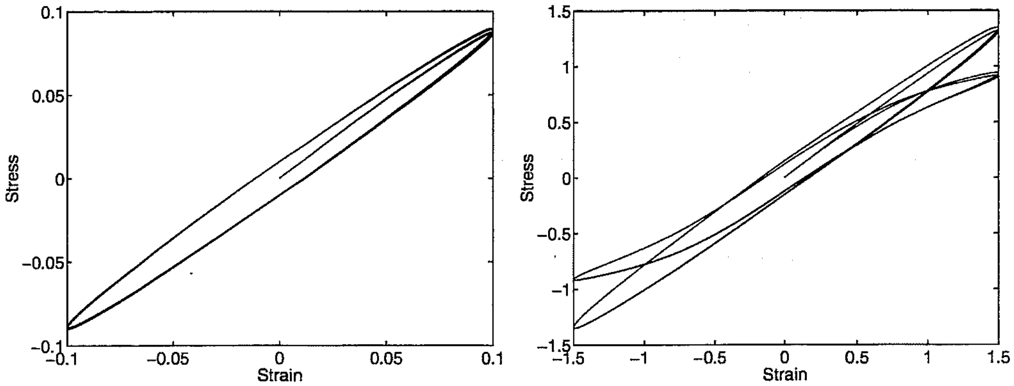

Figure 12.6: *Comparison of (the linear) Zener model and visco-hyperelastic Yeoh model in simple shear for sinusoidal shear strain. Left: Small strain amplitude (10%). Right: Large strain amplitude (150%).*

The model is compared with the linear Zener model with corresponding parameters, i.e. $G_\infty = 0.8MPa$, $G = 0.2MPa$, and $\eta = 0.03MPas$, in Figure 12.6. The figure shows shear stress τ versus shear strain κ according to (12.8).

The behavior for small strains is almost identical to the behavior of the linear viscoelastic Zener model. For large strains the nonlinearity in the elastic behavior of the Yeoh based model is seen in Figure 12.6 (to the right).

12.5. Summary

The nonlinear elastic property of rubber can be incorporated into the concept of viscoelasticity. A visco-hyperelastic large strain constitutive model was examined for uniaxial stress and simple shear. The model was evaluated for step strain and sinusoidal loading.

Similarities and differences compared to linear viscoelasticity were investigated. The behavior of the model is similar to the linear viscoelastic models described in Chapter 9 for small strains, whereas the behavior for large strains is influenced by the nonlinear elasticity included in the model.

13. A MULTIAXIAL VISCOPLASTIC MODEL

Rate-independent damping has been shown to be essential to capture the dynamic behavior of filled rubbers. Viscoelasticity with purely rate-dependent dissipation has been shown to be insufficient. The investigation in the previous chapters concerning the rheological models indicates that a viscoplastic model is more suitable. Such a model will be outlined here and evaluated for complete incompressibility in uniaxial stress and simple shear. The proposed model is a first attempt to model the dynamic behavior of filled rubbers by a multiaxial viscoplastic model, and it is merely a sketch of a possible model that has to be evaluated further. To make a thorough evaluation a finite element implementation is necessary. This is, however, outside the scope of the thesis and intended as future work.

The proposed model is a straightforward generalization of the one-dimensional models discussed previously. The frictional part is modeled for simplicity by Von Mises' ideal elasto-plasticity, although other more sophisticated models could be used.

Elasto-plasticity for large strains is a very involved subject and a lot of theories, using different stress and strain measures, have been proposed. However, there is yet no unified theory that everybody agrees upon when it comes to large strain plasticity. An overview and comparison of some existing theories can be found in [50].

13.1. The fraction model of Besseling

The multiaxial model relies on summing stress contributions obtained from simple constitutive models. This so-called fraction model was originally proposed by Besseling [8]. The basic concept of this model is that the material is thought to be subdivided into a number of parallel fractions, each with simple conventional properties. The more complicated behavior of real materials is approximated by choosing a number of parallel fractions with suitable models and model parameters. The original fraction model described in this section was formulated for small strains, and has been applied to metal plasticity and creep phenomena in metals.

The most general form of the model is a multiaxial version of the one-dimensional model of Kümmlee according to Figure 11.2, and it is a straightforward generalization of this one-dimensional model. In this form each fraction contains elastic, viscous, and plastic small strain components, which are added. However, purely elastic, viscoelastic or elasto-plastic fractions can be used to build specific models.

The one-dimensional models discussed so far are all special versions of the most general fractional model.

In the mathematical description, the total strain in a fraction k is denoted by ϵ which is the same for all fractions. The elastic part of this strain results in stresses σ_k in the fraction k according to Hooke's law, i.e.

$$\sigma_k = C^e \epsilon_k^e,$$

where σ_k is the stress in fraction k, C^e is the elastic moduli tensor, and ϵ_k^e is the elastic strain in fraction k. The total stress is the weighted sum of the stresses in the fractions, i.e.

$$\sigma = \sum_{k=1}^{N} \psi_k \sigma_k, \tag{13.1}$$

where σ is the total stress, ψ_k is the relative volume size of fraction k, and N is the number of fractions.

The total strain rate is divided into elastic, plastic, and viscous parts and the strain rates can therefore be divided according to

$$\dot{\epsilon} = \dot{\epsilon}_k^e + \dot{\epsilon}_k^p + \dot{\epsilon}_k^v,$$

where ϵ is the total strain, ϵ_k^p is the plastic strain in fraction k, and ϵ_k^v is the viscous strain in fraction k.

Several different constitutive models can be obtained by chosing different stress fractions. For example a model with constant kinematic hardening can be obtained by one ideal elasto-plastic fraction in parallel with a purely elastic fraction.

13.2. A fraction model for filled elastomers

Well-established models can be used for the fractions and the same strain is valid for each fraction. Realistic loading and unloading behavior can be obtained from fractions contributing to the total stress by using simple constitutive models for the stress fractions. This approach is consistent with the Prony series representation for the viscoelastic models described in Chapter 12, which can also be regarded as a fraction model.

In the proposed model the stress fractions are divided into viscoelastic and elasto-plastic fractions in analogy with the one-dimensional model according to Figure 11.1. The elasto-plastic stress fractions are here modeled by Von Mises' ideal plasticity analogous to the one-dimensional case. Things are simplified by choosing Von Mises' plasticity for the elasto-plastic fractions. Evaluation of the model and fulfillment of the consistency condition of plasticity are particularly simple in this model. The weights according to (13.1) are here put equal.

Hence, the total Cauchy stress tensor σ is the sum of visco-hyperelastic and elasto-plastic stress contributions

$$\sigma = \sigma^{ve} + \sigma^{ep} . \tag{13.2}$$

The viscous contribution has been discussed in Chapter 12. The viscoelastic part of the stress is given by a sum of fractions

$$\sigma^{ve} = \sum_{j=1}^{M} \sigma_j^{ve} \,.$$

The elasto-plastic contributions to the total stress are, as mentioned, expressed in terms of ideal Von Mises' plasticity, and the elasto-plastic part of the stress is given by a sum of elasto-plastic contributions

$$\sigma^{ep} = \sum_{k=1}^{N} \sigma_k^{ep} \,.$$

The elasto-plastic contributions to the total stress will be discussed next.

13.2.1. The elasto-plastic part

An elasto-plastic Von Mises' model in terms of Jaumann stress rate and the rate of deformation tensor will be used. A discussion of large strain plasticity and this model in particular can be found in [9]. The elasto-plastic stress fractions σ_k^{ep} are determined from the expression (with index k omitted)

$$\overset{\circ}{\boldsymbol{\sigma}} = (\boldsymbol{C}^e - \boldsymbol{C}^p)\boldsymbol{D} - \boldsymbol{\sigma} tr(\boldsymbol{D}) \tag{13.3}$$

where $\overset{\circ}{\boldsymbol{\sigma}}$ is the Jaumann rate of the Cauchy stress, $\boldsymbol{C}^e$ the elastic modulus tensor, $\boldsymbol{C}^p$ the plastic modulus tensor, and $\boldsymbol{D}$ is the rate of deformation tensor. If the stress is in the elastic range the plastic part of $\boldsymbol{C}^{ep}$ vanishes, i.e. $\boldsymbol{C}^p = \boldsymbol{0}$.

The Jaumann rate is defined as

$$\overset{\circ}{\boldsymbol{\sigma}} = \dot{\boldsymbol{\sigma}} - \boldsymbol{W}\boldsymbol{\sigma} + \boldsymbol{\sigma}\boldsymbol{W}$$

where $\boldsymbol{W}$ is the spin tensor defined from the decomposition of the velocity gradient $\boldsymbol{L} = \dot{\boldsymbol{F}}\boldsymbol{F}^{-1}$ according to

$$\boldsymbol{L} = \boldsymbol{D} + \boldsymbol{W} \quad \text{with} \quad \boldsymbol{D} = sym(\boldsymbol{L}) \quad \text{and} \quad \boldsymbol{W} = asym(\boldsymbol{L}) \,.$$

The elastic part of (13.4) for isotropic elasticity is expressed as

$$\boldsymbol{C}^e\boldsymbol{D} = 2G\boldsymbol{D} + Ktr(\boldsymbol{D})\boldsymbol{I}$$

where G is the shear modulus and K is the bulk modulus. The plastic modulus tensor can be expressed in terms of deviatoric Cauchy stress $\boldsymbol{s}$. The plastic part of (13.4) (active in plastic loading) is

$$C^p_{ijkl}D_{kl} = \frac{3G}{Y^2} s_{ij}s_{kl}D_{kl} \quad \text{or} \quad \boldsymbol{C}^p\boldsymbol{D} = \frac{3G}{Y^2}(\boldsymbol{s} : \boldsymbol{D})\boldsymbol{s}$$

where Y is the uniaxial Cauchy yield stress, and $\boldsymbol{s} : \boldsymbol{D} = s_{kl}D_{kl}$. The conditions for plastic loading can be expressed by the effective stress σ_e as

$$\sigma_e^2 = \frac{3}{2}\boldsymbol{s} : \boldsymbol{s} = Y^2 \quad \text{and} \quad \boldsymbol{s} : \boldsymbol{D} > 0$$

where the first is the yield condition and the second is the loading condition.

The complete expression for isotropic Von Mises' plasticity in plastic loading is

$$\dot{\boldsymbol{\sigma}} - \boldsymbol{W\sigma} + \boldsymbol{\sigma W} = 2G\boldsymbol{D} + Ktr(\boldsymbol{D})\boldsymbol{I} - \frac{3G}{Y^2}(\boldsymbol{s} : \boldsymbol{D})\boldsymbol{s} - \boldsymbol{\sigma} tr(\boldsymbol{D}) \tag{13.4}$$

It is required that the yield condition $\sigma_e^2 = Y^2$ is fulfilled during plastic loading.

Experimental curves for filled rubbers showing the amplitude dependence of the dynamic modulus indicate an onset of amplitude dependence at very small strains. In the proposed model this corresponds to small yield strains.

13.3. Evaluation of the model

The model will be evaluated for the complete incompressible case in simple shear and uniaxial stress. The total Cauchy stress tensor $\boldsymbol{\sigma}$ is the sum of visco-hyperelastic and elasto-plastic stress contributions

$$\boldsymbol{\sigma} = \boldsymbol{s}^{ve} + \boldsymbol{s}^{ep} + p\boldsymbol{I} \tag{13.5}$$

where $\boldsymbol{s}^{ve}$ and $\boldsymbol{s}^{ep}$ are the deviatoric viscoelastic and elasto-plastic stress components respectively and p is the hydrostatic stress given by

$$p = (\sigma_{11} + \sigma_{22} + \sigma_{33})/3$$

with p an independent variable due to incompressibility.

The visco-hyperelastic part of the deviatoric stress is

$$\boldsymbol{s}^{ve} = \boldsymbol{s}^{e} - \sum_{i=1}^{N} \boldsymbol{s}_i^{ve} \tag{13.6}$$

where $\boldsymbol{s}^e$ is the instantaneous hyperelastic deviatoric stress tensor described in Chapter 12.

The deviatoric elasto-plastic stress is given by

$$\boldsymbol{s}^{ep} = \sum_{i=1}^{M} \boldsymbol{s}_i^{ep} \; . \tag{13.7}$$

In the next section an elasto-plastic fraction will be evaluated for the incompressible case in cyclic compression/tension and simple shear.

13.4. Incompressible elasto-plastic fraction

The constitutive equation (13.4) can be simplified by taking incompressibility into account. The volumetric strain vanishes, i.e. $\dot{\epsilon}_v = tr(\boldsymbol{D}) \rightarrow 0$ and the term $Ktr(\boldsymbol{D})$ is replaced by the time derivative of the pressure, i.e. $\dot{p}$.

The Jaumann rate expressed in terms of the stress deviator is given by

$$\overset{\circ}{\boldsymbol{\sigma}} = \overset{\circ}{\boldsymbol{s}} + \dot{p}\boldsymbol{I} \; .$$

The volumetric strain vanishes giving an expression in terms of the stress deviator

$$\overset{\circ}{\boldsymbol{s}} = (\boldsymbol{C}^e - \boldsymbol{C}^p)\boldsymbol{D}$$

which can also be written

$$\dot{\boldsymbol{s}} - \boldsymbol{W}\boldsymbol{s} + \boldsymbol{s}\boldsymbol{W} = 2G\boldsymbol{D} - \frac{3G}{Y^2}(\boldsymbol{s} : \boldsymbol{D})\boldsymbol{s} \; . \tag{13.8}$$

Expression (13.8) giving the deviatoric Cauchy stress will be evaluated for uniaxial stress and simple shear.

13.4.1. Uniaxial stress

The expression (13.8) is specialized here to compression/tension. The state of stress and strain is according to

$$\sigma_1 = \sigma_{11}, \quad \sigma_2 = \sigma_3 = 0 \quad \text{and} \quad \lambda_1 = \lambda, \quad \lambda_2 = \lambda_3 = 1/\sqrt{\lambda}\,.$$

The deformation gradient and its time derivative for the equi-biaxial deformation are given by

$$\mathbf{F} = \begin{bmatrix} \lambda & 0 & 0 \\ 0 & \lambda^{-1/2} & 0 \\ 0 & 0 & \lambda^{-1/2} \end{bmatrix} \quad \text{and} \quad \dot{\mathbf{F}} = \begin{bmatrix} \dot\lambda & 0 & 0 \\ 0 & -\frac{1}{2}\lambda^{-3/2}\dot\lambda & 0 \\ 0 & 0 & -\frac{1}{2}\lambda^{-3/2}\dot\lambda \end{bmatrix}.$$

The velocity gradient $\boldsymbol{L} = \dot{\boldsymbol{F}}\boldsymbol{F}^{-1}$ is

$$\boldsymbol{L} = \frac{\dot\lambda}{\lambda}\begin{bmatrix} 1 & 0 & 0 \\ 0 & -\frac{1}{2} & 0 \\ 0 & 0 & -\frac{1}{2} \end{bmatrix}.$$

The rate of deformation tensor $\boldsymbol{D} = \boldsymbol{L}$ because $\boldsymbol{L} = \boldsymbol{L}^T$ and consequently $\boldsymbol{W} = 0$. The elasto-plastic equation in terms of the stress deviator is thus

$$\dot{\boldsymbol{s}} = 2G\boldsymbol{D} - \frac{3G}{Y^2}(\boldsymbol{s} : \boldsymbol{D})\boldsymbol{s} \quad \text{with} \quad \boldsymbol{s} : \boldsymbol{D} = \frac{\dot\lambda}{\lambda}(s_{11} - s_{22}) \tag{13.9}$$

By looking at the Cauchy stress

$$\begin{cases} \sigma_{11} = s_{11} + p \\ \sigma_{22} = \sigma_{33} = s_{22} + p = 0 \end{cases}$$

it follows that $\sigma_{11} = s_{11} - s_{22}$.

From (13.9) the components can be written

$$\begin{cases} \dot s_{11} = 2G\dfrac{\dot\lambda}{\lambda} - \dfrac{3G}{Y^2}\dfrac{\dot\lambda}{\lambda}(s_{11} - s_{22})s_{11} \\ \dot s_{22} = -G\dfrac{\dot\lambda}{\lambda} - \dfrac{3G}{Y^2}\dfrac{\dot\lambda}{\lambda}(s_{11} - s_{22})s_{22} \end{cases}.$$

Subtracting the equations yields the Cauchy stress for the uniaxial case according to

$$\dot\sigma_{11} = 3G\frac{\dot\lambda}{\lambda} - \frac{3G}{Y^2}\frac{\dot\lambda}{\lambda}\sigma_{11}^2\,. \tag{13.10}$$

It should be observed that the second term in (13.10) is zero in the elastic range. The condition for plastic loading is

$$\sigma_{11} = Y \quad \text{and} \quad \sigma_{11}\dot\lambda > 0.$$

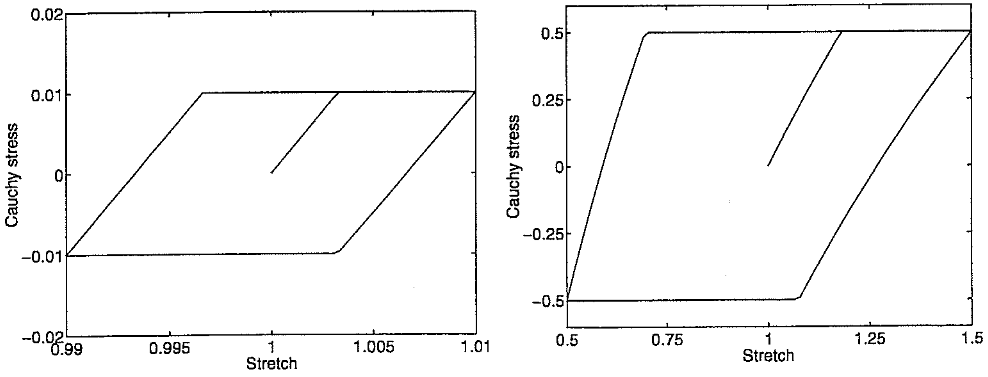

Figure 13.1: *Elasto-plastic stress strain loops, with elastic shear modulus $G = 1$. Left: Small strain amplitude (1%) and small yield stress ($Y = 0.01$). Right: Large strain amplitude (50%) and large yield stress ($Y = 0.5$).*

Equation (13.10) has been solved for cyclic loading giving hysteresis loops according to Figure 13.1, showing the elasto-plastic Cauchy stress σ_{11} versus stretch λ for two cases.

The first is for small stretch amplitudes $\Delta\lambda_0 = 0.01$ and the second is for large stretch amplitudes $\Delta\lambda_0 = 0.5$. The yield stress $Y = 0.01$ for the small amplitude case (left figure), and $Y = 0.5$ for the large amplitude case (right figure). The elastic shear modulus $G = 1$ for both cases. The elastic behavior for large strain case deviates from the small strain case by different stiffness in compression and tension.

13.4.2. Simple shear

The behavior of the Von Mises' model (13.8) is here evaluated for simple shear, with the velocity gradient

$$\boldsymbol{L} = \dot{\boldsymbol{F}}\boldsymbol{F}^{-1} = \begin{bmatrix} 0 & 0 & \dot{\kappa} \\ 0 & 0 & 0 \\ 0 & 0 & 0 \end{bmatrix} \begin{bmatrix} 1 & 0 & -\kappa \\ 0 & 1 & 0 \\ 0 & 0 & 1 \end{bmatrix} = \begin{bmatrix} 0 & 0 & \dot{\kappa} \\ 0 & 0 & 0 \\ 0 & 0 & 0 \end{bmatrix} .$$

From $\boldsymbol{D} = sym(\boldsymbol{L})$ and $\boldsymbol{W} = asym(\boldsymbol{L})$ it is found that

$$\boldsymbol{D} = \begin{bmatrix} 0 & 0 & \frac{1}{2}\dot{\kappa} \\ 0 & 0 & 0 \\ \frac{1}{2}\dot{\kappa} & 0 & 0 \end{bmatrix} \qquad \boldsymbol{W} = \begin{bmatrix} 0 & 0 & \frac{1}{2}\dot{\kappa} \\ 0 & 0 & 0 \\ -\frac{1}{2}\dot{\kappa} & 0 & 0 \end{bmatrix} .$$

Using (13.8) with $\boldsymbol{s} : \boldsymbol{D} = s_{13}\dot{\kappa}$ yields

$$\left\{\begin{aligned} \dot{s}_{13} &= (2G - s_{11} + s_{33} - 2\frac{3G}{Y^2}s_{13}^2)\dot{\kappa}/2 \\ \dot{s}_{11} &= s_{13}(1 - \frac{3G}{Y^2}s_{11})\dot{\kappa} \\ \dot{s}_{33} &= -s_{13}(1 + \frac{3G}{Y^2}s_{33})\dot{\kappa} \end{aligned}\right. . \tag{13.11}$$

We find that $s_{22} = 0$. The last term in the equations vanishes in the elastic range. Conditions for plastic loading are

$$\sigma_e^2 = \frac{3}{2}(s_{13}^2 + s_{11}^2 + s_{33}^2) = Y^2 \quad \text{and} \quad s_{13}\dot{\kappa} > 0,$$

where σ_e is the equivalent stress.

Solving (13.11) for cyclic loading yields an hysteresis loop according to Figure 13.2, with shear strain amplitude $\kappa_0 = 0.5$. The elastic shear modulus $G = 1$ and the uniaxial yield stress $Y = 0.1\sqrt{3}$ corresponding to a yield stress in shear $Y_s = 0.1$.

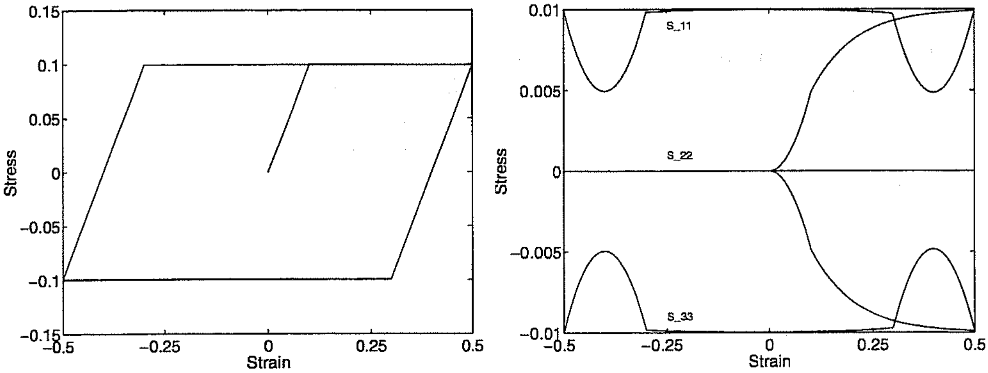

Figure 13.2: *Elasto-plastic stress strain loops in simple shear, with elastic shear modulus* $G = 1$*, yield strain* $Y = 0.173$ *and strain amplitude* $\kappa_0 = 0.5$ *(50%). Left: Shear stress* s_{13}*. Right: Deviatoric normal stress components* s_{ii}*.*

The left figure shows shear stress s_{13} versus shear strain κ and the right figure shows the deviatoric normal stresses versus shear strain κ. (Note that the sum of these stresses is zero.) The shear stress versus shear strain behavior is here identical to the one-dimensional case.

13.5. Nonlinear elastic plastic models

The behavior for quasi-static conditions of the fraction model with the viscoelastic contribution reduced to a hyperelastic fraction, is studied here. The Neo-Hooke and Yeoh models in combination with elasto-plastic stress fractions are considered. These models are examples of multiaxial nonlinear versions of the frictional models in Chapter 10. The elasto-plastic fraction parameters are adopted directly from the one-dimensional model according to (10.5). The parameters were $G = 0.7$ and

$$G_k = \begin{bmatrix} 0.778 & 0.185 & 0.174 \end{bmatrix} \quad Ys_k = \begin{bmatrix} 0.0211 & 0.0124 & 0.0235 \end{bmatrix} \qquad (13.12)$$

with values in MPa. The values Ys_k should be interpreted as the yield stresses in shear.

13.5.1. A Neo-Hooke based elastic plastic model

The hyperelastic part is here given by the Neo-Hooke model. The shear modulus $G = 0.7\ MPa$ yields $C_{10} = G/2 = 0.35\ MPa$. Model response to sinusoidal cyclic straining in simple shear and uniaxial stress is shown in Figure 13.3.

The left figure shows shear stress s_{13} versus shear strain κ. The simple shear strain history is the same as in Chapter 10. Due to the linearity of the Neo-Hooke model in simple shear, and the behavior of the elasto-plastic fractions in shear the hysteresis curves (left figure) are identical to the ones for the one-dimensional frictional model.

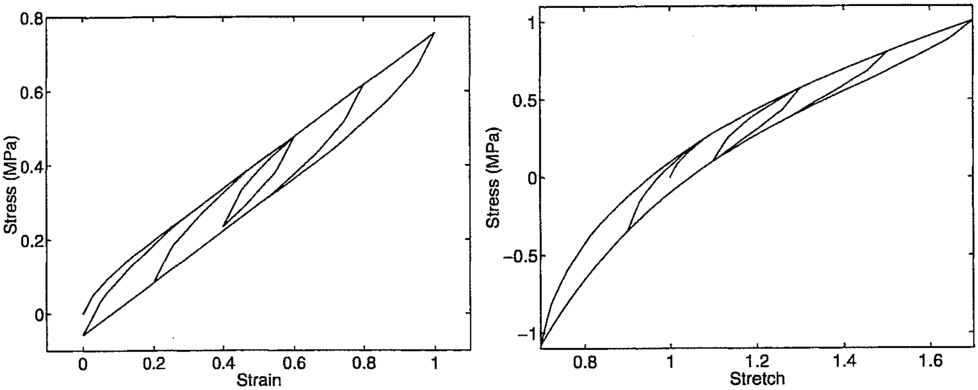

Figure 13.3: *Neo-Hooke based model in simple shear and uniaxial stress, with parameters according to the one-dimensional frictional model.*

The behavior of this Neo-Hooke based model in uniaxial stress is also shown in Figure 13.3 (right figure). The figure shows nominal stress σ_{11}/λ versus stretch λ for cyclic sinusoidal loading around a static strain of 20% ($\lambda = 1.2$) with strain amplitudes $\Delta\lambda_0 = 0.1, 0.3, 0.5$.

The overall nonlinear behavior (static and dynamic) is reasonably captured. However, the shape of the hysteresis loop in uniaxial stress is not quite what could be expected from real material behavior, because the hysteresis is larger in compression than in tension.

13.5.2. A Yeoh based elastic plastic model

By invoking a Yeoh hyperelastic model the nonlinear upturn, shown in the laboratory testing in simple shear, can be captured. The hyperelastic parameters are changed to

$$C_{10} = G/2 \quad C_{20} = -0.1\,G/2 \quad C_{30} = 0.06\,G/2,$$

and the other parameters remain unchanged. This model has the same initial shear modulus as the Neo-Hooke model (and the one-dimensional model). Figure 13.4 shows the model hysteresis loops compared to experiments for the same sinusoidal shear strain history as in the previous subsection. Shear stress s_{13} versus shear strain κ is shown.

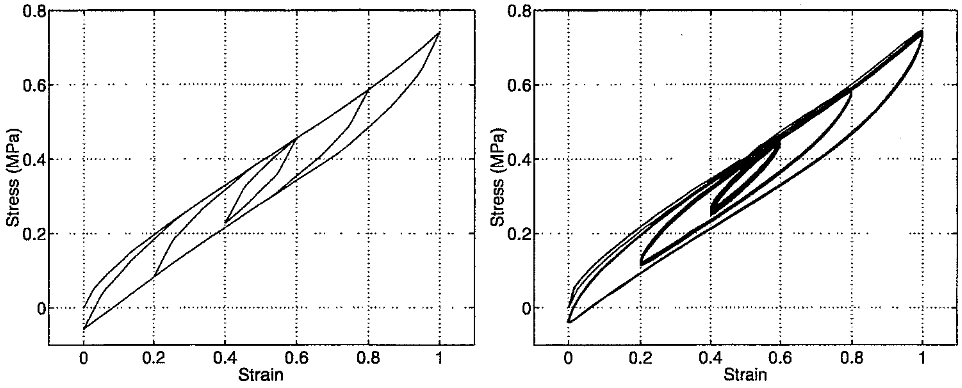

Figure 13.4: *Yeoh based elasto-plastic model (left) compared to quasi-static experiments in harmonic simple shear at* $f = 0.05$ *Hz (right).*

13.6. Discussion

Steady state dynamic behavior of filled rubbers is significantly influenced by strain amplitude. The main purpose was to show that some form of rate-independent damping mechanism is needed to capture the amplitude dependence in cyclic loading (and step size dependence in relaxation). The proposed model is a combination of the visco-hyperelastic model described in Chapter 12 and an elasto-plastic model built up from simple elasto-plastic fractions. The model is a straightforward generalization of the one-dimensional model in Chapter 11.

A first attempt used here for the elasto-plastic fraction was isotropic Von Mises' plasticity without hardening, and it was shown that this model in combination with Neo-Hooke hyperelasticity in simple shear is equivalent to the one-dimensional model in Chapter 10.

The behavior in uniaxial stress is however not quite satisfactory with an hysteresis smaller in tension than in compression. A possibility to model increasing hysteresis with increasing stretch would improve the model. This requires use of some other elasto-plastic fraction model or alternatively a completely different description of the elasto-plastic (rate-independent) fraction.

An inconsistency with the present formulation is that the elastic behavior in the elasto-plastic fraction is hypoelastic while the elastic behavior in the viscoelastic part is hyperelastic. This is due to the stress measure used in the elasto-plastic fractions i.e. Jaumann rate of Cauchy stress [50] (p. 95).

The proposed model should be relatively easy to implement in finite element code since it relies on existing constitutive models. This is also necessary in order to evaluate it more thoroughly. It should also be mentioned that the main drawback with the fraction model in connection to finite element analysis is the large number of state variables that must be stored.

Another possibility worth investigating is small viscoplastic vibrations imposed on a large elastic deformation in analogy with steady state viscoelastic analysis. Although complex analysis is not possible in this case, an analysis with a perturbation/linearization around a hyperelastically deformed state could be a useful development.

14. CONCLUDING REMARKS

14.1. Summary

Mechanical behavior of elastomeric materials was discussed in terms of constitutive models and calibration of these models to experiments. The main concern was to model static elastic and dynamic properties of elastomers containing fillers.

The first part of the thesis mainly concerns static elastic properties in terms of hyperelastic models and calibration of the models to test data. These models, defined from a strain energy density function, are used in finite element codes to define nonlinear elastic behavior. The choice of hyperelastic models was discussed and the fit of the models to experimental data was illustrated. Special interest was focused on the "cubic I1 model", with three parameters, well suited for modeling the elastic properties of carbon-black-filled rubbers.

A strain energy plot to check the behavior of the fitted model for a general state of strain was presented. The strain energy plot reveals whether the fitted model is physically reasonable and useful in finite element analysis.

Different test specimens and corresponding stress-strain relations were discussed, and analyses of the specimens to show deviations from the ideal homogeneous states of strain were presented.

Carbon-black-filled natural rubber vulcanizates are common in technical applications involving elastomeric units. These vulcanizates are highly elastic but not perfectly elastic; dissipation and damage (Mullins effect) are examples of inelastic effects. In order to use the well-established hyperelastic constitutive models in analysis of quasi-static mechanical behavior of carbon-black-filled rubber vulcanizates, the usual choice is to fit the elastic model to the loading curve for suitably pre-strained test specimens. The influences of the pre-straining or mechanical conditioning procedure were investigated and three different procedures for mechanical conditioning were compared.

The hyperelastic three-parameter model was fitted to test data for a number of carbon-black-filled natural rubber vulcanizates of different hardness.

Alternative test specimens and methods were also discussed. A new test specimen was proposed that can replace the standard dumbbell specimen, which is a very weak specimen that is difficult to use because of the small load-cell required and the risk for slippage in the connections to the loading heads. The "solid dumbbell" test specimen can also be used in compression. A method that uses a modified form of the hardness test to extract hyperelastic constants was presented. This method can rationalize the process of obtaining the hyperelastic constants, because the hardness test is an often-used standard test and it would be a benefit if more information could be derived from this test. Moreover, a method for contact-free strain measurement was presented that can be used for rubber membranes, for example in biaxial testing. Nonhomogeneous states of strain can be determined and experimental deformation gradients in different points in the membrane can be obtained.

The second part of the thesis concerns dynamic material properties. A description of damping mechanisms in filled elastomers and the ability to model the dependence of the dynamic modulus on frequency and amplitude were discussed. Rate-dependent and rate-independent damping were discussed in terms of one-dimensional and multiaxial models.

Linear viscoelasticity was discussed and basic concepts such as relaxation modulus, the hereditary integral and complex modulus were defined. Rheological models are used to illustrate the possibilities and limitations of constitutive models available in existing finite element codes in modeling of filled rubbers. Rate-independent damping was discussed in terms of one-dimensional elasto-plastic models. It was shown that the amplitude dependence of filled rubbers can be modeled by these rate-independent models. The models were fitted to quasi-static experiments and to experiments taken from literature.

The microstructure and the experimental results support a proposed rheologic model with elastic, viscous and frictional elements connected in parallel, i.e. the viscoelastic and elasto-plastic stress contributions are added. This model accurately captures elasticity and damping in filled elastomers. Moreover, it was shown that these models can be fitted to quasi-static and dynamic tests. A simple fitting procedure was outlined for both cases. The models were fitted to transient and periodic quasi-static loading, and they were shown to capture the amplitude and frequency dependence of the dynamic modulus with a reasonable engineering accuracy.

Finally a possible generalization of the one-dimensional viscoplastic model to the multiaxial case was discussed. The model combines large-strain viscoelasticity and elasto-plasticity by summing stress fractions. It was evaluated for simple shear and uniaxial stress, and shown to fit experiments in simple shear accurately, while the hysteresis in uniaxial stress was less accurate for the present elasto-plastic formulation.

14.2. Future work

It is important to emphasize the value of a close connection between experimental investigations and theoretical development in constitutive modeling. Both areas contribute to the development; experimental procedures can be developed through theoretical insights and theory benefits from experimental progress.

The experimental and modeling work presented in this study can be further developed in many ways.

One issue mentioned is to manufacture the short solid dumbbell with different filler content and check the accuracy and stability of the specimen. The results from the finite element analysis indicated that the relation between loading head and gauge length displacement was almost independent of rubber hardness. This should be verified experimentally, preferably also for other rubbers.

Another interesting subject would be to compare the accuracy of Yeoh's model with two and four parameter Ogden models for the tested filled rubbers according to Chapter 5.

An experimental verification of the modified hardness test is another subject of interest. This can be done by manufacturing specimens for hardness test, compression and shear tests from the same material batch and compare the hyperelastic constants obtained from the compression and shear tests with the constants obtained from the modified hardness test.

Future developments were also indicated in connection with the contact free strain measurement. The method can be simplified by using correlation techniques, in which a general texture applied to the specimens could be used instead of the distinct dots. From this texture it would be possible to estimate local deformations using linear mappings of subareas and correlate these maps and the actual deformed texture.

More research is also needed in order to obtain a better understanding of the dynamic behavior of filled rubbers. A systematic experimental investigation of carbon-black-filled rubbers with regard to amplitude and frequency in a wider frequency and amplitude range, can provide important information. Moreover, available experimental data are usually obtained in simple shear for steady-state sinusoidal loading or for relaxation. Tests with other load histories and in other modes of deformation can reveal additional information about the material behavior. The solid dumbbell can be used for this purpose to study compression and tension in the same test. The application of combined load cases, for example compression in combination with shear for different levels of static compression, is also of interest.

Experiments of the kind discussed above would also be helpful in the development of the proposed viscoplastic model. However, development and evaluation of the model require a finite element implementation, especially if combined load cases are taken into account.

It would also be of great interest to investigate small viscoplastic vibrations superposed on a large elastic deformation.

Many complicated issues in constitutive modeling of filled rubbers, such as damage and dissipative mechanisms in connection to large strains remains to be resolved. It is a field with many theoretical and experimental challenges and possibilities. Clearly, further research is needed to obtain a more complete understanding of the various phenomena encountered in engineering with rubber.

BIBLIOGRAPHY

[1] ALI A., (1996), *Hyperelastic Constants obtained from a Modified Hardness Test*, Report TVSM-5069, Lund University, Division of Structural Mechanics, 1996.

[2] AUSTRELL P.-E., (1994), *Hyperelastic Constants for Carbon-Black-Filled Rubber Vulcanizates*, Report TVSM-7093, Lund University, Division of Structural Mechanics, 1994.

[3] AUSTRELL P.-E., (1995), *Mechanical Properties of Carbon-Black-Filled Rubber Vulcanizates.*, International Rubber Conference (RubCon–95), Challenges in Compounding/Testing, Gothenburg, Sweden, May 9–12, 1995.

[4] AUSTRELL P.-E., ENQUIST B., HEYDEN A., AND SPANNE S., (1995), *Contact Free Strain Measurement using Matlab Image Processing Toolbox.*, Nordic Matlab Conference 95, Stockholm, Sweden, October 31–November 1, 1995.

[5] AUSTRELL P.-E., (1996), *Modeling and Testing of Rubber Materials for Finite Element Simulations : Elasticity and Damping*, Nordic Rubber Conference NRC 96, Helsinki, Finland, May 23–24, 1996.

[6] BEATTY M.F., (1987), *Topics in Finite Elasticity: Hyperelasticity of Rubber, Elastomers and Biological Tissues - with Examples*, Appl. Mech. Rev., vol. 40, no. 12, 1987.

[7] BERG M., (1995), *A Rubber Spring Model for Dynamic Analysis of Rail Vehicles*, Royal Institute of Technology, Department of Vehicle Engineering, 1995.

[8] BESSELING J.F., (1958), *A Theory of Elastic, Plastic, and Creep Deformation of an Initially Isotropic Material.*, J. Appl. Mech. 25, pp. 529-536, 1958.

[9] BESSELING J.F. AND VAN DER GIESSEN E., (1994), *Mathematical Modelling of Inelastic Deformation*, Chapman & Hall, London, 1994.

[10] CHANG W. V. AND SUN S. C., (1991), *Non-linear Elastic Analysis of Hardness Test on Rubber-like Materials*, Rubber Chemistry and Technology, Vol. 64, p. 202, 1991.

[11] Charlton D.J., Yang J., and Teh K.K., (1993), *A Review of Methods to Characterize Rubber Elastic Behaviour for use in Finite Element Analysis*, Rubber Chemistry and Technology, Vol. 67, pp. 481-503, 1993.

[12] Coveney V.A., Johnsson D.E., and Turner D.M., (1995), *A Triboelastic Model for the Cyclic Behavior of Filled Vulcanizates*, Rubber Chemistry and Technology, Vol. 68, 1995.

[13] Davis C.K.L., De D.K., and Thomas A.G., (1994), *Characterize of the Behaviour of Rubber for Engineering Design Purposes. 1. Stress-Strain Relations*, Rubber Chemistry And Technology, Vol. 67, pp. 716-728, 1994.

[14] Finkin, E.F., (1971), *The Determination of Young's Modulus from the Indentation of Rubber Sheets by Spherically Tipped Indentors*, Mechanical Technology Inc., August 1971.

[15] Finney R.H. and Kumar A., (1988), *Development of Material Constants for Nonlinear Finite Element Analysis* Rubber Chemistry and Technology, Vol.61, pp. 879-891, 1988.

[16] Freakly P.K. and Payne A.R., (1978), *Theory and Practise of Engineering with Rubber*, Applied science publishers, 1978.

[17] Godvinjee S. and Simo J.C., (1991), *A Micro-Mechanically Based Continuum Damage Model for Carbon-Black-Filled Rubbers Incorporating Mullin's Effect*, J. Mechanics and Physics of Solids, Vol. 39, No. 1, 1991.

[18] Godvinjee S. and Simo J.C., (1992), *Transition from Micro-Mechanics to Computationally Efficient Phenomenology: Carbon-Black-Filled Rubbers Incorporating Mullin's Effect*, J. Mechanics and Physics of Solids, Vol. 40, No. 1, 1992.

[19] Godvinjee S. and Simo J.C., (1992), *Mullin's Effect and the Strain Amplitude Dependence of the Storage Modulus*, Int. J. Solids Structures, Vol. 29, No. 14/15, 1992.

[20] Gonzales, R., C., Woods, R., E., (1992), *Digital Image Processing*, Addison-Wesley Publishing Company, 1992.

[21] Green A.E. and Adkins J.E., (1970), *Large Elastic Deformations*, Oxford University Press, 1970.

[22] Gregory M.J., (1985), *Dynamic properties of rubber in automotive engineering*, Elastomerics 19, November 1985

[23] Gåsvik, K.J., (1987), *Optical meteorology*, John Wiley and sons, Chichester, 1987.

[24] GÖBEL E.F., (1974), *Rubber Springs Design* London Newnes-Butte, 1974.

[25] HARRIS J. AND STEVENSON A., (1986), *On the Role of Nonlinearity in the Dynamic Behavior of Rubber Components*, Rubber chemistry and technology, Vol. 59, pp.741-764, 1986.

[26] HIBBITT, KARLSSON, AND SORENSEN, (1994), *ABAQUS/Standard, Theory and User's Manual* Version 5.4, 1994.

[27] JAMES A.G., GREEN A., AND SIMPSON G.M., (1975), *Strain Energy Functions of Rubber I. Characterization of Gum Vulcanizates*, J. appl. Polym. Sci. 19, pp.2033, 1975

[28] JAMES A.G. AND GREEN A., (1975), *Strain Energy Functions of Rubber II. Characterization of Filled Vulcanizates*, J. appl. Polym. Sci. 19, pp. 2319, 1975.

[29] JAPS D., (1979), *Ein Beitrag zur analytischen Bestimmung des statischen und dynamischen Verhaltens gummielastischer Wulst-Kupplungen unter Berücksichtigung von auftretenden Axialkräften.* Dissertation, Dortmund, 1979.

[30] JOHNSON A.R., QUIGLEY C.J., AND FREESE C.E., (1995), *A viscohyperelastic finite element model for rubber*, Computer Methods in Applied Mechanics and Engineering, Vol. 127, pp. 163-180, 1995.

[31] KRAUS G., (1984), *Mechanical Losses in Carbon-Black-Filled Rubbers*, J.Appl. Polym. Sci.: Applied Polymer Symposium 39, 1984.

[32] KÜMMLEE H., (1986), *Ein Verfahren zur Vorhersage des nichtlinearen Steifigkeits- und Dämpfungsverhaltens sowie der Erwärmung drehelasticher Gummikupplungen bei statinärem betrieb.*, VDI-Fortschr.-ber. Reihe 1, Nr. 136, Düsseldorf, VDI-Verlag, 1986.

[33] LINDLEY P.B., (1974), *Engineering Design with Natural Rubber*, MRPRA 1974.

[34] LUBLINER J., (1985), *A model of rubber viscoelasticity*, Mech. Res. Comm. 12, pp. 93-99, 1985.

[35] LÖNNQVIST K. AND THELIN A., (1995), *Design av vibrationsdämpare genom finit element-simulering*, Report TVSM-5063, Lund University, Division of Structural Mechanics, 1995.

[36] *MATLAB-High-Peformance Numerical Computation and Visualization Software.*, The Math Works Inc, Natick, Ma, USA 1992.

[37] MALVERN L.E., (1969), *Introduction to the Mechanics of a Continous Medium*, Prentice-Hall, 1969.

[38] MEDALIA A.I., (1978), *Effects of Carbon-black on Dynamic Properties of Rubber*, Rubber Chemistry and Technology, Vol.51, pp.437, 1978.

[39] MOONEY M., (1940), *A theory of elastic deformations*, J. Appl. Phys. 11, p. 582, 1940.

[40] MORMAN K.N. AND NAGTEGAAL J.C., (1983), *Finite Element Analysis of Sinusoidal Small-Amplitude Vibrations in Deformed Viscoelastic Solids*, Int. J. Numerical Methods in Engineering, Vol. 19, No.7, 1983.

[41] MUHR A.H. AND THOMAS A.G., (1989), *Allowing for Non-linear Stress-Strain Relationship of Rubber in Force-Deformation Calculations. Part2: Relationship of Hardness to Modulus*, 27 NR Technology Vol. 20, No. 2, 1989.

[42] MULLINS L., (1969), *Softening of Rubber by Deformation*, Rubber Chemistry and Technology, Vol. 42, pp. 339-362, 1969

[43] OGDEN R.W., (1972), *Large Deformation Isotropic Elasticity: On the Correlation of Theory and Experiments for Incompressible Rubberlike Solids*, Proc. Royal Society, Vol. A(326), 1972.

[44] OTTOSEN, N.S. AND PETERSSON, H., (1992), *Introduction to the Finite Element Method*, Prentice Hall, 1992.

[45] PAYNE A.R., (1965), in *Reinforcement of Elastomers*, G.Kraus, Ed., Interscience, Chap. 3, New York, 1965,

[46] PERSSON S., (1992), *Physical and Mechanical Properties: Natural Rubber: material 0*, material data shet; Svedala-Skega AB, 1992.

[47] PILCHER M., (1996), *Finite Element Modelling and Testing of Rubber Pipe Seals*, Report TVSM-5067, Lund University, Division of Structural Mechanics, 1996.

[48] PILCHER M. AND AUSTRELL P.-E., (1996), *Evaluation or Rubber Test Specimens by Finite Element Analysis*, Report TVSM-7115, Lund University, Division of Structural Mechanics, 1996.

[49] PIPKIN A.C., (1986), *Lectures on Viscoelasticity Theory*, 2nd ed., Springer-Verlag, 1986.

[50] RISTINMAA M. AND OTTOSEN N.S., (1996), *Large Strain Plasticity and Thermodynamics*, Report CODEN:LUTFD2/(TFHF-3072)/1-145/1996, Lund University, Solid Mechanics, 1996

[51] Rivlin R.S., (1948), *Large elastic deformations of isotropic materials, IV. Further developments of the general theory.*, Phil. Trans. R. Soc. A241, pp. 379-397, 1948.

[52] Rivlin R.S. and Saunders D.W., (1951), *Large elastic deformations of isotropic materials, VII. Experiments on the deformation of rubber*, Phil. Trans. R. Soc. A243, pp. 251-288, 1951.

[53] Scott J.R., (1948), *Improved method of expressing hardness of vulcanized rubber*, J. Rubb. Research 17, p. 145, 1948.

[54] Simo J.C., (1987), *On a Fully Three-Dimensional Finite-Strain Viscoelastic Damage Model: Formulation and Computational Aspects*, Computer Methods in Applied Mechanics and Engineering, Vol. 60, pp. 153-173, 1987.

[55] Sjödahl M., (1993), *An Electronic Speckle Photography System for In Plane Deformation Measurements,*, Licentiate thesis, LuTH, Luleå, Sweden, 1993.

[56] Thelandersson S., (1987), *Notes on Linear Viscoelasticity*, Report TVSM-3009, Lund University, 1987.

[57] Turner D.M., (1988), *A triboelastic model for the mechanical behaviour of rubber*, Plast. Rubb. Proc. Applic., 9, pp. 197-201, 1988

[58] Twizell E.H. and Ogden R.W., (1983), *Non-linear Optimization of the Material Constants in Ogden's Stress-Deformation Function for Incompressible Isotropic Elastic Materials*, J. Austral. Math. Soc., Ser. B, 1983.

[59] Ulmer J.D., (1995), *Strain Dependence of Dynamic Mechanical Properties of Carbon-Black-Filled Rubber Compounds*, Rubber Chemistry and Technology, Vol. 69, pp.15-47, 1995.

[60] Vieweg S. et. al., (1995), *Frequency and Temperature Dependence of the Small-Strain Behavior of Carbon-Black-Filled Vulcanizates*, Polym. Networks Blends, 5(4), pp. 199-204, 1995.

[61] Warnaka G.E., (1962), *Effects of Dynamic Strain Amplitude on the Dynamic Mechanical Properties of Polymers*, ASME Rubber and Plastics Div., New York, Pre-print 62-WA: 323, 1962.

[62] Williams M.L., Landel R., and Ferry J.D., (1955), *The Temperature Dependence of Relaxation Mechanisms in Amorphous Polymers and Other Glass Forming Liquids*, J. American Chemical Society, Vol. 77, pp. 3701-3707, 1955.

[63] Treloar L.R.C., (1975), *The Physics of Rubber Elasticity*, Clarendon Press, Oxford, 1975.

[64] YEOH O.H., (1984), *On hardness and Young's modulus of rubber*, Plastics and Rubber Proceding and Applications, Vol. 4, No. 2, 1984.

[65] YEOH O.H., (1990), *Characterization of Elastic Properties of Carbon-black-filled Rubber Vulcanizates* , Rubber Chemistry and Technology, Vol. 63, pp. 792-805, 1990.

[66] YEOH, O.H., (1993), *Some Forms of The Strain Energy Function for Rubber*, Rubber Chemistry and Technology, Vol. 66, pp. 754-772, 1993.

[67] ZDUNEK A.B., (1992), *On the Mechanics of Nearly Incompressible Solids*, PhD thesis, Royal Institute of Technology, Department of Solid Mechanics, 1992.

[68] ZIENKIEWICZ O.S. AND TAYLOR R.L., (1991), *The Finite Element Method*, Vol. 1 and 2, McGraw Hill, 1991.

A. BASIC MECHANICS

This appendix concerns measures of strain and stress used in constitutive relations for rubber elasticity and viscoelasticity. A more comprehensive treatment of these subjects can be found in Malvern [37].

Consider a deformable body occupying a region in space loaded by forces acting on its surface. The loading changes the shape of the body, and strain and stress develop in the deformed body. We are not assigning any particular material to the body, i.e. the connection between stress and strain is not discussed here.

The kinematics of large deformations, including a derivation of a proper measure of strain and the important concept of strain invariants and fundamentals about traction and the stress tensor, are subjects discussed in this chapter.

A.1. Kinematics

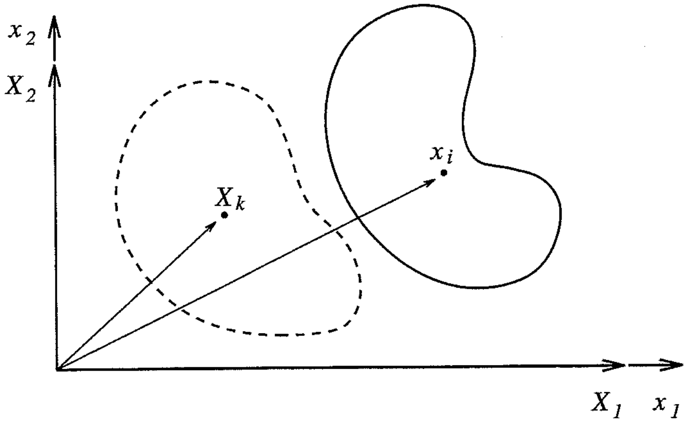

Figure A.1: *Deformable body in reference and current configuration.*

This section contains a brief description of the kinematics of finite deformations, including a derivation of a proper measure of strain and the strain invariants. The kinematic description concerns only deformation and strain, with no regard to what is causing the deformation of the body. The body is defined by a collection of *material particles.* The locations of the particles are determined by position vectors in a fixed Cartesian coordinate system. A configuration in which the positions of the particles are known is chosen to be the *reference configuration* of the body. This configuration is often taken to be the undeformed configuration. The deformation takes the particles to new positions, and the new configuration is called the *current or deformed configuration*, cf. Figure A.1.

A.1.1. Deformation

The deformation of the body is expressed by a mapping, from the reference to the current configuration, defined for every particle in the body. The location of a material particle in the reference configuration is uniquely determined by coordinates X_k and by x_i for the same material particle in the current configuration. The indices i and k can have the values 1, 2 and 3. The mapping

$$x_i = x_i(X_k) \tag{A.1}$$

determines the location of a material point as a function of the position in the reference configuration (cf. Figure A.1). The components of (A.1) can be collected in a column matrix and expressed in matrix notation as

$$\begin{bmatrix} x_1 \\ x_2 \\ x_3 \end{bmatrix} = \begin{bmatrix} x_1(X_1, X_2, X_3) \\ x_2(X_1, X_2, X_3) \\ x_3(X_1, X_2, X_3) \end{bmatrix} \qquad \Longleftrightarrow \qquad \mathbf{x} = \mathbf{x}(\mathbf{X}). \tag{A.2}$$

The convention of using capital letters for quantities referring to the reference configuration and lower case letters for the current configuration is used.

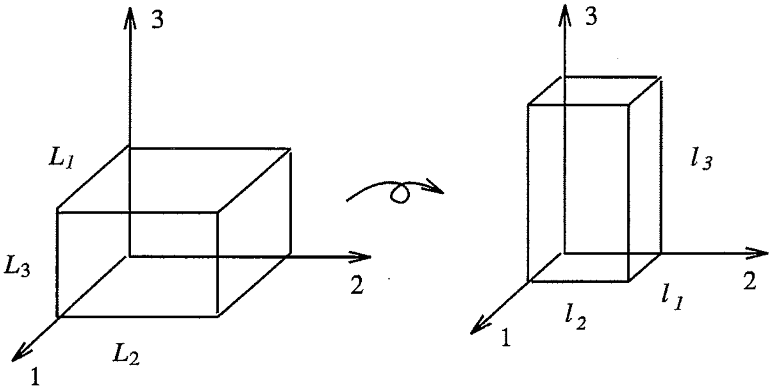

Figure A.2: *Deformation without shear of a prismatic block.*

Two important examples of the mapping (A.2) will be considered. The first is deformation without shear, illustrated in Figure A.2. This state of deformation is used in Chapter 4 to determine the kinematics of rubber test specimens.

A prismatic block is deformed by extension or compression to a new prismatic block. The undeformed side lengths of the block are L_i and the side lengths in the deformed configuration are l_i (cf. Figure A.2). The relation between the coordinates in the reference and the current configuration is

$$\begin{cases} x_1 = \lambda_1 X_1 \\ x_2 = \lambda_2 X_2 \\ x_3 = \lambda_3 X_3 \end{cases} \quad \text{where} \quad \lambda_i = l_i / L_i \,. \tag{A.3}$$

X_i and x_i are the coordinates in the original and deformed configuration respectively.

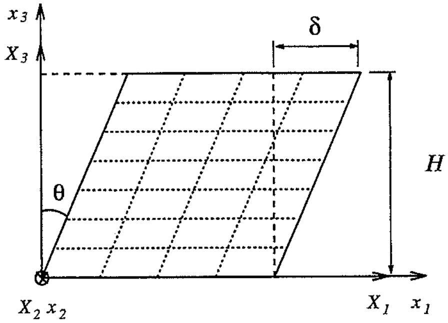

Figure A.3: *Simple shear.*

The other example of deformation is called *simple shear.* The deformation in this case is determined by

$$\begin{cases} x_1 = X_1 + \kappa X_3 \\ x_2 = X_2 \\ x_3 = X_3 \end{cases} \quad \text{with} \quad \kappa = tan\theta = \frac{\delta}{H} \,,$$

and θ is the shear angle according to Figure A.3. We observe that there is no displacement in the second and third direction. The only displacement of particles occurs in the first direction, and the displacement is proportional to X_3.

The two examples considered here are basic states of deformation used in the tests described in Chapter 4.

A.1.2. Deformation gradient

In order to determine the straining of the body we need to know how the distance between two neighboring particles in the reference configuration is affected by the deformation. This can be achieved by considering the length changes of an infinitesimal material line element. The line element is obtained by differentiation of (A.1) yielding

$$dx_i = \frac{\partial x_i}{\partial X_j} dX_j \,. \tag{A.4}$$

The explicit matrix expression of (A.4) is

$$\begin{bmatrix} dx_1 \\ dx_2 \\ dx_3 \end{bmatrix} = \begin{bmatrix} \frac{\partial x_1}{\partial X_1} & \frac{\partial x_1}{\partial X_2} & \frac{\partial x_1}{\partial X_3} \\ \frac{\partial x_2}{\partial X_1} & \frac{\partial x_2}{\partial X_2} & \frac{\partial x_2}{\partial X_3} \\ \frac{\partial x_3}{\partial X_1} & \frac{\partial x_3}{\partial X_2} & \frac{\partial x_3}{\partial X_3} \end{bmatrix} \begin{bmatrix} dX_1 \\ dX_2 \\ dX_3 \end{bmatrix} , \tag{A.5}$$

which can be expressed in compact matrix notation as

$$\mathbf{dx} = \mathbf{F}\,\mathbf{dX} . \tag{A.6}$$

The matrix $\mathbf{F}$, with the components

$$F_{ij} = \frac{\partial x_i}{\partial X_j} ,$$

is called the *deformation gradient.* The relation (A.6) describes how a material line element changes its length and direction by the deformation. The line element in the reference and current configuration is illustrated in Figure A.4.

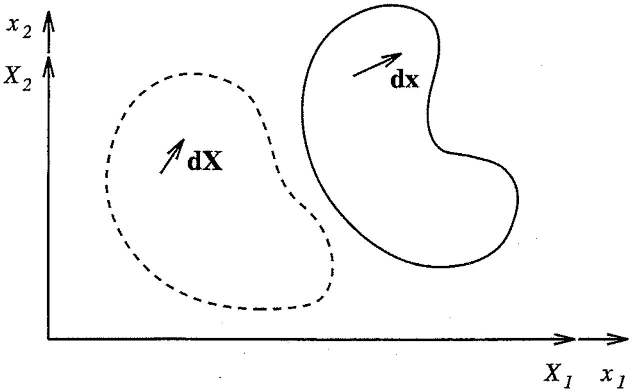

Figure A.4: *A material line element in original and deformed configuration.*

The deformation gradients of the two examples in the previous section are easily computed from (A.5). Deformation without shear yields the deformation gradient

$$\mathbf{F} = \begin{bmatrix} \lambda_1 & 0 & 0 \\ 0 & \lambda_2 & 0 \\ 0 & 0 & \lambda_3 \end{bmatrix} \tag{A.7}$$

where, as mentioned above, λ_i is the ratio between the deformed and the undeformed side lengths. The matrix is constant with respect to the coordinates, i.e. the deformation gradient is the same for all points in the prismatic block considered.

For the simple shear deformation we also obtain a constant deformation gradient

$$\mathbf{F} = \begin{bmatrix} 1 & 0 & \kappa \\ 0 & 1 & 0 \\ 0 & 0 & 1 \end{bmatrix} .$$

The deformation without shear and the simple shear deformation are *homogeneous* deformations. A body is subjected to a homogeneous deformation if the deformation gradient is constant for all material particles, i.e. there is no spatial variation of the deformation gradient.

Rubber test specimens are designed to give as homogeneous states of deformation as possible, in at least a clearly defined part of the specimen. This is discussed in Chapter 4 and Chapter 6.

A.1.3. Measures of strain

The question of a suitable measure of strain is the concern of this section. We know everything about the deformation of the material line element from relation (A.6) and should be able to determine the straining of the body. The deformation gradient, however, determines both rotation and length changes of the material line element.

To show that the deformation gradient is dependent on the rotation consider the deformation expressed by

$$\begin{cases} x_1 = cos\phi\, X_1 - sin\phi\, X_2 \\ x_2 = sin\phi\, X_1 + cos\phi\, X_2 \\ x_3 = X_3 \end{cases} .$$

This deformation is a pure rotation an angle ϕ around the X_3 axis and it is therefore not causing any straining of the body. The deformation gradient for this deformation is

$$\mathbf{F} = \mathbf{R} = \begin{bmatrix} cos\phi & -sin\phi & 0 \\ sin\phi & cos\phi & 0 \\ 0 & 0 & 1 \end{bmatrix} ,$$

i.e. a nonzero constant matrix. So a pure rigid rotation of the body considered yields a deformation gradient different from zero.

A suitable measure of strain should be independent of rigid body rotations. So the deformation gradient $\mathbf{F}$ is in itself not good as a measure of strain. But as will be shown later it can be combined into an expression that is independent of rigid body rotation.

Now let us focus on the subject of finding a suitable measure of strain. The mapping of the line element is therefore described in terms of pure rotation and pure stretch. This can be done in two ways, either by a rotation followed by stretch or, in the reversed order, stretch followed by rotation.

Suppose that the line element is first subjected to a rotation. The rotation of the line element can be expressed as

$$\mathbf{dx}' = \mathbf{R}\,\mathbf{dX} \tag{A.8}$$

where $\mathbf{R}$ is an orthogonal rotation matrix of the same type as in the example above and $\mathbf{dx}'$ is the intermediate rotated line element. Then the rotated line element is subjected to a pure stretch, expressed by

$$\mathbf{dx} = \mathbf{V}\,\mathbf{dx}'\,. \tag{A.9}$$

Inserting (A.8) into (A.9) yields

$$\mathbf{dx} = \mathbf{V}\,\mathbf{R}\,\mathbf{dX}\,, \tag{A.10}$$

and by comparing with (A.6) the decomposition

$$\mathbf{F} = \mathbf{V}\,\mathbf{R} \tag{A.11}$$

of the deformation gradient is obtained.

Alternatively we can start with the stretch and then rotate the line element. This yields in a similar manner the decomposition

$$\mathbf{F} = \mathbf{R}\,\mathbf{U}\,, \tag{A.12}$$

where $\mathbf{U}$ is the deformation gradient of the pure stretch and $\mathbf{R}$ is an orthogonal rotation matrix (i.e. $\mathbf{R}^T = \mathbf{R}^{-1}$). The relations (A.11) and (A.12) are shown in a more general way in the polar decomposition theorem [37]. This theorem states that the matrices $\mathbf{V}$ and $\mathbf{U}$ are positive definite and symmetric matrices and $\mathbf{R}$ is an orthogonal matrix.

The matrices $\mathbf{V}$ and $\mathbf{U}$ are suitable measures of strain because they do not involve any rigid body rotation. But it is difficult in practice to determine $\mathbf{V}$ and $\mathbf{U}$.

A more convenient way to determine the straining of the line element is by direct calculation of the element length in the original and deformed configuration and using the ratio of these two lengths as a measure of strain. This strain measure is called *stretch* and it is consequently defined as

$$\lambda = \frac{ds}{dS}\,, \tag{A.13}$$

where the lengths are computed as

$$ds^2 = \mathbf{dx}^T\mathbf{dx} \qquad \text{and} \qquad dS^2 = \mathbf{dX}^T\mathbf{dX}. \tag{A.14}$$

From (A.13) we conclude that $\lambda = 1$ if there is no straining of the line element. Inserting the vector notations (A.14) into expression (A.13) yields

$$\lambda^2 = \frac{\mathbf{dx}^T\mathbf{dx}}{\mathbf{dX}^T\mathbf{dX}}. \tag{A.15}$$

Use of (A.6) in (A.15) then gives an expression that only involves the line element in the reference configuration

$$\lambda^2 = \frac{\mathbf{dX}^T\mathbf{F}^T\mathbf{F}\mathbf{dX}}{\mathbf{dX}^T\mathbf{dX}}.$$

The product

$$\mathbf{C} = \mathbf{F}^T\mathbf{F} \tag{A.16}$$

forms a symmetric tensor called the *right Cauchy-Green deformation tensor.*

It is possible to use the polar decomposition theorem to show that $\mathbf{C}$ is independent of rigid body motion

$$\mathbf{C} = \mathbf{U}^T\mathbf{R}^T\mathbf{R}\mathbf{U} = \mathbf{U}^T\mathbf{U} = \mathbf{U}^2\ , \tag{A.17}$$

where the orthogonality of $\mathbf{R}$ and the symmetry of $\mathbf{U}$ are used. Expression (A.17) shows that $\mathbf{C}$ is independent of $\mathbf{R}$. We conclude that $\mathbf{C}$ can be used as a measure of strain, because rigid body motion do not affect expression (A.16).

The polar decomposition theorem can also be used to show similar properties for the deformation tensor called the *left Cauchy-Green deformation tensor.* It is defined as

$$\mathbf{B} = \mathbf{F}\mathbf{F}^T \tag{A.18}$$

which is also a symmetric tensor. The polar decomposition theorem yields

$$\mathbf{B} = \mathbf{V}\mathbf{R}\mathbf{R}^T\mathbf{V}^T = \mathbf{V}\mathbf{V}^T = \mathbf{V}^2 \tag{A.19}$$

and we conclude that $\mathbf{B}$ is also a suitable measure of strain.

$\mathbf{B}$ is used as strain measure in the constitutive relation for the nonlinear elastic, so called, hyperelastic material discussed in Chapter 3.

A.1.4. Principal axis of deformation

This section concerns the *principal axis of deformation* and the *principal stretches* in order to prepare for the discussion of strain invariants in the next section.

It is always possible to determine an orientation, in any point in a deformed body, in which a small cube in the original configuration is deformed without shearing. The three perpendicular directions, parallel to the sides of the cube, where there is no shear, are called the principal axis of deformation. The corresponding principal stretches can be shown to include the maximum and minimum stretch in the small region considered surrounding the point of interest.

For a general nonhomogeneous deformation, the principal directions will obviously be different from point to point in the deformed body. But the principal directions are also dependent on the size of the deformation. Consider the example of simple shear illustrated in Figure A.6. The example shows that the size of the deformation affects the principal directions.

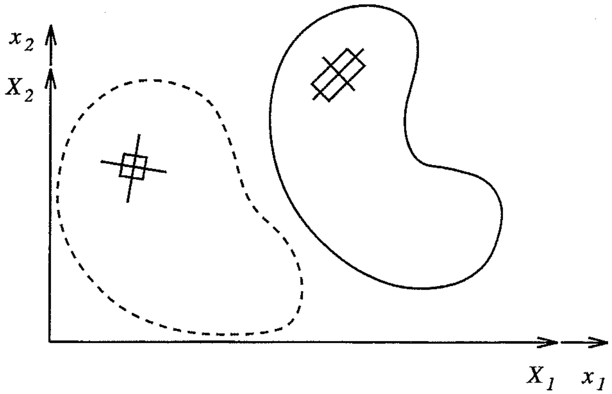

Figure A.5: *Principal directions*

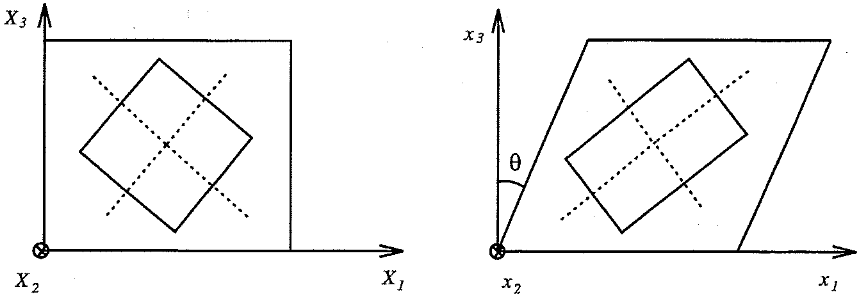

Figure A.6: *Principal directions in simple shear*

The principal axis and corresponding stretch values can be found by formulating and solving an eigenvalue problem. To show this we recall the polar decomposition theorem in the form (A.11), where the deformation gradient was decomposed by a rotation followed by a pure stretch. The differential material line elements are expressed by use of unit vectors

$$\mathbf{dx} = \mathbf{n}ds \quad \text{and} \quad \mathbf{dX} = \mathbf{N}dS \ , \tag{A.20}$$

where $\mathbf{n}$ is a unit vector in the current configuration and $\mathbf{N}$ is a unit vector in the original configuration. Inserting (A.11) and (A.20) into (A.6) yields

$$\mathbf{n}ds = \mathbf{VRN}dS \ , \tag{A.21}$$

where $\mathbf{RN}$ expresses the rotation of the unit vector $\mathbf{N}$. The second phase in the decomposed deformation, however, involves no rotation and the rotated line element will not change direction in the pure stretch. For this reason the relation

$$\mathbf{RN} = \mathbf{n} \tag{A.22}$$

must hold. Inserting (A.22) into (A.21) gives

$$\mathbf{n}ds = \mathbf{V}\mathbf{n}dS \tag{A.23}$$

and then using the definition of stretch (A.13) in (A.23) yields

$$\mathbf{V}\mathbf{n} = \lambda\mathbf{n} , \tag{A.24}$$

which is an eigenvalue problem for **V** with the stretch λ as the eigenvalue and the principal axis as the eigenvector. The eigenvectors are the principal axis referred to the deformed configuration, because the vector **n** is referred to this configuration.

Solving the eigenproblem yields a set of eigenvalues λ_1, λ_2, λ_3 and a set of eigenvectors $\mathbf{n}_1$, $\mathbf{n}_2$, $\mathbf{n}_3$. The eigenvalues are real values and the eigenvectors can be chosen to be perpendicular unit vectors, due to the symmetry of **V**.

The difficulties in obtaining **V** can be avoided by rewriting the eigenproblem in terms of the left Cauchy-Green deformation matrix **B**. The more convenient form of the eigenproblem is thus stated as

$$\mathbf{B}\mathbf{n} = \alpha\mathbf{n} \tag{A.25}$$

Using (A.19), where it was shown that **B** is the square of **V**, and (A.24) in (A.25) yields

$$\mathbf{V}^2\mathbf{n} = \lambda^2\mathbf{n} . \tag{A.26}$$

The principal values of **B** are thus the squared principal values of **V**. Solving (A.26) results in the set of eigenvalues ${\lambda_1}^2$, ${\lambda_2}^2$, ${\lambda_3}^2$ and the same set of eigenvectors as above. The eigenvectors $\mathbf{n}_i$ are the principal directions in the deformed configuration. These vectors correspond to a set of eigenvectors $\mathbf{N}_i$ connected by the relation (A.22).

The decomposition (A.12) can be used in the same way as above, to obtain an eigenvalue problem similar to (A.26);

$$\mathbf{U}^2\mathbf{N} = \lambda^2\mathbf{N} , \tag{A.27}$$

where $\mathbf{U}^2 = \mathbf{C}$ according to (A.17). The principal axis in the reference configuration is obtained by solving (A.27). The principal values of **C** can be shown to be the same as for **B**.

A.1.5. Strain invariants

The strain invariants are central in defining the nonlinear elastic, so called hyperelastic, material.The strain invariants of the left Cauchy-Green deformation tensor are derived from the eigenproblem (A.26). The eigenvalues are found from the characteristic polynomial of **B** according to

$$det(\mathbf{B} - \lambda^2\mathbf{I}) = 0 . \tag{A.28}$$

This polynomial is the same regardless of what coordinate system is used to express the components of **B**, i.e. the characteristic polynomial is *invariant* of coordinate transformations.

Expression (A.28) can be written in terms of the principal values as

$$(\lambda^2 - {\lambda_1}^2)(\lambda^2 - {\lambda_2}^2)(\lambda^2 - {\lambda_3}^2) = 0$$

which can be rewritten as

$$(\lambda^2)^3 - I_1(\lambda^2)^2 + I_2\lambda^2 - I_3 = 0 \tag{A.29}$$

where the coefficients I_1, I_2 and I_3 have the values

$$\begin{cases} I_1 = {\lambda_1}^2 + {\lambda_2}^2 + {\lambda_3}^2 \\ I_2 = {\lambda_1}^2{\lambda_2}^2 + {\lambda_1}^2{\lambda_3}^2 + {\lambda_2}^2{\lambda_3}^2 \\ I_3 = {\lambda_1}^2{\lambda_2}^2{\lambda_3}^2 \end{cases} . \tag{A.30}$$

If the characteristic polynomial is invariant then the coefficients according to (A.30) must also be invariants. The *strain invariants* of the left Cauchy-Green deformation tensor **B** are the coefficients (A.30) of the characteristic polynomial of **B**.

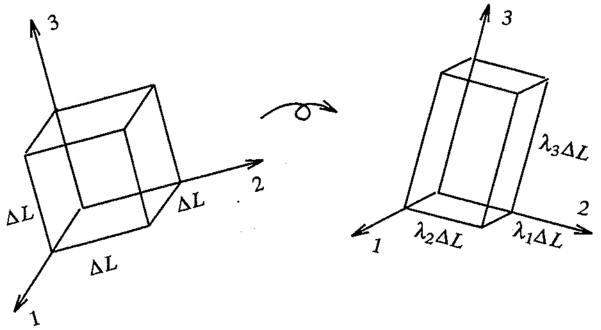

Figure A.7: *Stretching of a small cube oriented in the principal directions.*

The strain invariants can be found without solving the eigenproblem (A.28). The trace, i.e. the sum of the diagonal components, and the determinant of **B** can also be shown to be invariants. To take advantage of this property we have to rewrite the second strain invariant in expression (A.30). The second invariant can be expressed as

$$I_2 = ({\lambda_1}^2 + {\lambda_2}^2 + {\lambda_3}^2)^2 - (({\lambda_1}^2)^2 + ({\lambda_2}^2)^2 + ({\lambda_3}^2)^2) \tag{A.31}$$

Where the trace of **B** and the trace of $\mathbf{B}^2$ can be recognized. Because of the invariant property of the trace and the determinant, expression (A.30) can be written in terms of **B** only as

$$\begin{cases} I_1 = tr(\mathbf{B}) \\ I_2 = \frac{1}{2}(tr(\mathbf{B})^2 - tr(\mathbf{B}^2)) \\ I_3 = det(\mathbf{B}) \end{cases} . \tag{A.32}$$

The advantage of (A.32) is that an invariant measure of strain can be obtained by simple matrix operations without solving an eigenvalue problem.

It is possible to give a geometric interpretation of the strain invariants. A small cube oriented in the principal directions is deformed without shearing, as illustrated in Figure A.7. The side lengths of the cube are originally dL and the stretched cube has the side lengths $dl_i = \lambda_i dL$.

Computation of the space diagonal, the free surface and the volume of the cube before and after deformation generates the expressions (A.30).

The ratio of the square of the space diagonal in the deformed and the undeformed cube can be written as

$$\frac{(\lambda_1 dL)^2 + (\lambda_2 dL)^2 + (\lambda_3 dL)^2}{3dL^2} = \frac{1}{3} I_1 . \tag{A.33}$$

The ratio of the square of the surface of the deformed and the undeformed cube can be written as

$$\frac{2(\lambda_1 \lambda_2 dL^2)^2 + 2({\lambda_1}^2 {\lambda_3}^2 dL^2)^2 + 2({\lambda_2}^2 {\lambda_3}^2 dL^2)^2}{6(dL^2)^2} = \frac{1}{3} I_2 . \tag{A.34}$$

The ratio of the square of the volume in the deformed and the undeformed cube can be written as

$$\frac{(\lambda_1 dL \lambda_2 dL \lambda_3 dL)^2}{(dL^3)^2} = I_3 . \tag{A.35}$$

This interpretation of the third invariant is important in connection with incompressible materials. The condition

$$I_3 = 1$$

must be fulfilled for the deformation of an incompressible material.

A.2. Traction and Stress

Traction, the Cauchy stress tensor and its decomposition into deviatoric and hydrostatic components are the subject of this section.

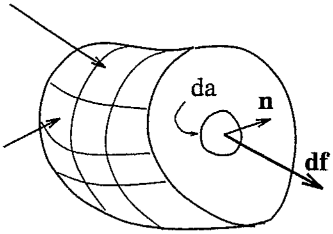

Figure A.8: *Force acting on a surface element with normal* **n**.

Neglecting body forces, the only force acting on the body is the *surface traction* t_i that acts on the boundary of the considered body, and it has the dimension of force per unit area. The *traction vector* t_i and the *stress tensor* are defined in this section.

A.2.1. Cauchy's stress tensor

The stress tensor is introduced as a quantity that determines the traction vector, in a given point, on a surface, internal or external, with arbitrary orientation. But let us first define the traction vector.

Consider a surface element da of a part of the loaded body as illustrated in Figure A.8. The surface can be internal or external i.e. it can be a part of a cross section of the body or a part of the outer surface of the body. The orientation of the surface element in the deformed body is given by the unit normal vector $\mathbf{n}$. A force $\mathbf{df}$ is acting on the surface element. The *traction vector* $\mathbf{t}$ on the surface with normal $\mathbf{n}$ is defined as

$$\mathbf{t} = \frac{\mathbf{df}}{da} \,. \tag{A.36}$$

Consider the special surfaces that are perpendicular to the coordinate directions according to Figure A.9. The traction vectors acting on surfaces with normals parallel to the axis x_1, x_2 and x_3 are denoted $\mathbf{t}_1$, $\mathbf{t}_2$ and $\mathbf{t}_3$ respectively. The components of the vectors are denoted by σ_{ij}, where i indicates the normal direction and j indicates the direction of the traction.

$$\mathbf{t}_1 = \begin{bmatrix} \sigma_{11} \\ \sigma_{12} \\ \sigma_{13} \end{bmatrix} \qquad \mathbf{t}_2 = \begin{bmatrix} \sigma_{21} \\ \sigma_{22} \\ \sigma_{23} \end{bmatrix} \qquad \mathbf{t}_3 = \begin{bmatrix} \sigma_{31} \\ \sigma_{32} \\ \sigma_{33} \end{bmatrix} , \tag{A.37}$$

where σ_{ij} are *stress components.* Components with equal indices are *normal stresses* and components with unequal indices are *shear stresses.*

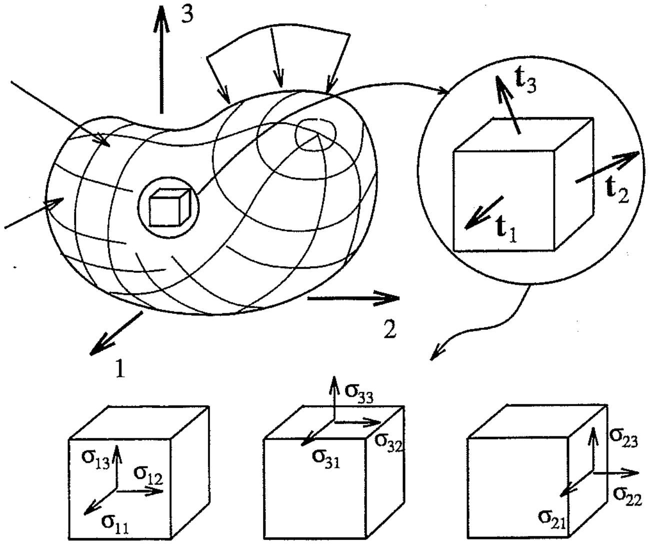

Figure A.9: *Stress components on an infinitesimal cube in a loaded body.*

The *stress tensor* σ_{ij}, in terms of the Cartesian components, can be represented by a matrix where the rows consist of the traction vectors (A.37) giving

$$\sigma = \begin{bmatrix} \sigma_{11} & \sigma_{12} & \sigma_{13} \\ \sigma_{21} & \sigma_{22} & \sigma_{23} \\ \sigma_{31} & \sigma_{32} & \sigma_{33} \end{bmatrix} . \tag{A.38}$$

In order to satisfy moment equilibrium the matrix (A.38) can be shown to be symmetric, i.e.

$$\sigma = \sigma^T . \tag{A.39}$$

The matrix (A.38) contains all the information on the state of stress in a specific point of the loaded body; cf. Figure A.9. It should be observed that the Cauchy stress components are established in the current configuration as force per deformed area.

From (A.38) we can compute the traction on a surface with arbitrary normal direction $\mathbf{n}$, by using *Cauchy's stress principle*

$$\mathbf{t} = \sigma \mathbf{n} . \tag{A.40}$$

A.2.2. Principal directions and components

The principal directions of the stress tensor are three perpendicular directions where the traction is parallel to the normal of the considered surface i.e.

$$\sigma = \begin{bmatrix} \sigma_1 & 0 & 0 \\ 0 & \sigma_2 & 0 \\ 0 & 0 & \sigma_3 \end{bmatrix} \tag{A.41}$$

there is no shear stress on the surfaces whose normals are the principal directions. The principal directions and stresses are determined from an eigenvalue problem similar to the treatment of the kinematics.

A.2.3. Stress deviator and pressure stress

The stress tensor can be divided into two parts

$$\sigma_{ij} = s_{ij} + \frac{1}{3}\sigma_{kk}\delta_{ij} \quad \text{and} \quad p = \frac{1}{3}\sigma_{kk} \tag{A.42}$$

where s_{ij} is the *deviatoric stress tensor* and p is the *mean pressure* or the pressure stress. The stress deviator tensor has the property $s_{ii} = 0$. Expressed in matrix notation,

$$\sigma = s + p\mathbf{1} \quad \text{with} \quad p = \frac{1}{3}tr(\sigma)\,. \tag{A.43}$$

A.2.4. Nominal stress

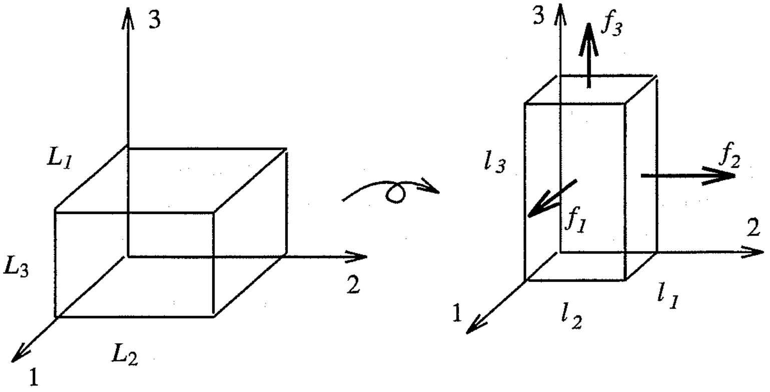

Figure A.10: *Rectangular block loaded by uniformly distributed stress.*

The *nominal stress* is defined as the current force divided by the original cross section area. The nominal stress is easy to derive from the force recorded in laboratory tests. The Cauchy stress can be computed only if the deformation is known.

A common situation in laboratory tests is that the principal axes are held fixed. This applies to the rectangular block in Figure A.10. The state of deformation is the deformation without shear given by (A.3). Suppose that the surfaces are loaded by forces f_i uniformly distributed according to Figure A.10. The nominal stress S_i and the true or Cauchy stress σ_i are

$$\begin{cases} S_1 = \dfrac{f_1}{L_2 L_3} \\ S_2 = \dfrac{f_2}{L_1 L_3} \\ S_3 = \dfrac{f_3}{L_1 L_2} \end{cases} \qquad \begin{cases} \sigma_1 = \dfrac{f_1}{l_2 l_3} \\ \sigma_2 = \dfrac{f_2}{l_1 l_3} \\ \sigma_3 = \dfrac{f_3}{l_1 l_2} \end{cases} .$$

We can get a connection between the nominal and true stress by introducing the stretch, giving the relations

$$\begin{cases} \sigma_1 = \dfrac{S_1}{\lambda_2 \lambda_3} \\ \sigma_2 = \dfrac{S_2}{\lambda_1 \lambda_3} \\ \sigma_3 = \dfrac{S_3}{\lambda_1 \lambda_2} \end{cases} .$$

The laboratory tests described in Chapter 4, except the tests that use the simple shear deformation, use the state of deformation and stress given above.